Energy deposition in air from femtosecond laser filamentation for the control of high voltage spark discharges

Guillaume Point

ECOLE POLYTECHNIQUE

ECOLE DOCTORALE ED 447 (EDX)

THESE DE DOCTORAT

par

Guillaume Point

pour l'obtention du grade de

Docteur ès sciences, mention physique

Dépôt d'énergie dans l'air par filamentation laser femtoseconde pour le contrôle des décharges électriques haute-tension

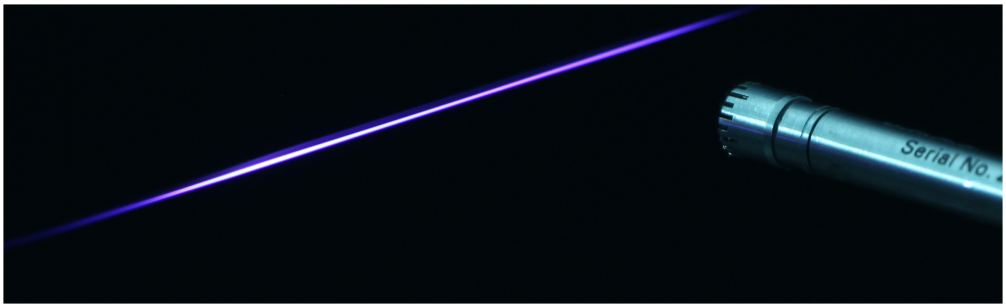

Soutenue le 10 septembre 2015 devant la commission d'examen formée de :

Patrick Mora	CNRS	Président du jury
Howard M. Milchberg	The University of Maryland	Rapporteur
Jerome V. Moloney	The University of Arizona	Rapporteur
Pascal Chabert	CNRS	Examinateur
Olivier Gobert	CEA	Examinateur
Aurélien Houard	Ecole Polytechnique	Directeur de Thèse
André Mysyrowicz	ENSTA ParisTech	Co-directeur de Thèse

Cette Thèse a été préparée au Laboratoire d'Optique Appliquée, UMR 7639.

ECOLE POLYTECHNIQUE

GRADUATE SCHOOL ED 447 (EDX)

DISSERTATION

by

Guillaume Point

submitted in partial fulfillment of the requirements for the degree of

Doctor of Philosophy, Physics

Energy deposition in air from femtosecond laser filamentation for the control of high voltage spark discharges

Defended on September 10, 2015 before the following Jury:

Patrick Mora	CNRS	President of the Jury
Howard M. Milchberg	The University of Maryland	Reviewer
Jerome V. Moloney	The University of Arizona	Reviewer
Pascal Chabert	CNRS	Examiner
Olivier Gobert	CEA	Examiner
Aurélien Houard	Ecole Polytechnique	Ph. D. supervisor
André Mysyrowicz	ENSTA ParisTech	Ph. D. co-supervisor

This Ph. D. Thesis was prepared at the Laboratoire d'Optique Appliquée, UMR 7639.

Acknowledgments

If I had to summarize the time I spent during the preparation of my Thesis in a few words only, I would say that this time went too fast. These last three (and a half, including my internship!) years have really been delightful. Professionally, of course, because I learned a lot in optics, in physics in general, but not only. This time as a Ph. D. student was also an incredible personal experience. I had the chance to meet very interesting people that taught me a great many things.

First, all my gratitude goes to my supervisors, Aurélien Houard and André Mysyrowicz. Since the very first day in the lab, I have really felt at home due to their warm welcome and kindness. Thank you Aurélien for always being available, for sharing your vast knowledge and for your permanent support in all my endeavors. This Thesis would definitively not have been possible without you. Though I am still working with you these days, I will deeply miss all the good time we had together once I have left. Who knows, perhaps I will keep playing badminton with you and the rest of the group. Just remember that I am a sore loser, in the improbable case you might win the match! In any case, we will certainly keep meeting around a glass or two some other times. André, I deeply thank you for trusting me from the very beginning, giving me enough self-confidence to achieve most of the work performed during my Thesis, not to mention the numerous discussions we had about the latest experimental results. I am really indebted to you and to your incredible physical knowledge and physical sense. Be sure that I will gladly keep joining you for one of the weekly (or so) "out-of-the-Magnan" lunches, either at the Chinese restaurant or at the Balto, that became the norm when the food quality began to deteriorate at Polytechnique.

I also want to thank Antoine Rousse for giving me the opportunity to perform research at the Laboratoire d'Optique Appliquée and for his precious advice for my future career.

Of course, these years of hard work would not have been the same without the rest of the ILM team. I warmly thank Yohann Brelet, with whom I shared a lot of (good) time in the experiment room from the beginning, but also in the outside for a football session in the bar or around a bottle of good [1] wine. As for the experiments themselves, I doubt I could have made them without Jérôme Carbonnel [2], our talented laser/mechanics expert with a rock-solid sense of humor. Another great thank to Leonid Arantchouk, with whom I had the chance to work. I was (and still am) amazed by his mastery of high-voltage equipment. Of course I wanted to thank Yi Liu for all the discussions we shared about the lasing effect, Yves-Bernard André for his unmatched ability to find solutions to even the most desperate situations, Bernard Prade for his incredible knowledge of optics, my fellow former Ph. D. students Amélie Jarnac and Sergey Mitryukovskiy with whom I spent a lot of good time, and my fellow current Ph. D. student Peng-Ji Ding, always willing to take a drink or

[1] actually, the quality of the wine appeared not to matter as long as it was red

[2] or JCE, for those who are familiar with the term

more, especially during conferences. Also a big thank to the last arrived in the team: Emmanuelle Thouin [3] and Vytautas Jukna, with whom I have been sharing the experiment room for the last year, but also very good time home or in the bar. Although not (formally) part of the team, I also wanted to thank Julien Labaune for the nice time we had together.

Now I come to all the people with whom I had the chance to collaborate outside of my team. I am particularly indebted to Arnaud Couairon and Carles Milián from the CPhT, Ecole Polytechnique, for their never-ending theoretical support of the experimental work done at the LOA. I would like to also thank Carles for the good time we have been spending for the last few months [4]. I am grateful to Jean Larour from the LPP, Ecole Polytechnique for the collaboration we shared on several projects. As the main funding of my research, the DGA needs a special dedication. It was a real pleasure to take part in the contracts for the virtual plasma antenna, but also to participate to reunions with Sylvain Flajolet, Besma Larbi and Michel Pellet. I would also like to thank all the industrial partners of my team: the Airbus group and particularly Denis Chapuis for his permanent interest in my research, but also Trumpf Scientific for allowing us to perform research using their lasers.

Of course, I thank the Ecole Polytechnique and all its former students for funding me during the last three years.

I already thanked my research team, but my whole lab deserves to be thanked as well. First, I am really grateful to the skilled administration: Patricia Toullier, Octavie Verdun, Sandrine Tricaud, Carole Gratpanche and Lucie Huguet. No experiment would have been possible without the technical assistance of the mechanics division: Jean-Lou Charles, Mickaël Martinez and Bernard Allali. This is not to mention the help of Maxence Le Sourd and his expertise with computers. I also want to thank Magali Lozano, Geoffrey Gallé, Maxence Thévenet for the numerous coffee breaks we shared, and everyone else in the lab.

I wanted to renew my thanks to all the members of the Jury for being present at my defense: Howard Milchberg and Jerome Moloney, who had to cross the Atlantic Ocean, Patrick Mora for accepting to preside the Jury, but also Pascal Chabert and Olivier Gobert.

Last but definitely not least, I thank my family and particularly my parents. To finish, I wanted to express all my gratitude to Tania for being here and supporting me during all this time. I owe you a lot for the quality of the work I performed in this Thesis, and I hope I will be able to repay my debt soon enough (hopefully before the next spring!).

Guillaume Point
September 16, 2015

[3] who was expected to replace Yohann in every aspect but it proved be too ambitious, particularly concerning the red wine

[4] despite the apparent lack of time due to the manuscript redaction

Contents

General introduction

Laser filamentation is a fascinating phenomenon. While linear optics taught us to expect any light beam to eventually diffract and dilute its intensity with propagation distance, sufficiently powerful laser pulses instead tend to self-focus and collapse in the form of very thin and intense light strings. These strings, or filaments, are able to maintain their high intensity level over several Rayleigh lengths, which is a spectacular manifestation of nonlinear optics. This effect can occur in any transparent medium and, in the case of air, results from the establishment of a dynamic competition between opposite effects: on the one hand the Kerr effect, which is responsible for the beam self-focusing and, on the other hand, nonlinear absorption of laser energy through ionization and rotational Raman excitation of air molecules, plasma defocusing and diffraction. The first part of this Thesis is dedicated to the description of the propagation of laser pulses in air, first in the linear regime and then in a nonlinear medium where the dominant nonlinearity is of order 3. The origin of the air dielectric response is studied and discussed. It is shown that given a laser pulse is powerful enough, it will eventually evolve spontaneously to form a filament. The characteristics of filaments are then detailed, and a brief state of the art of filament properties and applications is given. Finally a brief introduction to the numerical methods used to model filamentation is made.

As an ultrashort laser pulse propagates through air and forms a filament, it deposits energy in the medium mainly through ionization and rotational Raman absorption. This energy is converted into translational energy of neutral molecules after plasma recombination and rotational de-coherence, which takes on the order of 1 ns. The quick heating of a small volume of air yields a high thermal energy density, which relaxes by launching an outward-propagating cylindrical pressure wave. This wave ejects matter from the center and leaves an underdense air channel, which then evolves diffusively. The second part of this Thesis focuses on the study of energy deposition from laser filamentation in air. In the Chapter 2, I detail all the physical mechanisms involved in this process, and I present the experimental diagnostics I implemented on filaments to characterize deposited energy. Chapter 3 is dedicated to the results recorded during the study of single filaments. More specifically I showed that single filamentation can easily result in an initial air heating at the ~ 1000 K level, resulting in the generation of a shock wave and of a very long-lived (~ 100 ms) underdense channel. I also investigated a potential application for such laser-induced air structures: a virtual axicon lens. Finally, Chapter 4 deals with energy deposition from laser pulses with very high peak power, generating a large bundle of co-propagating filaments. In a first part, I studied such bundles created using moderate focusing of laser pulses. I showed this resulted in a new propagation regime reached in the focal zone where standard filaments give way to a large ionized volume with a few plasma channels with a peak electron density one order of magnitude higher. In a second part, energy deposition resulting from these *superfilaments* is characterized in a

similar way as in Chapter 3. I show that if reached peak energy densities are not significantly higher than for single filaments, the corresponding heated volume is much larger. This could prove crucial in the optimization and improvement of the applications of filamentation-induced hydrodynamics.

One of the main features of these laser-induced effects in air is the generation of very long-lived low-density air channels. As density is decreased along the laser path, this can be used to trigger electric discharges using a voltage below the natural breakdown voltage in atmospheric air following the Paschen's law. Such discharges will also display a characteristic, unnatural straight form, being effectively guided by the laser. The third and final part of this Thesis is dedicated to the study of this beautiful phenomenon and of its numerous applications. All mechanisms related to the triggering and guiding of electric discharges are first presented in the Chapter 5. Chapter 6 deals with a sensitive and accurate plasma diagnostic for electron density that I developed specifically for the study of filamentation-guided discharges. This instrument, a two-color interferometer, has the ability to give a simultaneous recording of electron density and of neutral density in the plasma, which proves invaluable to catch both the discharge plasma dynamics and the breakdown-induced strong hydrodynamics encountered in sparks. The three last Chapters individually focus on different applications of filamentation-triggered sparks. Chapter 7 is dedicated to the studies I performed on a filamentation-triggered gap switch designed at the Laboratoire d'Optique Appliquée for contactless transfer of high currents and high voltages. This gap switch was then used as the building block for a new Marx generator entirely triggered by filaments, which is able to deliver a voltage pulse with a very steep initial wavefront. Chapter 8 focuses on a new kind of virtual radio-frequency plasma antenna, where the metallic emitter is replaced by the plasma from guided discharges. I contributed to the proof of principle experiments using filamentation-guided discharges from a Tesla coil. A 1 m long emitting antenna was thus demonstrated over a broad frequency range (500 - 1200 MHz). However the on-state time of this antenna is directly dependent on the spark plasma lifetime, initially a few microseconds. The lengthening of this lifetime is achieved using a secondary electric circuit injecting charges in the plasma over the ms timescale. This technique was tested using our filamentation-triggered Marx generator and characterized using my plasma diagnostic. Finally, Chapter 9 is dedicated to prospective studies done in collaboration with the Airbus Group for the development of a laser lightning rod. Thus, I took part in an experimental campaign at high-voltage facilities where the feasibility of the most realistic scenario for the lightning rod was demonstrated. These results give good hope that one day mankind would be able to control the fascinating, though destructive, phenomenon of lightning.

Part I

Description of filamentation in air

Chapter 1

Propagation of intense ultrashort laser pulses in air

Contents

Introduction

A brief history of optics

Linear optics phenomena have been known for centuries. Since this regime characterizes the propagation of low intensity radiation, it was therefore readily observable by mankind. This led to the development of the geometrical optics framework in the 16^{th} and 17^{th} century with the works of Galileo Galilei, Snell and Descartes. From the 17^{th} century on, the wave theory of light started to develop, thanks to the founding works of Huygens and his principle enunciating that any point of space on which falls an incoming light wave in turn radiates a new, spherical wave. However, the rejection of this theory by Newton, who had previously established a corpuscular theory of light, hampered further study in this field for almost a century. It is only in the 19^{th} century that the wave theory prevailed with the impressive contribution of Fresnel, eventually modeling phenomena such as interference or diffraction that geometrical optics were unable to explain. Almost at the same time, Maxwell, relying on previous discoveries by Faraday, managed to develop his unified electromagnetic theory and formed the hypothesis that light waves are actually electromagnetic waves, which was experimentally demonstrated by Hertz at the end of the century. The early 20^{th} century was marked by the advent of quantum physics following Planck and Bohr. Einstein, on the basis of Planck's work, revived the corpuscular theory in his description of the photoelectric effect, re-conciliating corpuscular and wave theories through the wave-particle duality characteristic of quantum mechanics [1].

In his other famous papers from 1916-1917, Einstein established the working principles of basic light-matter interaction and, more specifically, of stimulated emission [2, 3]. Science had to wait for several decades before this idea could be finally experimentally implemented, first in the microwave frequency domain with the maser [4], and then by Maiman in 1960 when he was the first to demonstrate a working laser [5]. With such a tool at hand, optics truly underwent a revolution. Soon, lasers were well developed as to reach significant intensities, high enough to witness the appearance of nonlinear effects. The first identified nonlinear optical effect was second-harmonic generation from a ruby laser by Franken *et al.* [6]. The nonlinear response of the medium can also lead to a change of its refractive index, which in turn reacts on the propagating pulse, modifying its properties.

Since then, the peak intensity reached by lasers has steadily increased due to the development of specific techniques aimed at increasing pulse energies and/or decreasing pulse durations. First, the Q-switching technology, which postdates the laser by only two years, brought available peak power at the gigawatt level with pulses on the order of 10 ns [7]. Mode-locking technology, which was developed in the 1960s as well, proved to be able to generate pulses down to picosecond durations with solid lasers [8]. Dye lasers, characterized by a very broadband emission spectrum, were able to reach down the femtosecond regime using this technique [9]. Finally, the advent of the chirped pulse amplification (CPA) technique allowed the generation of arbitrarily energetic pulses with very short pulse duration [10]. Together with Ti:sapphire crystal-based mode-locked lasers, the CPA technique brought about the age of femtosecond lasers. Nowadays, most ultrashort pulsed lasers are using this technology, which truly democratized the study of nonlinear optics phenomena.

Presentation of the chapter

This chapter is dedicated to the physical description of nonlinear optics. More specifically, it focuses on the role of the Kerr effect and its consequences on the propagation of ultrashort pulses. Finally,

the filamentation propagation regime is described, with a detailed presentation of the physical mechanisms involved and a brief introduction to numerical simulations.

1.1 Propagation of light in transparent media in the linear regime

1.1.1 Derivation of the propagation equation

Propagation of light in any transparent medium is described by Maxwell's equations which can be macroscopically written as:

$$\begin{cases} \vec{\nabla}.\vec{D}(\vec{r},t) = \rho(\vec{r},t) \\ \vec{\nabla} \times \vec{E}(\vec{r},t) = -\dfrac{\partial \vec{B}}{\partial t}(\vec{r},t) \\ \vec{\nabla}.\vec{B}(\vec{r},t) = 0 \\ \vec{\nabla} \times \vec{H}(\vec{r},t) = \vec{j}(\vec{r},t) + \dfrac{\partial \vec{D}}{\partial t}(\vec{r},t), \end{cases} \tag{1.1}$$

where the displacement field $\vec{D}$ and magnetizing field $\vec{H}$ read as:

$$\begin{cases} \vec{D} = \epsilon_0 \vec{E} + \vec{P} \\ \vec{H} = \dfrac{\vec{B}}{\mu_0} - \vec{\mathcal{M}}, \end{cases} \tag{1.2}$$

$\vec{E}$ being the electric field, $\vec{P}$ the polarization field, $\vec{B}$ the magnetic field and $\vec{\mathcal{M}}$ the magnetization field. We will consider that the propagation medium is not magnetized ($\vec{\mathcal{M}} = \vec{0}$), an hypothesis that we will keep in all the presented work. We can thus derive the following equation:

$$\vec{\nabla} \times \left(\vec{\nabla} \times \vec{E}(\vec{r},t)\right) = \vec{\nabla}\left(\vec{\nabla}.\vec{E}(\vec{r},t)\right) - \Delta\vec{E}(\vec{r},t) = -\mu_0 \left(\frac{\partial \vec{j}}{\partial t}(\vec{r},t) + \frac{\partial^2 \vec{D}}{\partial t^2}(\vec{r},t)\right). \tag{1.3}$$

If we suppose the medium being without free charges ρ or current $\vec{j}$, then we have:

$$\begin{cases} \vec{\nabla}.\vec{D} = 0 \\ \vec{\nabla}\left(\vec{\nabla}.\vec{E}(\vec{r},t)\right) - \Delta\vec{E}(\vec{r},t) = -\mu_0 \dfrac{\partial^2 \vec{D}}{\partial t^2}(\vec{r},t). \end{cases} \tag{1.4}$$

We first consider the propagation of electromagnetic waves with a corresponding intensity low enough so that no nonlinear effects can occur (we will come back to this point later and give appropriate quantification to that assertion). In this *linear* regime, the polarization $\vec{P}$ and the electric field $\vec{E}$ are linked through the following relation:

$$\vec{P}(\vec{r},t) = \epsilon_0 \int_{-\infty}^{+\infty} H(t')\overline{\chi_e^{(1)}}(\vec{r},t') : \vec{E}(\vec{r},t-t')\ \mathrm{d}t', \tag{1.5}$$

where $\overline{\chi_e^{(1)}}$ is a second-order tensor and $\overline{\chi_e^{(1)}} : \vec{E} = \chi_{e\ \beta}^{(1)\ \alpha} E^\beta$ is the dyadic product operation using the Einstein notation. This last equation can be physically understood as if the medium response to the excitation of the electric field was delayed, thus resulting in the cumulative contribution from all times before t. Causality imposes, of course, that this integral stops at t, hence the Heaviside step function H. Thus defining the frequency domain linear susceptibility $\overline{\chi_e^{(1)}}(\vec{r},\omega)$ as:

$$\overline{\chi_e^{(1)}}(\vec{r},\omega) = \frac{1}{\sqrt{2\pi}} \int_{\mathbb{R}} H(t)\overline{\chi_e^{(1)}}(\vec{r},t)\mathrm{e}^{i\omega t}\ \mathrm{d}t, \tag{1.6}$$

we find the constitutive relation between $\vec{P}$ and $\vec{E}$ in the Fourier domain:

$$\vec{P}(\vec{r},\omega) = \epsilon_0 \overline{\chi_e^{(1)}}(\vec{r},\omega) : \vec{E}(\vec{r},\omega). \tag{1.7}$$

Finally, the propagation equation for the electric field reads:

$$\vec{\nabla}\left(\vec{\nabla}.\vec{E}(\vec{r},\omega)\right) - \Delta\vec{E}(\vec{r},\omega) = \frac{\omega^2}{c^2}\left(\vec{E}(\vec{r},\omega) + \overline{\chi_e^{(1)}}(\vec{r},\omega) : \vec{E}(\vec{r},\omega)\right). \tag{1.8}$$

The propagation media which will be studied in this Thesis are mostly gaseous, such as air. In this respect, we can make two important approximations: first, gases are isotropic media, meaning we can write the susceptibility tensor as:

$$\overline{\chi_e^{(1)}} = \chi_e^{(1)}\overline{\delta}, \tag{1.9}$$

where $\overline{\delta}$ is the unity tensor. Second, since gases are a dilute medium, their linear refractive index n, defined as $n^2 = 1 + \chi_e^{(1)}$, is close to 1 (usually, $n - 1 \sim 10^{-4}$), meaning that their polarization response is very low [11]. We thus have:

$$\vec{D} = \epsilon_0\left(1 + \chi_e^{(1)}\right)\vec{E} \approx \epsilon_0\vec{E}, \tag{1.10}$$

then:

$$\vec{\nabla}.\vec{D} = 0 \approx \vec{\nabla}.\vec{E}, \tag{1.11}$$

and we finally have the following simplified propagation equation:

$$\Delta\vec{E}(\vec{r},\omega) + \frac{\omega^2 n^2(\vec{r},\omega)}{c^2}\vec{E}(\vec{r},\omega) = \vec{0}. \tag{1.12}$$

It is worth mentioning that the magnetic field $\vec{B}$ obeys exactly the same propagation equation.

We will now consider the propagation of a light pulse defined as:

$$\vec{E}(\vec{r},t) = \frac{1}{2}\vec{\mathcal{E}}(\vec{r},t)\mathrm{e}^{i(\vec{k}(\omega_0).\vec{r}-\omega_0 t)} + c.\ c., \tag{1.13}$$

where $\mathcal{E}$ corresponds to the envelope of the electric field and $\vec{k}(\omega_0) = k(\omega_0)\vec{e_z}$. If we introduce the wavevector $k(\omega) = \omega n(\omega)/c$, equation (1.12) yields:

$$\left(\Delta_\perp + \partial_z^2 + 2ik(\omega_0)\partial_z + k(\omega)^2 - k(\omega_0)^2\right)\vec{\mathcal{E}}(\vec{r},\omega) = \vec{0}. \tag{1.14}$$

We do not expect the pulse spread in both spatial frequency and time frequency domains to be large compared to $k(\omega_0)$ and ω_0, respectively, so that we can derive a Taylor expansion of $k(\omega)$:

$$k(\omega)^2 = k(\omega_0)^2 + 2k(\omega_0)\frac{\partial k}{\partial\omega}(\omega_0)(\omega-\omega_0) + \left(\left(\frac{\partial k}{\partial\omega}(\omega_0)\right)^2 + k_0\frac{\partial^2 k}{\partial\omega^2}(\omega_0)\right)\frac{(\omega-\omega_0)^2}{2} + o(\omega^2). \tag{1.15}$$

An expansion to order 2 is usually sufficient to have an adequate simulation of the propagation of a femtosecond pulse [12]. We should take the notation $k(\omega_0) = k_0$, $\partial k/\partial\omega(\omega_0) = k_0'$ and $\partial^2 k/\partial\omega^2(\omega_0) = k_0''$. The inverse of k_0' and k_0'' are usually referred to as the group velocity and the group velocity dispersion, respectively. Injecting this expansion in equation (1.14) and getting back to the temporal space gives:

$$\left(\Delta_\perp + \partial_z^2 + 2ik_0\partial_z + 2ik_0k_0'\partial_t - (k_0'^2 + k_0k_0'')\partial_t^2\right)\vec{\mathcal{E}}(\vec{r},t) = \vec{0}. \tag{1.16}$$

We now rewrite the propagation equation in the reference frame of the laser pulse by the following variable change:

$$\begin{cases} t' = t - k_0'z \\ z' = z. \end{cases} \tag{1.17}$$

Equation (1.16) thus gives:

$$\left(\Delta_\perp + \partial_{z'}^2 + k_0'^2\partial_{t'}^2 - 2k_0'\partial_{z'}\partial_{t'} + 2ik_0\partial_{z'} - 2ik_0k_0'\partial_{t'} + 2ik_0k_0'\partial_{t'} - (k_0'^2 + k_0k_0'')\partial_{t'}^2\right)\vec{\mathcal{E}}(\vec{r},t) = \vec{0}. \tag{1.18}$$

After simplification, we finally find:

$$\left(\Delta_\perp + \partial_{z'}^2 - 2k_0'\partial_{z'}\partial_{t'} + 2ik_0\partial_{z'} - k_0k_0''\partial_{t'}^2\right)\vec{\mathcal{E}}(\vec{r},t) = \vec{0}. \tag{1.19}$$

A last approximation can be made at this point, which is the well know slowly varying envelope approximation (SVEA), namely:

$$\partial_{z'}^2 \ll k_0\partial_{z'}, \tag{1.20}$$

which means that spatial variations of the envelope occur over distances much larger than the wavelength. Fulfilling the SVEA is usually not difficult, but can become tricky in the case of pulses as short as a single cycle. Brabec and Krausz proved that a modified approximation, so-called *slowly evolving wave approximation*, characterized by $\partial_{z'} \ll k_0$, would be able to cope with such short pulses [13]. Now introducing the operator $\hat{K} = k_0 + ik_0'\partial_{t'}$, the linear propagation equation is finally expressed as:

$$\left(\Delta_\perp + 2i\hat{K}\partial_{z'} - k_0k_0''\partial_{t'}^2\right)\vec{\mathcal{E}}(\vec{r},t) = \vec{0}. \tag{1.21}$$

1.1.2 Discussion of the solutions to the propagation equation

1.1.2.1 Gaussian beams

In the simplest case, we can neglect the group velocity dispersion. Likewise, if we assume the frequency spread of the pulse to be narrow with respect to ω_0, we can simplify the $\hat{K}$ operator since, in the frequency Fourier space, it reads:

$$\mathcal{F}(\hat{K}) = k_0 + k_0'(\omega - \omega_0) \sim k_0\left(1 + \frac{\omega - \omega_0}{\omega_0}\right) \approx k_0. \tag{1.22}$$

The propagation equation, in this case, is reduced to:

$$\left(\Delta_\perp + 2ik_0\partial_{z'}\right)\vec{\mathcal{E}}(\vec{r},t) = \vec{0}, \tag{1.23}$$

which is known as the paraxial approximation of the Helmholtz propagation equation. Solutions for this last equation are well known. Depending on the symmetry properties of the system, it gives rise to a complete orthogonal basis of transverse electromagnetic solutions like Hermite-Gauss modes for a Cartesian reflection symmetry, or like Laguerre-Gauss modes for a cylindrical symmetry [14]. For all these bases, the lowest order solution is always given by the well-known Gaussian beam described by:

$$E(\vec{r},t) = E(r,z,t) = \frac{1}{2}\mathcal{E}_0(t)\frac{w_0}{w(z)}\exp\left(-\frac{r^2}{w(z)^2} - ik_0\frac{r^2}{2R(z)} + i\varphi_G(z)\right)\exp(i(k_0z - \omega_0t)) + c.\,c., \tag{1.24}$$

where the spot characteristic half-width $w(z)$, radius of curvature $R(z)$ and Gouy phase φ_G are given by:

$$\begin{cases} w(z) = w_0\sqrt{1 + \dfrac{z^2}{L_R^2}} \\ R(z) = z\left(1 + \dfrac{L_R^2}{z^2}\right) \\ \varphi_G = \arctan\left(\dfrac{z}{L_R}\right). \end{cases} \tag{1.25}$$

Here, we introduced the beam waist $w_0 = w(0)$, which is the minimum radial extension that the beam will be able to reach during its propagation, and the Rayleigh length:

$$L_R = \pi w_0^2/\lambda, \tag{1.26}$$

which is the characteristic length for diffraction, or transverse spread, of Gaussian beams. Figure 1.1 displays the evolution of the beam radial extension $w(z)$ with z for a 800 nm beam with a 500 µm waist. From the definition of L_R, it can readily be seen that the narrower the beam waist, the faster the beam diffraction.

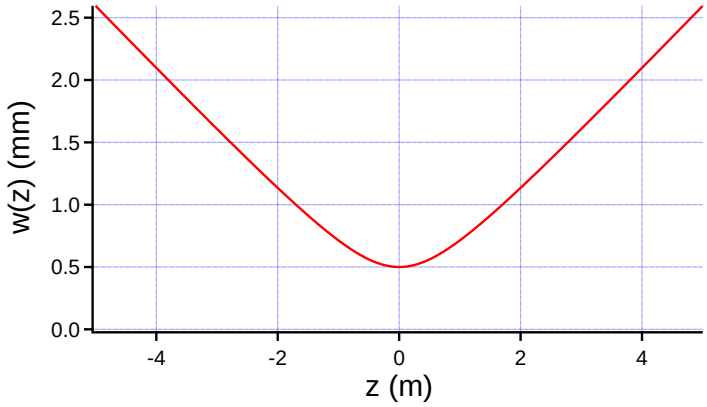

Figure 1.1: Evolution of the width $w(z)$ of a Gaussian beam of waist $w_0 = 500$ µm at a wavelength of 800 nm.

Gaussian beams are fundamental in optics, so much that most real beams are effectively modeled as Gaussian. One can use the M^2 parameter to evaluate the closeness of any beam to that of an ideal Gaussian beam, formally defined through the following relation:

$$W_{x/y}^2(z) = W_{x/y}(z_0)^2 + (M_{x/y}^2)^2 \frac{\lambda^2}{\pi^2 W_{x/y}(z_0)^2}(z - z_{0,x/y})^2. \tag{1.27}$$

Here, $z_{0,x}$ defines the position along the propagation axis where the second moment width W_x is minimum. The latter parameter is defined by:

$$W_x^2(z) = \frac{\int_{\mathbb{R}} (x - x_0)^2 I(x,y,z)\ \mathrm{d}x\mathrm{d}y}{\int_{\mathbb{R}} I(x,y,z)\ \mathrm{d}x\mathrm{d}y}, \tag{1.28}$$

I being light intensity and $x_0 = \int_{\mathbb{R}} xI(x,y,z)\ \mathrm{d}x\mathrm{d}y / \int_{\mathbb{R}} I(x,y,z)\ \mathrm{d}x\mathrm{d}y$ is the average position of the intensity distribution at z [15]. In this respect, the beam waist and therefore the Rayleigh length can be used generally for a quick estimation of diffraction effects on a given beam, whatever its real spatial profile.

1.1.2.2 Linear propagation of ultrashort pulses: group velocity dispersion

We will now look at the effect of group velocity dispersion, which was neglected in the previous section, on the propagation of laser pulses. Let us make the widespread supposition that the temporal shape of the pulse is Gaussian:

$$\vec{\mathcal{E}}(\vec{r},t) = \vec{\mathcal{E}_0}(\vec{r})\mathrm{e}^{-t^2/2\sigma_t^2}. \tag{1.29}$$

The propagation equation for this envelope is given by (1.21). In this equation, we will reduce the $\hat{K}$ operator in the same way as before ($\hat{K} \approx k_0$), and neglect the transverse Laplacian operator (that is, diffraction). This last hypothesis is valid if the characteristic propagation distance of the pulse is far shorter than the Rayleigh length L_R, which we will suppose true (this condition can be readily satisfied by, for instance, using a large beam). We thus have:

$$\left(2i\partial_z - k_0''\partial_t^2\right)\vec{\mathcal{E}}(\vec{r},t) = \vec{0}. \tag{1.30}$$

In the Fourier frequency space, this gives immediately:

$$\left(\partial_z - \frac{ik_0''\omega^2}{2}\right)\vec{\mathcal{E}}(\vec{r},\omega) = \vec{0}. \tag{1.31}$$

Expressing the Fourier transform of $\vec{\mathcal{E}}(\vec{r},t)$, we find, for an arbitrary position z:

$$\vec{\mathcal{E}}(\vec{r},\omega) = \vec{\mathcal{E}_0}(x,y,z=0)\sigma_t \mathrm{e}^{-\sigma_t^2\omega^2/2}\mathrm{e}^{ik_0''\omega^2 z/2}. \tag{1.32}$$

Bringing back this expression in the temporal domain using inverse Fourier transform yields:

$$\vec{\mathcal{E}}(\vec{r},t) = \vec{\mathcal{E}_0}(x,y,z=0)\frac{\sigma_t}{\sqrt{\sigma_t^2 - ik_0''z}}\exp\left(-\frac{t^2}{2\sigma_t^2\left(1+\frac{k_0''^2z^2}{\sigma_t^4}\right)} + i\frac{k_0''z}{\sigma_t^4 + k_0''^2z^2}\right). \tag{1.33}$$

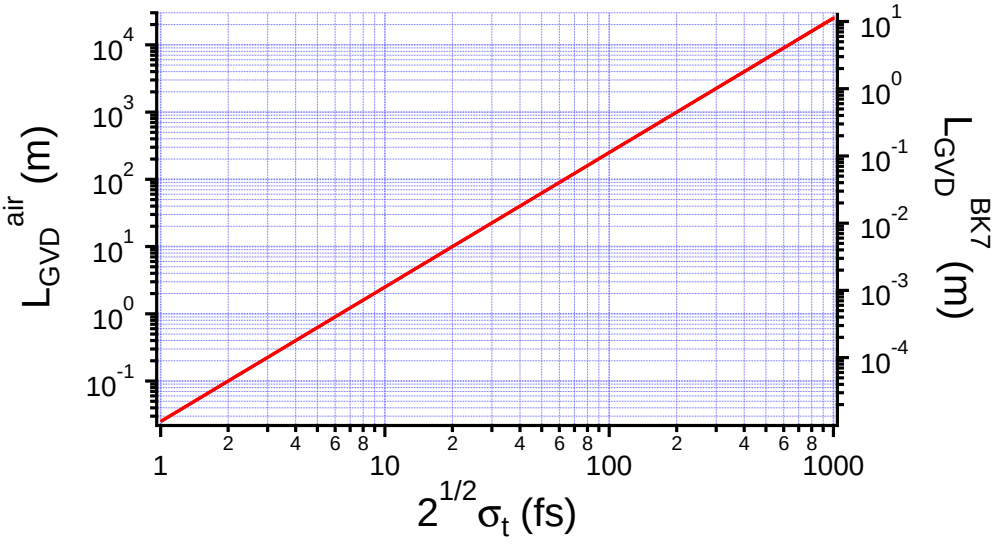

Figure 1.2: Evolution of L_{GVD} with the initial duration of a 800 nm laser pulse propagating in air (left) and BK7 optical glass (right).

Finally, we find another Gaussian temporal envelope, but with a characteristic width:

$$\sigma_t(z) = \sigma_t\sqrt{1 + \frac{k_0''^2z^2}{\sigma_t^4}}. \tag{1.34}$$

This equation is analogous to the expression of $w(z)$ for a Gaussian beam in equation system (1.25). In the same way as we introduced the Rayleigh length as a characteristic length for diffraction, i.

e. transverse spatial spread of the beam during propagation, we can define a characteristic length for the temporal spread of the pulse due to group velocity dispersion. This length, L_{GVD}, can be readily expressed as:

$$L_{GVD} = \frac{\sigma_t^2}{k_0''}. \tag{1.35}$$

It corresponds to the propagation distance for which dispersion results in the pulse being lengthened by a factor $\sqrt{2}$. Using the value $k_0'' = 20$ fs^2 $\cdot$ m^{-1} for atmospheric air and $k_0'' = 4.5 \times 10^4$ fs^2 $\cdot$ m^{-1} for BK7 glass at 800 nm, we can estimate the influence of group velocity dispersion on the propagation of ultrashort pulses. Figure 1.2 displays the evolution of L_{GVD} at 800 nm with the pulse initial duration in these two media. A typical experimental setup usually involves propagation through $\sim 1-10$ cm of glass and $\sim 1-10$ m of air, meaning that group velocity dispersion will affect significantly pulses with initial duration shorter than 100 fs.

1.1.3 Conclusion on the linear regime

The study of the propagation of pulses in the linear regime already brings useful information. We first highlight the importance of Gaussian beams and the fact that any beam spatial profile can be related to the Gaussian case through the use of the M^2 parameter. This enables one to quickly estimate diffraction effects on the beam by the simple evaluation of the corresponding Rayleigh length. Second, it also showed the deleterious effect of group velocity dispersion on pulses with duration shorter than ~ 100 fs for relatively long range propagation.

Both diffraction and group velocity dispersion result in the quick decrease of the peak intensity of an ultrashort laser pulse during propagation. Because of this, it was thought that such pulses could not efficiently propagate in air over long distances, until the fundamental discovery of Braun *et al.* [16], which first demonstrated self-channeling of femtosecond pulses, a new propagation regime with negligible diffraction and group velocity dispersion effects, that is typically a nonlinear propagation regime.

1.2 Dielectric response of propagation media and non-linearity

1.2.1 Linear dielectric response

1.2.1.1 Origin of the linear dielectric response

In the previous section, we introduced the linear dielectric susceptibility tensor $\overline{\chi_e^{(1)}}$ without any comments on its physical origin. To this purpose, we will now get back on this point and link $\overline{\chi_e^{(1)}}$ to the microscopic properties of the propagation medium. The classical Lorentz model (or so-called elastically-bound electron model) for the linear susceptibility considers excitation of an atom-bound electron by the laser electromagnetic field. As we consider a non-relativistic electron (i. e. $v_e \ll c$), we can neglect the magnetic Lorentz force. Dynamics of the electron are thus solution of the following equation:

$$m_e \partial_t^2 \vec{r} = -e\vec{E}(\vec{r},t) - m_e\omega_0^2 \vec{r} - 2m_e\gamma\partial_t \vec{r}, \tag{1.36}$$

where m_e is the electron mass and $-e$ its charge. In this modeling, the at-rest electron is located at an equilibrium position corresponding to the bottom of a harmonic potential well. When the electron is taken away from this equilibrium position by the electric field, it starts oscillating

around it with a frequency ω_0. These oscillations are damped with a characteristic time $1/2\gamma$. Taking equation (1.36) in the Fourier frequency domain, we find:

$$-m_e\omega^2\vec{r}(\omega) = -e\vec{E}(\vec{r},\omega) - m_e\omega_0^2\vec{r} + im_e\omega 2\gamma\vec{r}. \tag{1.37}$$

This leads to:

$$\vec{r}(\omega) = \frac{-e\vec{E}(\vec{r},\omega)/m_e}{\omega_0^2 - \omega^2 - 2i\gamma\omega}. \tag{1.38}$$

Polarization can be expressed as $\vec{P} = -n_n e\vec{r}$, n_n being the density of all species with bound electrons, and so the linear dielectric susceptibility is finally found to be:

$$\overline{\chi_e^{(1)}}(\vec{r},\omega) = \frac{n_n(\vec{r})e^2/\epsilon_0 m_e}{\omega_0^2 - \omega^2 - 2i\gamma\omega}. \tag{1.39}$$

Several remarks can be made about this simple modeling. The first one is that does not account for the tensor nature of $\overline{\chi_e^{(1)}}$. However, as we are working in isotropic media, this point can be turned down. The second one is that most atoms and molecules have more than one bound electron.

The correct way to link $\overline{\chi_e^{(1)}}$ to the properties of the medium is to use a quantum mechanical approach. Such modeling is based on a first-order perturbative development of the atomic wavefunction with respect to the atomic Hamiltonian:

$$\hat{H}(t) = \hat{H}_0 + \hat{V}(t) = \hat{H}_0 - \hat{\vec{\mu}}.\vec{E}(t) = \hat{H}_0 + e\hat{\vec{r}}.\vec{E}(t), \tag{1.40}$$

where we suppose that $\langle\hat{V}\rangle \ll \langle\hat{H}_0\rangle$ [17]. Supposing that all the population lies in the ground state $|g\rangle$, this leads to the following expression for the linear susceptibility tensor components:

$$\chi_{e,i,j}^{(1)}(\vec{r},\omega) = \frac{n_n(\vec{r})}{\epsilon_0\hbar}\sum_n\left(\frac{\mu_{g,n}^i\mu_{n,g}^j}{\omega_{n,g} - \omega - i\gamma_{n,g}} + \frac{\mu_{n,g}^i\mu_{g,n}^j}{\omega_{n,g} + \omega + i\gamma_{n,g}}\right). \tag{1.41}$$

In this equation, $\mu_{g,n}^i = \langle g|\,\hat{\vec{\mu}}\,|n\rangle.\vec{e}_i$ is the expectation value of the dipole operator between levels $|n\rangle$ and $|g\rangle$, of which characteristic resonance frequency is $\omega_{n,g}$. For an isotropic medium (which, once more, will be our case), assuming that relaxation factors $\gamma_{n,g} \ll \omega,\omega_{n,g}$, we find:

$$\chi_e^{(1)}(\vec{r},\omega) \approx \sum_n f_{n,g}\frac{N(\vec{r})e^2/\epsilon_0 m_e}{\omega_{n,g}^2 - \omega^2 - 2i\omega\gamma_{n,g}}. \tag{1.42}$$

Surprisingly enough, the factor inside the sum is the same as the expression obtained from the classical modeling (equation (1.39)). The summation operation, which corresponds to the contribution of all atomic $|g\rangle \to |n\rangle$ dipole transitions excited by the electric field, can be classically considered as the superposition of dipole responses from all electrons bound to the atom. The factor $f_{n,g}$, defined as:

$$f_{n,g} = \frac{2m_e\omega_{n,g}}{3\hbar e^2}|\,\langle n|\,\hat{\vec{\mu}}\,|g\rangle\,|^2, \tag{1.43}$$

is called *oscillator strength* for the $|g\rangle \to |n\rangle$ dipole transition. This name is obviously related to the classical Lorentz model relying on electrons confined in harmonic potential wells. Moreover, oscillator strengths obey the following sum rule:

$$\sum_n f_{n,g} = N_e, \tag{1.44}$$

where N_e is the total number of electrons for the atom ($N_e = Z$ if the atom is not ionized) [18]. The quantum mechanical result can therefore be classically interpreted as if the excitation of an atom by an external field results in the appearance of many dipoles with different characteristic frequencies. For each dipole, the number of bound electrons actually involved is then given by the value of the oscillator strength for this transition.

1.2.1.2 Linear dielectric response, dispersion and absorption

We already spoke about dispersion, particularly about group velocity dispersion in section 1.1.2.2. We thus observed that the dependence of the refractive index n on the frequency resulted in the temporal spread of ultrashort pulses. Yet we did not mentioned absorption. Still, these two phenomena are intrinsically linked. If we come back to the definition of light pulses that will be investigated in this work, given by equation (1.13), we shall now focus on the propagation factor $\exp(i(\vec{k_0}.\vec{r}-\omega_0 t))$. From equation (1.39) or, similarly, from equation (1.42), we clearly see that the refractive index and, therefore, the wavevector, is a complex number. We can consequently rewrite equation (1.13) as:

$$\vec{E}(\vec{r},t) = \vec{\mathcal{E}}(\vec{r},t)\mathrm{e}^{(-\mathrm{Im}(\vec{k_0}).\vec{r})}\mathrm{e}^{i(\mathrm{Re}(\vec{k_0}.\vec{r}-\omega_0 t)} + c.\,c.. \tag{1.45}$$

This result shows that the complex nature of $\vec{k}$ results in an exponentially-decaying term depending on the imaginary part of the wavevector, which is absorption. The real part of $\vec{k}$, conversely, leads to dispersion.

We can now use the modeling of the linear dielectric response from the previous section to look at its physical implications on the propagation of light. To this purpose, we simply look at the evolution of the dielectric constant ϵ with frequency considering only a single dipole transition with arbitrary resonance frequency ω_0 and damping rate γ so that $\gamma/\omega_0 = 10^{-5}$. The corresponding plot is given in figure 1.3.

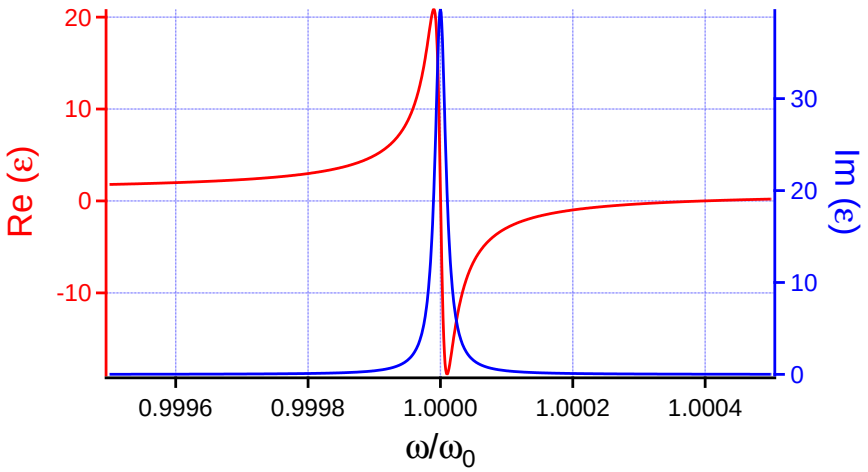

Figure 1.3: Evolution of the real part (left, red) and of the imaginary part (right, blue) of the dielectric constant ϵ with the frequency for a dipole transition of resonance frequency ω_0. The damping rate is chosen as $\gamma/\omega_0 = 10^{-5}$.

From these graphs, we can clearly define two regions: far before or after the resonance frequency, ϵ is almost real, meaning that absorption is very low and can usually be neglected. Its value is also increasing with frequency. This domain is referred to as *normal dispersion region* because in this frequency range, light with short wavelengths propagates slower than light with long wavelengths, as it is commonly observed in most transparent media. Near the resonance frequency, however, absorption becomes very intense with a characteristic Lorentzian shape, and the real part of ϵ now becomes a decreasing function of frequency, which is characteristic of the *anomalous dispersion region*.

The nature of the dispersion region, either normal or anomalous, has a direct influence on the propagation of ultrashort pulses since it will define the sign of the group velocity dispersion. Thus, in a normal dispersion region, $k_0'' \geq 0$, while $k_0'' \leq 0$ in an anomalous dispersion region.

1.2.1.3 Conclusion on the linear dielectric response

In the case of isotropic propagation media, a rigorous quantum mechanical calculation and the classical Lorentz model give a very similar expression for the linear susceptibility $\chi_e^{(1)}$, save for oscillator strength factors. From the classical point of view, bound electrons are at the bottom of a harmonic potential well when at rest, and start to oscillate in this well when excited by an external field. One can then intuitively think that if the exciting field amplitude steadily approaches the value of intra-atomic field, the response of the system will deviate from a perfect harmonic behavior, much in the same way that overstretching a spring results in anharmonicity of the system. This is precisely what happens for the dielectric response of the medium when the amplitude of the exciting field increases: it will switch from linear to nonlinear.

1.2.2 Nonlinear dielectric response

The intra-atomic electric field for any atom is on the order of E_{at}, the value of this field for a hydrogen atom:

$$E_{at} = \frac{e}{4\pi\epsilon_0 a_0^2} \approx 5 \times 10^{11}\ \mathrm{V} \cdot \mathrm{m}^{-1}, \tag{1.46}$$

a_0 being the Bohr radius. We consider an exciting external electric field:

$$\vec{E}(\vec{r},t) = \vec{\mathcal{E}}(\vec{r},t)\mathrm{e}^{i(\vec{k_p}.\vec{r}-\omega_p t)}/2 + c.\ c., \tag{1.47}$$

so that $E \ll E_{at}$. Using the classical approach initiated by Lorentz (which was shown to be quite similar to the rigorous quantum mechanical approach), we can then do an expansion of the electron restoring force such as:

$$\vec{F}_{restoring} = -m_e\omega_0^2\vec{r} - m_e\sum_{n=1}^{+\infty}\alpha_n r^n\vec{r}, \tag{1.48}$$

where the expansion coefficients verify $\forall n \in \mathbb{N}^*, \alpha_n r^n \ll 1$ and $\forall n \in \mathbb{N}^*, \alpha_{n+1} r \ll \alpha_n$. This expansion results from the addition of anharmonic terms in the expression of the potential well for the electron, the latter being reshaped away from the harmonic potential well. The considered bound electron then obeys the following equation of motion:

$$m_e\partial_t^2\vec{r} = -e\vec{E} - m_e\omega_0^2\vec{r} - m_e\sum_{n=1}^{+\infty}\alpha_n r^n\vec{r} - 2m_e\gamma\partial_t\vec{r}. \tag{1.49}$$

Looking for a perturbative solution to this problem, one can decompose the solution as $\vec{r} = \sum_{n=0}^{+\infty}\vec{r}^{(n)}$. As the external field $\vec{E}$ is supposed to be a first-order perturbation, we have the following equation system in the Fourier frequency space:

$$\begin{cases} -\omega^2\vec{r}^{(1)} = -\dfrac{e}{m_e}\vec{E} - \omega_0^2\vec{r}^{(1)} + 2i\omega\gamma\vec{r}^{(1)} \\ \forall i > 1, -\omega^2\vec{r}^{(i)} = -\omega_0^2\vec{r}^{(i)} - \displaystyle\sum_{j=1}^{i-1}\alpha_j[r^{(j)}]^j\vec{r}^{(i-j)} + 2i\omega\gamma\vec{r}^{(i)}. \end{cases} \tag{1.50}$$

Solving these equations step by step enables one to compute $\vec{r}^{(i+1)}$ from $\vec{r}^{(i)}$, and therefore to extract nonlinear susceptibilities $\chi_e^{(i)}$. In the temporal domain and Fourier frequency domain, these are defined through the following expansions of the polarization:

$$\begin{cases} \vec{P}(\vec{r},t) = \epsilon_0 \sum_{n=1}^{+\infty} \int_{\mathbb{R}^n} H(t_1)...H(t_n)\overline{\chi_e^{(n)}}(\vec{r},t_1,...,t_n) : \vec{E}(\vec{r},t-t_1)...\vec{E}(\vec{r},t-t_n)\ \mathrm{d}t_1...\mathrm{d}t_n \\ \vec{P}(\vec{r},\omega) = \epsilon_0 \sum_{n=1}^{+\infty} \overline{\chi_e^{(n)}}(\vec{r},\omega=\omega_1+...+\omega_n,\omega_1,...,\omega_n) : \vec{E}(\vec{r},\omega_1)...\vec{E}(\vec{r},\omega_n). \end{cases} \tag{1.51}$$

The rank of the tensor $\overline{\chi_e^{(n)}}$ is thus $n+1$.

If we evaluate the first expansion terms for the radius, we find:

$$\begin{cases} r^{(1)}(\omega) = -\dfrac{e}{2m_e D(\omega)} \left(\mathcal{E}(\vec{r},\omega+\omega_p)\mathrm{e}^{i\vec{k_p}.\vec{r}} + \mathcal{E}^*(\vec{r},\omega-\omega_p)\mathrm{e}^{-i\vec{k_p}.\vec{r}} \right) \\ r^{(2)}(2\omega) = -\dfrac{\alpha_1 e^2}{4m_e D(2\omega)D(\omega)^2} \left(\mathcal{E}(\vec{r},\omega+\omega_p)^2\mathrm{e}^{2i\vec{k_p}.\vec{r}} + \mathcal{E}^*(\vec{r},\omega-\omega_p)^2\mathrm{e}^{-2i\vec{k_p}.\vec{r}} \right) \\ r^{(2)}(0) = -\dfrac{\alpha_1 e^2}{2m_e D(0)D(\omega)D(-\omega)} \left(\mathcal{E}(\vec{r},\omega+\omega_p) + \mathcal{E}^*(\vec{r},\omega-\omega_p) \right), \end{cases} \tag{1.52}$$

where the function $D(\omega) = \omega_0^2 - \omega^2 - 2i\gamma\omega$. If the excitation at ω, located around ω_p, is far from any resonance of the propagation medium (which is the case for most transparent materials in the visible range), the function D is slowly varying. We then write $D(\omega) \approx D$. This approximation means that the medium responds instantly to the excitation. In the time domain, we can thus rewrite the expressions for the radius as:

$$\begin{cases} r^{(1)}(t) = -\dfrac{e}{2m_e D} \left(\mathcal{E}(\vec{r},t)\mathrm{e}^{i(\vec{k_p}.\vec{r}-\omega_p t)} + c.\ c. \right) \\ r^{(2)}(t) = -\dfrac{\alpha_1 e^2}{4m_e D^3} \left(\mathcal{E}(\vec{r},t)^2\mathrm{e}^{2i(\vec{k_p}.\vec{r}-\omega_p t)} + c.\ c. + 2|\mathcal{E}(\vec{r},t)|^2 \right). \end{cases} \tag{1.53}$$

These equations are already displaying characteristic nonlinear phenomena: the second one corresponds to the addition of an electric field oscillating at twice the exciting frequency, that is second harmonic generation (SHG), and of a DC electric field in the nonlinear medium, which is called optical rectification. Computing higher order terms will result in other nonlinear phenomena, such as third harmonic generation or Kerr effect.

This classical approach suffers from the same shortcomings as the Lorentz model: it cannot take the tensor nature of dielectric susceptibilities $\overline{\chi_e^{(n)}}$ into account, and once more it only considers a single bound electron. For a rigorous determination, the perturbative quantum mechanical calculation presented in section 1.2.1.1 with the perturbated Hamiltonian given in equation (1.40), must be carried on at higher orders.

1.2.3 Propagation of an ultrashort pulse in an isotropic medium: Kerr effect and self-focusing

1.2.3.1 Kerr effect and Kerr index

We will now look at nonlinear effects that could affect the propagation of an ultrashort laser pulse in an isotropic medium, typically diatomic gases or monoatomic/diatomic gas mixtures. Such media are called *centrosymmetric*, because they exhibit symmetry with respect to a given point. They

represent an important family of nonlinear materials because, due to the symmetry properties of the medium, the interaction potential for a bound electron $U(\vec{r})$ is an even function of space:

$$U(\vec{r}) = U(-\vec{r}). \tag{1.54}$$

As U is defined by:

$$\vec{\nabla} U = -\vec{F}_{restoring}, \tag{1.55}$$

$\vec{F}_{restoring}$ being described by equation (1.48), we can see that the parity of U implies that all even terms in the perturbative development of $\vec{r}$ and, therefore, of $\vec{P}$, must vanish. As a consequence, all even-order susceptibilities are equal to 0.

In this study, we will stop the nonlinear expansion of the polarization at the third order. For isotropic materials, it can be shown that only 21 components of the $\overleftrightarrow{\chi_e^{(3)}}$ tensor out of 81 are nonzero, of which only 3 are independent [17]:

$$\begin{cases} yyzz = zzyy = xxyy = yyxx = xxzz = zzxx \\ yzyz = zyzy = xyxy = yxyx = xzxz = zxzx \\ yzzy = zyyz = xyyx = yxxy = xzzx = zxxz \\ xxxx = yyyy = zzzz = xxyy + xyxy + xyyx. \end{cases} \tag{1.56}$$

Considering an input laser field defined as:

$$\vec{E}(\vec{r},t) = \frac{\mathcal{E}(\vec{r},t)}{2} \mathrm{e}^{i(k_0 z - \omega_0 t)} \vec{e}_x + c.\ c., \tag{1.57}$$

we can write the expressions of the different components of the polarization in the Fourier frequency space:

$$\begin{cases} \vec{P}(\omega) = \epsilon_0 \dfrac{\chi_e^{(1)}(\omega)}{2} \left(\mathcal{E}(\omega+\omega_0)\mathrm{e}^{ik_0 z} + \mathcal{E}^*(\omega-\omega_0)\mathrm{e}^{-ik_0 z} \right) \vec{e}_x + \\ \qquad \epsilon_0 \dfrac{3\chi_{e,xxxx}^{(3)}(\omega)}{8} \left(\mathcal{E}(\omega+\omega_0)^2 \mathcal{E}^*(\omega-\omega_0)\mathrm{e}^{ik_0 z} + \mathcal{E}^*(\omega-\omega_0)^2 \mathcal{E}(\omega+\omega_0)\mathrm{e}^{-ik_0 z} \right) \vec{e}_x \\ \vec{P}(3\omega) = \epsilon_0 \dfrac{\chi_{e,xxxx}^{(3)}(3\omega)}{8} \left(\mathcal{E}(\omega+\omega_0)^3 \mathrm{e}^{3ik_0 z} + \mathcal{E}^*(\omega-\omega_0)^3 \mathrm{e}^{-3ik_0 z} \right) \vec{e}_x. \end{cases} \tag{1.58}$$

Supposing that the phase matching condition for third harmonic generation ($\vec{k}(3\omega) - 3\vec{k}(\omega) = \vec{0}$) is not satisfied, this process can be neglected. If we again make the hypothesis that susceptibilities are slow varying functions of the frequency, as it is the case in the visible range, we find that:

$$\vec{P}(\vec{r},t) = \epsilon_0 \left(\chi_e^{(1)} + \frac{3\chi_{e,xxxx}^{(3)}}{4} |\mathcal{E}(\vec{r},t)|^2 \right) \vec{E}(\vec{r},t). \tag{1.59}$$

We see that the polarization is still proportional to the electric field, although it results from nonlinear interaction. We can define an effective refractive index n_{eff} such as:

$$n_{\text{eff}}^2 = 1 + \chi_e^{(1)} + \frac{3\chi_{e,xxxx}^{(3)}}{4} |\mathcal{E}|^2 = n^2 + \frac{3\chi_{e,xxxx}^{(3)}}{4} |\mathcal{E}|^2. \tag{1.60}$$

Defining the Kerr index n_2 as:

$$n_2 = \frac{3\chi_{e,xxxx}^{(3)}}{4\epsilon_0 c n^2}, \tag{1.61}$$

the effective index is thus given by:

$$n_{\text{eff}} \approx n + n_2 I, \tag{1.62}$$

where I is the intensity corresponding to the electric field $\vec{E}$. This third order nonlinear effect is called the Kerr effect, from the name of its discoverer [19]. Typically, values for the Kerr index n_2 are on the order of 10^{-23} m^2 · W^{-1} for gases and 10^{-20} m^2 · W^{-1} for glasses.

Actually, in the case of molecular propagation media, the Kerr response is not instantaneous but is made up of two distinct components: the response of bound electrons to the laser field, which is considered as instantaneous (response time < 1 fs), and the response due to molecular alignment by Raman rotational excitation. This is because the inherent wide bandwidth of femtosecond pulses enables them to collectively excite a large ensemble of rotational molecular states [20, 21, 22]. This effect can be modeled simply in this way:

$$n_{eff}(\vec{r},t) = n(\vec{r}) + n_2(\vec{r})I(\vec{r},t) + \int_{\mathbb{R}} \mathcal{R}(t')H(t')I(\vec{r},t-t')\ \mathrm{d}t', \tag{1.63}$$

where $\mathcal{R}$ is the Raman response function [12]. This function can be determined by different approaches. We will get back to this point later.

1.2.3.2 Self-focusing of intense laser pulses and catastrophic collapse

A very important consequence of the Kerr effect is self-focusing of high power laser pulses. Indeed, most laser pulses have a spatial profile characterized by a maximum of intensity at the center. Following equation (1.62) we see that, given the pulse intensity is high enough to generate a strong Kerr effect, it will result in a refractive index profile with value at the center higher than at the periphery, just like a positive lens (cf. figure 1.4). This effect is cumulative: as the pulse is focused

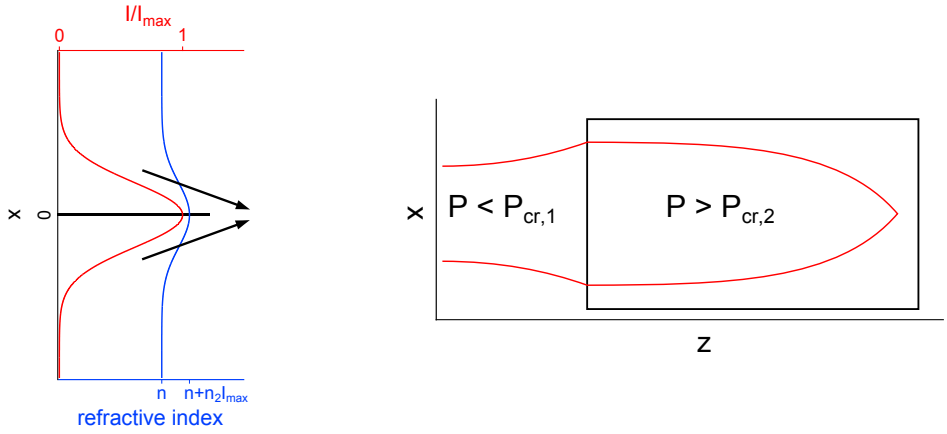

Figure 1.4: Left: schematic depiction of self-focusing due to Kerr effect. Right: evolution of the radius of a laser pulse with a peak power P during its propagation first through a medium where $P < P_{cr}$ and then in a medium with $P_{cr} < P$.

by the Kerr index profile, its intensity will increase, leading to an even stronger Kerr focusing. This positive feedback loop tends to counteract natural diffraction.

To estimate the impact of Kerr effect and self-focusing on the pulse during its propagation, one can evaluate the cumulative nonlinear phase it has accumulated, defined by the B-integral:

$$B(z) = \frac{2\pi}{\lambda_0} \int_0^z n_2(z')I(z')\ \mathrm{d}z'. \tag{1.64}$$

The characteristic length for self-focusing L_{sf} can then be defined as the propagation length needed for the B-integral to reach 1 rad, that is approximately:

$$L_{sf} = \frac{1}{n_2 k_0 I_0}. \tag{1.65}$$

One can intuitively think that if self-focusing occurs over a shorter distance than diffraction, then it will dominate and lead to beam collapse. This condition reads:

$$\frac{\lambda_0}{2\pi n_2 I_0} < \frac{\pi w_0^2 n}{\lambda_0}, \tag{1.66}$$

leading to:

$$P_0 > \frac{\lambda_0^2}{2\pi n n_2}. \tag{1.67}$$

Surprisingly, this last equation involves the beam initial peak power P_0, and not its intensity I_0. It means that if the peak power of a laser pulse exceeds a given value, generally called critical power, Kerr self-focusing will overcome diffraction. This critical power can be rigorously defined as the input value leading to beam self-trapping in a Kerr medium, that is a perfect equilibrium between self-focusing and diffraction. Chiao *et al.* found that the cylindrically-symmetric solution for such a trapped beam was given by the so-called *Townes mode* [23], with a corresponding critical power:

$$P_{cr}^{Townes} \approx \frac{3.72\lambda_0^2}{8\pi n n_2}. \tag{1.68}$$

This expression is quite close to the rough approximation given in equation (1.67). In fact, it is possible to have an estimate of the critical power for any initial beam profile by changing the numerical factor given for the Townes mode. For instance, in the case of a Gaussian beam, the factor 3.72 in equation (1.68) must be replaced by 3.77 [24]. In air at 800 nm, the critical power is not precisely fixed and varies with experimental conditions, for instance with pulse duration, due to the retarded Kerr response. Measurements done over the past decade thus spread between 3 and 10 GW, with higher values being recorded for shorter pulses [25, 22].

It should be noted that if the peak power of a laser pulse is higher than its corresponding critical power, diffraction will be unable to stop the resulting collapse. This means the beam will converge towards a singularity with an infinite intensity (figure 1.4). The propagation distance L_c needed to reach this point can be approximated by a semi-empirical formula from Marburger [24]:

$$L_c = \frac{0.367 L_R}{\sqrt{\left(\sqrt{\frac{P_0}{P_{cr}}} - 0.852\right)^2 - 0.0219}}. \tag{1.69}$$

For instance the collapse distance for a $2P_{cr}$ laser pulse with waist $w_0 = 5$ mm at 800 nm is $L_c = 66.4$ m.

1.2.3.3 Consequences of Kerr effect: self-phase modulation, self-steepening

The propagation term for the electric field defined in equation (1.13) is given by $e^{i(k_0 z - \omega_0 t)}$. We can define the instantaneous phase and frequency of this pulse by:

$$\begin{cases} \varphi(\vec{r},t) = k_0 z - \omega_0 t = \omega_0 (z n(\vec{r},t)/c - t) \\ \omega(t) = -\dfrac{\partial \varphi}{\partial t}(\vec{r},t). \end{cases} \tag{1.70}$$

Replacing $n(\vec{r},t)$ by $n(\vec{r})+n_2(\vec{r},t)I(\vec{r},t)$ and assuming time-independent linear and Kerr indexes, leads to the instantaneous frequency:

$$\omega(t) = \omega_0 - \frac{n_2\omega_0 z}{c}\frac{\partial I}{\partial t}(t). \tag{1.71}$$

According to this last equation, the Kerr effect will result in the generation of new frequencies in the spectrum of the pulse. Thus, the leading front of the pulse, characterized by a rising intensity, will generate red frequencies with respect to the pulse central frequency, while the trailing front will create blue frequencies. This spectacular effect is called self-phase modulation (SPM) and can significantly broaden the spectrum of a laser pulse during its propagation through a Kerr medium.

Another self-induced effect experienced by the pulse due to Kerr effect is the self-steepening. Indeed, as the Kerr index will be stronger for the most intense part of the pulse, it will therefore slow it down. The low-intensity, trailing part of the pulse will progressively catch-up with the peak, leading to the eventual formation of a smooth pulse leading front and a very steep trailing front. This asymmetry, together with self-phase modulation, is responsible for the spectral broadening being more pronounced in the blue part of the spectrum than in the red part [26, 27].

1.2.4 Conclusion on the nonlinear dielectric response

The propagation of powerful laser pulses in transparent media, such as air, results in effects opposite to what one could expect from linear optics. The most spectacular one, perhaps, is the Kerr effect, which results in the self-focusing of the beam. While diffraction reigns over linear optics, nonlinear effects generated by intense pulses are able to reverse this situation. In the case where the pulse input power exceeds the critical power, it will collapse sooner or later, tending to form a singularity. Before this could happen, various mechanisms, depending on the propagation medium, can stop the collapse, resulting in the establishment of a dynamic balance between focusing and defocusing effects. This balance is characteristic of the filamentation propagation regime, which we will study in the next section.

1.3 The filamentation propagation regime

The critical power being far lower in condensed transparent media than in gases, filamentation had already been witnessed in the early days of nonlinear optics in the form of damage tracks left in the propagation medium [28] or long and thin fluorescent channels [29, 30]. However, it was not before the advent of powerful femtosecond lasers in the early 1990s that this effect could be seen in air as well [16]. Since then, filamentation and its applications has attracted the attention of a relatively small, but very active scientific community, which has progressively elucidated many physical mechanisms describing this propagation regime (see, e. g., review articles from Couairon and Mysyrowicz [12], Bergé *et al.* [31], Kasparian and Wolf [32], Chin *et al.* [33] and Milchberg *et al.* [34]).

In this section, we will first describe the onset of filamentation due to the arrest of the Kerr-induced collapse and the resulting propagation dynamics. We will then present a brief review of the main characteristics of this fascinating propagation regime. Finally, a rapid introduction to numerical simulation of filamentation will be given.

1.3.1 Onset of filamentation

1.3.1.1 Arrest of the Kerr-induced collapse

As we mentioned earlier, when the peak power of a laser pulse exceeds the corresponding critical power for the propagation medium, it self-focuses and will eventually, collapse to form an optical singularity. However, before this point could be reached, various physical mechanisms are able to stop the collapse, depending on experimental conditions, particularly the pulse input power and the nature of the propagation medium.

In the case of solids, it has been shown that group velocity dispersion alone was able to prevent catastrophic collapse by spreading the pulse along the propagation axis, and even to promote the splitting of the pulse in several components, ensuring propagation beyond the nonlinear focus of the intial pulse, that is the position of the theoretical beam collapse [35, 36]. This regime, however, is only valid for a relatively modest input power, up to a few times the critical power [37]. At higher power, self-focusing dominates GVD and intensity increases up to the photoionization threshold through multiphoton absorption and/or tunnel ionization, depending on the field strength. Further field energy can be absorbed by the resulting plasma by inverse Bremsstrahlung or above-threshold ionization [38, 39]. Laser-induced plasma is also responsible for a defocusing effect on the trailing part of the pulse because free electrons decrease the local refractive index [40]. In gases such as air, GVD is almost negligible for propagation over laboratory characteristic distances, so the arrest of the Kerr-induced collapse is mainly due to ionization, plasma absorption and plasma defocusing. Moreover, laser energy absorption owing to Raman rotational excitation was also shown to deplete significantly the laser pulse [41, 42]. This constitutes the standard paradigm for filamentation: the dynamic competition established between Kerr-induced self-focusing, pulse energy depletion due to ionization, plasma absorption and Raman absorption, diffraction and the plasma defocusing effect promotes the formation of a thin, intense central channel called *filament* surrounded by a more dilute energy bath. The ensemble is able to propagate without diffracting over several Rayleigh lengths beyond the nonlinear focus.

Another paradigm, the so called *higher order Kerr effect* paradigm, was also proposed in the early 2000s [43, 44]. It involves the inclusion of higher order terms in the perturbative expansion of the nonlinear polarization given by equation (1.51). For instance, assuming an instantaneous response of the propagation medium, we have:

$$\vec{P}(\vec{r},t) = \epsilon_0 \left(\chi_e^{(1)} \vec{E}(\vec{r},t) + \chi_e^{(3)} \left(\vec{E}.\vec{E}\right) \vec{E}(\vec{r},t) + \chi_e^{(5)} \left(\vec{E}.\vec{E}\right)^2 \vec{E}(\vec{r},t) + ... \right). \tag{1.72}$$

It was thus supposed that at very high intensities, typically on the order of those encountered near the nonlinear focus, high order effects could play a significant role if the corresponding susceptibilities were negative. In this case, arrest of collapse without plasma generation was predicted [45]. However in the past few years, several experimental papers [46, 47, 48] demonstrated unambiguously that higher order Kerr contributions to the refractive index are negligible for filamentation in gases and, as such, the standard paradigm for filamentation remains valid in all the work presented in this Thesis.

1.3.1.2 Lens-promoted filamentation

Self-focusing usually necessitates long propagation distances to eventually lead beam collapse and to initiate filamentation, as estimated using the Marburger's formula (equation (1.69)). Consequently, most experimental setups make use of focusing optics to promote filamentation. In this case, the

lens-imposed phase is another effect involved in the dynamic balance defining filamentation. The theoretical position of the beam collapse is then displaced to a new position L_c' given as:

$$\frac{1}{L_c'} = \frac{1}{L_c} + \frac{1}{f}, \tag{1.73}$$

where L_c is the collapse position given by the Marburger's formula and f the focal length of the lens. Another benefit linked to the use of external focusing is the stabilization of the filament position. If focusing is strongly increased, the influence of the Kerr effect on the filament formation accordingly wanes, and the initial pulse propagation is very close to the linear regime as it is *lens-dominated*. This can lead to the formation of plasmas much denser than in the case of Kerr-dominated filamentation, but with a spatial extension much smaller [49]. Recently, Lim and co-authors evaluated the transition between the lens-dominated and the Kerr-dominated filamentation regimes in terms of numerical aperture around 4.10^{-3}, which corresponds roughly to a $f/125$ focusing [50].

1.3.2 Physical effects involved in filamentation in air

1.3.2.1 Raman transient nonlinearity, Raman rotational absorption and molecular alignment

We saw in section 1.2.3.1 that the Kerr effect comprises two distinct components, as highlighted in equation (1.63). The first one comes from the bound electronic response and is faster than 1 fs and therefore considered instantaneous. The other one originates from Raman excitation of molecular rotational states, which transfers laser energy to molecular rotational degrees of freedom (cf. figure 1.5-(a)). This effect is characterized by the formation of a laser field-induced dipole $\vec{p}(\omega) = \overline{\alpha}(\omega) : \vec{E}(\omega)$, where $\overline{\alpha}$ is the molecular polarizability tensor. The molecule starts to rotate to align along the electric field, and does so at a speed depending on the level of excitation of rotational states (figure 1.5-(b)). This effect is called laser molecular alignment.

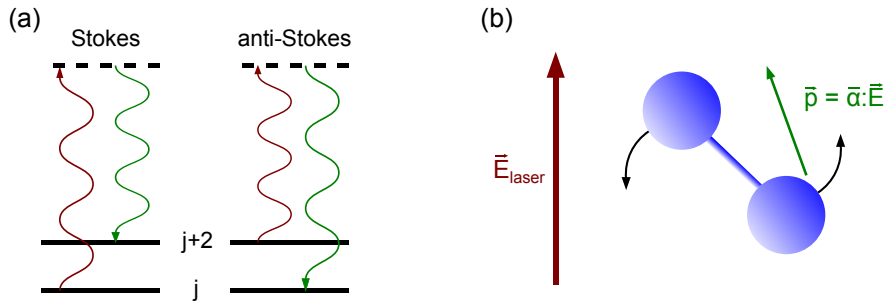

Figure 1.5: (a): principle of Raman rotational absorption to form either a Stokes or an anti-Stokes component. (b): illustration of molecular alignment. The laser field $\vec{E}_{laser}$ induces a dipole $\vec{p} = \overline{\alpha} : \vec{E}$ in the molecule, which starts to rotate to align along the laser field.

Several methods can be employed to derive the expression of the Raman response function $\mathcal{R}$ in equation (1.63). The most rigorous one uses a full quantum mechanical evaluation that we will briefly present here (more thoroughly described in references [21] and [51]). Considering only linear propagation of a laser pulse in a medium constituted by homonuclear, nonpolar diatomic molecules

and using the Lorenz-Lorentz formula [11], we can define the time-dependent refractive index as:

$$n(t) = \sqrt{n(-\infty) + \frac{n_n}{\epsilon_0}\Delta\alpha\left(\langle\cos(\theta(t))^2\rangle - \frac{1}{3}\right)} \approx n(-\infty) + \frac{n_n}{2\epsilon_0 n(-\infty)}\Delta\alpha\left(\left\langle\cos(\theta(t))^2\right\rangle - \frac{1}{3}\right), \tag{1.74}$$

where $\Delta\alpha = \alpha_{/\!/} - \alpha_\perp$ is the difference between molecular polarizability along the molecular axis and perpendicular to this axis, θ is the angle between the molecular axis and the laser field polarization direction, and $\langle . \rangle$ represents the ensemble average operation. Using the density operator formalism, we have:

$$\left\langle\cos(\theta(t))^2\right\rangle = \mathrm{Tr}(\hat{\rho}\widehat{\cos(\theta(t))}^2) = \sum_{i,k=0}^{+\infty}\rho_{ik}\left\langle k\right|\widehat{\cos(\theta(t))}^2\left|i\right\rangle, \tag{1.75}$$

$\hat{\rho}$ being the density operator. Assuming the effect of the laser field is very weak, we can use a time-dependent perturbative approach to find the value of $\hat{\rho}$. First we have:

$$\begin{cases} \hat{H} = \hat{H}^{(0)} + \hat{H}^{(1)} = \hat{H}^{(0)} - \Delta\alpha|E|^2\widehat{\cos(\theta(t))^2} - \alpha_\perp\hat{\delta}|E|^2 \\ \hat{\rho} = \hat{\rho}^{(0)} + \hat{\rho}^{(1)}. \end{cases} \tag{1.76}$$

We can express $\hat{\rho}^{(1)}$ as:

$$[\hat{\rho}^{(1)}(t)]_{ik} = \left\langle k\right|\rho^{(1)}(t)\left|i\right\rangle = -\frac{i}{\hbar}\int_{-\infty}^{t}[\hat{H}^{(1)}(t'),\hat{\rho}^{(0)}]_{ik}\mathrm{e}^{(i\omega_{ik}+\gamma_{ik})(t'-t)}\,\mathrm{d}t', \tag{1.77}$$

[.] being the commutator operator, $\omega_{ik} = (E_k - E_i)/\hbar$ and $\gamma_{i,k}$ the dipole dephasing rate between states $|k\rangle$ and $|i\rangle$. Remarking that rotational eigenstates are the spherical harmonics $|i\rangle = |j,m\rangle = Y_{jm}(\theta,\varphi)$, we can find that matrix elements $\langle j',m'|\widehat{\cos(\theta(t))^2}\,|j,m\rangle$ are nonzero only if:

$$\begin{cases} \Delta m = m' - m = 0 \\ \Delta j = j' - j = \pm 2, 0. \end{cases} \tag{1.78}$$

We can see here that rotational state coupling corresponds to a two-photon non-resonant Raman process, either Stokes or anti-Stokes (figure 1.5-(a)), or to elastic Rayleigh scattering. Although this is a first-order effect in terms of polarizability/susceptibility, it turns out to have a quadratic dependence on the electric field, behaving like a third-order nonlinear contribution to the refractive index. We finally get:

$$\begin{aligned}\left\langle\cos(\theta(t))^2\right\rangle =& \frac{1}{3} + \frac{1}{\hbar}\sum_{j=0}^{+\infty}\sum_{m=-j}^{j}(\rho^{(0)}_{j,m} - \rho^{(0)}_{j+2,m})\Delta\alpha \\ &\times\left\langle j+2,m\right|\widehat{\cos(\theta(t))^2}\left|j,m\right\rangle^2 \mathrm{Im}\left(\int_{-\infty}^{t}|\mathcal{E}(t')|^2\mathrm{e}^{(i\omega_{j,j+2}+\gamma_{j,j+2})(t'-t)}\,\mathrm{d}t'\right).\end{aligned} \tag{1.79}$$

We can evaluate the sum over m to eventually find:

$$\left\langle\cos(\theta(t))^2\right\rangle = \frac{1}{3} + \frac{2}{15\hbar}\sum_{j=0}^{+\infty}\frac{(j+2)(j+1)}{2j+3}(\rho^{(0)}_j - \rho^{(0)}_{j+2})\Delta\alpha\mathrm{Im}\left(\int_{-\infty}^{t}|\mathcal{E}(t')|^2\mathrm{e}^{(i\omega_{j,j+2}+\gamma_{j,j+2})(t'-t)}\,\mathrm{d}t'\right). \tag{1.80}$$

The retardated Raman rotational response $\mathcal{R}$ can then be expressed:

$$\mathcal{R}(\vec{r},t) = \frac{2}{15}\frac{n_n(\vec{r},t)\Delta\alpha^2}{\hbar\epsilon_0^2 c n(\vec{r})}\sum_{j=0}^{+\infty}\frac{(j+2)(j+1)}{2j+3}(\rho^{(0)}_j(\vec{r}) - \rho^{(0)}_{j+2}(\vec{r}))\sin(\omega_{j,j+2}t)\mathrm{e}^{-\gamma_{j,j+2}t}. \tag{1.81}$$

Density matrix elements of order 0 are obtained from the thermodynamic equilibrium state populations:

$$\rho_j^{(0)} = \frac{D_j(2j+1)\mathrm{e}^{-E_j/k_BT}}{\sum_{k=0}^{\infty} D_k(2k+1)\mathrm{e}^{-E_k/k_BT}}. \tag{1.82}$$

The factors D_j are degeneracy factors due to the nuclear spin. In the case of $^{14}N_2$, we have $D_j = 6$ if j is even, and 3 otherwise. For $^{16}O_2$, only odd rotational levels can be populated, meaning $D_j = 0$ if j is even, and 1 otherwise [52]. The energy of a rotational level E_j is given by:

$$E_j = hcBj(j+1), \tag{1.83}$$

where B is the characteristic rotational constant for the considered molecule.

A consequence of molecular alignment using pulses with short duration with respect to the rotation period of the highest excited rotational state is the appearance of periodic echoes in the Raman-induced refractive index shift [20, 21, 53]. Indeed, the laser pulse first coherently excites a rotational wavepacket that can be described as:

$$|\psi\rangle = \sum_{j=0}^{j_{max}} \sum_{m=-j}^{j} a_{jm}\mathrm{e}^{-i\omega_j t}\,|j,m\rangle\,. \tag{1.84}$$

Afterwards the phase of each $|j,m\rangle$ state evolves independently, yielding a null average value. However, as time reaches specific values, coherent revival of the delayed refractive index shift is observed. Thus, if $t = p/2cB = pT$, where $p \in \mathbb{N}^*$, the rotational wavepacket components are again in phase, yielding a surge in the refractive index similar to the initial index shift. Partial re-coherence can also be witnessed at times $T/2^{p+1}$ with corresponding weaker strength. Half-revival time $T/2$ yields an alignment perpendicular to the initial laser-induced alignment because at this time, odd and even rotational state subsets are separately in phase, with a π phase shift between these subsets (see figure 1.6 for illustration in the case of N_2).

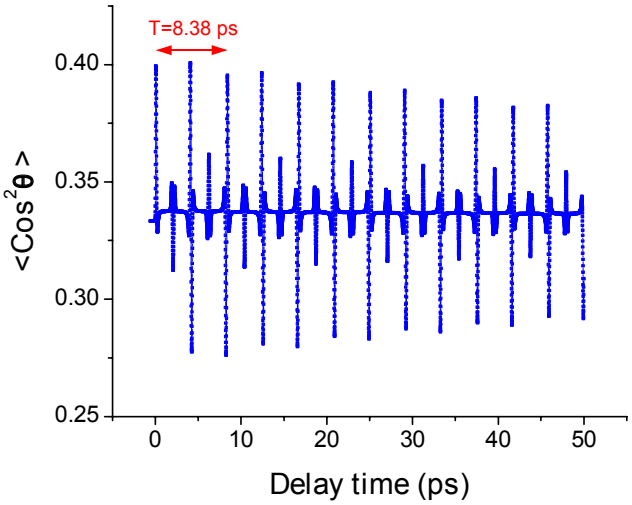

Figure 1.6: Simulated alignment parameter after the propagation of a 50 fs laser pulse with intensity 5×10^{17} W $\cdot$ m^{-2} in nitrogen with standard pressure and temperature conditions. From Azarm *et al.* [53].

To conclude, Raman rotational excitation has two different effects: first, it results in a retarded contribution to the Kerr index and, as such, promotes self-focusing of the laser pulse. On the other

hand, it is also a source for laser energy absorption which can significantly deplete the laser pulse even before ionization occurs, since absorption scales as I^2.

1.3.2.2 Photoionization of air

Usually, plasma generation is the main channel for laser energy absorption and is also a crucial component of the dynamic balance characteristic of filamentation. Air is mostly composed of molecular nitrogen and molecular oxygen. Their respective ionization potentials are $U^i_{N_2} = 15.2$ eV and $U^i_{O_2} = 12.1$ eV, well above the photon energy at 800 nm which is 1.54 eV. As a consequence, photoionization of air is highly improbable at low intensity. However, as a laser pulse experiences self-focusing, intensity increases strongly , especially close to the nonlinear focus. At relatively moderate intensity, the first process occurring will be the simultaneous absorption of several photons to bring a bound electron into the continuum (figure 1.7-(a)). This process follows the law:

$$W = \sigma_K I^K, \tag{1.85}$$

where W is the ionization rate, K the number of simultaneously absorbed photons and σ_K the corresponding cross section [12]. In the case of air, we have $K = 8$ for O_2 and $K = 10$ for N_2. This means that multiphoton ionization is negligible below intensities on the order of 10^{16} W $\cdot$ m^{-2} (figure 1.7-(c)). This also implies that the laser-induced plasma is mainly formed of molecular oxygen cations O_2^+.

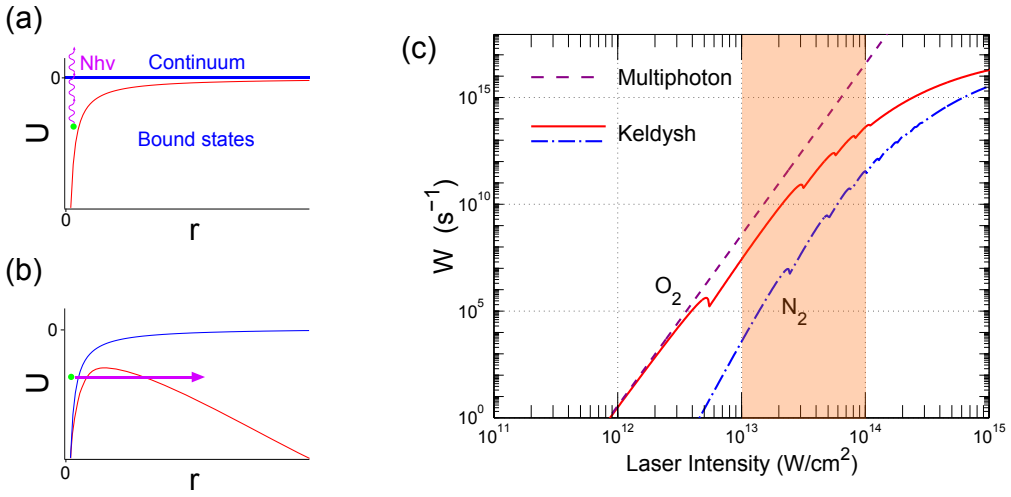

Figure 1.7: Schematic description of multiphoton ionization (a) and of tunnel ionization (b). (c): computed ionization rates considering only multiphoton ionization (purple dashed) and both multiphoton and tunnel ionization (red solid and blue dash-dotted) using the Keldysh model for O_2 and N_2 (from Couairon and Mysyrowicz [12]). The light orange rectangle highlights the intensity range typically encountered in filaments in air.

At higher intensities, the laser field becomes intense enough as to distort significantly the Coulomb potential binding electrons to the nucleus. If the Coulomb barrier is sufficiently decreased, a bound electron will then be able to directly tunnel through it to reach the continuum (figure 1.7-(b)). This photoionization regime is consequently referred to as tunnel ionization.

These two different regimes for photoionization were united by Keldysh in his famous 1965 paper [54]. In this article, Keldysh introduced a single formula for the ionization rate in both regimes,

depending on a dimensionless parameter γ, now known as the Keldysh adiabaticity parameter, defined as:

$$\gamma = \sqrt{\frac{U^i}{2U_p}} = \sqrt{\frac{\epsilon_0 c m_e \omega_0^2 U^i}{e^2 I}}, \tag{1.86}$$

where $U_p = e^2|E|^2/4m_e\omega_0^2$ is the ponderomotive potential. In the limit $\gamma \gg 1$, the ionization rate as described by Keldysh is reduced to the expression given in equation (1.85), meaning that this limit case corresponds to multiphoton absorption. Conversely, if $\gamma \ll 1$, then photoionization is dominated by the tunnel regime. The Keldysh model was later further refined by Perelomov, Popov and Terent'ev to yield the Keldysh-PPT model for photoionization of atoms [55].

Evolution of photoionization rates for molecular oxygen and nitrogen with pulse intensity using this model are plotted in figure 1.7-(c) and compared with multiphoton ionization only. One can clearly see that at low intensity (i. e. high γ value), the ionization rate given by Keldysh-PPT is equal to the multiphoton ionization rate. However, between 10^{17} and 10^{18} W $\cdot$ m^{-2}, a discrepancy appears, meaning that tunnel ionization is no longer negligible. As peak intensities encountered in filaments typically lie between these two values, we are clearly in a hybrid domain where no ionization regime dominates. Computing the value of γ for O_2 at 800 nm and for $I = 5 \times 10^{13}$ W $\cdot$ m^{-2}, we find $\gamma \approx 1.4$, confirming this situation. Though, as indicated on the same figure, the ionization rate departs only slightly from the power law characteristic of the multiphoton regime, meaning that photoionization in the filamentation regime can be well approximated by a corrected law:

$$W = \sigma_{K'} I^{K'}, \tag{1.87}$$

where K' is the corrected number of photons necessary to achieve ionization, with $K' < K$. This approach yields $K' \approx 7.5$ instead of 11 for N_2 and $K' \approx 6.5$ instead of 8 for O_2 [56].

1.3.2.3 Inverse Bremsstrahlung and plasma defocusing

Considering a classical approach using the Drude model, we can write the equation of motion for a free electron in the plasma:

$$m_e \frac{\mathrm{d}\vec{v}}{\mathrm{d}t} = -e\vec{E} - 2\pi m_e \nu_c \vec{v}, \tag{1.88}$$

where ν_c is the time-averaged collision frequency between electrons and other species in the plasma [57]. In the Fourier frequency domain, this equation can be used to write the electron current density $\vec{j_e} = -en_e\vec{v}$, where n_e is the electron density in the plasma. Therefore, we have:

$$\vec{j_e}(\vec{r},\omega) = \frac{n_e(\vec{r})e^2}{2\pi m_e \nu_c} \frac{1 + i\omega/2\pi\nu_c}{1 + \omega^2/4\pi^2\nu_c^2} \vec{E}(\vec{r},\omega). \tag{1.89}$$

The time-averaged power per unit volume transferred from the electric field to electrons, that is *classical inverse Bremsstrahlung losses*, is then given by:

$$\begin{aligned} \left\langle \frac{\partial P}{\partial V}(\vec{r},t) \right\rangle_t &= \frac{1}{2} Re\left(\vec{j_e}(\vec{r},\omega).\vec{E}(\vec{r},\omega)^*\right) \\ &= \frac{n_e(\vec{r},t)e^2}{4\pi m_e \nu_c} \frac{1 + i\omega_0/2\pi\nu_c}{1 + \omega^2/4\pi^2\nu_c^2} |E(\vec{r},t)|^2 \\ &= \sigma_{iB}(\omega_0) n_e(\vec{r},t) I(\vec{r},t), \end{aligned} \tag{1.90}$$

where the cross-section for classical inverse Bremsstrahlung σ is defined as [58]:

$$\sigma_{iB}(\omega) = \frac{e^2}{\epsilon_0 m_e n c} \frac{1/2\pi\nu_c}{1+\omega^2/4\pi^2\nu_c^2}. \tag{1.91}$$

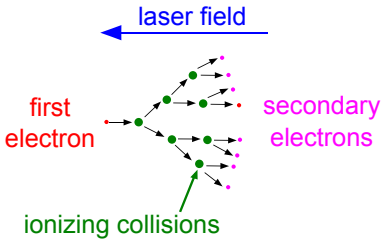

Figure 1.8: Schematic depiction of an avalanche ionization process.

As the filamentation plasma is weakly ionized, collision processes are dominated by electron-neutral collisions. The corresponding collision frequency can be well approximated by:

$$\nu_c \text{ [Hz]} \approx 2.3 \times 10^7 p \text{ [Pa]}, \tag{1.92}$$

where p is the neutral gas pressure [59]. As we always work with air in standard pressure and temperature conditions, we find:

$$\nu_c \approx 2 \text{ THz}, \tag{1.93}$$

meaning that for an exciting field in the visible range we are clearly in the limit $\omega_0 \gg \nu_c$. The classical inverse Bremsstrahlung cross-section can then be simplified:

$$\sigma_{iB} \approx \frac{e^2}{\epsilon_0 m_e n c} \frac{2\pi\nu_c}{\omega_0^2}. \tag{1.94}$$

At this point, one can take another ionization process into account: avalanche ionization. This phenomenon occurs when plasma free electrons are given enough energy by the laser field as to be able to ionize neutral molecules by collision (see figure 1.8). The corresponding ionization rate is given by:

$$W_{avalanche} = \frac{\sigma_{iB} I}{U^i}. \tag{1.95}$$

Usually, avalanche is a process which is neglected for pulses shorter than the typical collision time between electrons and neutrals, which is on the order of 1 ps.

Plasma generation is also responsible for a defocusing effect on the laser pulse. Starting back from equation (1.88), we can write the position vector for the free electron in the Fourier frequency space:

$$\vec{r}(\omega) = \frac{e\vec{E}(\vec{r},\omega)/m_e\omega^2}{1-2i\pi\nu_c/\omega}. \tag{1.96}$$

Since the resulting polarization for free electrons is defined as $\vec{P_f} = -en_e\vec{r}$, we thus have:

$$\vec{P_f}(\vec{r},\omega) = -\epsilon_0 \frac{\omega_p(\vec{r})^2}{\omega^2(1-2i\pi\nu_c/\omega)} \vec{E}(\vec{r},\omega), \tag{1.97}$$

where the plasma frequency $\omega_p^2 = n_e e^2/m_e\epsilon_0$, that is the frequency below which the plasma becomes opaque to electromagnetic waves, was introduced. As we showed earlier, we are in the limit $2\pi\nu_c \ll$

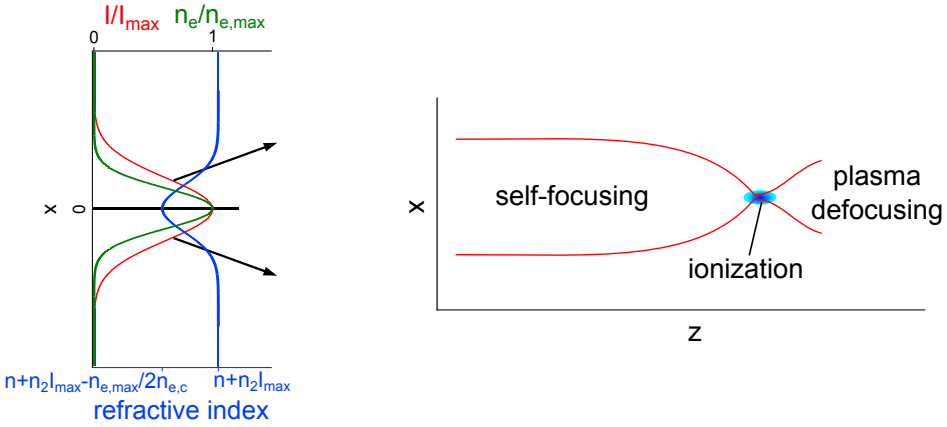

Figure 1.9: Left: schematic representation of plasma-induced defocusing. Right: evolution of the radius of a laser pulse first undergoing Kerr-induced self-focusing until reaching the intensity ionization threshold, resulting in a defocusing effect.

ω, enabling us to simplify the polarization:

$$\vec{P_f}(\vec{r},\omega) \approx \epsilon_0 \frac{n_e(\vec{r})}{n_{e,c}(\omega)} \vec{E}(\vec{r},\omega), \tag{1.98}$$

where the critical electron density $n_{e,c}(\omega) = \epsilon_0 m_e \omega^2 / e^2$ was introduced. The total polarization in the medium is then given by:

$$\vec{P}(\vec{r},\omega) = \epsilon_0 \left(\chi_e^{(1)}(\vec{r}) + \frac{3\chi_e^{(3)}(\vec{r})}{4} |\mathcal{E}(\vec{r},\omega)|^2 - \frac{n_e(\vec{r})}{n_{e,c}(\omega)} \right) \vec{E}(\vec{r},\omega). \tag{1.99}$$

The effective refractive index of the medium n_{eff} becomes:

$$\begin{aligned} n_{\text{eff}}(\vec{r},\omega) &= \sqrt{1 + \chi_e^{(1)}(\vec{r}) + \frac{3\chi_e^{(3)}(\vec{r})}{4} |\mathcal{E}(\vec{r},\omega)|^2 - \frac{n_e(\vec{r})}{n_{e,c}(\omega)}} \\ &\approx 1 + \frac{\chi_e^{(1)}(\vec{r})}{2} + \frac{3}{8}\chi_e^{(3)}(\vec{r}) |\mathcal{E}(\vec{r},\omega)|^2 - \frac{n_e(\vec{r})}{2n_{e,c}(\omega)} \\ &\approx n(\vec{r}) + n(\vec{r}) n_2(\vec{r}) I(\vec{r},\omega) - \frac{n_e(\vec{r})}{2n_{e,c}(\omega)}. \end{aligned} \tag{1.100}$$

As $n_2 I \ll n$ and $n - 1 \ll 1$, we have $n n_2 I \approx n_2 I$, thus yielding the refractive index for the medium:

$$n_{\text{eff}}(\vec{r},\omega) = n(\vec{r}) + n_2(\vec{r}) I(\vec{r},\omega) - \frac{n_e(\vec{r})}{2n_{e,c}(\omega)}. \tag{1.101}$$

Free electrons are thus locally lowering the refractive index. As the intensity and electron density spatial profiles are related through field ionization processes, the laser-induced plasma will result, for an intensity profile with a central maximum, in a refractive index profile with a lower value at the center than at the edges, thus behaving like a negative lens (figure 1.9).

1.3.2.4 Evolution of the plasma

We will now try to figure out how the laser-induced plasma will evolve in time. To this purpose, we can clearly distinguish three different time windows:

- the first one corresponds to the presence of the laser field inside the plasma, which lasts from 50 fs up to ~ 1 ps depending on experimental conditions.
- the second one corresponds to a relaxation regime. Indeed, during its propagation, the laser pulse excites coherent longitudinal free electronic population oscillations at the plasma frequency ($\omega_p/2\pi \sim 1$ THz in the case of a filament) through ponderomotive interaction. These oscillations are damped over timescales characteristic of the mean collision time (that is, ~ 1 ps from the estimation given in equation (1.93)) [60].
- finally the last one corresponds to a current-free plasma which slowly diffuses and disappears.

We are mostly interested in the first and the last time windows, as the first one has direct implications on the propagation of the laser pulse itself, and the last one can alone be easily modeled to give a good approximate of the plasma lifetime.

Plasma recombination processes The different plasma generating processes have already been discussed in sections 1.3.2.2 and 1.3.2.3. We now need to present the different channels for the plasma reabsorption. This involves four major processes:

- first, radiative electron-ion recombination, that is the scheme:

$$e^- + M^+ \longrightarrow M + h\nu, \tag{1.102}$$

  where M^+ denotes any singly ionized heavy species of air. The cross-section for this recombination process can be evaluated by means of the expression derived by Kramers in 1923 [61]:

$$\sigma_{RR}(n,K_e)\ [\mathrm{m}^2] = 2.105\times10^{-26}\frac{{\mathrm{R_y}}^2 Z^4}{nK_e[\mathrm{eV}](n^2K_e[\mathrm{eV}]+\mathrm{R_y}Z^2)}, \tag{1.103}$$

  where K_e is the electron initial kinetic energy, n the principal quantum number to which the electron recombines, Z is the atomic number and $\mathrm{R_y} = 13.6$ eV is the Rydberg constant. In the case of an oxygen plasma with electron temperature ~ 1 eV, we find $\sigma_{RR} \sim 10^{-23}$ m^2.
- second, dissociative recombination:

$$e^- + M_2^+ \longrightarrow M + M^*. \tag{1.104}$$

  It has been experimentally measured that for the O_2^+ cation, the reaction rate for this reaction quickly falls with the electron kinetic energy, being on the order of 10^{-14} m$^3\cdot$s^{-1} around 1 eV [62]. This corresponds to a cross-section $\sigma_{DR} \sim 10^{-20}$ m^2.
- third, three-body recombination, corresponding to the reaction:

$$e^- + M^+ + M \longrightarrow M + M^*. \tag{1.105}$$

  This reaction has already been studied thoroughly in the case of a plasma filament in air, giving a reaction rate $\beta = 5.3\times10^{-14}$ m$^3\cdot$s^{-1} [63]. This yields a cross-section $\sigma_{3BR} \sim 10^{-19}$ m^2.
- fourth, the attachment of free electrons to electronegative O_2 molecules, with a characteristic frequency $\nu_a = 2.5\times10^7$ s^{-1} [64]. With an electron temperature of 1 eV, we have a corresponding cross-section $\sigma_a \sim 10^{-23}$ m^2.

The two most important channels for plasma recombination are therefore dissociative recombination and three-body recombination.

Plasma evolution during laser pulse propagation The time evolution of the electron density follows the conservation law:

$$\partial_t n_e - \frac{1}{e}\vec{\nabla}.\vec{j_e} = S, \tag{1.106}$$

where S takes all source and absorption terms into account. During the laser pulse propagation, the electron current $\vec{j_e}$ is given by equation (1.89). We can compare the magnitude of $\partial_t n_e$ with that of the divergence term in the Fourier frequency domain:

$$\left|\frac{e\partial_t n_e}{\vec{\nabla}.\vec{j_e}}\right| = \left|\frac{m_e\omega^2 n_e}{e\vec{\nabla}n_e.\vec{E}}\right| \sim \frac{\omega^2 m_e L}{eE}, \tag{1.107}$$

where L is the characteristic length over which electron density gradients are encountered. Typically, $L \sim \lambda \sim 1$ µm, $\omega \sim 10^{15}$ rad $\cdot$ s^{-1} and $E \sim 10^{10}$ V $\cdot$ m^{-1} for $I \sim 10^{18}$ W $\cdot$ m^{-2}, yielding:

$$\left|\frac{e\partial_t n_e}{\vec{\nabla}.\vec{j_e}}\right| \sim 500 \gg 1. \tag{1.108}$$

We can thus neglect current effects in the time evolution of n_e.

Electrons are generated by means of photoionization and avalanche ionization. At short times when electron temperature is at its highest, dominant recombination processes were shown to be dissociative recombination and three-body recombination. The time evolution of n_e is then given by:

$$\partial_t n_e(\vec{r},t) = \sigma_{K'} I(\vec{r},t)^{K'}(n_n(\vec{r},t=0) - n_e(\vec{r},t)) + \frac{\sigma_{iB}}{U^i} n_e(\vec{r},t)I(\vec{r},t) - \beta_{eff} n_e(\vec{r},t)^2, \tag{1.109}$$

where $\beta_{eff} = \beta_{DR} + \beta_{3BR}$ is the effective recombination rate. The approximation $n_i \approx n_e$, where n_i is the ion density, was made because the Debye length is small with respect to the system spatial dimensions ($\lambda_D \sim 100$ nm).

Plasma evolution after laser excitation After the relaxation of plasma oscillations, plasma dynamics can be well described by a mobility/diffusion approach, meaning that we can neglect any inertial term in fluid equations for the evolution of momentum for plasma species:

$$\vec{v}_a = \mu_a \vec{E} - D_a\left(\frac{\vec{\nabla}T_a}{T_a} + \frac{\vec{\nabla}n_a}{n_a}\right), \tag{1.110}$$

$\mu_a = q_a/m_a\nu_a$ and $D_a = k_B T_a/m_a\nu_a$ being the mobility and diffusion coefficient for species a, respectively. This approach is valid if the mean free path of plasma species is small with respect to the characteristic length of the system. For electrons with $T_e \sim 1$ eV, we find a mean free path of ~ 300 nm, which is well below the size of a filament (diameter ~ 100 µm). Using the relation $n_e \approx n_i$ and using the last equation for both electrons and ions, we can find that the time evolution of electrons is given by:

$$\partial_t n_e - D_a \Delta(n_e) = S, \tag{1.111}$$

where $D_a = (\mu_i D_e + \mu_e D_i)/(\mu_i + \mu_e)$ is the ambipolar coefficient diffusion. This regime is characterized by the simultaneous diffusion of ionic and free electronic species to prevent the generation of a space charge electric field. Neglecting both radiative recombination and electron attachment, we find:

$$\partial_t n_e(\vec{r},t) - D_a(\vec{r},t)\Delta(n_e(\vec{r},t)) = -\beta_{eff} n_e(\vec{r},t)^2. \tag{1.112}$$

1.3.3 Characteristics of filamentation in air

1.3.3.1 Propagation dynamics of the laser pulse

A first approach: dynamic competition at the global scale As filamentation results from the dynamic competition between Kerr-induced self-focusing, a very simple way to derive key parameters of filaments is to balance focusing (Kerr effect) and defocusing contributions (plasma and diffraction) to the refractive index, yielding:

$$n_2 I = \frac{n_e}{2n_{e,c}} + \frac{(1.22\lambda_0)^2}{8\pi n w_0^2}. \tag{1.113}$$

Linking electron density to intensity by means of equation (1.87) leads to:

$$\begin{cases} I \sim \left(\dfrac{2n_{e,c}(\lambda_0)}{\sigma_{K'}\tau\rho_o}\left(n_2 - \dfrac{(1{,}22\lambda_0)^2}{8nP_{cr}}\right)\right)^{1/(K'-1)} & \sim 1.6\times10^{17}\ \mathrm{W\cdot m^{-2}} \\ n_e \sim (\sigma_N\tau n_n(t=0))^{(1-K')}\left(2n_{e,c}(\lambda_0)\left(n_2 - \dfrac{(1{,}22\lambda_0)^2}{8nP_{cr}}\right)\right)^{K'/(K'-1)} & \sim 7\times10^{21}\ \mathrm{m^{-3}} \\ w_0 \sim \sqrt{\dfrac{P_{cr}}{\pi}}\left(\dfrac{2n_{e,c}(\lambda_0)}{\sigma_{K'}\tau n_n(t=0)}\left(n_2 - \dfrac{(1{,}22\lambda_0)^2}{8nP_{cr}}\right)\right)^{1/(2(1-K'))} & \sim 50\ \mu\mathrm{m}. \end{cases} \tag{1.114}$$

Here, $\tau \sim 100$ fs is the pulse duration. This crude modeling was first done by Javan and Kelley for the self-focusing of pulses propagating in media with anomalous GVD [65], and applied to filamentation by Braun *et al.* [16]. It enables one to have an estimation of the order of magnitude for key filament parameters, despite its simplicity. It also predicts that, due to the competitive nature of filamentation, the corresponding values remain constant during propagation, resulting in the clamping of intensity and electron density. Becker *et al.* experimentally tested this prediction by recording plasma fluorescence from filamentation in nitrogen, recording evidence of intensity clamping [66].

It is worth mentioning this modeling only includes the Kerr effect as a focusing term. The use of external focusing for filamentation generation can therefore result in significantly different observed values for intensity and electron density in filaments, especially when pulse focusing is lens-dominated [50]. In this case, the very notion of intensity clamping becomes irrelevant [49]. Moreover, being static, the model completely fails to reproduce the dynamics of pulse propagation, not to mention the fact it assumes that the dynamic competition occurs on a global scale, whereas it is actually fulfilled only on a local scale.

Spatial structure of the filament: need for a new interpretation In the first experiment demonstrating filamentation in air, Braun *et al.* already characterized the spatial repartition of intensity inside of a filament. They showed that it is composed of a central intense core with FWHM ~ 100 µm surrounded by a more diffuse and far larger background [16], containing up to 90% of the pulse energy [67]. Progressively, new experiments highlighted the crucial role of this background in maintaining the filament. For instance, it was demonstrated that when the core of the filament was stopped, the surrounding energy bath was able to reform it later during propagation [68, 69], an effect called self-healing by Kolesik and Moloney [70]. Similarly, cutting a given portion of the energy bath significantly shortens the total filament length [71]. Recently, Scheller *et al.* even proved that using a low-intensity secondary beam acting as an auxiliary energy bath, the filament can propagate over longer distances than usual [72].

At the end of the 1990s, Mlejnek, Wright and Moloney presented a dynamic modeling of filamentation based on complex interaction of different spatio-temporal components of the laser pulse. This *spatial replenishment* model is characterized by the successive splitting of the laser pulse during plasma defocusing/Kerr self-focusing cycles [73, 74].

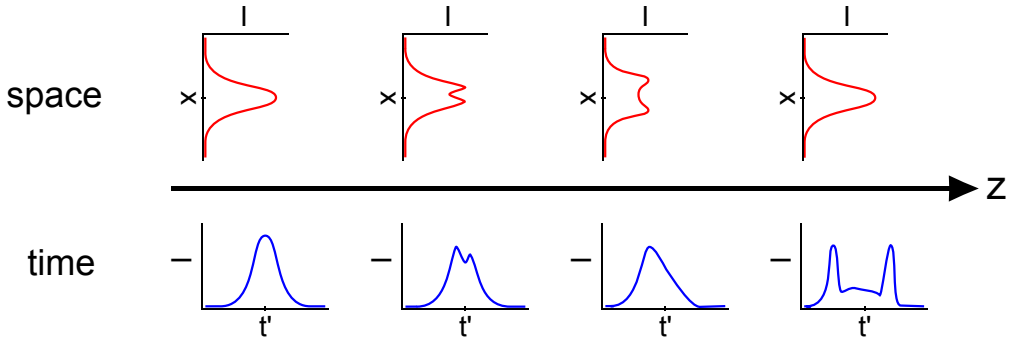

Figure 1.10: Evolution of 1D spatial profiles (top) and on-axis temporal profiles (bottom) of an initially Gaussian pulse undergoing filamentation. When intensity reaches the ionization threshold, plasma generation depletes the front part of the pulse, shifting the pulse at later times, while a dip appears at the center of the spatial profile due to laser energy depletion. The plasma in turn defocuses the tail of the pulse, resulting in the formation of a doughnut-like spatial profile. As on-axis laser energy is reduced, ionization slows down, enabling the pulse to self-focus again. This yields two pulses: the first one corresponds to the initial pulse, the other one is formed from the background (from Mlejnek, Wright and Moloney [73]).

Such a cycle is presented in figure 1.10. Starting from a Gaussian pulse, Kerr self-focusing will bring about ionization through multiphoton absorption and tunneling. In time, ionization occurs at the front of the pulse, before maximum intensity is reached. This front part still propagates straight along z but gradually damps due to nonlinear losses. This results in the peak intensity being shifted towards the tail of the pulse. As this part of the pulse propagates in an ionized medium, it also suffers from plasma defocusing and is repelled away from the axis, giving a doughnut-like spatial profile. When the ionizing, on-axis pulse component is depleted so that plasma generation is no longer efficient, Kerr self-focusing can overcome plasma defocusing and the ring-like pulse is attracted back towards the axis. In the time domain, this is characterized by the formation of a second trailing pulse from the background. A new ionization-defocusing-self-focusing cycle then occurs. This scenario can repeat many times depending on the pulse initial peak power, leading to the filament propagation lasting over several Rayleigh lengths without diffracting. For a collimated or loosely focused beam, filamentation can therefore span hundreds of meters [75, 76].

The spatial replenishment model is characterized by the transformation of an initial Gaussian-like pulse into a complex spatial profile with an on-axis leading component followed by a ring-like trailing component, a structure similar to that of a Bessel beam. Such a transition was experimentally observed in water by Dubietis *et al.*, and modeled by the sole inclusion of multiphoton absorption in the propagation equation, highlighting the crucial role of nonlinear losses in establishing the dynamic balance of filamentation [69]. The same year, Porras *et al.*, using the same "plasma-free" modeling, identified unbalanced Bessel beams as a family of stationary solutions for the envelope propagation equation, and that such solutions behaved as strong attractors for the self-focusing dynamics in Kerr media [77]. Other numerical solutions shown to exist are X-waves,

called as such because of their form in the (ω,$k_\perp$) space [78]. They, too, take the form of conical, localized wavepackets.

Within this framework, filamentation can be seen as a the steady-state propagation of a wavepacket with a strong on-axis maximum, responsible for nonlinear energy absorption, surrounded by a cone-like, low intensity energy bath that continuously feeds energy to the central part.

Spectral broadening and pulse compression As shown in section 1.2.3.1, Kerr self-focusing itself results in the spectral broadening of the pulse by self-phase modulation and self-steepening. When ionization occurs, free electrons will also modify the refractive index, and contribute to the instantaneous laser frequency similarly to equation (1.71):

$$\omega(t) = \omega_0 - \frac{n_2\omega_0 z}{c}\frac{\partial I}{\partial t}(t) + \frac{1}{2n_{e,c}}\frac{\partial n_e}{\partial t}(t). \tag{1.115}$$

As the back of the pulse encounters a significantly larger electron density than the front, plasma tends to generate blue-shifted frequencies at the tail of the pulse, much in the same way as self-phase modulation. As a consequence, the initial spectrum of the pulse will be strongly modified after filamentation, exhibiting an important broadening ranging from the near ultraviolet to the far infrared [79, 80].

This effect of spectral broadening, coupled to the profound distortion experienced by the pulse temporal profile during its propagation, can be used for its temporal compression if the frequency chirp is somehow compensated. Using this technique, pulses of a few fs down from $\sim$ 50 fs were produced by filamentation in argon [81, 82]. During refocusing cycles of the trailing part of the pulse, it was also shown both numerically [83] and experimentally [84] that sub-fs pulses can be generated and extracted from the filament.

End of filamentation The progressive depletion of laser energy during propagation due to Rayleigh scattering, nonlinear absorption or redistribution of the spectrum far from the initial wavelength leads to the end of filamentation when the pulse peak power decreases below P_{cr}, meaning that Kerr self-focusing will be too weak to counterbalance diffraction. Filamentation can also stop while still being over-critical due to a too large spatial phase curvature resulting from plasma generation and defocusing, which Kerr effect is unable to compensate [85].

1.3.3.2 Plasma columns generated by filamentation

As seen previously in section 1.3.2.2, self-focusing in air leads to the formation of plasma, which corresponds to the main mechanism for stopping the pulse collapse.

From the estimation given by the equation system (1.114), we found $n_e \sim 10^{22}\ \mathrm{m}^{-3} \ll n_{e,c}(800\ \mathrm{nm}) = 1.7 \times 10^{27}\ \mathrm{m}^{-3}$, meaning laser energy is only weakly absorbed by the plasma. Filament-generated plasma therefore takes the form of a continuous column with a transverse dimension of the same order of magnitude as the intense filament core ($\sim$ 100 µm) and a length depending on how long the pulse peak intensity remains above the ionization threshold. This behavior is completely opposite to what is observed with long and energetic pulses (typically 10 ns pulses from Q-switched Nd:YAG lasers or equivalent), which tend to generate discrete bubbles of plasma dense enough so that it becomes opaque at the laser wavelength.

As air is mainly composed of molecular nitrogen, filamentation plasma generates luminescence in the blue region of the spectrum, between 300 and 450 nm (as seen on the photograph displayed

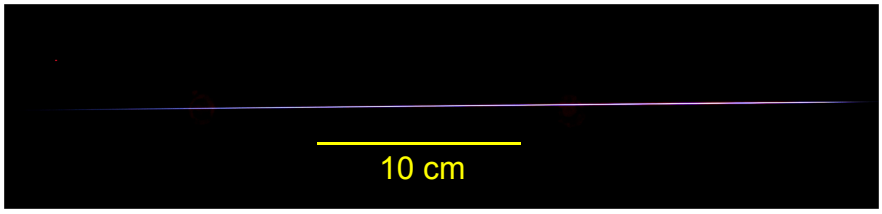

Figure 1.11: Characteristic luminescence of an air plasma column generated by a 1 mJ, 40 fs laser pulse at 800 nm focused at $f/100$.

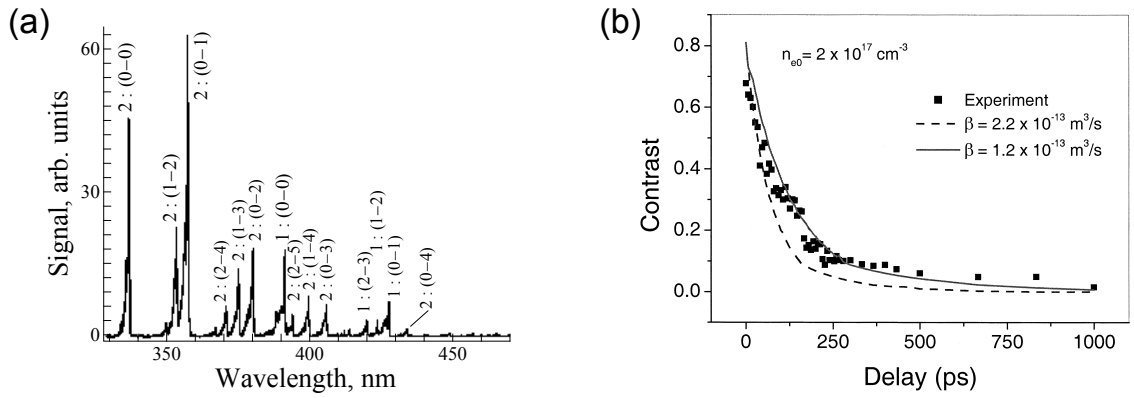

Figure 1.12: (a): emission spectrum of filamentation plasma in air, showing characteristic lines from molecular nitrogen. 1 corresponds to the first negative system ($B^2\Sigma_u^+ - X^2\Sigma_g^+$) of N_2^+ and 2 to the second positive system ($C^3\Pi_u - B^3\Pi_g$) of N_2. The numbers ($\nu - \nu'$) are the quantum vibrational numbers for the lower state and the upper state of the transition, respectively (from Talebpour *et al.* [86]). (b): measured time evolution of the filament plasma density (squares) and two different modeling for various values of the recombination rate β (from Tzortzakis *et al.* [87]).

in figure 1.11 and on the spectrum given in figure 1.12-(a)). Being a low-temperature plasma, it also exhibits a negligible Bremsstrahlung contribution [86].

Measuring electron density in the filament plasma and its subsequent decay is a challenging task because of its small size, short lifetime and low ionization. Tzortzakis *et al.* were the first to realize a direct optical measurement by means of time-resolved diffractometry [87]. The corresponding initial electron density was estimated as $n_e(t=0) = 10^{23}$ m^{-3}. The decay is characterized by two different phases: the first one is marked by the quick decrease of n_e in about 250 ps, followed by a slower evolution (figure 1.12-(b)). The first phase was attributed to recombination to parent ions, while the second was attributed to electron attachment to O_2. Electric measurements of plasma conductivity confirmed this slow, exponentially damped evolution [88]. Overall, these measurements give a characteristic plasma lifetime at $n_e(t=0)/10$ on the order of 1 ns. Later measurements using even more precise interferometry give similar results with respect to initial plasma density and plasma lifetime [89, 90].

1.3.3.3 Energy deposition by filamentation in air

As the filament propagates, it deposits energy in the medium because of photoionization, plasma absorption and Raman rotational absorption. Even if the deposited energy is modest, the small vol-

ume involved and the rapidity of the phenomenon leads to important instantaneous power density, that is eventually converted into heat. The medium will then react by generating an outward-propagating hydrodynamic wave, leaving an underdense air channel at the center (see figure 1.13).

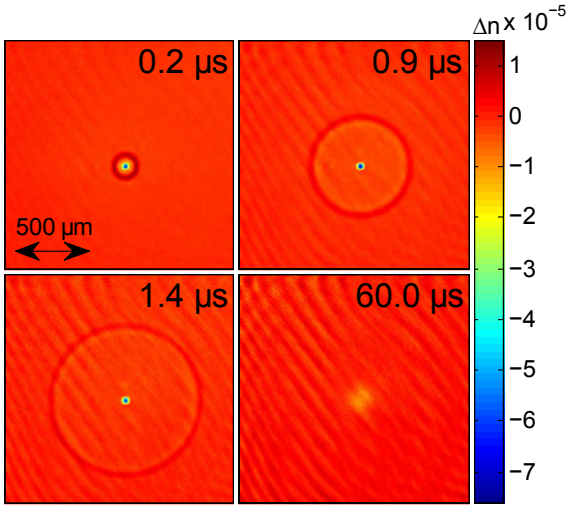

Figure 1.13: Interferometrically-recorded refractive index shifts at various delays after filamentation of a 60 µJ laser pulse in air, showing the formation of a radial sound wave and of a central low-density channel. From Wahlstrand *et al.* [91].

These laser-induced hydrodynamic phenomena have numerous promising applications, such as remotely-generated optical index structures in air, leading, for instance, to virtual waveguides [92]. Moreover, the low-density channel resulting from filamentation plays a crucial role in the field of filamentation-guided discharges, as proved by Tzortzakis *et al.* [93], and as such opens wide perspectives towards virtual plasma antennas, the laser lightning rod and many other applications.

1.3.3.4 Secondary coherent emission from filaments

Filamentation leads to the transfer of laser energy into several radiating secondary emissions that will be briefly reviewed here.

Conical emission of colored rings Witnessed since the first days of filamentation, the conical emission is truly characteristic of this propagation regime. It takes the form of several colored rings surrounding the white light continuum generated during filamentation appearing in the reversed order as diffraction, meaning that blue rings have a larger opening angle than red rings (cf. figure 1.14).

The most complete explanation for the formation of conical emission, to date, was published by Faccio *et al.* [94]. It states that a phase-matched four-wave mixing process between two X-wave modes of the medium and two strongly localized pump wavepackets leads to the parametric amplification of the X-waves and in the formation of the characteristic conical pattern observed experimentally.

Terahertz coherent emission We saw in section 1.3.2.4 that the laser pulse excites a coherent free electronic oscillations at the plasma frequency by ponderomotive interaction. Since the average

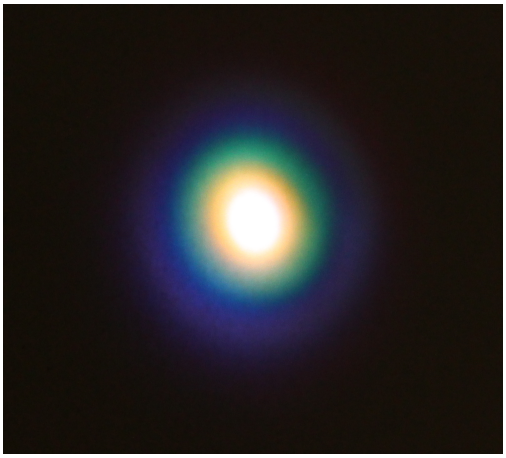

Figure 1.14: Photograph of the conical emission resulting from filamentation in air.

electron movement in the direction of a linearly polarized laser field is zero, there is no transverse current in the filament. The only current is induced by the ponderomotive force resulting from the laser pulse, which tends to push newly-generated electrons to the back of the pulse, thus creating a space charge. As the pulse leaves, displaced electrons start to oscillate in this space charge field at their characteristic frequency, the plasma frequency, and radiates electromagnetic waves at this frequency. As $n_e \sim 10^{22}$ m^{-3} in filaments, this frequency $f_p = \omega_p/2\pi$ lies around 1 THz. Plasma oscillations are quickly damped by electron-neutral collisions and disappear within a few ps.

The laser pulse is therefore responsible for the generation of a short-lived dipole structure left in its wake. This dipole can be seen as propagating at the group velocity of the laser pulse. Terahertz emission takes the form of a radially-polarized cone propagating in the same direction as the laser pulse (figure 1.15), a feature similar to the Cherenkov radiation, that is radiation emitted by a charged particle propagating faster than the phase velocity $c/n(\omega)$ of the emitted light in the medium. Strictly speaking, terahertz radiation is not a Cherenkov emission because the Cherenkov criterion $v/v_\phi > 1$ is not fulfilled. It appears more related to a transition-like radiation due to the finite displacement length of emitting dipoles [95]. However, because of the Cherenkov-like conical emission pattern, terahertz radiation was dubbed "transition-Cherenkov" radiation [60].

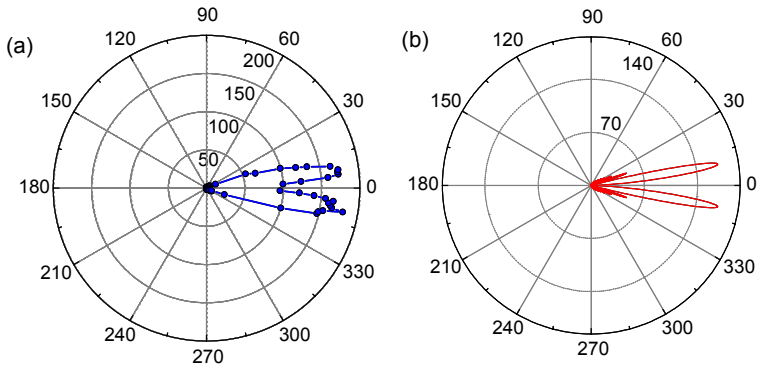

Figure 1.15: Measured (a) and calculated (b) terahertz radiation pattern from a 8 cm long filament. From D'amico *et al.* [96].

Terahertz generation by filamentation is a promising way for remotely generating a broadband radiation source, paving the way for many applications ranging from biology to security concerns.

Lasing effect from filaments In 2003, Luo and coworkers measured a backscattered molecular nitrogen fluorescence signal from filamentation growing exponentially with the filament length [97]. The authors attributed this result to an amplified spontaneous emission from the $(C^3\Pi_u - B^3\Pi_g)$ second positive system of N_2. A few years later, Yao *et al.* demonstrated a forward lasing action from filaments generated by mid-infrared pulses in air [98]. By switching the pump wavelength, the authors were able to select different emission lines from the $(B^2\Sigma_u^+ - X^2\Sigma_g^+)$ first negative system of N_2^+. They suggested the lasing action was seeded by one of the harmonics of the pump pulse. The same group later showed that similar lasing effect could be achieved using 800 nm pump pulses and seeding the resulting filament by the second harmonic signal at 400 nm in nitrogen [99]. Later, Liu *et al.* from LOA experimentally proved that the seed was redundant and that coherent emission could be "self-seeded" by in-situ generation of the second harmonic signal in the plasma and by the spectral broadening resulting from filamentation (see figure 1.16-(b)). A maximum pulse energy at 428 nm of 2.6 µJ was achieved using a terawatt-level pump pulse [100]. Since then, backward lasing action at 337 nm in pure nitrogen has also been demonstrated using circularly-polarized 800 nm pump pulses (figure 1.16-(a)).

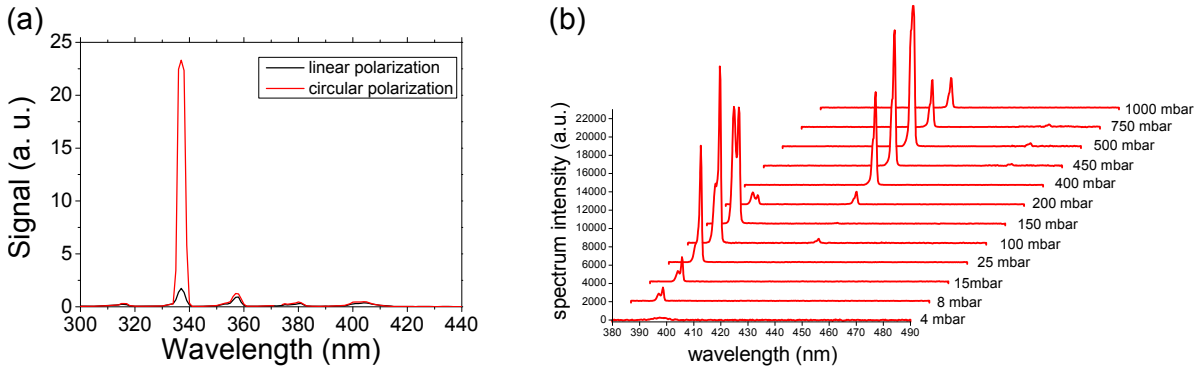

Figure 1.16: (a) recorded on-axis backward emission from filamentation plasma in the case of linear and circular polarization, exhibiting the coherent emission at 337 nm (from Mitryukovskiy *et al.* [101]). (b): on-axis forward plasma emission spectrum in pure nitrogen at different pressures, showing lasing action of the $(B^2\Sigma_u^+ - X^2\Sigma_g^+)$ first negative system of N_2^+ (from Liu *et al.* [102]).

Up to now, the underlying physics for the forward, ionic stimulated emission from filaments are not well elucidated. Many experiments highlighted the role of a seeding action, either external or induced by the filament itself, but the mechanism of formation of the excited $B^2\Sigma_u^+$ is still debated. As for the backward lasing action, Mitryukovskiy *et al.* suggested that the formation of the upper $C^3\Pi_u$ state in the case of filamentation was similar to how population inversion is achieved in nitrogen lasers, that is by impact collision of energetic electrons with nitrogen molecules. They notably showed that this mechanism was possible in case of circularly polarized pump pulses because in this case, electron kinetic energy distribution could easily reach the collision threshold of 10 eV [103].

Lasing action from filaments opens interesting perspectives in the field of remote sensing in the atmosphere because, unlike LIDAR techniques, the coherent emission makes signal detection far

easier.

1.3.3.5 Multifilamentation

When the peak power of a laser pulse increases above P_{cr}, it can break down in the form of several copropagating filaments. This effect, known as multifilamentation, can be triggered by several effects. The oldest explanation for the formation of multifilamentation was suggested by Bespalov and Talanov, stating that powerful pulses become modulationally unstable [104]. This means that noise-induced inhomogeneities in the originally-smooth beam spatial profile will amplify exponentially during propagation, depending on their characteristic transverse spatial frequency $k_\perp/2\pi$. Bespalov and Talanov showed that fastest growing instabilities are characterized by a transverse wavevector $k_\perp^{max} \approx 2\sqrt{\pi I/P_{cr}}$. As a consequence, inhomogeneities grow until they become large enough to collapse and form their own filament, resulting in the beam breaking down into several filaments separated by an average distance $d = 2\pi/k_\perp^{max}$. One can thus estimate the power of each of these short-scale filaments as $P_{fil} \approx P_{cr}$, giving a total number of multifilaments in the beam $N_{MF} \approx P/P_{cr}$ [105]. By nature, modulational instabilities give rise to a completely random multifilamentation pattern, making control of the phenomenon very difficult. Mlejnek *et al.* showed numerically that propagation of a powerful ultrashort laser pulse breaking, of which breaking down was due to modulational instabilities, had much in common with a turbulent system [106]. This model is characterized by many simultaneous collapses leading to short-scale filaments, fed from the large scale energy reservoir and losing energy at the small spatial scale characteristic of areas where ionization takes place, a mechanism similar to a Kolmogorov energy cascade.

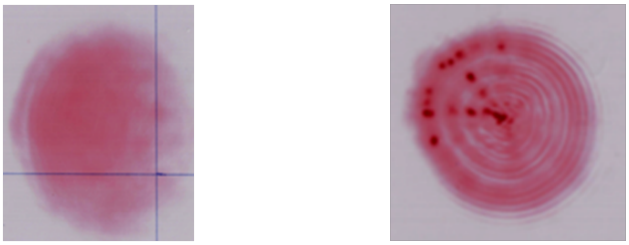

Figure 1.17: Impacts on photographic paper of a 260 mJ, 2 ps laser pulse focused at 110 m recorded at the output of the laser (left) and at a distance of 74 m (right). Energy is initially concentrated in the upper left quadrant, and the beam is cut on the left side. During propagation, filaments appear preferentially on diffraction rings resulting from this cut, also in the upper left quadrant.

Another theory regarding the formation of multifilaments was published in the early 2000s by Fibich and Ilan. Taking into account usually neglected vectorial terms in the propagation equation (like $\vec{\nabla}.\vec{E}$), equivalent to allowing the pulse polarization to change during propagation in a Kerr medium, they proved that beam break-up could occur at relatively low input power and that such effects could surpass modulational instability in amplitude [107, 108]. Contrary to modulational instabilities, vectorial and non-paraxial effects are also deterministic.

The same authors also simulated the propagation of a powerful noisy Gaussian beam that eventually collapsed in the form of a single filament instead of forming multifilaments. The failure of modulational instabilities was attributed to the fact that Bespalov and Talanov used a monochromatic plane wave unchanged during propagation in their approach, an hypothesis that becomes valid during propagation of powerful laser pulses if the beam undergoes self-phase modulation with-

out any significant self-focusing [109]. The transition between the two multifilamentation regimes was estimated around 100 P_{cr}, depending on the noise level of the beam. Below this threshold, laser beams undergo a whole beam collapse with the initial formation of a single filament. Above, they break down into short-scale filaments before the nonlinear focus corresponding to the whole beam collapse can be reached.

Still, it is possible to have a limited control over multifilamentation in high-energy regimes that should be dominated by modulational instability. This control is achieved in a very simple way by imposing an initial inhomogeneous spatial profile, for instance by using amplitude masks. If inhomogeneities have an amplitude strong enough, they will be able to locally self-focus before modulational instabilities could act, and lead to a pre-determined, non-turbulent filamentation pattern [110]. Even phase and/or amplitude distortions induced by optics can overcome modulational instabilities and lead to a reproducible multifilament spatial repatition, as evidenced in figure 1.17, where the initially cut laser beam generates diffraction rings during propagation, on which multifilaments preferentially appear.

After the initial beam break-up, multifilaments can interact in a complex way. For instance, once first multifilaments are born, interference between ring structures developed by each one of them and the energy bath can lead to the formation of new filaments [111, 112]. They are also able to attract or repel each other, and to experience fusion, depending on their relative phase [113].

1.3.4 Simulating filamentation

Numerical simulations of filamentation are crucial for a good understanding of physical processes taking place in experiments. To this purpose, my research group has been working in collaboration with Arnaud Couairon from the Centre de Physique Théorique (CPHT) of Ecole Polytechnique, who was responsible for the development of an advanced nonlinear envelope propagation code, for more than 10 years. This section is only intended to give some hints about how to properly simulate filamentation. More insight about propagation equation derivation and numerical recipes can be found in reference [114].

1.3.4.1 Derivation of the nonlinear propagation equation system

To derive the equation system solved by the code, we first start back from Maxwell equations to get the propagation equation for the electric field:

$$\Delta\vec{E}(\vec{r},t) - \frac{1}{c^2}\partial_t^2 \int_0^{+\infty} n(\vec{r},t')^2\vec{E}(\vec{r},t-t')\ \mathrm{d}t' = \mu_0\left(\partial_t^2\vec{P}_{nl}(\vec{r},t) + \partial_t\vec{j}(\vec{r},t)\right), \tag{1.116}$$

where we decomposed polarization between a linear and a nonlinear part $\vec{P}_{nl}$. Using the envelope formalism for the electric field described by equation (1.13) in the slowly varying envelope approximation, we already know from equation (1.21) that:

$$\Delta\vec{\mathcal{E}}(\vec{r},t) - \frac{1}{c^2}\partial_t^2 \int_0^{+\infty} n(\vec{r},t')^2\vec{\mathcal{E}}(\vec{r},t-t')\ \mathrm{d}t' = \left(\Delta_\perp + 2i(k_0 + ik_0'\partial_{t'})\partial_{z'} - k_0k_0''\partial_{t'}^2\right)\vec{\mathcal{E}}(\vec{r},t). \tag{1.117}$$

In the Fourier frequency domain, equation (1.116) reads:

$$\left(\Delta_\perp + 2i(k_0 + k_0'(\omega-\omega_0))\partial_{z'} + k_0k_0''(\omega-\omega_0)^2\right)\vec{\mathcal{E}}(\vec{r},\omega) = -\mu_0(\omega-\omega_0)^2\left(\vec{\mathcal{P}}_{nl}(\vec{r},\omega) + i\frac{\vec{\mathcal{J}}(\vec{r},\omega)}{\omega-\omega_0}\right), \tag{1.118}$$

where $\mathcal{P}_{nl}$ and $\mathcal{J}$ correspond to the slowly varying envelopes of P_{nl} and j. The nonlinear polarization can be expressed by using equation (1.59):

$$\vec{\mathcal{P}}_{nl}(\vec{r},\omega) = \mathcal{F}\left(2\epsilon_0 n(\vec{r})\left(n_2(\vec{r})I(\vec{r},t) + \int_{\mathbb{R}^+} \mathcal{R}(\vec{r},t')I(\vec{r},t-t')\,\mathrm{d}t'\right)\vec{\mathcal{E}}(\vec{r},t)\right). \tag{1.119}$$

The free current j is made up of two components: one of them is the plasma current j_p due to the movement of electrons in the laser field. The other is a resistive equivalent current due to laser energy losses through ionization, j_{loss}. Using the expression of the plasma current derived in equation (1.89) and the inverse Bremsstrahlung cross-section given in equation (1.91), we have immediately:

$$\vec{j}_p(\vec{r},\omega) = -\epsilon_0 c n(\vec{r}) n_e(\vec{r})\sigma_{iB}(\omega)\left(1 + i\frac{\omega}{2\pi\nu_c}\right)\vec{E}(\vec{r},\omega). \tag{1.120}$$

To derive the expression for j_{loss} we can write the time-averaged power lost per unit volume:

$$\frac{1}{2}\vec{j}_{loss}(\vec{r},\omega).\vec{E}(\vec{r},\omega)^* = -K'\hbar\omega_0\sigma_{K'}I(\vec{r},\omega)^{K'}(n_n(t=0) - n_e(\vec{r})), \tag{1.121}$$

so that finally we have for the loss current:

$$\begin{aligned}\vec{j}_{loss}(\vec{r},\omega) &= 4\epsilon_0 c n(\vec{r},\omega_0)K'\hbar\omega_0\sigma_{K'}I(\vec{r},\omega)^{K'-1}(n_n(t=0) - n_e(\vec{r}))\vec{E}(\vec{r},\omega)\\ &= -\beta_{K'}I(\vec{r},\omega)^{K'-1}\left(1 - \frac{n_e(\vec{r})}{n_n(t=0)}\right)\vec{E}(\vec{r},\omega).\end{aligned} \tag{1.122}$$

The envelope current $\mathcal{J}$ is then expressed as:

$$\mathcal{J}(\vec{r},\omega) = -\left(cn(\vec{r})n_e(\vec{r})\sigma_{iB}(\omega)\left(1 + i\frac{\omega}{2\pi\nu_c}\right) + \beta_{K'}I(\vec{r},\omega)^{K'-1}\left(1 - \frac{n_e(\vec{r})}{n_n(t=0)}\right)\right)\vec{\mathcal{E}}(\vec{r},\omega). \tag{1.123}$$

Finally, the nonlinear envelope equation in the Fourier frequency space reads:

$$\begin{cases}\left(\left(1 + \frac{k_0'}{k_0}(\omega-\omega_0)\right)\partial_{z'} - \frac{i}{2k_0}\Delta_\perp - \frac{i}{2}k_0''(\omega-\omega_0)^2 - \hat{B}_{current}\right)\vec{\mathcal{E}} = i\mu_0\frac{(\omega-\omega_0)^2}{2k_0}\mathcal{F}\left(\hat{A}_{Kerr}\vec{\mathcal{E}}\right)\\ \hat{A}_{Kerr} = 2\epsilon_0 n(\vec{r})\left(n_2(\vec{r})I(\vec{r},t) + \int_{\mathbb{R}^+}\mathcal{R}(\vec{r},t')I(\vec{r},t-t')\,\mathrm{d}t'\right)\\ \hat{B}_{current} = \frac{n(\omega_0)(\omega-\omega_0)}{k_0 c}\left(\frac{1}{2}n_e\sigma_{iB}\left(1 + \frac{i\omega}{2\pi\nu_c}\right) + 2K'\hbar\omega_0\sigma_{K'}I^{K'-1}(n_n(t=0) - n_e)\right).\end{cases} \tag{1.124}$$

We can make some comments about the different terms of this last equation. The first term is characterized by the space derivative $\partial_{z'}$, and is the sole term accounting for the evolution of the laser pulse along z during propagation. The second term, with the transverse Laplacian operator, is characteristic of diffraction. The third term in k_0'' accounts for the effect of group velocity dispersion on the temporal shape of the pulse. The fourth term, the operator $\hat{B}_{current}$, models both plasma retro-action on the laser pulse and nonlinear energy absorption due to multiphoton and tunnel ionization. More specifically, the real part of the first term of $\hat{B}_{current}$ accounts for plasma defocusing, and the imaginary part gives inverse Bremsstrahlung absorption. Finally, the $\hat{A}_{Kerr}$ operator accounts for Kerr effect and rotational Raman excitation.

The propagation equation (1.124) is not self-consistent. Indeed, to have a full description of the system, one must also model the evolution of electron density in both space and time. We already modeled this evolution during the propagation of the laser pulse in section 1.3.2.4, which is described by equation (1.109).

1.3.4.2 Example of simulation

Examples of numerical simulations for the filamentation propagation regime are given in figure 1.18. The evolution of the beam radius, on-axis intensity and electron density with propagation distance z are plotted for three different focusing conditions.

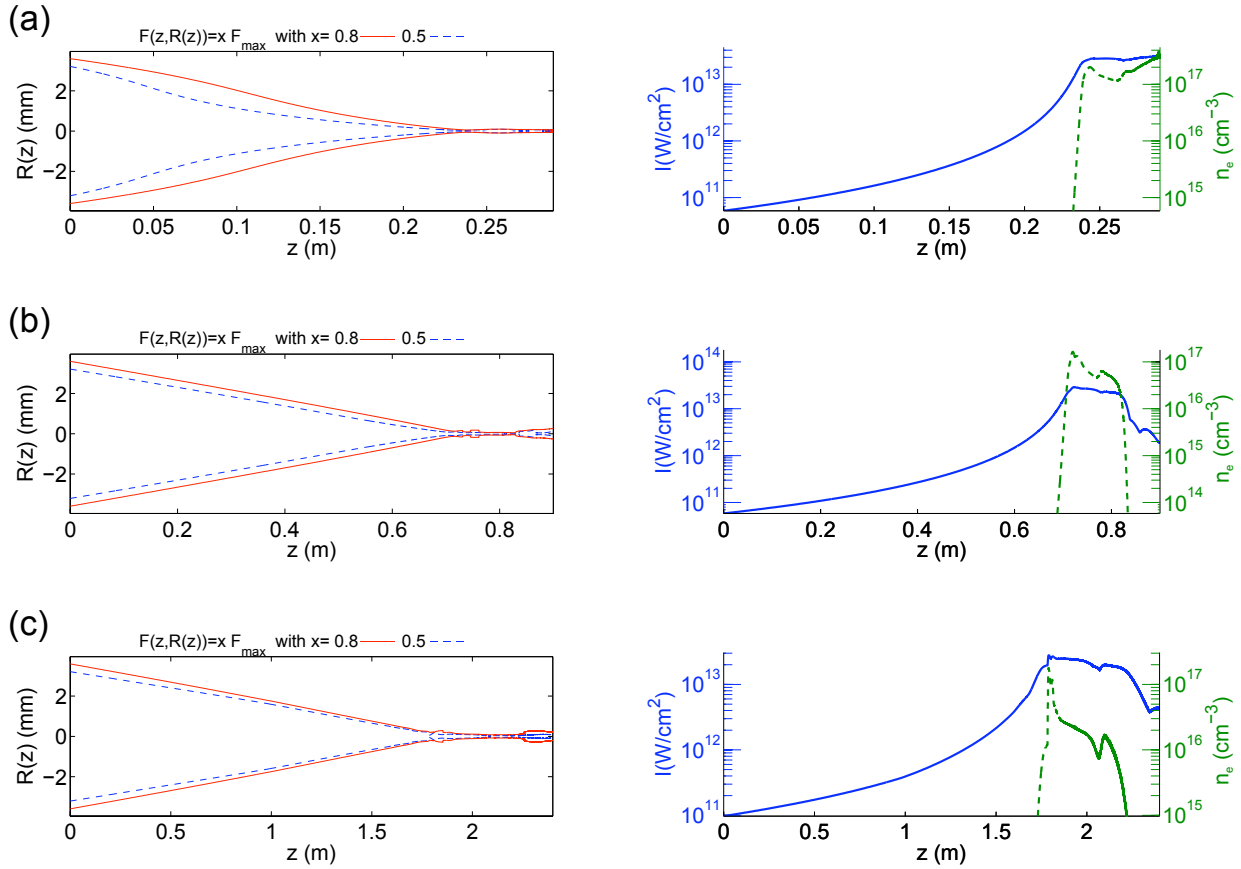

Figure 1.18: Simulations for the propagation of a 3 mJ, 100 fs laser pulse with Gaussian spatial profile of initial waist $w_0 = 1$ cm. Plots on the left give fluence isosurfaces for $0.5F_{max}$ (red solid curves) and $0.8F_{max}$ (blue dashed curves), plots on the right give on-axis intensity (blue solid curves) and on-axis electron densities (green dashed curves). Focusing conditions are 25 cm or $f/12$ (a), 75 cm or $f/35$ (b) and 2 m or $f/100$ (c). Courtesy of Arnaud Couairon.

These results display striking characteristic features of filamentation: first, they correctly predict the beam collapse, which occurs at a distance smaller than the focal length of the focusing length, as indicated by equation (1.73). This collapse phase is followed by filamentation itself: the core of the beam remains confined in a ~ 100 µm wide channel and propagates with an almost constant diameter. In the filamentation zone, simulation also indicate that intensity is clamped, as evidenced by the dramatic plateau. Plasma generation is confined to this clamped area, since it is one of the components of the dynamic competition leading to filamentation. We can see that the stronger the focusing, the denser the generated plasma, with a plasma about 10 times denser at $f/12$ than at $f/100$. Moreover, one can see hints of spatial replenishment, especially at weaker focusing, characterized by surges in electron density, indicating a refocusing cycle of the trailing part of the

pulse. Finally, ionization stops, peak intensity quickly decreases and the pulse diverges, marking the end of filamentation.

Numerical simulations are therefore able to model the propagation of an ultrashort pulse in a regime as complex as filamentation. However, they are extremely sensitive to input physical parameters, for instance ionization cross-sections, meaning that only the comparison with experiments can prove the validity of a given simulation. Moreover, in cases as complex as multifilamentation, a large number of approximations is necessary to keep computation time at an acceptable level. Still, they are also precious tool because they give access to many physical parameters of the beam, like peak intensity or transverse fluence distribution, which would be otherwise extremely difficult to measure.

Conclusion

Nonlinear optics is truly a fascinating field of physics, because it enables one to touch the very fabric of matter, giving rise to spectacular effects. Filamentation, for instance, is nowadays very easy to observe, due to the democratization of ultrashort lasers. One only needs to launch a femtosecond pulse in air to eventually see filamentation occur. Yet the underlying physics are, as we saw, extremely complex. This apparent simplicity also contributes to the beauty of filamentation.

Filamentation results from a dynamic competition involving Kerr-induced self-focusing on the one hand, and diffraction, photoionization, plasma absorption and plasma defocusing on the other hand. As such, filaments are able to propagate over several Rayleigh lengths before disappearing, meaning that the beam can keep a very high intensity level for long distances: for collimated beams, filaments can reach over 100 m. A very important consequence of filamentation is laser energy deposition in the medium through ionization, plasma absorption and Raman rotational excitation. This leads to the generation of strong and long-lived hydrodynamic effects in air, as we will see in the first part of this Thesis. A major application of these hydrodynamic effects consists in guiding electric discharges over long distances, a thematic that will be investigated in the second part of this work.

Bibliography

[1] A. Einstein, Annalen der Physik **322**, 132 (1905).

[2] A. Einstein, Verhandlungen der Deutschen Physikalischen Gesellschaft **18**, 318 (1916).

[3] A. Einstein, Physikalische Zeitschrifft **18**, 121 (1917).

[4] J. P. Gordon, H. J. Zeiger, and C. H. Townes, Physical Review **99**, 1264 (1955).

[5] T. H. Maiman, Nature **187**, 493 (1960).

[6] P. A. Franken, A. E. Hill, C. W. Peters, and G. Weinreich, Physical Review Letters **7**, 118 (1961).

[7] F. J. McClung and R. W. Hellwarth, Journal of Applied Physics **33**, 828 (1962).

[8] A. J. DeMaria, W. H. Glenn, M. J. Brienza, and M. E. Mack, Proceedings of the IEEE **57**, 2 (1969).

[9] R. L. Fork, B. I. Greene, and C. V. Shank, Applied Physics Letters **38**, 671 (1981).

[10] D. Strickland and G. Mourou, Optics Communications **56**, 219 (1985).

[11] M. Born and E. Wolf, *Principles of Optics*, 7^{th} ed. (Cambridge University Press, Cambridge, UK, 1999).

[12] A. Couairon and A. Mysyrowicz, Physics Reports **441**, 47 (2007).

[13] T. Brabec and F. Krausz, Physical Review Letters **78**, 3282 (1997).

[14] A. E. Siegman, *Lasers* (University Science Books, Mill Valley, CA, USA, 1986).

[15] A. E. Siegman, Proceedings of SPIE **1868**, 2 (1993).

[16] A. Braun, G. Korn, X. Liu, D. Du, J. Squier, and G. Mourou, Optics Letters **20**, 73 (1995).

[17] R. W. Boyd, *Nonlinear Optics*, 3^{rd} ed. (Academic Press, Burlington, MA, USA, 2008).

[18] E. U. Condon and G. H. Shortley, *The Theory of Atomic Spectra* (Cambridge University Press, Cambridge, UK, 1951).

[19] J. Kerr, Philosophical Magazine Series 5 **3**, 321 (1877).

[20] J.-F. Ripoche, G. Grillon, B. Prade, M. Franco, E. Nibbering, R. Lange, and A. Mysyrowicz, Optics Communications **135**, 310 (1997).

[21] E. Nibbering, G. Grillon, M. Franco, B. Prade, and A. Mysyrowicz, Journal of the Optical Society of America B **14**, 650 (1997).

[22] J. K. Wahlstrand, Y.-H. Cheng, and H. M. Milchberg, Physical Review A **85**, 043820 (2012).

[23] R. Chiao, E. Garmire, and C. Townes, Physical Review Letters **13**, 479 (1964).

[24] J. H. Marburger, Progress in Quantum Electronics **4**, 35 (1975).

[25] W. Liu and S. L. Chin, Optics Express **13**, 5750 (2005).

[26] J. E. Rothenberg, Optics Letters **17**, 1340 (1992).

[27] N. Aközbek, M. Scalora, C. M. Bowden, and S. L. Chin, Optics Communications **191**, 353 (2001).

[28] M. Hercher, Journal of the Optical Society of America **54**, 563 (1964).

[29] Y. R. Shen and Y. J. Shaham, Physical Review Letters **15**, 1008 (1965).

[30] E. Garmire, R. Y. Chiao, and C. H. Townes, Physical Review Letters **16**, 347 (1966).

[31] L. Bergé, S. Skupin, R. Nuter, J. Kasparian, and J.-P. Wolf, Reports on Progress in Physics **70**, 1633 (2007).

[32] J. Kasparian and J.-P. Wolf, Optics Express **16**, 466 (2008).

[33] S. L. Chin, T.-J. Wang, C. Marceau, J. Wu, J. S. Liu, O. Kosareva, N. Panov, Y. P. Chen, J.-F. Daigle, S. Yuan, A. Azarm, W. W. Liu, T. Seideman, H. P. Zeng, M. Richardson, R. Li, and Z. Z. Xu, Laser Physics **22**, 1 (2012).

[34] H. M. Milchberg, Y.-H. Chen, Y.-H. Cheng, N. Jhajj, J. P. Palastro, E. W. Rosenthal, S. Varma, J. K. Wahlstrand, and S. Zahedpour, Physics of Plasmas **21**, 100901 (2014).

[35] J. E. Rothenberg, Optics Letters **17**, 583 (1992).

[36] J. K. Ranka, R. W. Schirmer, and A. L. Gaeta, Physical Review Letters **77**, 3783 (1996).

[37] G. G. Luther, J. V. Moloney, A. C. Newell, and E. M. Wright, Optics Letters **19**, 862 (1994).

[38] A. Couairon, E. Gaižauskas, D. Faccio, A. Dubietis, and P. Di Trapani, Physical Review E **73**, 016608 (2006).

[39] E. W. Rosenthal, J. P. Palastro, N. Jhajj, S. Zahedpour, J. K. Wahlstrand, and H. M. Milchberg, Journal of Physics B **48**, 094011 (2015).

[40] M. D. Feit and J. A. Fleck, Applied Physics Letters **24**, 169 (1974).

[41] D. V. Kartashov, A. V. Kirsanov, A. M. Kiselev, A. N. Stepanov, N. N. Bochkarev, Y. N. Ponomarev, and B. A. Tikhomirov, Optics Express **14**, 7552 (2006).

[42] Y.-H. Cheng, J. K. Wahlstrand, N. Jhajj, and H. M. Milchberg, Optics Express **21**, 4740 (2013).

[43] N. Aközbek, C. M. Bowden, A. Talebpour, and S. L. Chin, Physical Review E **61**, 4540 (2000).

[44] A. Couairon, Physical Review A **68**, 015801 (2003).

[45] W. Ettoumi, P. Béjot, Y. Petit, V. Loriot, E. Hertz, O. Faucher, B. Lavorel, J. Kasparian, and J.-P. Wolf, Physical Review A **82**, 033826 (2010).

[46] O. Kosareva, J.-F. Daigle, N. Panov, T. Wang, S. Hosseini, S. Yuan, G. Roy, V. Makarov, and S. L. Chin, Optics Letters **36**, 1035 (2011).

[47] J. K. Wahlstrand, Y.-H. Cheng, and H. M. Milchberg, Physical Review Letters **107**, 103901 (2011).

[48] D. L. Weerawarne, X. Gao, A. L. Gaeta, and B. Shim, Physical Review Letters **114**, 093901 (2015).

[49] P. P. Kiran, S. Bagchi, C. L. Arnold, S. R. Krishnan, G. R. Kumar, and A. Couairon, Optics Express **18**, 21504 (2010).

[50] K. Lim, M. Durand, M. Baudelet, and M. Richardson, Scientific Reports **4**, 7217 (2014).

[51] Y.-H. Chen, S. Varma, A. York, and H. M. Milchberg, Optics Express **15**, 11341 (2007).

[52] J. M. Hollas, *Modern Spectroscopy*, 4th ed. (John Wiley and Sons, Hoboken, NJ, USA, 2004).

[53] A. Azarm, S. Ramakrishna, A. Talebpour, S. Hosseini, Y. Teranishi, H. L. Xu, Y. Kamali, J. Bernhardt, S. H. Lin, T. Seideman, and S. L. Chin, Journal of Physics B **43**, 235602 (2010).

[54] L. V. Keldysh, Soviet Physics JETP **20**, 1307 (1965).

[55] A. M. Perelomov, V. S. Popov, and M. V. Terent'ev, Soviet Physics JETP **23**, 924 (1966).

[56] J. Kasparian, R. Sauerbrey, and S. L. Chin, Applied Physics B **71**, 877 (2000).

[57] P. Drude, Annalen der Physik **306**, 566 (1900).

[58] Y. P. Raizer, Soviet Physics Uspekhi **8**, 650 (1966).

[59] K. Akhtar, J. E. Scharer, S. M. Tysk, and E. Kho, Review of Scientific Instruments **74**, 996 (2003).

[60] C. D'Amico, A. Houard, M. Franco, B. Prade, A. Mysyrowicz, A. Couairon, and V. T. Tikhonchuk, Physical Review Letters **98**, 235002 (2007).

[61] H. A. Kramers, Philosophical Magazine Series 6 **46**, 836 (1923).

[62] R. Peverall, S. Rosén, J. R. Peterson, M. Larsson, A. Al-Khalili, L. Vikor, J. Semaniak, R. Bobbenkamp, A. Le Padellec, A. N. Maurellis, and W. J. van der Zande, The Journal of Chemical Physics **114**, 6679 (2001).

[63] M. Durand, A. Jarnac, Y. Liu, B. Prade, A. Houard, V. Tikhonchuk, and A. Mysyrowicz, Physical Review E **86**, 036405 (2012).

[64] X. M. Zhao, J.-C. Diels, C. Y. Wang, and J. M. Elizondo, IEEE Journal of Quantum Electronics **31**, 599 (1995).

[65] A. Javan and P. L. Kelley, IEEE Journal of Quantum Electronics **2**, 470 (1966).

[66] A. Becker, N. Aközbek, K. Vijayalakshmi, E. Oral, C. M. Bowden, and S. L. Chin, Applied Physics B **73**, 287 (2001).

[67] A. Brodeur, C. Y. Chien, F. A. Ilkov, S. L. Chin, O. G. Kosareva, and V. P. Kandidov, Optics Letters **22**, 304 (1997).

[68] F. Courvoisier, V. Boutou, J. Kasparian, E. Salmon, G. Méjean, J. Yu, and J.-P. Wolf, Applied Physics Letters **83**, 213 (2003).

[69] A. Dubietis, E. Gaižauskas, G. Tamošauskas, and P. Di Trapani, Physical Review Letters **92**, 253903 (2004).

[70] M. Kolesik and J. V. Moloney, Optics Letters **29**, 590 (2004).

[71] W. Liu, F. Théberge, E. Arévalo, J.-F. Gravel, A. Becker, and S. L. Chin, Optics Letters **30**, 2602 (2005).

[72] M. Scheller, M. S. Mills, M.-A. Miri, W. Cheng, J. Moloney, M. Kolesik, P. Polynkin, and D. N. Christodoulides, Nature Photonics **8**, 297 (2014).

[73] M. Mlejnek, E. M. Wright, and J. V. Moloney, Optics Letters **23**, 382 (1998).

[74] M. Mlejnek, E. M. Wright, and J. V. Moloney, Optics Express **4**, 223 (1999).

[75] G. Méchain, C. D'Amico, Y.-B. André, S. Tzortzakis, M. Franco, B. Prade, A. Mysyrowicz, A. Couairon, E. Salmon, and R. Sauerbrey, Optics Communications **247**, 171 (2005).

[76] M. Durand, A. Houard, B. Prade, A. Mysyrowicz, A. Durécu, B. Moreau, D. Fleury, O. Vasseur, H. Borchert, K. Diener, R. Schmitt, F. Théberge, M. Chateauneuf, J.-F. Daigle, and J. Dubois, Optics Express **21**, 26836 (2013).

[77] M. A. Porras, A. Parola, D. Faccio, A. Dubietis, and P. Di Trapani, Physical Review Letters **93**, 153902 (2004).

[78] M. A. Porras and P. Di Trapani, Physical Review E **69**, 066606 (2004).

[79] J. Kasparian, R. Sauerbrey, D. Mondelain, S. Niedermeier, J. Yu, J.-P. Wolf, Y.-B. André, M. Franco, B. Prade, S. Tzortzakis, A. Mysyrowicz, M. Rodriguez, H. Wille, and L. Wöste, Optics Letters **25**, 1397 (2000).

[80] F. Théberge, M. Châteauneuf, V. Ross, P. Mathieu, and J. Dubois, Optics Letters **33**, 2515 (2008).

[81] C. Hauri, W. Kornelis, F. Helbing, A. Heinrich, A. Couairon, A. Mysyrowicz, J. Biegert, and U. Keller, Applied Physics B **79**, 673 (2004).

[82] A. Mysyrowicz, A. Couairon, and U. Keller, New Journal of Physics **10**, 025023 (2008).

[83] M. B. Gaarde and A. Couairon, Physical Review Letters **103**, 043901 (2009).

[84] X. Sun, S. Xu, J. Zhao, W. Liu, Y. Cheng, Z. Xu, S. L. Chin, and G. Mu, Optics Express **20**, 4790 (2012).

[85] W. Liu, Q. Luo, F. Théberge, H. L. Xu, S. A. Hosseini, S. M. Sarifi, and S. L. Chin, Applied Physics B **82**, 373 (2006).

[86] A. Talebpour, M. Abdel-Fattah, A. D. Bandrauk, and S. L. Chin, Laser Physics **11**, 68 (2001).

[87] S. Tzortzakis, B. Prade, M. Franco, and A. Mysyrowicz, Optics Communications **181**, 123 (2000).

[88] H. D. Ladouceur, A. P. Baronavski, D. Lohrmann, P. W. Grounds, and P. G. Girardi, Optics Communications **189**, 107 (2001).

[89] Y.-H. Chen, S. Varma, T. M. Antonsen, and H. M. Milchberg, Physical Review Letters **105**, 215005 (2010).

[90] S. Bodrov, V. Bukin, M. Tsarev, A. Murzanev, S. Garnov, N. Aleksandrov, and A. Stepanov, Optics Express **19**, 6829 (2011).

[91] J. K. Wahlstrand, N. Jhajj, E. W. Rosenthal, S. Zahedpour, and H. M. Milchberg, Optics Letters **39**, 1290 (2014).

[92] N. Jhajj, E. W. Rosenthal, R. Birnbaum, J. K. Wahlstrand, and H. M. Milchberg, Physical Review X **4**, 011027 (2014).

[93] S. Tzortzakis, B. Prade, M. Franco, A. Mysyrowicz, S. Hüller, and P. Mora, Physical Review E **64**, 057401 (2001).

[94] D. Faccio, M. A. Porras, A. Dubietis, F. Bragheri, A. Couairon, and P. Di Trapani, Physical Review Letters **96**, 193901 (2006).

[95] T. Takahashi, Y. Shibata, K. Ishi, M. Ikezawa, M. Oyamada, and Y. Kondo, Physical Review E **62**, 8606 (2000).

[96] C. D'Amico, A. Houard, S. Akturk, Y. Liu, J. Le Bloas, M. Franco, B. Prade, A. Couairon, V. T. Tikhonchuk, and A. Mysyrowicz, New Journal of Physics **10**, 013015 (2008).

[97] Q. Luo, W. Liu, and S. L. Chin, Applied Physics B **76**, 337 (2003).

[98] J. Yao, B. Zeng, H. Xu, G. Li, W. Chu, J. Ni, H. Zhang, S. L. Chin, Y. Cheng, and Z. Xu, Physical Review A **84**, 051802 (2011).

[99] J. Yao, G. Li, C. Jing, B. Zeng, W. Chu, J. Ni, H. Zhang, H. Xie, C. Zhang, H. Li, H. Xu, S. L. Chin, Y. Cheng, and Z. Xu, New Journal of Physics **15**, 023046 (2013).

[100] G. Point, Y. Liu, Y. Brelet, S. Mitryukovskiy, P. Ding, A. Houard, and A. Mysyrowicz, Optics Letters **39**, 1725 (2014).

[101] S. Mitryukovskiy, Y. Liu, P. Ding, A. Houard, and A. Mysyrowicz, Optics Express **22**, 12750 (2014).

[102] Y. Liu, Y. Brelet, G. Point, A. Houard, and A. Mysyrowicz, Optics Express **21**, 22791 (2013).

[103] S. Mitryukovskiy, Y. Liu, P. Ding, A. Houard, A. Couairon, and A. Mysyrowicz, Physical Review Letters **114**, 063003 (2015).

[104] V. I. Bespalov and V. I. Talanov, JETP Letters **3**, 307 (1966).

[105] A. Couairon and L. Bergé, Physics of Plasmas **7**, 193 (2000).

[106] M. Mlejnek, M. Kolesik, J. V. Moloney, and E. M. Wright, Physical Review Letters **83**, 2938 (1999).

[107] G. Fibich and B. Ilan, Optics Letters **26**, 840 (2001).

[108] G. Fibich and B. Ilan, Physica D **157**, 112 (2001).

[109] G. Fibich, S. Eisenmann, B. Ilan, Y. Erlich, M. Fraenkel, Z. Henis, A. Gaeta, and A. Zigler, Optics Express **13**, 5897 (2005).

[110] G. Méchain, A. Couairon, M. Franco, B. Prade, and A. Mysyrowicz, Physical Review Letters **93**, 035003 (2004).

[111] S. A. Hosseini, Q. Luo, B. Ferland, W. Liu, S. L. Chin, O. G. Kosareva, N. A. Panov, N. Aközbek, and V. P. Kandidov, Physical Review A **70**, 033802 (2004).

[112] M. Centurion, Y. Pu, M. Tsang, and D. Psaltis, Physical Review A **71**, 063811 (2005).

[113] T.-T. Xi, X. Lu, and J. Zhang, Physical Review Letters **96**, 025003 (2006).

[114] A. Couairon, E. Brambilla, T. Corti, D. Majus, O. de J. Ramírez-Góngora, and M. Kolesik, The European Physical Journal Special Topics **199**, 5 (2011).

Part II

Study of energy deposition in air from filamentation

Chapter 2

Mechanisms for energy deposition by filamentation in air - experimental diagnostics

Contents

Introduction

In the previous chapter introducing the filamentation propagation regime, energy deposition in the medium by the laser pulse was briefly presented. In this chapter, we will see that laser energy is mostly transferred to rotational excitation of air molecules and to free electrons potential and kinetic energy in the laser-induced plasma, and that this deposed energy is eventually almost entirely converted into translational energy of neutral molecules, that is heat. This gives rise to spectacular hydrodynamics effects that we will address in this part of the Thesis.

As such, filamentation affects all air thermodynamic parameters, namely pressure, temperature and density, over timescales that can reach well over 1 ms. The complete study of the phenomenon therefore asks for many different diagnostics. To investigate energy deposition, I first built a space and time-resolved interferometry, enabling me to precisely measure the evolution of air density profiles with time. This study was complemented by the recording of acoustic signals emitted from the filamentation area using a precision sensitive microphone. Actual laser energy losses were recorded using a Joule meter. Finally, filamentation plasma was also characterized by means of luminescence study.

2.1 Mechanisms for energy deposition from filamentation in air

2.1.1 Laser energy losses during propagation

As briefly seen in the Chapter 1, laser energy is redistributed during its propagation in air. We will now detail the different mechanisms involved in this redistribution and their relative importance.

2.1.1.1 Scattering losses

The first channel for laser energy losses is scattering. During propagation, laser photons are elastically scattered on air molecules, that is Rayleigh scattering. When propagating in an ionized medium, the laser pulse can also scatter inelastically on free electrons, leading to Thomson scattering.

Rayleigh scattering Rayleigh scattering induces energy losses in the initial beam because most involved photons are scattered in different directions as that of the laser pulse propagation direction. This process involves the non-resonant absorption of a pump photon, bringing the involved atom/molecule in a virtual energy state, and the simultaneous emission of another photon at the same frequency. Rayleigh scattering cross-section is given by [1]:

$$\sigma_{Rayleigh}(\vec{r},t) = \frac{2k_0^4}{3\pi n_n(\vec{r},t)^2}|n(\vec{r},t) - 1|^2, \tag{2.1}$$

n_n being the number density of neutral species. Intensity attenuation is governed by the relation:

$$\partial_z I(\vec{r},t) = -\sigma_{Rayleigh}(\vec{r},t) n_n(\vec{r},t) I(\vec{r},t). \tag{2.2}$$

We can therefore define an attenuation coefficient $\alpha_{Rayleigh}$ as:

$$\alpha_{Rayleigh}(\vec{r},t) = n_n(\vec{r},t)\sigma_{Rayleigh}(\vec{r},t) = \frac{2k_0^4}{3\pi n_n(\vec{r},t)}|n(\vec{r},t) - 1|^2. \tag{2.3}$$

At 800 nm in air at standard pressure and temperature conditions, we find:

$$\alpha_{Rayleigh} = 2.38 \times 10^{-6}\ \mathrm{m}^{-1}. \tag{2.4}$$

To get a clearer picture of the phenomenon, a laser beam propagating in air over 1 m will lose a fraction of its energy of $\sim 10^{-6}$.

Thomson scattering Thomson scattering results in laser energy losses because of two effects: first, photons are scattered isotropically, with a marginal portion of them being re-emitted in the initial propagation direction of the laser pulse. Second, it is an inelastic scattering process, leading to a shift in frequency for the pump photons. In the Fourier frequency domain, Thomson scattering is characterized by a continuous, low amplitude broadening at the bottom of the Rayleigh line, symmetric with respect to the pump wavelength. The Thomson scattering cross section is given by [2]:

$$\sigma_{Thomson} = \frac{8\pi}{3}\left(\frac{e^2}{4\pi\epsilon_0 m_e c^2}\right)^2. \tag{2.5}$$

The criterion for incoherent Thomson scattering, that is the limit case for which photons can be scattered several times, reads $\lambda \gg \lambda_D$, where λ_D is the Debye electronic characteristic shielding

length. In the chapter 1, we evaluated $\lambda_D \sim 100$ nm in the case of the plasma filament. At 800 nm, the condition is then fulfilled and the scattered intensity simply corresponds to the sum of intensities scattered by each free electron. Similar to Rayleigh scattering, we can therefore define a characteristic attenuation factor:

$$\alpha_{Thomson}(\vec{r},t) = n_e(\vec{r},t)\sigma_{Thomson}(\vec{r},t) \sim 10^{-6}\ \mathrm{m}^{-1}. \tag{2.6}$$

Depending on the electron density, Thomson scattering can be either a few times stronger or weaker than Rayleigh scattering, yielding approximately the same order of magnitude for attenuation.

2.1.1.2 Raman rotational absorption

Rotational Raman scattering was introduced in Chapter 1 as an important contributor to the nonlinear index (section 1.3.2.1). We will try to quantify energy absorption due to this channel during propagation. First, we introduce an effective rotational dielectric susceptibility from equation (1.81):

$$\chi_{rot} = \frac{n_n \Delta\alpha}{4\pi\epsilon_0}\left(\langle\cos(\theta)^2\rangle - \frac{1}{3}\right) \tag{2.7}$$

The electromagnetic energy density absorbed by this effective dielectric is given by:

$$u_{em}(\vec{r},t) = \epsilon_0 \int_{-\infty}^{t} \frac{\partial\chi_{rot}}{\partial t}(\vec{r},t')E(\vec{r},t-t')^2\ \mathrm{d}t', \tag{2.8}$$

meaning that lineic energy absorption due to Raman rotational scattering is given by:

$$\frac{\partial U}{\partial z}(\vec{r},t) = \epsilon_0 \int_{\mathbb{R}^2}\int_{-\infty}^{t} \frac{\partial\chi_{rot}}{\partial t}(\vec{r},t')E(\vec{r},t-t')^2\ \mathrm{d}t'\mathrm{d}S \tag{2.9}$$

From this last equation, we can deduce the order of magnitude for the Raman attenuation factor:

$$\alpha_{Raman} \sim \frac{2\chi_{rot}}{cn\tau}, \tag{2.10}$$

τ being the laser pulse characteristic duration. Evaluation of the effective permittivity χ_{rot} can be made using values for $\langle\cos(\theta)^2\rangle - 1/3$ measured in filamentation experiments. Maximum values of ~ 0.05 were reported in the case of a ~ 100 µJ, 100 fs laser pulse at 800 nm [3]. Using the value $\Delta\alpha/4\pi\epsilon_0 = 6.7 \times 10^{-31}$ m^3 for N_2 [4], this gives:

$$\alpha_{Raman} \sim 0.06\ \mathrm{m}^{-1}. \tag{2.11}$$

Rotational Raman absorption appears as an efficient channel for laser energy deposition in air.

2.1.1.3 Ionization losses

Another channel for laser energy losses results from the ionization of the propagation medium. Bringing a bound electron into the continuum requires the absorption of at least the ionization potential for the considered species. In this case, freed electrons have an initial null kinetic energy. The laser field can also ionize the medium by bringing an energy above the ionization threshold, resulting in newborn electrons with some kinetic energy, so-called above threshold ionization. Finally, free plasma electrons can acquire kinetic energy from the laser field through inverse Bremsstrahlung.

Photoionization Photoionization was detailed in Chapter 1 (section 1.3.2.2). As a brief reminder, the intensity range encountered in filaments in air lies in a transitory regime between multiphoton absorption and tunnel ionization in the formalism established by Keldysh [5]. Still, the ionization rate W can be well approximated by a corrected multiphoton-like law:

$$W = \sigma_{K'} I^{K'}, \tag{2.12}$$

where K' is an effective number of photons that must be absorbed to bring a bound electron into the continuum. The dissipated power density due to photoionization was evaluated in equation (1.121), reading:

$$P_v = K' \hbar \omega_0 \sigma_{K'} I^{K'} (n_n(t=0) - n_e) = \partial_z I. \tag{2.13}$$

Therefore we can evaluate an attenuation coefficient for photoionization as:

$$\alpha_{pi} = K' \hbar \omega_0 \sigma_{K'} I^{K'-1} (n_n(t=0) - n_e). \tag{2.14}$$

Using the values $K = 8$, $\sigma_8 = 3.7 \times 10^{-128}$ m^{16} $\cdot$ W^{-8} $\cdot$ s^{-1} and $I \sim 10^{17}$ W $\cdot$ m^{-2} corresponding to a pure multiphoton regime in a molecular oxygen plasma [6], we have:

$$\alpha_{pi} \sim 0.1 \text{ m}^{-1}. \tag{2.15}$$

Above-threshold ionization Considering a photoionization process, it is supposed that the freed electron reaches the continuum with a null kinetic energy, therefore only bearing a potential energy, which is equal to the ionization potential of its parent atom. The latter can also absorb more energy than its ionization potential from the laser field, yielding a newborn electron carrying excess energy as kinetic energy, that is *above-threshold ionization* (ATI).

In the classical model developed by Burnett and Corkum in the tunnel ionization regime for a linear polarization, this surplus energy can be seen as originating from a timing mismatch between ionization time and the moment when the electric field reaches its maximum amplitude [7]. Indeed, when an electron is released at this instant (corresponding, for an electric field in $\sin(\omega_0 t) = \sin(\varphi)$, to $\varphi = \pi/2$), it will only follow the electric field transversally to the laser propagation direction, gaining or losing energy depending on the phase of the field, with a resulting null total energy when the pulse has left. If the electron is instead released with a phase mismatch $\Delta\varphi$ with respect to $\pi/2$, it will drift along the laser propagation direction, with a corresponding excess kinetic energy

$$U_{excess} = 2U_p \sin(\Delta\varphi)^2 \tag{2.16}$$

where $U_p = e^2|E_0|^2/4m_e\omega_0^2$ is the ponderomotive energy. Averaging this energy over half a period yields the mean average ATI energy:

$$U_{ATI} = \frac{\int_0^{\pi/2} 2U_p W_s \cos(\varphi)^2 \, \mathrm{d}\varphi}{\int_0^{\pi/2} W_s \, \mathrm{d}\varphi}, \tag{2.17}$$

W_s being the ionization rate in a static electric field in the tunneling limit (that is a Keldysh parameter $\gamma \ll 1$). If we make the approximation for the ionization rate to behave like a corrected multiphoton ionization rate, as we did before, we can write $W = \sigma_{K'} I^{K'}$, with the phase dependence of I being in $\sin(\varphi)^2$. In this case, we can find:

$$U_{ATI} = \frac{U_p}{K'+1}. \tag{2.18}$$

At 800 nm and an intensity level of $\sim 10^{17}$ W $\cdot$ m^{-2}, we have $U_{ATI} \sim 0.5$ eV. This value is in good agreement with simulated electron energy distribution in the case of linearly polarized laser pulses undergoing filamentation [8].

Similarly to photoionization losses, we can define an absorption coefficient for above threshold ionization:

$$\alpha_{ATI} = U_{ATI}\sigma_{K'}I^{K'-1}(n_n(t=0) - n_e) \tag{2.19}$$

which, for the same values as in the previous section, gives:

$$\alpha_{ATI} \sim 10^{-2}\ \mathrm{m}^{-1}. \tag{2.20}$$

Inverse Bremsstrahlung absorption Inverse Bremsstrahlung is a collisional phenomenon by which energy is transferred from an ambient electric field to the free electronic population. A free electron in a harmonic electric field simply follows its oscillations, gaining and losing kinetic energy with each optical cycle with a resulting null average value. If this free electron collide with another particle, either an electron, an ion or a neutral, this will result in its current oscillation energy to be transferred into random translational movement energy.

Energy losses due to classical inverse Bremsstrahlung in the plasma filament were described in Chapter 1 (section 1.3.2.3). They are governed by equation (1.90):

$$\left\langle \frac{\partial P_{abs}}{\partial V}(\vec{r},t) \right\rangle_t = -\frac{1}{T}\int_0^T \frac{\partial I}{\partial z}(\vec{r},t')\ \mathrm{d}t' = \sigma_{iB}(\omega_0)n_e(\vec{r},t)I(\vec{r},t). \tag{2.21}$$

Typically, the time average is considered over the duration of the laser pulse, τ, while the characteristic time step for integration corresponds to the average time between two electronic collisions:

$$\frac{1}{T}\int_0^T \frac{\partial I}{\partial z}(\vec{r},t')\ \mathrm{d}t' \sim \frac{1}{\tau\nu_c}\frac{\partial I}{\partial z}(\vec{r},t). \tag{2.22}$$

The absorption coefficient for inverse Bremsstrahlung is then given by:

$$\alpha_{iB} = \tau\nu_c\sigma_{iB}(\omega_0)n_e. \tag{2.23}$$

In the case of a plasma filament in air generated at 800 nm by a $\sim$ 100 fs laser pulse, we have $n_e \sim 10^{23}$ m^{-3}, which yields:

$$\alpha_{iB} \sim 0.1\ \mathrm{m}^{-1}. \tag{2.24}$$

2.1.1.4 Conclusions at the timescale of the laser pulse

Finally, we can conclude that during the laser pulse propagation, laser energy is preferentially absorbed through ionization processes, namely photoionization by multiphoton and/or tunnel processes, corresponding above-threshold ionization and field energy transfer to free electrons by inverse Bremsstrahlung. Raman rotational absorption was also shown to play an important role in depleting the laser energy, all the more that this process occurs from the very beginning of the pulse propagation and, as such, has a far greater spatial extension than ionization. Finally, scattering losses are completely negligible.

Right after the laser pulse has left, energy is then stored in three main components:

- first, in the form of rotational energy of air molecules,
- second, in the form of potential energy of free electrons, corresponding to the ionization potential of air molecules,
- third, in the form of kinetic energy of free electrons.

2.1.2 Energy transfer processes during the relaxation of the system

The relaxation of the system is characterized by several simultaneous processes. Several of them are related to the evolution of the laser-induced plasma and lead to the formation of excited heavy species. At the same time, these excited heavy species de-excite by collisional processes, leading to the global relaxation of the system.

2.1.2.1 Plasma thermalization

Initially, the laser-induced plasma is not at equilibrium: electrons have a significantly higher mean kinetic energy, that is temperature, than neutral and ionic species which are left almost unaffected by the laser pulse. Since the plasma filament is weakly ionized, its relaxation dynamics are dominated by electron-neutral collisions. Right after the laser pulse has left, we have typically:

$$T_e \gg T_i \approx T_n, \tag{2.25}$$

where T_e, T_i and T_n denote electron temperature, ion temperature and neutral temperature, respectively. Relaxation of the plasma in terms of distribution functions for electrons and heavy species, $f_{e,h}$, can be well approximated by a Krook model:

$$\partial_t(f_e - f_h) = -\nu_c(f_e - f_h), \tag{2.26}$$

where ν_c is the effective electron-heavy species collision frequency [9]. In our case, ν_c is entirely determined by the electron-neutral collision frequency, estimated in Chapter 1 to be $\nu_c \sim 1$ THz (equation (1.93)). This means that after a few ps, all plasma species have a similar Maxwellian distribution function and, as such, the same temperature.

2.1.2.2 Plasma recombination

The relaxation of the system is characterized by several simultaneous processes. One of them is the recombination of the laser-induced plasma, which was studied in Chapter 1 (section 1.3.2.4). This process typically takes on the order of ~ 1 ns and is dominated by three-body recombination and dissociative recombination:

$$\begin{cases} e^- + M_2^+ \longrightarrow M + M^* \\ e^- + M^+ + M \longrightarrow M + M^*, \end{cases} \tag{2.27}$$

where M denotes any neutral species in the plasma. We can see that these recombination channels lead invariably to the formation of excited heavy species, which constitute the final intermediary before full thermalization of the gas.

2.1.2.3 Final thermalization of the neutral gas

The last step for the thermalization of the neutral gas is de-excitation of excited heavy species. Collisional processes enable rotational, vibrational and translational energy distributions to relax to a common Maxwellian distribution function. Dephasing of initial coherent excitation of molecular rotational states also leads to the transfer of stored rotational energy into translational energy, and typically takes ~ 100 ps [3]. Globally, relaxation is therefore almost instantaneous with respect to plasma recombination, meaning that the plasma disappearance marks the transition to a neutral gas at thermodynamical equilibrium. De-excitation of excited heavy species can also be radiative,

as evidenced by the fluorescence of filamentation channels. This channel for energy losses can easily be shown to be negligible. If we suppose that every free electron recombining leads to an excited molecule that will eventually emit a photon, and considering that fluorescence is mainly emitted between 300 and 400 nm, that is a photon energy of ~ 3 eV, we can estimate the lineic energy losses as ~ 40 µJ $\cdot$ m^{-1} for $n_e \sim 10^{22}$ m^{-3}, which is indeed far below the measured deposed energies by at least one order of magnitude.

2.1.3 Conclusion on laser energy deposition

Using simple estimations for the various channels of laser energy deposition in the medium, we showed that energy absorption due to ionization and inverse Bremsstrahlung are undoubtedly the most effective processes in the ionized region of filamentation. Raman rotational absorption, on the other hand, appears slightly less effective than these deposition channels, but it appears at lower intensity than laser-induced plasma. As such, it might well be as effective as ionization to transfer laser energy to air.

After plasma recombination and de-excitation of neutral molecules of air, we conclude that the major part of deposed laser energy is finally converted into translational energy of neutrals, that is heat. We will now study the consequences of this sudden heating of the medium.

2.2 Reaction of the medium to laser energy deposition

2.2.1 Short times: hydrodynamic regime

2.2.1.1 Initial conditions

Given the rapid dynamics of energy transfer and of the relaxation of the system, almost no hydrodynamic reaction is expected to occur during the temperature build-up. This means that once plasma recombination is finished, the system is in a highly unstable state, characterized by a flat density profile, equal to the air density in normal pressure and temperature conditions ($p = 1.013 \times 10^5$ Pa, $T = 300$ K, giving $n_n = 2.47 \times 10^{25}$ m^{-3}). As for the temperature profile, it has typically a bell-like shape, since energy deposition in the ionized zone occurs preferentially through ionization, and that the electron density profile is strongly related to the pulse intensity profile. Its amplitude was reported to go from 100 K above room temperature for ~ 100 µJ laser pulses [10] to more than 1000 K above room temperature for strongly focused 5 mJ pulses [11]. Consequently, the pressure profile is similar to that of temperature, with a peak value ranging between 1.4 and 4.4×10^5 Pa, depending on experimental conditions.

2.2.1.2 Generation of a hydrodynamic wave and relaxation of the system

Starting from the previously presented initial conditions, the medium will react by launching an outward-propagating, cylindrically-symmetrical pressure and density wave, owing to the initial symmetry of the laser pulse and of the resultant deposited energy profile. This wave enables the system to relax the pressure unbalance between the initially pressurized air core and the surrounding cold air at equilibrium. Pressure equilibrium is therefore relaxed over a timescale τ_{relax} such as:

$$\tau_{relax} \sim \frac{r_0}{v_{wave}}, \tag{2.28}$$

where r_0 is the characteristic initial half width at half maximum (HWHM) of the pressure profile and v_{wave} the characteristic velocity of the hydrodynamic wave. Using $r_0 \sim 100$ µm and $v_{wave} \sim$

$c_s = 340\ \mathrm{m} \cdot \mathrm{s}^{-1}$, we find $\tau_{relax} \sim 1\ \mu\mathrm{s}$. After a few τ_{relax}, the system will be back at pressure equilibrium. At this point, as matter was ejected from the central part by the hydrodynamic wave, an underdense channel has formed and mirrors the persistence of a hot temperature profile following the ideal gas law:

$$n_n(\vec{r},t)k_BT(\vec{r},t) = p_{air}. \tag{2.29}$$

2.2.2 Long times: diffusive regime

After the relaxation of the system and the establishment of pressure equilibrium, it will slowly evolve in a diffusive regime. Indeed, the equation for the evolution of the gas internal energy yields:

$$\frac{\partial U}{\partial t} + \vec{\nabla}.(U+p)\vec{v} = -\vec{\nabla}.\vec{q}, \tag{2.30}$$

where $\vec{v}$ represents the fluid velocity field and $\vec{q}$ the heat flux vector. At this stage the fluid bulk velocity is zero because it is at pressure equilibrium. Using the thermal conductivity law:

$$\vec{q} = -\kappa\vec{\nabla}T, \tag{2.31}$$

we can rewrite equation (2.30) as:

$$\frac{\partial T}{\partial t} - \vec{\nabla}.\left(\frac{\kappa}{C_p}\vec{\nabla}T\right) = 0, \tag{2.32}$$

where the heat capacity $C_p = 7Nk_B/2$ in the case of an ideal gas of diatomic molecules with a temperature low enough so that no vibration mode is excited. Supposing the thermal conductivity κ is constant, we find the well-known thermal diffusion equation:

$$\partial_t T = \frac{\kappa}{C_p}\Delta T. \tag{2.33}$$

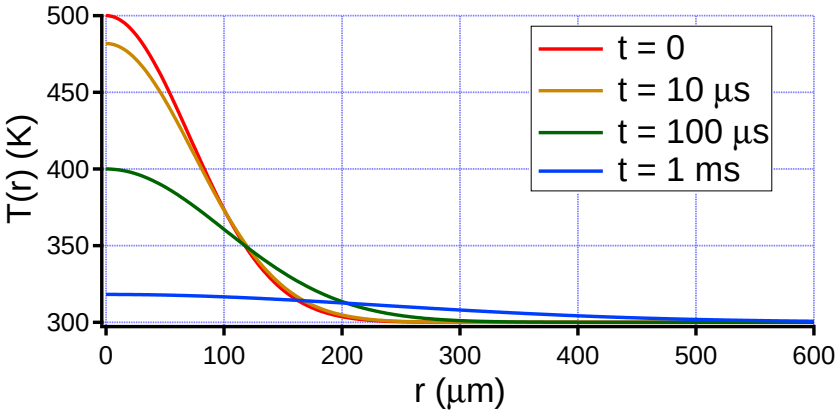

Figure 2.1: Simulated evolution of an initially Gaussian air temperature profile with time in the diffusion regime following equation (2.35). The parameters for the initial profile are $r_0 = 100\ \mu\mathrm{m}$ and $T_0 = 500\ \mathrm{K}$.

It can be shown that in 2-dimensional Cartesian coordinates, the general solution for this equation is:

$$T(x,y,t) = \int_{\mathbb{R}^2} \frac{C_p}{4\pi\kappa t} \mathrm{e}^{C_p\left((x-x')^2+(y-y')^2\right)/4\kappa t} f(x',y')\ \mathrm{d}x'\mathrm{d}y', \tag{2.34}$$

where f is the initial temperature profile. In the particular case where this initial profile is given by a Gaussian of which amplitude is T_0 and 1/e radius is r_0, we have:

$$T(r,z,t) = T_{air} + \frac{(T_0 - T_{air})r_0^2}{r_0^2 + 4\kappa t/C_p} \mathrm{e}^{-r^2/\left(r_0^2+4\kappa t/C_p\right)}. \tag{2.35}$$

The temperature profile, and consequently the density profile, therefore evolve in width as $\sim \sqrt{\kappa t/C_p}$ and in amplitude as $\sim C_p/\kappa t$ (figure 2.1). We can define a characteristic time τ_{diff} for which the amplitude of the temperature/density perturbation is one tenth of its initial value:

$$\tau_{diff}\ [\mathrm{s}] \sim \frac{9C_p r_0^2}{4\kappa} \sim 10^5 r_0^2\ [\mathrm{m}^2] \tag{2.36}$$

for air at moderate temperature (≤ 500 K) so that $C_p \approx constant$.

2.2.3 Conclusions

We saw that the energy deposed in air by an ultrashort laser pulse undergoing filamentation leads to a strongly unbalanced initial condition characterized by the quick build-up of temperature and pressure with respect to air response time, meaning that air density level remains at its equilibrium value. As a consequence, an outward-propagating pressure and density hydrodynamic wave will form, enabling the system to get back to pressure equilibrium by a few microseconds. Beyond this point, the evolution of the remaining central underdense channel and associated temperature profile is dictated by thermal and particle diffusion, which can take more than 1 ms to resorb, depending on initial conditions.

2.3 Diagnostics for the study of energy deposition from filamentation

2.3.1 Direct measurement of energy deposition: Joule meter

The most obvious way to measure laser energy deposition in air due to filamentation is to use a Joule meter. Recording the laser input energy, usually right after the focusing lens used to promote filamentation, and the laser output energy some distance after the end of filamentation, it is possible to have a direct estimation of the energy effectively transferred from the laser pulse to air (cf. figure 2.2). In the case of lenses with long focal lengths, as filaments tend to propagate further beyond the focal point, it is necessary to place the detector further as well to avoid damaging it. In this case, it might be necessary to use another lens to somehow collimate the diverging beam so that the full energy could be indeed measured.

Our Joule meter is a 50×50 mm^2 detector, model QE50LP-H-MP from Gentec-EO equipped with a calibrated attenuator. It enables us to measure down to a single laser shot energy with a ~ 10 µJ precision.

2.3.2 Density diagnostic: transverse interferometry

During my time as a Ph. D. student, I developed an interferometric plasma diagnostic for the measurement of electron density in laser-guided discharges. This diagnostic proved to be readily usable for measuring neutral air density as well, which brings crucial information on the hydrodynamic response of the system following filamentation. This section is only a succinct introduction

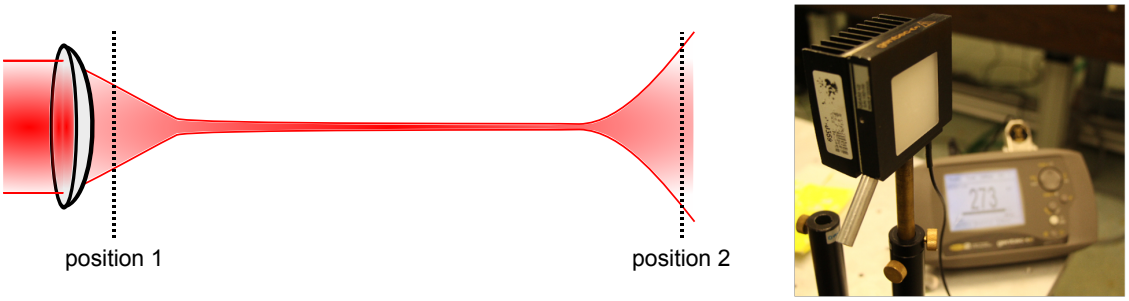

Figure 2.2: Left: schematic description of the experimental setup used to measure absorbed energy. The Joule meter is placed right after the focusing lens, and far beyond the end of the filament. Right: photograph of the Joule meter used in the experiments.

to this kind of diagnostic. For a full description, the reader is kindly advised to read the Chapter 6, dedicated to the description of the two-color interferometric plasma diagnostic in this Thesis.

2.3.2.1 Principle

An interferometer works as a refractive index shift recorder, meaning that this diagnostic is able to measure the refractive index difference between two media with a high precision. In our case, we want to use this technique for the measurement of air density. From the study of the linear dielectric response of transparent media presented in Chapter 1, we were able to link the linear susceptibility $\chi_e^{(1)}$ to the number density n_n of the medium (equation (1.42)). It reads:

$$\chi_e^{(1)}(\vec{r},\omega) = n_n(\vec{r}) f(\omega), \tag{2.37}$$

meaning that air refractive index yields:

$$n(\vec{r},\omega) \approx 1 + \frac{n_n(\vec{r})}{2} f(\omega). \tag{2.38}$$

In the visible range, the function f is weakly dependent on ω and the last equation can be rewritten as:

$$n(\vec{r}) = 1 + \frac{\beta}{n_0} n_n(\vec{r}), \tag{2.39}$$

which is called the Gladstone-Dale law. Here, β is the Gladstone-Dale constant, which defines the value of the refractive index at a reference density n_0. With standard pressure and temperature conditions, we have $n_0 = 2.47 \times 10^{25}$ m^{-3}. Using the empirical Ciddor equation [12], which links the air refractive index to pressure, temperature and humidity level, to have a precise estimation of air refractive index in the visible/near infrared range, we find:

$$\beta = 2.7 \times 10^{-4}. \tag{2.40}$$

This modeling for air refractive index was shown to be valid up to at least 5000 K [13]. Indeed, molecular oxygen starts to dissociate below this threshold but as the polarizability of an oxygen atom is almost one half that of an oxygen molecule, it does not change significantly the air refractive index. This is not true in the case of molecular nitrogen, which starts to dissociate as well above 5000 K.

Interference between a reference beam propagating through unperturbed air and air at a different density gives access to the phase shift $\Delta\varphi$ between the two beams:

$$\Delta\varphi = \frac{2\pi\beta}{n_0\lambda}\int_{s_1}^{s_2}(n_n(s) - n_0)\ \mathrm{d}s, \tag{2.41}$$

where s define the curvilinear coordinate along the probe beam. Therefore, one can theoretically deduce the air density profile from the measurement of $\Delta\varphi$.

2.3.2.2 Experimental setup

The interferometer is built in a standard Mach-Zehnder configuration (figure 2.3). The probe laser (Quanta Ray GCR-290-10 from Spectra Physics) is a Nd:YAG Q-switched laser delivering ~ 100 µJ, 8 ns FWHM pulses at 1064 nm. The probe beam is spatially cleaned and magnified by means of a 100 µm pinhole placed in an afocal telescope, resulting in a quasi-Gaussian spatial profile with a 8.3 mm FWHM. The whole interferometer is built on a 60×60 cm^2 breadboard mounted on mechanic isolation feet to reduce vibrations, and entirely enclosed to limit the influence of air turbulence on measurements.

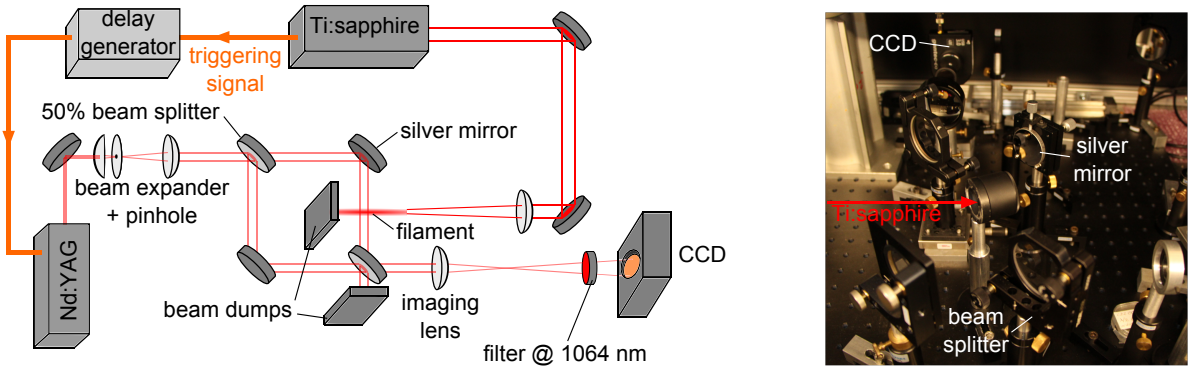

Figure 2.3: Left: schematic depiction of the experimental setup for interferometry on underdense channels generated by filamentation. Right: photograph of the actual setup.

The studied underdense channels are generated using a Ti:sapphire laser chain generating pulses powerful enough to undergo filamentation when focused. The resulting filaments are created in one of the arms of the interferometer perpendicularly to the probe beam. A beam dump stops the filament before it reaches the reference arm, which would affect refractive index measurements. The probe laser is synchronized with the Ti:sapphire laser using the latter's internal clock, which grants us the possibility to set the pump/probe delay with a 1 ns precision and a 1.5 ns jitter. Interferograms are recorded by a CCD camera (model TaperCamD-UCD12 from DataRay, Inc.) with a 10.5 µm pixel size and a 1024×1360 pixel array, giving a field of view of more than 1 cm in each direction. The CCD matrix is placed in the conjugated plane of the filament using a 75 mm imaging lens and a $2f/2f$ layout.

2.3.2.3 Data processing

Phase is first evaluated from interferograms (example in figure 2.4) using a one dimensional continuous wavelet transform algorithm [14] coupled to a cost function ridge extraction routine [15]. Phase planes are then unwrapped by a local, quality-guided phase unwrapping algorithm [16].

Phase shift is obtained after removal of the background carrier phase from blank interferograms (figure 2.4-(b)).

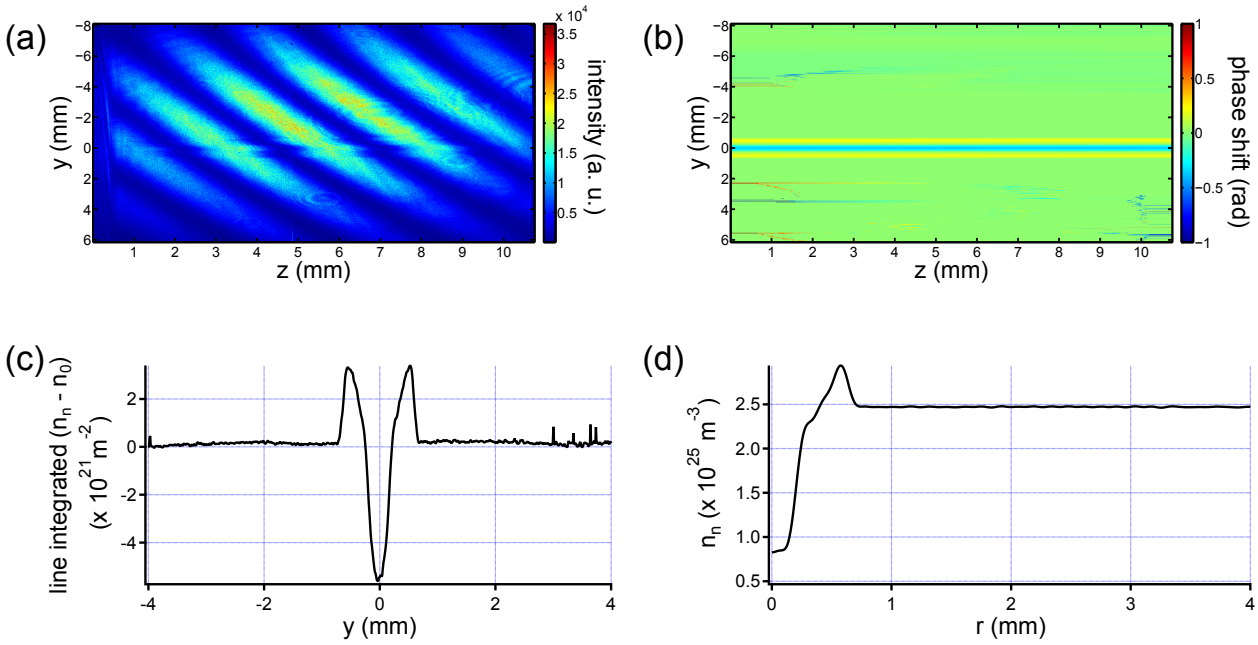

Figure 2.4: Data processing for interferometry. (a): example of recorded interferogram 1 µs after the filamentation of a 5 mJ, 50 fs laser pulse focused at $f/30$. (b): corresponding extracted phase shift map. (c): line-integrated density profile obtained from the phase shift map. (d): density profile computed after Abel inversion of the previous integrated profile.

A phase offset might remain after this step, so average phase shift outside the filamentation-affected area is evaluated and subtracted from the whole phase shift map. Phase noise can also be estimated from the same unaffected zone. A minimum root mean square (RMS) phase noise of 2 mrad was achieved, which is sensitive enough to monitor the evolution of filamentation-generated underdense channels in most experimental conditions, as we will see. As the interaction length between the probe and the phase object is very short ($\sim$ 100 µm), we can also completely neglect any probe deflection effect [17].

Phase shift maps give direct access to line-integrated air density following equation (2.41). The last step is to recover the true density spatial profile. In the case of a transverse probing geometry and if this profile presents an azimuthal symmetry, which is precisely our case, it can be shown that an integral transform, called *inverse Abel transform*, allows retrieving a radial function from the value of its lineic integral. To perform this operation, we use a Fourier-Hankel algorithm [18], to finally obtain air density profiles (figure 2.4-(d)). Using this rigorous method results in unambiguous density profiles, unlike *longitudinal* interferometry, which relies on the axial density distribution to retrieve full three-dimensional density profiles.

2.3.3 Pressure detectors: microphones

2.3.3.1 Principle of the diagnostic

Due to hydrodynamic initial conditions detailed in section 2.2.1.1, initial peak pressure is proportional to initial peak temperature. It is consequently approximately proportional to the longitudinal

derivative of energy deposition. Indeed, since almost all the deposed energy is converted into heat at a timescale far shorter than air characteristic reaction time, air heating can be considered as an isochoric process. In this case, the first law of thermodynamics reads:

$$\begin{aligned}\Delta U &= c_v \int_{\mathbb{R}^3} n_n(\vec{r})\,(T(\vec{r}) - T_{air})\ \mathrm{d}^3\vec{r} = c_v \int_{\mathbb{R}^3} n_0\,(T(\vec{r}) - T_{air})\ \mathrm{d}^3\vec{r} \\ &= \frac{c_v}{k_B} \int_{\mathbb{R}^3} (p(\vec{r}) - p_{air})\ \mathrm{d}^3\vec{r} \\ &\approx \frac{\pi c_v}{k_B} \int_{\mathbb{R}} (p_{max}(z) - p_{air})\, r_0(z)^2\ \mathrm{d}z, \end{aligned} \tag{2.42}$$

where c_v is the air isochoric heat capacity per molecule, and $r_0(z)$ corresponds to the HWHM of the pressure profile. We can here consider r_0 as being constant. Indeed, in the filamentation zone, energy deposition takes place in the intense core, of which diameter does not vary much during propagation. Outside the filamentation zone, this hypothesis is much more arguable because of the intensity profile is broader here than in the filament, meaning that temperature and pressure profiles should be broader as well since energy deposition occurs through Raman rotational absorption, which scales as I^2. Still, comparison between sonographic experiments and simulations for energy deposition yield an excellent agreement [19]. Moreover, as energy deposition is at least one order of magnitude lower in this peripheral zone than in the filament, a slight deviation from the hypothesis $r_0 \approx constant$ would not lead to a significant error. Finally we find:

$$p_{max}(z) - p_{air} \propto \frac{\partial \Delta U}{\partial z}(z). \tag{2.43}$$

Recording the pressure field enables one to have access to energy deposition. This diagnostic has already been used in the past both for the quick estimation of the length of laser-induced plasma columns [20] and for the study of energy deposition in an intensity regime below the ionization threshold [21].

In our case, we make use of microphones, of which bandwidth typically covers the whole audible frequency range, placed at a given distance from filaments. Two questions arise here about the use of this diagnostic:

- first, is the bandwidth of our detectors adapted to our needs?
- second, since we must record the pressure waveform at some distance from the filament, how faithfully can be related the recorded waveform to the original signal at $r = 0$?

The answer to the first question is easy to find. The frequency range covered by the hydrodynamic wave can be roughly estimated at $v_{wave}/r_0 \sim 3$ MHz, meaning that this range is far greater than the bandwidth of our detectors. In this case, the acoustic signal can be well approximated by $s(t) = p_{max}\delta(t)$, meaning that the output signal of the microphone corresponds to its impulse response multiplied by p_{max}, giving direct access to this parameter. About the second question, the propagation of sound between the filament and the microphone is expected to be linear, which means that the pressure encountered at r is proportional to $p(r = 0)$.

In the end, the use of a microphone allows for a convenient and simple diagnostic of local energy deposition by ultrashort laser pulses in air.

2.3.3.2 Sensors used

The acoustic study of the major part of the propagation length of an ultrashort laser pulse is a challenging task because of the need for a high dynamic range, especially when using powerful (TW)

pulses. Indeed, the amplitude of the acoustic wave can vary over several orders of magnitude. To this purpose, we adopted a scheme using two different microphones.

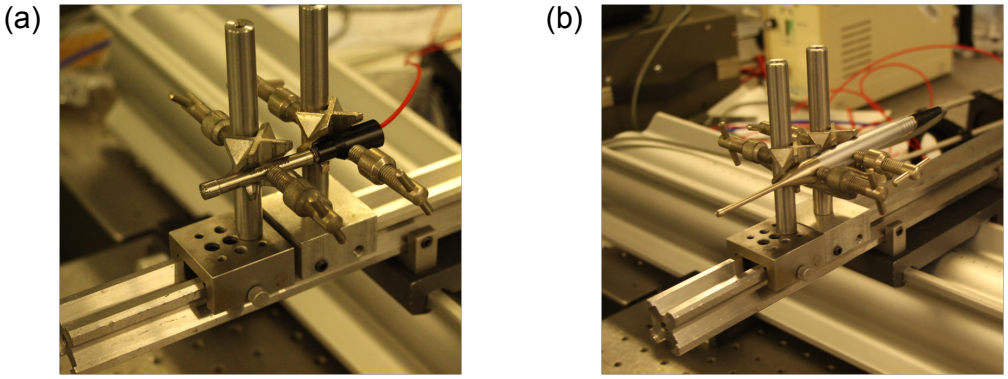

Figure 2.5: Photographs of the microphones used in experiments: G.R.A.S. 40 BE (a) and B&K 4138 (b).

The first one is a $1/4''$ pre-polarized free-field electret microphone (model 40BE from G.R.A.S. Sound & Vibration) with a 4 Hz – 100 kHz bandwidth (-3 dB) and a dynamic range upper limit of 160 dB (reference 20 µPa). The other one is a $1/8''$ pressure field electret microphone (model 4138 from Brüel & Kjaer) with a 6.5 Hz – 140 kHz bandwidth and a dynamic range upper limit of 168 dB. Both detectors offer a spatial resolution < 1 cm (see figure 2.5).

Due to its greater sensibility, we used the G.R.A.S. 40 BE in low-intensity regions where the acoustic signal is of moderate amplitude, typically by placing it at $1-2$ cm from the center of the laser beam. Around the focal zone, energy deposition becomes so important, especially at high input energies, that the microphone is saturated. We consequently shifted to the other microphone, which can withstand higher acoustic amplitudes.

2.3.4 Plasma diagnostic: plasma luminescence

2.3.4.1 Origins of the plasma luminescence

The study of the plasma luminescence has been used as a plasma diagnostic since the early days of filamentation. Due to its relative implementation simplicity, it can be readily used for a full characterization of a filament over its whole length. The corresponding spectrum was briefly studied in Chapter 1 (section 1.3.3.2). It consists mainly of emission lines of molecular nitrogen and molecular nitrogen cation with a negligible continuum component, highlighting the low temperature of the plasma. These emission lines were identified by Talebpour *et al.* at the end of the 1990s as resulting from vibronic transitions of two particular energy systems of N_2 and N_2^+ (figure 2.6) [22]:

- the second positive system of N_2 between the excited triplet states $C^3\Pi_u$ and $B^3\Pi_g$,
- the first negative system of N_2^+ between the excited doublet state $B^2\Sigma_u^+$ and the ionic fundamental state $X^2\Sigma_g^+$.

We will now look in detail how are currently explained the origins of the luminescence from these two systems of nitrogen.

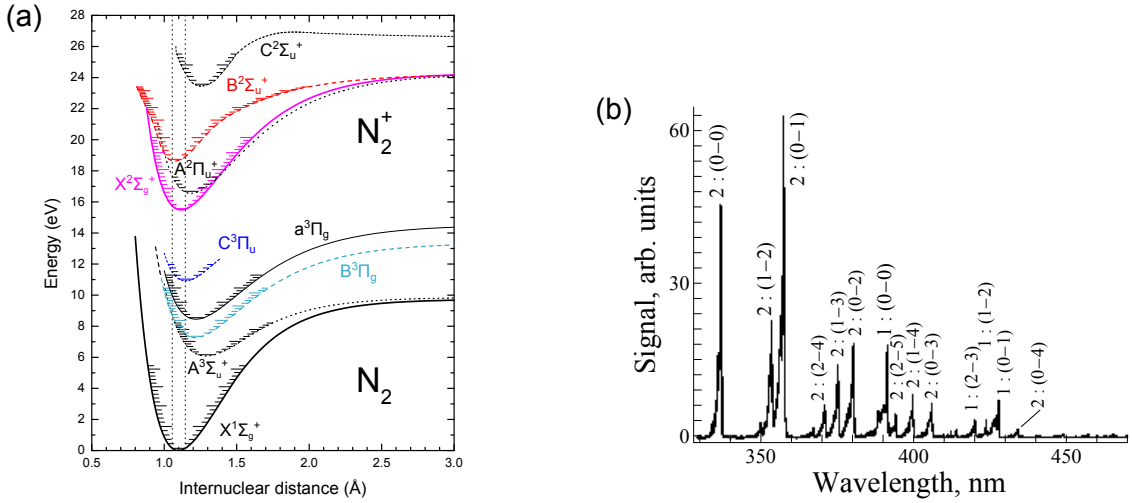

Figure 2.6: (a): energy levels for the N_2 molecule and the N_2^+ cation. The second positive system of N_2 and the first negative system of N_2^+ are highlighted in blue/cyan and red/magenta, respectively. (b): plasma fluorescence resulting from filamentation. 1 corresponds to the first negative system of N_2^+ and 2 to the second positive system of N_2. The numbers $(\nu - \nu')$ are the quantum vibrational numbers for the lower state and the upper state of the transition, respectively (from Talebpour *et al.* [23]).

First negative system of N_2^+ The origin of the formation of $N_2^+(B^2\Sigma_u^+)$ can be explained by the removal of an inner valence electron of N_2 by the laser field, either in a multiphoton or a tunnel process, yielding an excited N_2^+ state instead of the fundamental ionic state [24]. Indeed the number of N_2^+ ions in the $B^2\Sigma_u^+$ state was also found to have a similar intensity dependence as the nitrogen ionization rate given by the Keldysh model [23]. This means both that the formation of $N_2^+(B^2\Sigma_u^+)$ results from a direct photon process, and not from a collisional process, and that the number of ions in the $(B^2\Sigma_u^+)$ state is approximately proportional to the total number of N_2^+. This method has already been used experimentally to measure electron density in filaments [25].

Second positive system of N_2 The mechanism for the formation of $N_2(C^3\Pi_u)$ is not well elucidated. In this case, a direct photon process is spin-forbidden and must consequently have a negligible contribution. On the other hand, it is well known that electron impact on nitrogen molecules can result in the formation of the triplet state, given that the electron has a kinetic energy high enough. The threshold for this reaction lies around 11 eV with a maximum cross-section at 14.5 eV [26], and is the basis for the development of nitrogen lasers where energetic free electrons are generated by electric discharges [27]. In filaments generated by circularly-polarized laser pulses, electrons can indeed have a high energy as to form $N_2(C^3\Pi_u)$, as it was shown by Mitryukovskiy *et al.* [8]. However, this process cannot take place in the case of linearly-polarized laser pulses because electron energy is too low.

Another mechanism presented by Xu *et al.* relies on the formation of the N_4^+ intermediary following the reaction path [28]:

$$\begin{cases} N_2^+(X^2\Sigma_g^+) + N_2 + N_2 \longrightarrow N_4^+ + N_2 \\ N_4^+ + e^- \longrightarrow N_2(C^3\Pi_u) + N_2(X^1\Sigma_g^+). \end{cases} \tag{2.44}$$

In this case, as the number of N_2^+ ions in the fundamental state is proportional to the number of free electrons in the plasma, N_e, the population of $N_2(C^3\Pi_u)$ is roughly proportional to N_e^2.

A final mechanism was suggested by Arnold *et al.* in 2012. They explained that N_2 can be brought in a high-energy singlet state through an spin-allowed photon absorption process. These excited nitrogen molecules then collide with N_2 molecules in their ground state to yield $N_2(C^3\Pi_u)$, a process called inter system crossing [29]. However, experimental conditions described in this article are different from ours, with filamentation occuring either in pure nitrogen, or in a nitrogen/helium gas mixture. Moreover, no clue about the actual gas pressure used is given by the authors, although they mention an electron density on the order of 10^{19} m^{-3} in pure N_2 for an input energy > 1 mJ, which seems to indicate that low pressure gas was used in experiments.

The mechanism responsible for the generation of $N_2(C^3\Pi_u)$ in our experimental conditions is therefore not clear, and necessitates further study.

2.3.4.2 Experimental implementation

Plasma luminescence was first collected in the transverse direction to that of the filament by means of a simple optical system using two positive lenses in the form of an inverted telescope (figure 2.7-(a) and (b)). This system was conjugated so that the image of the entrance of the optical fiber was projected in the central plane of the filament. Luminescence was therefore coupled into the 10 m-long fused silica fiber, which could be used very conveniently to place the light analysis system away from the experimental setup.

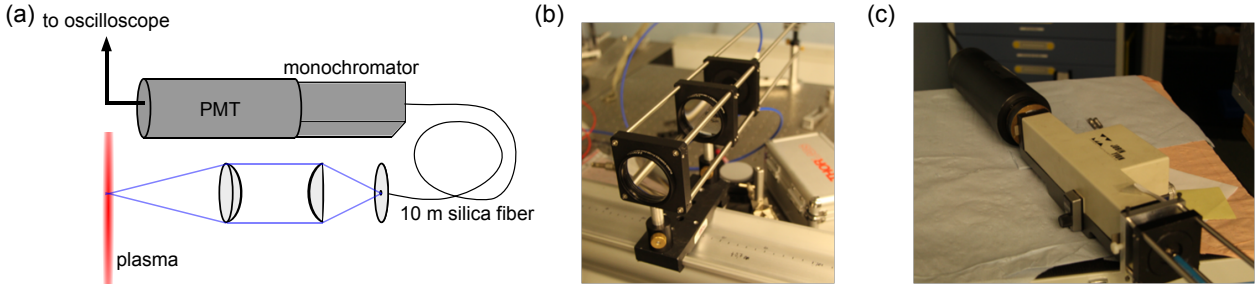

Figure 2.7: (a): drawing of the setup used for plasma luminescence recording. (b): photograph of the light collection system. (c): photograph of the light analysis system displaying the monochromator and the photomultiplier tube.

The other end of the fiber was mechanically fitted at the entrance of a monochromator (model H-20 from Jobin Yvon) with a ~ 1.5 nm spectral resolution. The output of the monochromator is attached to a photomultiplier tube (PMT) linked to an oscilloscope.

Since plasma fluorescence is isotropically emitted, and as the image of the entrance of the fiber has typically a similar diameter ~ 100 µm and can then be considered as a source point, we can link the measured signal from the first negative system of N_2^+, S, to the total number of electrons in the filament N_e:

$$\int_{\mathbb{R}} S(z)\ \mathrm{d}z \propto N_e = \int_{\mathbb{R}^3} n_e(\vec{r})\ \mathrm{d}^3\vec{r}. \tag{2.45}$$

This leads to:

$$S(z) \propto \int_{\mathbb{R}^2} n_e(r,\theta,z) r\ \mathrm{d}\theta\mathrm{d}r. \tag{2.46}$$

Using the same approximation for the electron density profile as for the pressure profile, that is a constant relative HWHM, we therefore find:

$$S(z) \propto n_{e,max}(z). \tag{2.47}$$

Using this spectroscopic diagnostic, we are therefore able to have an estimate of the electron density in the filament by means of a simple technique.

Conclusion

Energy deposition by the laser pulse into air during filamentation is a complex process involving numerous channels. Estimating the relative weight of each channel enabled us to find that ionization, plasma absorption and Raman rotational absorption from air molecules is responsible for most of the pulse energy depletion. This energy, initially stored either as free electron potential/kinetic energy or internal molecular rotational energy, is transferred to molecular translational degrees of freedom through collisional processes. These are complete by the end of plasma recombination, ~ 1 ns after the arrival of the laser pulse. This thermalization process results in the very rapid heating of an air volume roughly corresponding to the filamentation plasma volume, which occurs in an isochoric fashion. The medium reacts by launching an outward-propagating cylindrical hydrodynamic wave ejecting matter from the center of the channel and goes back to pressure equilibrium. The remaining central density hole then decays by diffusion, which can take more than 1 ms depending on experimental conditions.

To efficiently study the processes involved in laser energy deposition, we can make use of numerous diagnostics adapted to various physical parameters: energy deposition can be directly measured by means of a Joule meter. Interferometry enables us to have space and time-resolved measurements of air density profiles. Acoustics measurements give access to the lineic deposited energy. Finally study of plasma luminescence gives precious information about electron density.

Bibliography

[1] J. D. Jackson, *Classical Electrodynamics*, 3^{rd} ed. (John Wiley and Sons, Hoboken, NJ, USA, 1999).

[2] I. H. Hutchinson, *Principles of Plasma Diagnostics*, 2^{nd} ed. (Cambridge University Press, Cambridge, UK, 2002).

[3] Y.-H. Chen, S. Varma, A. York, and H. M. Milchberg, Optics Express **15**, 11341 (2007).

[4] J. K. Wahlstrand, Y.-H. Cheng, and H. M. Milchberg, Physical Review A **85**, 043820 (2012).

[5] L. V. Keldysh, Soviet Physics JETP **20**, 1307 (1965).

[6] A. Couairon and A. Mysyrowicz, Physics Reports **441**, 47 (2007).

[7] N. H. Burnett and P. B. Corkum, Journal of the Optical Society of America B **6**, 1195 (1989).

[8] S. Mitryukovskiy, Y. Liu, P. Ding, A. Houard, A. Couairon, and A. Mysyrowicz, Physical Review Letters **114**, 063003 (2015).

[9] J. A. Bittencourt, *Fundamentals of Plasma Physics*, 3rd ed. (Springer, New York, NY, USA, 2004).

[10] Y.-H. Cheng, J. K. Wahlstrand, N. Jhajj, and H. M. Milchberg, Optics Express **21**, 4740 (2013).

[11] G. Point, C. Milián, A. Couairon, A. Mysyrowicz, and A. Houard, Journal of Physics B **48**, 094009 (2015).

[12] P. E. Ciddor, Applied Optics **35**, 1566 (1996).

[13] R. A. Alpher and D. R. White, Physics of Fluids **2**, 153 (1959).

[14] C. Torrence and G. P. Compo, Bulletin of the American Meteorological Society **79**, 61 (1998).

[15] H. Liu, A. N. Cartwright, and C. Basaran, Applied Optics **43**, 850 (2004).

[16] M. A. Herráez, D. R. Burton, M. J. Lalor, and M. A. Gdeisat, Applied Optics **41**, 7437 (2002).

[17] G. Point, Y. Brelet, L. Arantchouk, J. Carbonnel, B. Prade, A. Mysyrowicz, and A. Houard, Review of Scientific Instruments **85**, 123101 (2014).

[18] L. Montgomery Smith, D. R. Keefer, and S. Sudharsanan, Journal of Quantitative Spectroscopy and Radiative Transfer **39**, 367 (1988).

[19] E. W. Rosenthal, J. P. Palastro, N. Jhajj, S. Zahedpour, J. K. Wahlstrand, and H. M. Milchberg, Journal of Physics B **48**, 094011 (2015).

[20] J. Yu, D. Mondelain, J. Kasparian, E. Salmon, S. Geffroy, C. Favre, V. Boutou, and J.-P. Wolf, Applied Optics **42**, 7117 (2003).

[21] D. V. Kartashov, A. V. Kirsanov, A. M. Kiselev, A. N. Stepanov, N. N. Bochkarev, Y. N. Ponomarev, and B. A. Tikhomirov, Optics Express **14**, 7552 (2006).

[22] A. Talebpour, S. Petit, and S. L. Chin, Optics Communications **171**, 285 (1999).

[23] A. Talebpour, M. Abdel-Fattah, A. D. Bandrauk, and S. L. Chin, Laser Physics **11**, 68 (2001).

[24] A. Becker, A. D. Bandrauk, and S. L. Chin, Chemical Physics Letters **343**, 345 (2001).

[25] F. Théberge, W. Liu, P. T. Simard, A. Becker, and S. L. Chin, Physical Review E **74**, 036406 (2006).

[26] Y. Itikawa, Journal of Physical and Chemical Reference Data **35**, 31 (2006).

[27] R. S. Kunabenchi, M. R. Gorbal, and M. I. Savadatti, Progress in Quantum Electronics **9**, 259 (1984).

[28] H. L. Xu, A. Azarm, J. Bernhardt, Y. Kamali, and S. L. Chin, Chemical Physics **360**, 171 (2009).

[29] B. R. Arnold, S. D. Roberson, and P. M. Pellegrino, Chemical Physics **405**, 9 (2012).

Chapter 3

Energy deposition in the single filamentation regime

Contents

Introduction

The previous Chapter presented the physical mechanisms involved in laser energy deposition in air resulting from filamentation. We now focus on the case of single filamentation, a regime that extends roughly from $P \sim P_{cr}$ to $P \sim 10P_{cr}$. This case is interesting for several reasons. First, it can be reached with modest energies and can typically be achieved with virtually any Ti:sapphire laser chain. Second, the single filament regime can be well controlled in laboratory conditions, and displays far more stability than multifilaments. Last but not least, it is also a regime that can be relatively easy to model and simulate, because cylindrical symmetry can usually be assumed, resulting in far less time-intensive computations than, for instance, full 3-dimensional and temporal simulations.

This chapter is made up of two parts: the first one consists of a study of the evolution of deposited energy with different experimental parameters, namely laser pulse energy, focusing conditions, polarization and wavelength. The second part presents a brief review of applications for filamentation-induced hydrodynamics in air.

3.1 Evolution of energy deposition in air with experimental conditions

3.1.1 Influence of laser pulse energy

Laser pulse energy is the most obvious parameter that could influence energy deposition. Of course, the input pulse energy represents the upper limit of what can indeed be transferred to the medium. But this parameter also strongly influences propagation dynamics of the resulting filament and, as such, local energy deposition through the channels detailed in Chapter 2.

Several results in the *low-energy* single filamentation regime have been published over the past few years, mainly from the Milchberg group of the University of Maryland. We here compare these results with our own results obtained in the *high-energy* single filamentation regime, close to the appearance of multifilamentation.

3.1.1.1 Experimental conditions

The studied filaments were generated by a 5 mJ, 50 fs laser pulse at 800 nm focused at $f/30$ by means of a 1 m fused silica lens, that is a moderately strong focusing. In this case, the recorded

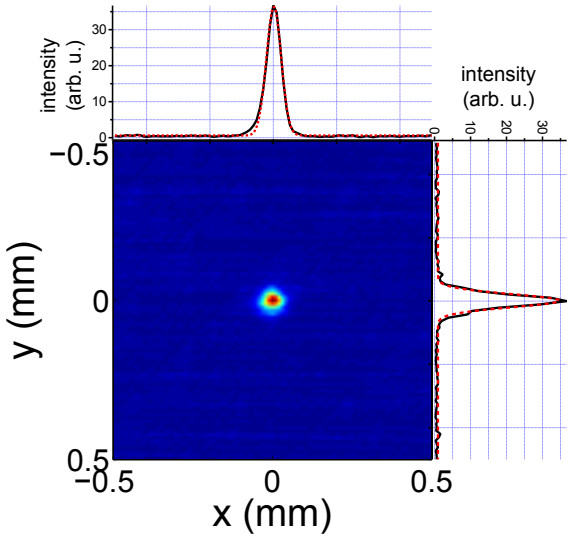

Figure 3.1: Measured focal spot of our femtosecond laser focused at $f/30$ in the linear propagation regime, and corresponding (x,y) intensity profiles taken at $y = 0$ and $x = 0$, respectively (black curves). Gaussian fits for these profiles are also displayed (red dashed curves).

focal spot in the linear regime is well fitted by a Gaussian curve (cf. figure 3.1). The corresponding beam waist is measured to be $w_0 = 31$ µm, resulting in a Rayleigh length $L_R = 3.8$ mm. As evidenced by plasma luminescence, laser-induced plasma in these experimental conditions is over 1 cm long, much larger than L_R. This proves that we are indeed in the filamentation propagation regime. Still, as the focusing is strong, beam collapse and filament generation are lens-dominated, leading to a quasi-linear propagation of the pulse until ionization occurs [1].

These experimental conditions corresponds well to those used by Wahlstrand *et al.* in reference [2]: the authors made use of a 50 fs laser pulse focused at $f/30$, but with a significantly lower pulse energy (65 µJ), enabling them to perform distortionless longitudinal interferometry on re-

sulting filaments. We can therefore compare their results with those obtained in our experimental conditions.

3.1.1.2 Global scale: energy deposition and energy density

We first made a direct measurement of energy deposition over the whole propagation distance of the laser pulse using a Joule meter (cf. Chapter 2, section 2.3.1). We measured the deposited energy in air to be:

$$\Delta U = 780 \pm 160 \ \mu\text{J}, \tag{3.1}$$

where the confidence interval corresponds to ± one standard deviation taken over 500 shots. This value is almost one order of magnitude higher than the laser input pulse energy used by Wahlstrand *et al.*. We then made use of a 1/4" electret microphone (model 40 BE from G.R.A.S. Sound & Vibration) to perform a scan of the laser-induced acoustics along the laser propagation axis, the microphone being placed at 1 cm from the center of the beam. As detailed in Chapter 2 (section 2.3.3), the amplitude of the acoustic signal is approximately proportional to the lineic deposited energy. Recording acoustics signals at a fixed position (example given in figure 3.2-(a)) and extracting the peak value of the signal, one can build a 1-D map of the acoustic amplitude. The last step consists in equating the integral of this map and the deposited energy ΔU, yielding the graph displayed in figure 3.2-(b).

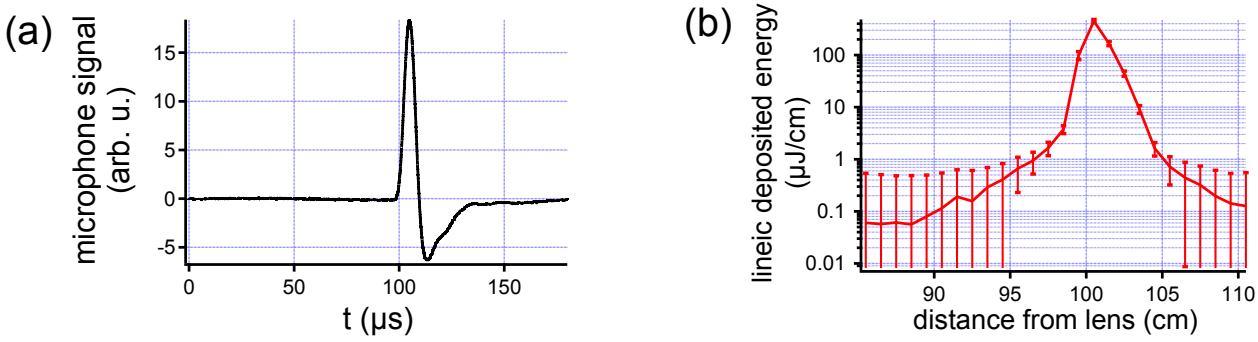

Figure 3.2: (a): example of a recorded acoustic signal from the filament, displaying a characteristic single-cycle acoustic wave. The amplitude of the first peak is then used for estimation of deposited energy. (b): acoustic scan along the laser propagation direction averaged over 200 shots. Results have been translated in terms of deposited energy using the measured value for ΔU.

In our case, we find that most of the energy deposition takes place in a very limited area about 5 cm long around the position of the lens' linear focus. The reached peak value is of 400 $\mu\text{J} \cdot \text{cm}^{-1}$. Wahlstrand *et al.* measured the length of their filament to be only 2 mm [2]. In their case, assuming that all of the laser energy is deposited leads to a mean lineic energy of 480 $\mu\text{J} \cdot \text{cm}^{-1}$. Even in this low-energy case, they might therefore have been able to reach comparable peak deposited lineic energy.

We also investigated plasma axial distribution since it was seen in Chapter 2 that plasma generation and absorption make up a good part of laser energy deposition. As presented in Chapter 2 (section 2.3.4), recording plasma emission at 391 nm allows to estimate the local electron density. We therefore made a scan of plasma luminescence along the laser propagation direction. Corresponding results are plotted in figure 3.3, together with microphone scan results.

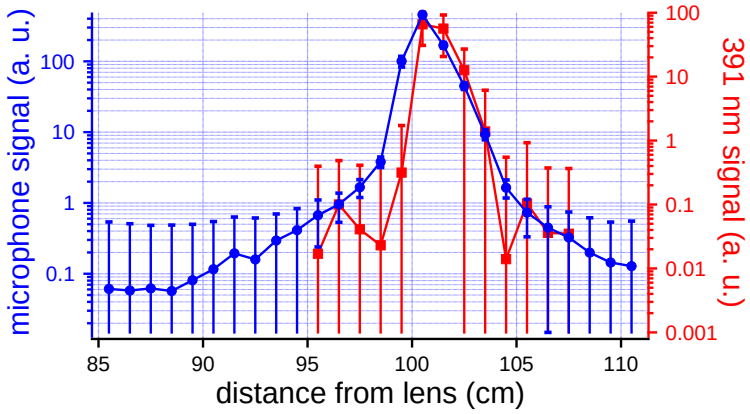

Figure 3.3: Evolution of microphone signal (blue circles) and of plasma luminescence at 391 nm (red squares) along the laser propagation direction. Data was averaged over 200 shots for the two data sets.

These last graphs display the same characteristic trends: plasma luminescence is maximum precisely where the sound signal is strongest, showing the correlation between the two phenomena. Still, agreement is not perfect, notably shortly before 1 m, where energy deposition increases much faster than plasma luminescence. This can be seen as an evidence of rotational Raman absorption, which starts for intensity levels several orders of magnitude lower than required for ionization. As the pulse propagates towards the lens' focus, intensity increases strongly, leading first to a more important Raman absorption, and then to ionization once the corresponding threshold is reached. This was simulated by Rosenthal *et al.* for a similar pulse energy but a significantly weaker focusing [3].

3.1.1.3 Local scale: air hydrodynamics in the focal zone

Filamentation-induced air hydrodynamics are characterized by the formation of an outward propagating hydrodynamic wave, which enables the system to reach pressure equilibrium. It also ejects matter from the center of the channel, creating an underdense air channel that then slowly resorbs by diffusion. These phenomena can be easily seen using transverse interferometry followed by Abel inversion. Results we obtained in the case of 5 mJ laser pulses are displayed in figure 3.4.

This figure regroups two-dimensional (r,z) air density profiles taken in the single-shot regime at three different instants after filamentation. The pump/probe experimental setup was such as the probe intercepted the filament shortly after the lens geometrical focus. Figure 3.4-(a) was recorded at delay 500 ns. At this time, the hydrodynamic wave is still linked to the central underdense channel, ejecting matter from it. The amplitude of this wave stands at more than 3×10^{25} m^{-3}, that is 120 % of the density of air at rest, n_0. The underdense channel is conversely very deep, with a decrease of more than 60 % with respect to n_0.

At delay 5 µs (figure 3.4-(b)), the wave has separated from the central channel and reached a radius of more than 2 mm, and its amplitude has also significantly decreased. A very rough estimation of its propagation speed v_{wave} between these two instants gives:

$$v_{wave} = 440 \text{ m} \cdot \text{s}^{-1}, \tag{3.2}$$

that is a speed significantly higher than the speed of sound in air in normal temperature and

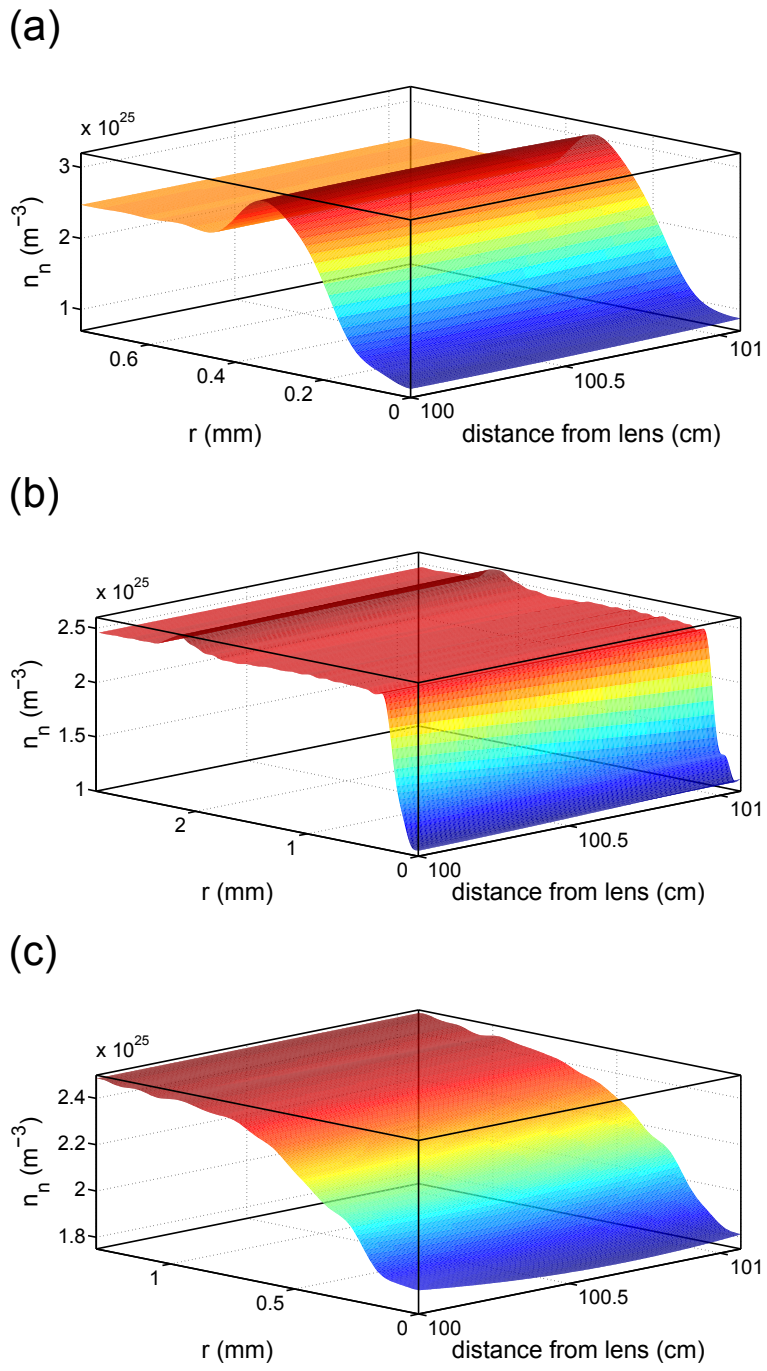

Figure 3.4: Two-dimensional (r,z) neutral density profiles resulting from the filamentation of a 5 mJ, 50 fs laser pulse at 800 nm focused at $f/30$ at delay 500 ns (a), 5 µs (b) and 500 µs (c).

pressure conditions $c_s = 340\ \mathrm{m} \cdot \mathrm{s}^{-1}$. This feature is characteristic of shock waves, along with a steep wavefront. As for the central underdense channel, its depth and width have stabilized at $\sim 10^{25}\ \mathrm{m}^{-3}$ and $\sim 500\ \mu\mathrm{m}$, respectively.

Finally, at delay 500 µs (figure 3.4-(b)), the shock wave has disappeared from the field of view and can be considered negligible in the Abel inversion process. Only the central underdense air channel remains. By this time it has significantly enlarged and decreased in amplitude due to

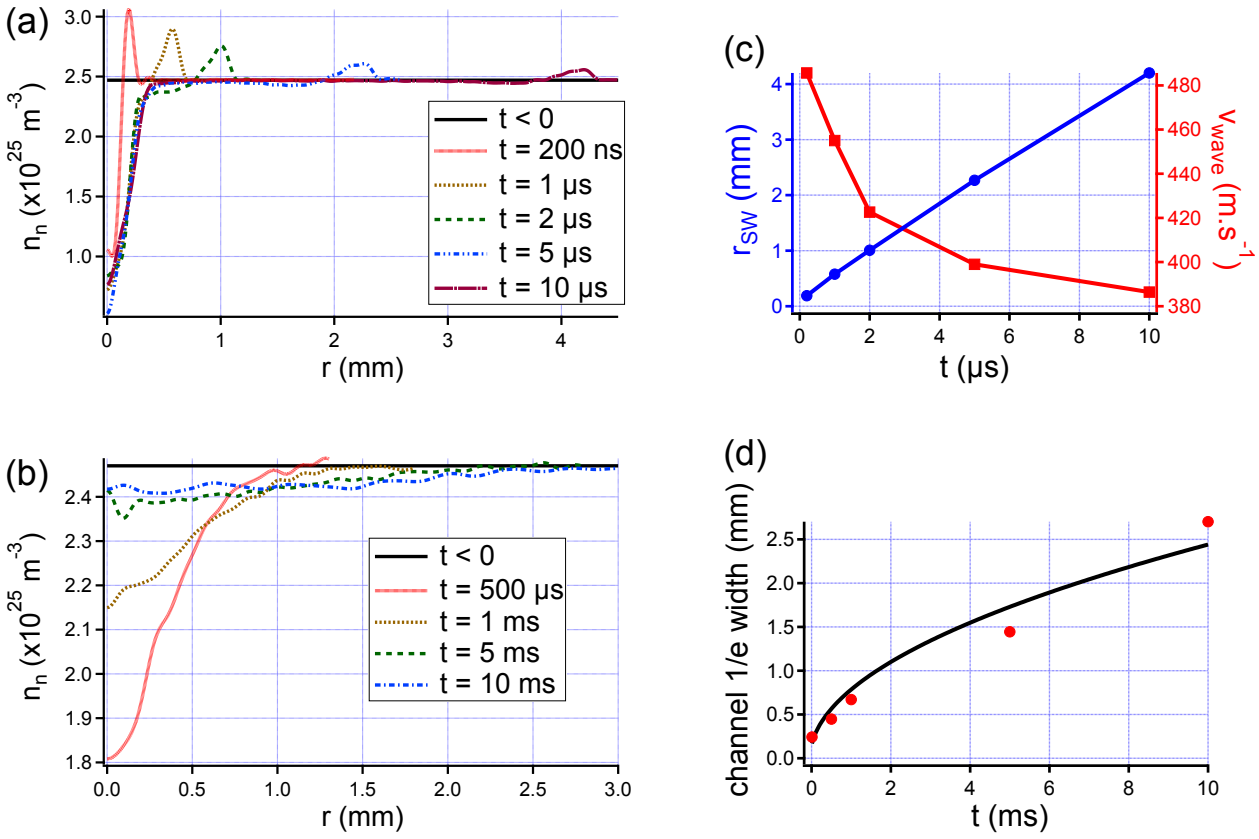

Figure 3.5: 1-D z-averaged density profiles resulting from the filamentation of a 5 mJ, 50 fs laser pulse at 800 nm focused at $f/30$ at short delays (a) and long delays (b). (c): evolution of the radial shock wave position r_{SW} (blue circles) and of shock wave speed v_{wave} (red squares) with time. (d): evolution of the channel $1/e$ width with time (red circles), and diffusive fitting (black solid curve).

diffusion, with a FWHM reaching 750 µm. Since at this point the system has long been back at pressure equilibrium, the density profile mirrors the temperature profile of the gas. As the mimimum density stands at 1.8×10^{25} m^{-3}, the ideal gas law with a pressure of 1.013×10^5 Pa gives:

$$T(r = 0, t = 500\ \mu\text{s}) = 400\ \text{K}. \tag{3.3}$$

The core of the channel therefore remains hot for a very long time.

Two-dimensional (r,z) density profiles bring a lot of information but are also difficult to read. To this purpose, we extracted 1-D profiles from 2-D profiles by averaging over the whole length of the probed area. Results are given in figure 3.5-(a) and (b). Figure 3.5-(a) displays density profiles measured in the hydrodynamic regime, for which it is possible to record the shock wave propagating away from the center. These results are plotted in figure 3.5-(c), showing the evolution of the shock wave radius r_{SW} with time. Using a simple finite difference as derivative approximation, one can then extract the shock wave speed from this parameter. In this case we find the initial wave speed to be in excess of 480 m $\cdot$ s^{-1}, an impressive speed compared to the relatively modest energy given to the system.

At longer times, density profiles are characterized by the persistence of the central underdense air channel (figure 3.5-(b)). This channel progressively broadens while its depth decreases due to

the thermal diffusion process governed by equation (2.35). In figure 3.5-(d) is plotted the evolution of the channel $1/e$ width with time. Width was estimated from profiles displayed in figure 3.5-(b) by means of a Gaussian fit. These data are rather well fitted by the function $f(x) = \sqrt{a + bx}$, corresponding to the exact solution from equation (2.35). At delay 90 ms, it was still possible to record a phase shift of a few tens of mrad but, by then, the underdense channel was so large that it was not possible to perform Abel inversion to retrieve density profiles. Undoubtedly, the system will not be back at equilibrium at 100 ms, corresponding to the repetition period of our laser. This means that a permanent underdense air channel will be formed while the laser is shooting at 10 Hz. Such cumulative effect has already been observed by Cheng *et al.* but using 780 µJ laser pulses with a kHz repetition rate [4]. More energetic laser pulses could then prove very useful in this respect since 10 Hz laser chains are more readily available than kHz ones.

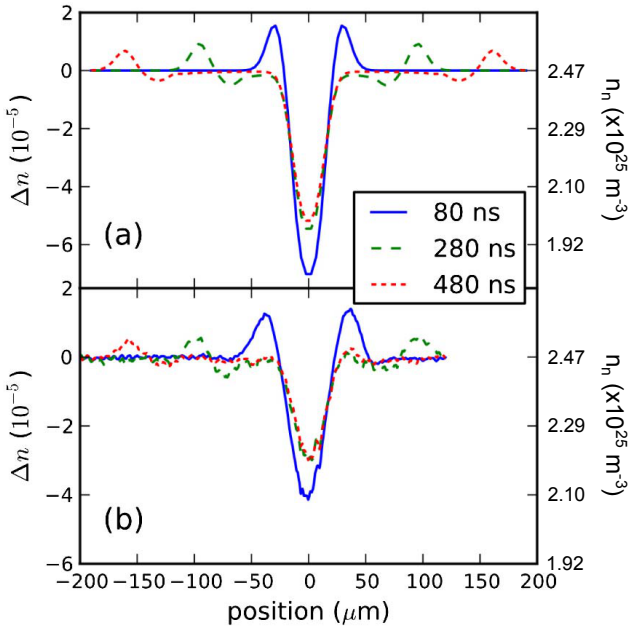

Figure 3.6: Simulated (a) and experimental (b) refractive index/air density profiles resulting from the filamentation of a 96 µJ, 50 fs laser pulse at 800 nm focused at $f/30$, from Wahlstrand *et al.* [2].

We can compare our results to those obtained by Wahlstrand *et al.* in the same experimental conditions but with an energy 50 times lower [2]. In their case, the authors found that filamentation resulted in the generation of a single cycle acoustic wave with a speed equal to c_s. Moreover, the corresponding density profiles, displayed in figure 3.6, are notably shallower than in our case with a minimum reached density of 2.1×10^{25} m^{-3}. Another significant difference lies in the channel width. We recorded a FWHM of more than 200 µm at delay 200 ns while low-energy filamentation results in a central channel with an initial width of less than 100 µm.

Locally, laser-induced hydrodynamics therefore appear to dramatically change as laser energy is increased, resulting in a larger and deeper underdense air channel and in the generation of a supersonic shock wave instead of a sound wave. Clearly, focal lineic deposited energy must be far higher in the case of a 5 mJ laser pulse than for a 96 µJ pulse, despite the fact that energy deposition takes place over a far longer area.

3.1.1.4 Air temperature

Initial air temperature resulting from energy deposition can be estimated by different methods. A first way to derive it is to use the first law of thermodynamics. Since air heating due to filamentation is a quasi-isochoric process, this reads:

$$\Delta U = \int_{\mathbb{R}^3} c_v n_n(\vec{r}) \left(T(\vec{r}) - T_{air}\right) \, \mathrm{d}^3\vec{r}, \tag{3.4}$$

where c_v is the isochoric heat capacity of air per molecule. For an ideal diatomic molecular gas, which is a good approximation for air in standard pressure and temperature conditions, $c_v = 5k_B/2$. As initially we have $n_n(\vec{r}) = n_0 = 2.47 \times 10^{25}$ m^{-3}, the neutral density of air at $p = 1013$ hPa and $T = 300$ K, equation (3.4) can be rewritten as:

$$\Delta U = \frac{5}{2} k_B n_0 \int_{\mathbb{R}^3} \left(T(\vec{r}) - T_{air}\right) \, \mathrm{d}^3\vec{r} \approx \frac{5}{2} k_B n_0 \pi r_0^2 \int_{\mathbb{R}} \left(T_{max}(z) - T_{air}\right) \, \mathrm{d}z, \tag{3.5}$$

where r_0 is the HWHM of the initial temperature profile considered as constant along the filament. This leads to:

$$T_{max}(z) - T_{air} \approx \frac{2}{5k_B n_0 \pi r_0^2} \frac{\partial \Delta U}{\partial z}(z). \tag{3.6}$$

Using the measured value for the deposited energy by unit length (figure **??**-(b)) and a typical radius $r_0 \sim 100$ µm characteristic of filamentation, we find, for a 5 mJ, 50 fs laser pulse focused at $f/30$, a maximum reached initial temperature of:

$$T_{max} - T_{air} \sim 1600 \text{ K}. \tag{3.7}$$

This first estimate gives a very important initial heating due to laser energy deposition. This can be explained by the modest air volume in which energy is lost, yielding large energy densities and, eventually, temperature values.

To check the physical implications of such a large initial temperature we ran numerical simulations of the hydrodynamic evolution of air in the focal zone to be compared with experimental results. To this purpose, a code written by Carles Milián solving the compressible Euler equations was used. These equations were written in cylindrical coordinates neglecting azimuthal and axial fluxes:

$$\begin{cases} \partial_t E + \vec{\nabla}.\vec{F} = S \\ E = \begin{bmatrix} \rho \\ \rho\vec{v} \\ e \end{bmatrix} \\ F = \begin{bmatrix} \rho\vec{v} \\ \rho\vec{v} \otimes \vec{v} + p\overline{\delta} \\ (e+p)\vec{v} \end{bmatrix} \\ S = \begin{bmatrix} 0 \\ \vec{0} \\ \vec{\nabla}(\kappa\vec{\nabla}T). \end{bmatrix} \end{cases} \tag{3.8}$$

Here $\rho = n_n M/\mathcal{N}_A$ is the mass density, where M is the air molar mass and $\mathcal{N}_A$ the Avogadro number, $e = u + \rho v^2/2$ denotes the total energy density, u being the internal energy density, $\overline{\delta}$ is the unity tensor, and κ is the thermal conductivity of air. $\vec{v} \otimes \vec{v} = v_i v_j$ is the tensor product of the fluid bulk velocity $\vec{v} = v(r)\vec{e}_r$ by itself. The integration of the fluid equations is carried out by means of the Harten Lax van Leer first order Godunov method with restoration of the contact

surface [5]. This method is able to capture the shock wave formation, as it is typically observed in the experiment. Internal energy density u and adiabatic coefficient γ are used to compute the speed of sound $c_s = \sqrt{\partial_\rho p|_u + p/\rho \partial_u p|_\rho}$ at each step, necessary to determine the fluxes F. In accordance with the hydrodynamic initial conditions described in Chapter 2 (section 2.2.1.1), our simulations are initialized with an initial Gaussian temperature distribution and a flat density profile of magnitude n_0. Simulation outcomes therefore depend only on two parameters: initial maximum temperature T_{max} and standard deviation of the temperature profile σ_T.

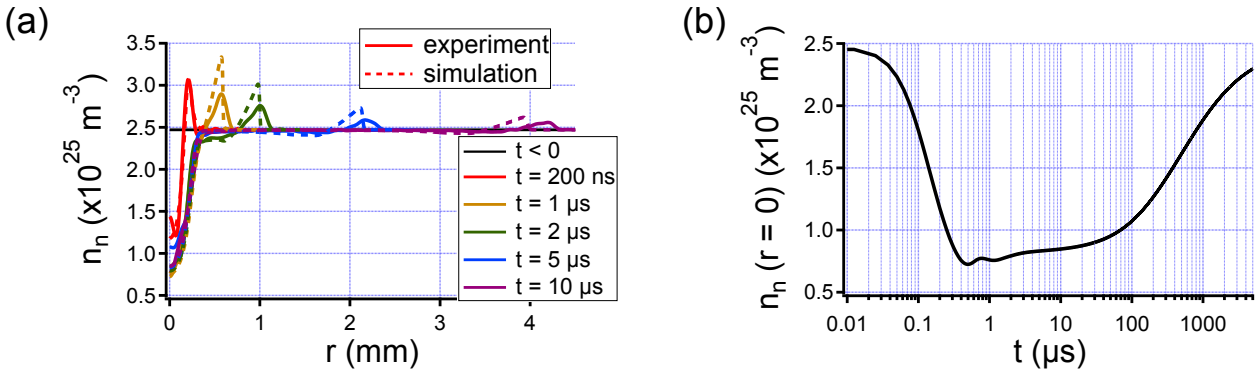

Figure 3.7: (a): simulated air density profiles for different times (dashed lines) compared to experimental ones (sold lines). (b): simulated time evolution of on-axis air density $n_n(r = 0)$.

The best fit to experimental data (presented in figure 3.5) was obtained for $T_{max} = 1400$ K and $\sigma_T = 85$ µm. By varying the width in about ±15 µm and the peak temperature by ±200 K, the overall agreement worsens significantly in terms of the shock wave position and amplitude. Corresponding results are displayed in figure 3.7. Air density profiles at various times are plotted in figure 3.7-(a) together with experimental measurements from figure 3.5-(a). Accordance between the two data sets is very good, especially concerning the central underdense channel. There is a slight mismatch concerning the shock wave position, which might be linked to slightly different air thermodynamic properties between simulation and experiment.

Numerical simulations enabled us to have a more precise estimation of the initial gas temperature than the rough result given by equation (3.7). Still, it confirms that we are in a high-temperature regime with characteristic values above 1000 K. As a comparison, typical heating values estimated for filamentation of a 720 µJ, 40 fs laser pulse focused at $f/65$, also using numerical hydrodynamic simulations, was $\Delta T = 100$ K, more than one order of magnitude lower than for a 5 mJ pulse [4].

3.1.2 Influence of focusing conditions

External focusing conditions of an ultrashort laser pulse have been shown to have a strong impact on the resulting filament. The influence of this parameter has been thoroughly investigated by Théberge *et al.* in the single filamentation regime [6]. Corresponding results are displayed in figure 3.8.

Moderate to strong focusing (up to $\sim f/60$) results in a gentle enlargement of the filament core and a rise of the plasma density . This is attributed to the increase of laser energy at the center of the beam due to the lens-imposed phase which, in turn, increases peak intensity and plasma density. As a new dynamic balance between focusing, self-focusing, diffraction, non-linear absorption and

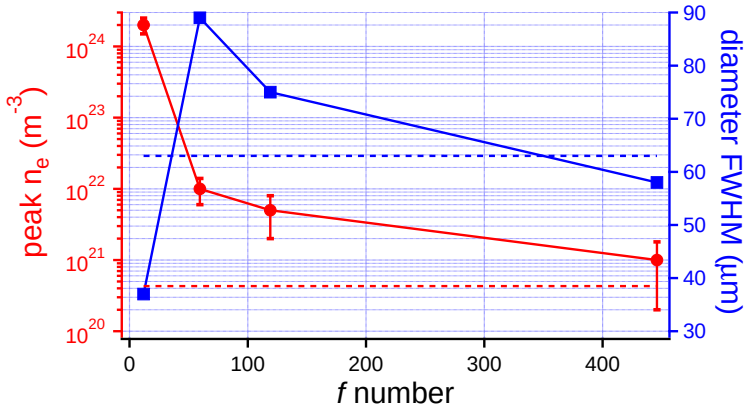

Figure 3.8: Measured peak electron density (red circles) and electron density profile FWHM (blue squares) for different f numbers with an input power $P = 2.5P_{cr}$. Parameter values in the case of free propagation for $P = 9P_{cr}$ are given by the dashed lines. From Théberge *et al.* [6].

plasma defocusing is reached, the intense core of the filament swells to compensate the increase in electron density. Below $f/60$, plasma density dramatically increases while plasma width decreases. This is explained by the fact that, with such a strong focusing, pulse propagation is almost entirely dominated by the lens' phase, concentrating laser energy into a spot with a minimum size equal to the diffraction limit. In this case, filament size is constrained and therefore electron density needs to reach a very high value to balance focusing and self-focusing, here corresponding to an ionization degree of 10 %. Experimental results and numerical simulations in very tight focusing conditions ($< f/5$) indeed demonstrated that lens-induced beam curvature completely dominates over plasma defocusing, leading to a quasi-breakdown regime where high ionization degrees (> 0.8) can be reached [7, 8].

We investigated the influence of the focusing parameter on energy deposition from the filamentation of a 5 mJ, 50 fs laser pulse at 800 nm. We first measured deposited energy in each case using a Joule meter. Data averaged over 500 shots yield following results:

$$\begin{cases} \Delta U(f/80) = 570 \pm 150 \text{ µJ} \\ \Delta U(f/55) = 590 \pm 130 \text{ µJ} \\ \Delta U(f/30) = 780 \pm 160 \text{ µJ}. \end{cases} \tag{3.9}$$

To assess filamentation length in each case, we took transverse time-integrated pictures of plasma fluorescence using a standard commercial camera (Canon EOS 650 D fitted with a 18-135 mm $f/3.5-5.6$ objective). Longitudinal profiles were extracted by selecting signal from blue pixels only, since plasma luminescence lies mostly below 400 nm, and averaged in the transverse direction over the filament width. Pictures and corresponding profiles are displayed in figure 3.9. This diagnostic, though less precise and informative than a rigorous spectral study, is easy to implement and gives a first idea about the plasma spatial extension.

The main result that can be deduced from figure 3.9 is that the stronger the focusing, the shorter the filament, with an apparent length starting at ~ 1 cm at $f/30$ and reaching ~ 10 cm at $f/80$. We can also see that filaments present more pronounced irregularities with weaker focusing, with hints of refocusing cycles occurring over the plasma length.

The two main channels for energy deposition are plasma generation/absorption and Raman

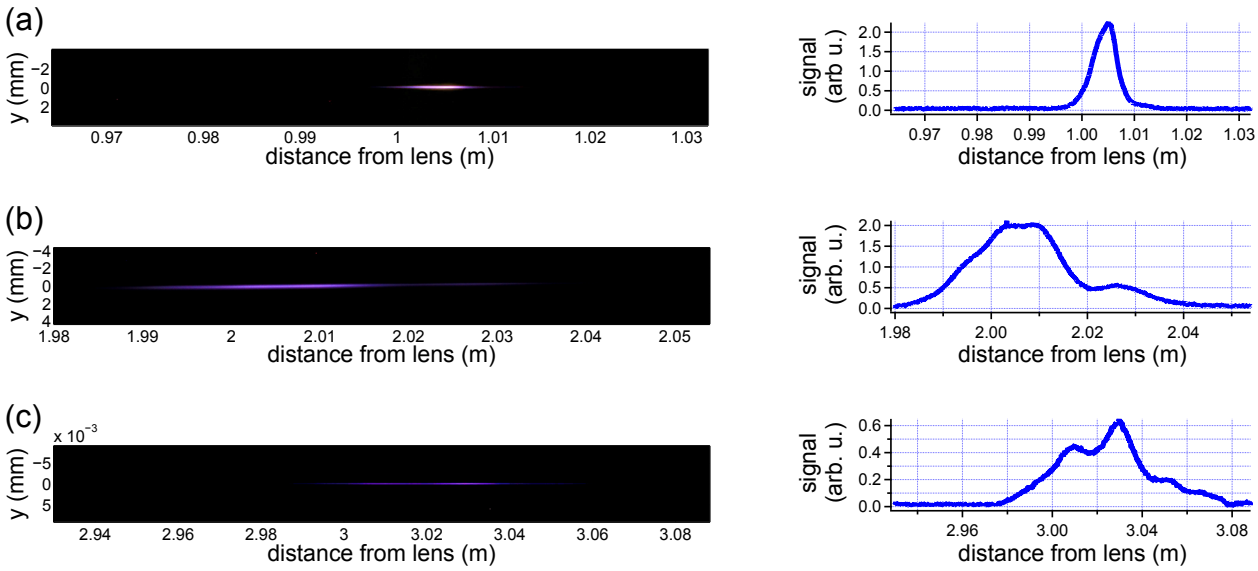

Figure 3.9: Photographs of plasma luminescence resulting from the filamentation of a 5 mJ, 50 fs laser pulse at 800 nm (left) and corresponding blue pixel longitudinal profiles (right). Focusing conditions are $f/30$ (a), $f/55$ (b) and $f/80$ (c).

rotational absorption (cf. Chapter 2). Intensity varies moderately with focusing conditions, with a peak value ranging from 10^{18} to 10^{19} W $\cdot$ m^{-2} [8]. As Raman absorption scales as I^2 and plasma generation as $\sim I^{6.5}$ (see Chapter 1, section 1.3.2.2), the only vector for energy transfer from the laser pulse to the medium that is strongly affected by the focusing parameter is plasma generation. We can therefore use measured deposited energy and luminescence profiles to roughly estimate absorbed lineic energies:

$$\begin{cases} \Delta U/L(f/80) \approx 60\ \mu\text{J} \cdot \text{cm}^{-1} \\ \Delta U/L(f/55) \approx 100\ \mu\text{J} \cdot \text{cm}^{-1} \\ \Delta U/L(f/30) \approx 500\ \mu\text{J} \cdot \text{cm}^{-1}. \end{cases} \tag{3.10}$$

A clear transition is observed between $f/55$ and $f/30$, characterized by a sudden increase of deposed lineic energy. This is in good agreement with the results of Théberge *et al.* where plasma density strongly increases between $f/60$ and $f/12$ while plasma radius decreases at the same time, resulting in the rise of deposited energy density.

To get a more rigorous picture of energy deposition, we also implemented transverse interferometry probing the area right after the linear focus, like it was done in the previous section. This was used to extract the time evolution of the FWHM and of the depth of filamentation-generated underdense air channels. Results are plotted in figure 3.10.

Here, we can see that using strong focusing results in a deeper underdense channel, that is a higher air temperature. This result therefore mirrors the estimation of the lineic deposited energy from equation (3.10). More interesting, the size of this channel is noticeably larger in the case of the strongest focusing ($f/30$) while the initial size of the plasma channel is smaller in this case. However, results presented in figure 3.10 start at delay 200 ns. By this time, the shock wave has already formed and propagated some distance away but has not yet separated from the underdense channel, enlarging it.

When the initial energy deposition is too low to result in such a shock wave but yields a sound

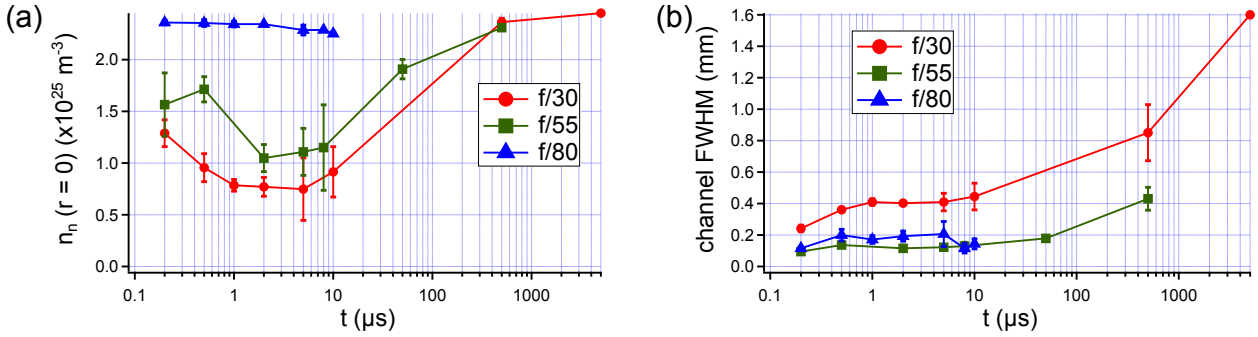

Figure 3.10: Interferometrically recorded on-axis air density $n_n(r = 0)$ (a) and underdense channel FWHM (b) at different times in three distinct focusing conditions: $f/30$ (red circles), $f/55$ (green squares) and $f/80$ (blue triangles). Single filamentation was induced by a 5 mJ, 50 fs laser pulse at 800 nm.

wave instead, channel width should depend marginally on focusing as long as this threshold is not exceeded, because of the constant speed of the wave. This can be seen by comparing the $f/55$ and $f/80$ cases that share the same underdense channel width (figure 3.10-(b)). Once the threshold for shock wave generation is reached, the picture is different because the initial wave speed is strongly dependent on the initial maximum pressure (that is, temperature and deposited energy). As a consequence filamentation-induced underdense air channels are expected to be larger when energy deposition is increased, which is the case when focusing is tightened.

Finally, it is worth mentioning that results displayed in figure 3.10 compare well with the estimation of equation (3.10). Underdense channels generated using a $f/55$ focusing have the same width as in the $f/80$ case, but are about 2 times deeper with a lineic deposited energy almost 2 times higher. As for the $f/30$ focusing, it gives birth to underdense air channels ~ 20 % deeper and ~ 2 times wider than channels observed in the $f/55$ case. Lineic deposited energy in the $f/30$ case should then theoretically be given by:

$$\Delta U/L(f/30) \approx 1.2 \times 2^2 \Delta U/L(f/55) = 5\Delta U/L(f/55). \tag{3.11}$$

This is precisely the factor given in equation (3.10).

To conclude on the influence of focusing conditions on energy deposition, we showed that increasingly strong focusing conditions results in two main consequences: first, total energy deposition increases, due to the increased density of the laser-induced plasma. Second, plasma length decreases, resulting in a rise of deposed energy density and in an increased heating. If strong enough, the latter can generate a cylindrical shock wave that is responsible for the formation of a larger underdense air channel.

3.1.3 Influence of polarization

The effect of laser polarization on the filamentation process is not well elucidated. It is agreed that critical power in case of circularly polarized pulses is higher than for linear pulses, and that multiple filamentation is more difficult to achieve in these conditions [9, 10]. Numerical studies in the case of $\sim 3P_{cr}$ pulses have shown that the generated plasma is less dense for circular polarization than for linear polarization [9]. However, experiments, both at filamentation threshold and at higher power

($\sim 20P_{cr}$) gave either a similar electron density in both cases [11], or a higher plasma density with circularly polarized pulses [12].

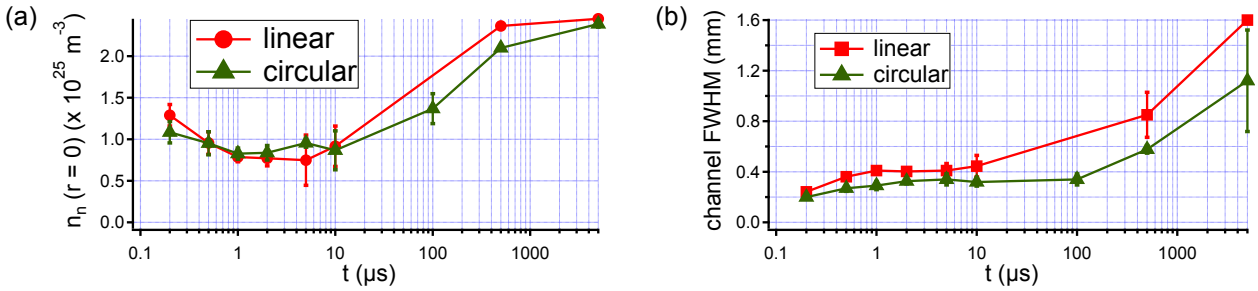

Figure 3.11: Interferometrically recorded on-axis air density $n_n(r = 0)$ (a) and underdense channel FWHM (b) at different times in linear (red circles) and circular (green triangles) polarization. Single filamentation was induced by a 5 mJ, 50 fs laser pulse at 800 nm focused at $f/30$.

However one also has to bear in mind that energy transfer from the laser pulse to the plasma in these two different configurations is not the same. First, as evidenced by previous experimental results, the total number of electrons produced at the center of the filamentation channel for circular polarization is equal or superior to that in the case of linear polarization. In a similar volume, more laser energy is then transferred to the medium in the form of free electron potential energy for circular polarization. Moreover, it has been calculated that on average, electron kinetic energy in the case of circular polarization is well defined around a value almost proportional to the laser intensity, since electron mostly acquire energy through ponderomotive interaction [13]. This value can reach up to 15 eV, as evidenced by the existence of collision-assisted population inversion of the triplet manifold of molecular nitrogen in plasma filaments [14]. On the other hand, in the case of linear polarization, the electron energy distribution is peaked at low energy and weakly extends up to only a few electronvolts. As a consequence, plasma generation should then be a better vector for energy transfer from the laser pulse to the medium in the case of circular polarization. The results of our experiments are presented in figure 3.11. Figure 3.11-(a), which displays the minimum neutral density in the underdense channel with time, does not show a strong difference between the two cases. Regarding the channel size (figure 3.11-(b)), experimental observations are however different with a slightly larger channel for the linear case than for the circular one. Therefore lineic deposited energy must be higher for a linearly-polarized laser pulse because the channel width after $\sim$ 100 ns is mainly dependent on the deposited energy density through the shock wave speed. According to Petit *et al.*, a smaller filament transverse size is observed for a circular polarization due to less effective photoionization processes, resulting in the beam self-focusing over a longer distance than for linear polarization [12]. This gives a smaller plasma section in the circular case and, even though deposited energy density is higher than for linear pulses, a total deposited energy that is less important.

3.1.4 Influence of wavelength

The same comparative study is performed for 5 mJ, 50 fs pulses focused at $f/30$ at both 800 and 400 nm. The corresponding results are displayed in figure 3.12. As it can be seen in 3.12-(a), blue filaments are responsible for the generation of a slightly deeper underdense channel than in the case of infrared filamentation, with a minium recorded density level of 4×10^{24} m^{-3} reached at 10 µs,

that is a density reduction of more than 75% with respect to n_0. This channel also appears larger in the 400 nm case (figure 3.12-(b)).

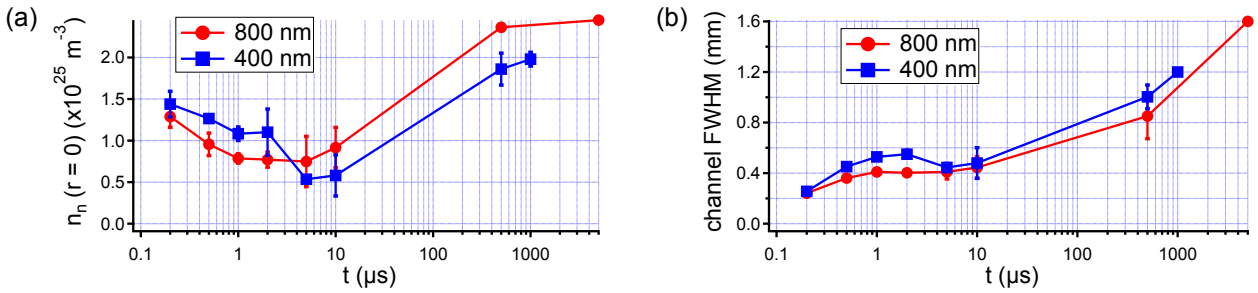

Figure 3.12: Interferometrically recorded on-axis air density $n_n(r = 0)$ (a) and underdense channel FWHM (b) at different times at 800 (red circles) and 400 nm (blue squares). Single filamentation was induced by a 5 mJ, 50 fs laser pulse focused $f/30$.

These results are in good agreement with what was observed by Zhang *et al.* [15]. They characterized the filamentation of focused and collimated 6 mJ, 170 fs pulses at 400 nm, which almost corresponds to the same regime as ours. They found that blue filaments focused at $f/35$ resulted in a $\sim$ 160 µm wide plasma channel with a typical density 2×10^{23} m^{-3}, while infrared filaments had a FWHM of only 110 µm in the same conditions. We can also estimate from the work of Théberge *et al.* that infrared filaments obtained with similar focusing have a density around 10^{23} m^{-3} [6]. Therefore, plasma columns generated by blue filamentation are slightly larger and denser than their infrared counterpart, leading to a more important energy deposition and to deeper and larger underdense channels, as it is observed.

3.1.5 Conclusion on energy deposition in the single filamentation regime

To conclude on the influence of the laser parameters on energy deposition, we saw that the deposited energy increases with the input laser energy. If it becomes locally important enough, initial air temperature can lead to the generation of a shock wave instead of a sound wave, and can reach levels well above 1000 K. Focusing is also an experimental parameter of the utmost importance since it has a crucial influence on both total energy deposition and deposited energy density, with strong focusing giving the best results. The use of short wavelengths apparently gives also more important energy deposition, though we only investigated the cases of 800 nm and of its second harmonic. Finally, linear polarization was shown to be slightly more favorable than circular polarization for laser energy deposition.

3.2 Applications for filamentation-induced hydrodynamics in air: laser-induced optical structures

Filamentation-induced hydrodynamics present several strong advantages that can make them very useful:

- first, as they arise from the air hydrodynamic response following the laser-induced rapid heating, their characteristic timescale ranges from $\sim$ 1 µs for the initial dynamic regime (generation and propagation of density wave), and up to tens of milliseconds in the diffusive

regime (slow resorption of the underdense channel). Such timescales are extremely long with respect to the pump pulse duration, and far longer than previously demonstrated laser-generated optical structures based on the filamentation plasma [16];

- second, they can be remotely generated at distances limited only by the occurrence of filamentation, which can reach 1 km [17].

This is why laser filamentation is so promising for many applications, particularly for the realization of remotely-generated virtual optical structures and of guided electric discharges. The latter case will be thoroughly reviewed in the second part of this Thesis. Therefore we will only focus here on filamentation-induced optical structures.

3.2.1 Single-filament structures

Results presented in the first part of this Chapter unambiguously proved that single filamentation results in the formation of an underdense air channel and of a shock or a sound wave, depending on the initial density of deposited energy. The central underdense channel alone behaves as a negative, diverging lens since it forms a continuous refractive index profile which is lower at the center than at the edge. Its potential use is therefore very limited since applications are looking for a way to guide or locally increase intensity. However, the complete structure formed by the underdense channel and the overdense ridge of the hydrodynamic wave presents interesting features that will be presented in this section.

3.2.1.1 Single-filament waveguides

Waveguiding effect was recently shown to exist in single-filament induced air structures by Lahav *et al.* [18]. In their work, the authors generated a filament by focusing a 1 mJ, 50 fs infrared laser pulse at $f/100$. They then sent a weak green probe pulse with 150 ns duration in the resulting hydrodynamic structure and studied the temporal evolution of its spatial profile at the filament output plane.

Figure 3.13 shows the formation of a ring structure at the center of the spatial profile, of which diameter increases with time while its intensity decreases. The authors explained that the formation of this ring is directly linked to the filamentation-generated sound wave, which presents a higher refractive index than surrounding air and consequently behaves as a converging lens. As the underdense channel is still present, light is expelled from the center while photons propagating close to the sound wave are actually guided and trapped, hence the ring structure. As time goes on, the sound wave amplitude decreases, resulting in a reduced guiding effect. Such a waveguide was shown to support only annular eigenmodes [19], which could prove to be a serious limitation to potential applications.

3.2.1.2 Virtual axicon lens from single filamentation

At the same time at the Laboratoire d'Optique Appliquée, I also investigated the effects of filamentation-induced air structures on the propagation of a ns probe pulse, looking at different positions far after the interaction region. This study was motivated by the insight provided by Wahlstrand *et al.* [2] about the apparent waveguiding effect using single filamentation presented by Levi *et al.* on Arxiv [20], which eventually led to the publication of reference [18].

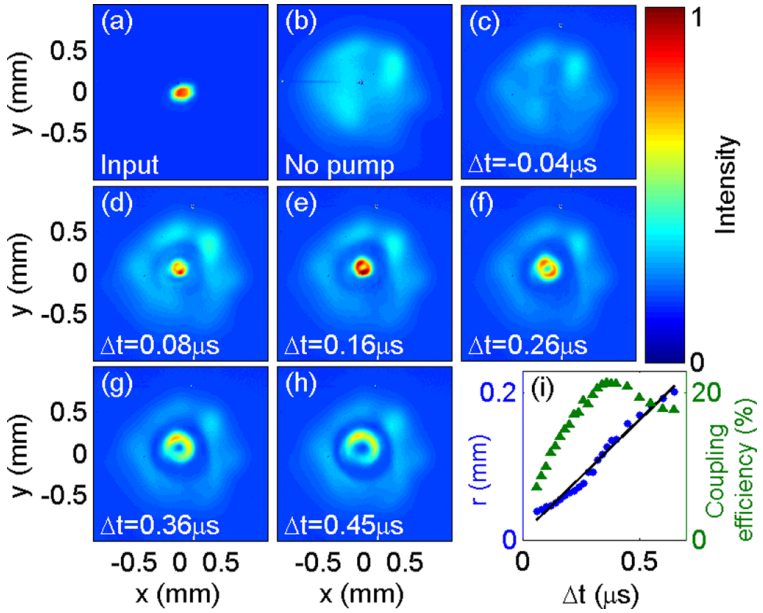

Figure 3.13: Waveguiding effect from a single filament air structure. (a): spatial profile of the probe beam at the entrance of the air structure. (b): spatial profile of the probe beam at the output of the air structure when no filament is generated. (c)-(h): spatial profiles of the probe beam at the output of the air structure at various delays after filamentation occurred. (i): radius of the acoustic wave (blue dots) and coupling efficiency (green triangles) as a function of the delay between the probe and the filament. From Lahav *et al.* [18].

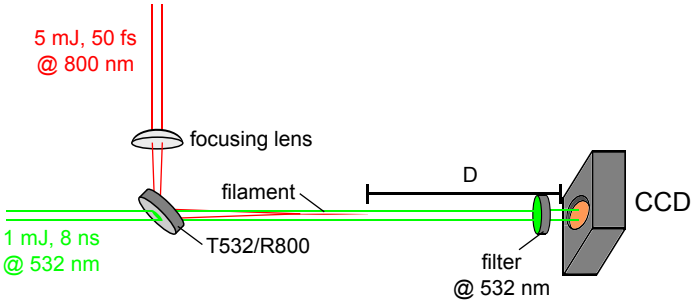

Figure 3.14: Experimental setup used for the demonstration of the filament-generated virtual axicon.

The experimental setup used in this campaign is described in figure 3.14. A filament is generated by focusing a 5 mJ, 50 fs laser pulse at 800 nm. A weak collimated probe beam from a frequency-doubled Nd:YAG ($\sim$ 1 mJ, 8 ns at 532 nm) is sent co-linearly with the pump femtosecond pulse using an adapted dichroic mirror and interacts with filamentation-induced optical structures in the filamentation area. A CCD camera is placed at a distance D after the end of the filament to record the spatial profile of the probe beam. To this purpose, a narrow ($\sim$ 1 nm bandwidth) interference filter at 532 nm is used to cut white light emission from filaments. The delay between the pump and probe pulse is electronically-controlled with a ns precision and jitter, which is far lower than the probe pulse duration. Some results of this experiment using a $f/80$ focusing for the pump beam are displayed in figure 3.15.

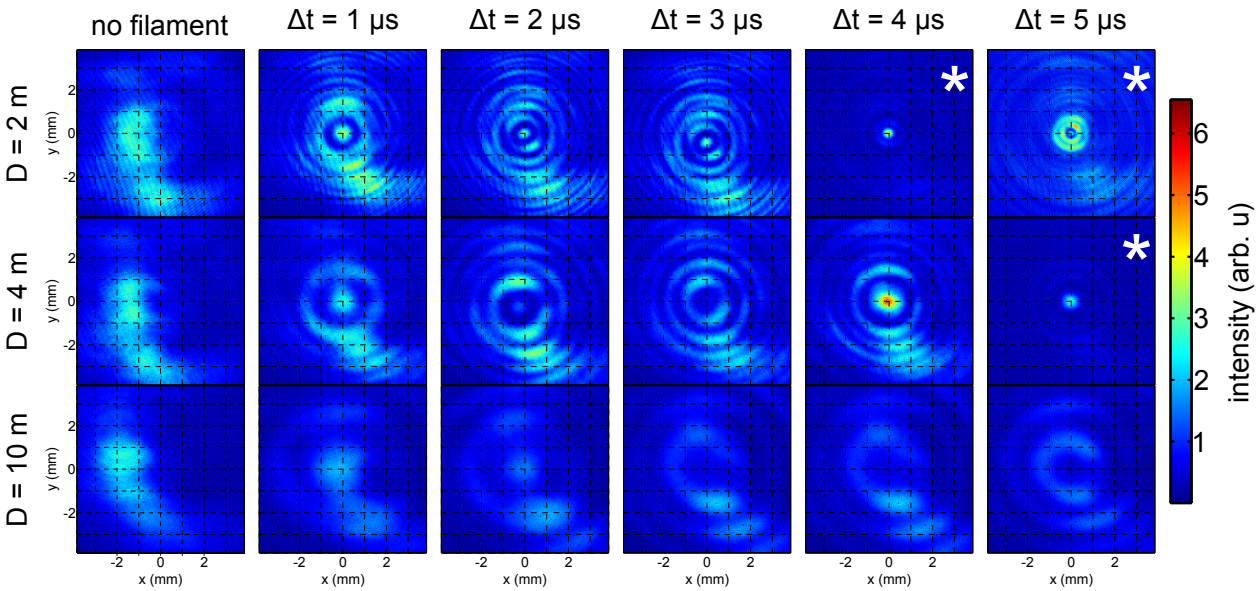

Figure 3.15: Filamentation-generated virtual axicon lens. Presented images are recorded spatial profiles of the probe pulse (1 mJ, 8 ns at 532 nm) at delay Δt and distance D after filamentation. The filament was generated by a 5 mJ, 50 fs pulse at 800 nm focused at $f/80$. All images share the same color scale, except for the three ones marked by a white asterisk, for which the actual intensity level is thrice that of the figure.

This figure gathers probe spatial profiles taken at three different distances D and five delays Δt between the probe and the pump. As a reference, probe spatial profiles when no filament is generated are also given. One can see that probe-filament interaction results in a profound modification of the probe profile, which characteristically displays annular structures reminiscent of the measurements of Lahav *et al.*. However, some also show another interesting feature: an on-axis intensity maximum. This one takes the form of a $\sim$ mm-size central spot with variable intensity. Looking at pictures at a constant delay, e. g. 1 µs, we can clearly see that this central maximum can span several meters, though it clearly broadens along z. As Δt changes, the position and intensity of this on-axis maximum evolves as well, as it seems to be displaced further along z. The maximum on-axis intensity was recorded at $D = 2$ m and $\Delta t = 4$ µs and was 4 times the maximum intensity reached at 2 m without filament, a modest focusing parameter. Because of the transformation imparted to the probe spatial profile, with the formation of a long and weak on-axis maximum surrounded by several rings, we call the optical structure resulting from filamentation a *virtual axicon lens*.

To elucidate the underlying mechanisms of the formation of such spatial profiles, I designed a stationary linear propagation code to simulate the propagation of the probe beam. This code is based on the paraxial Beam Propagation Method developed by Feit and Fleck in 1978 [21]. Filamentation-induced optical structures were reconstructed using experimental characterization of laser-induced hydrodynamics. Interferometry was used to record air refractive index distributions in the focal zone where hydrodynamics are stronger. Longitudinal distribution for the strength of the hydrodynamic response was estimated using a side photograph of the plasma luminescence, yielding a normalized z-window (cf. figure 3.9). Consequently, 3-D spatial distribution for the refractive index at a given time was built correlating the z position with the deepest underdense

air channel with the global maximum of the z-window. The real initial probe beam spatial profile was used as the code input. Results of these simulations in the case of a pump pulse focused at $f/55$ are given in figure 3.16.

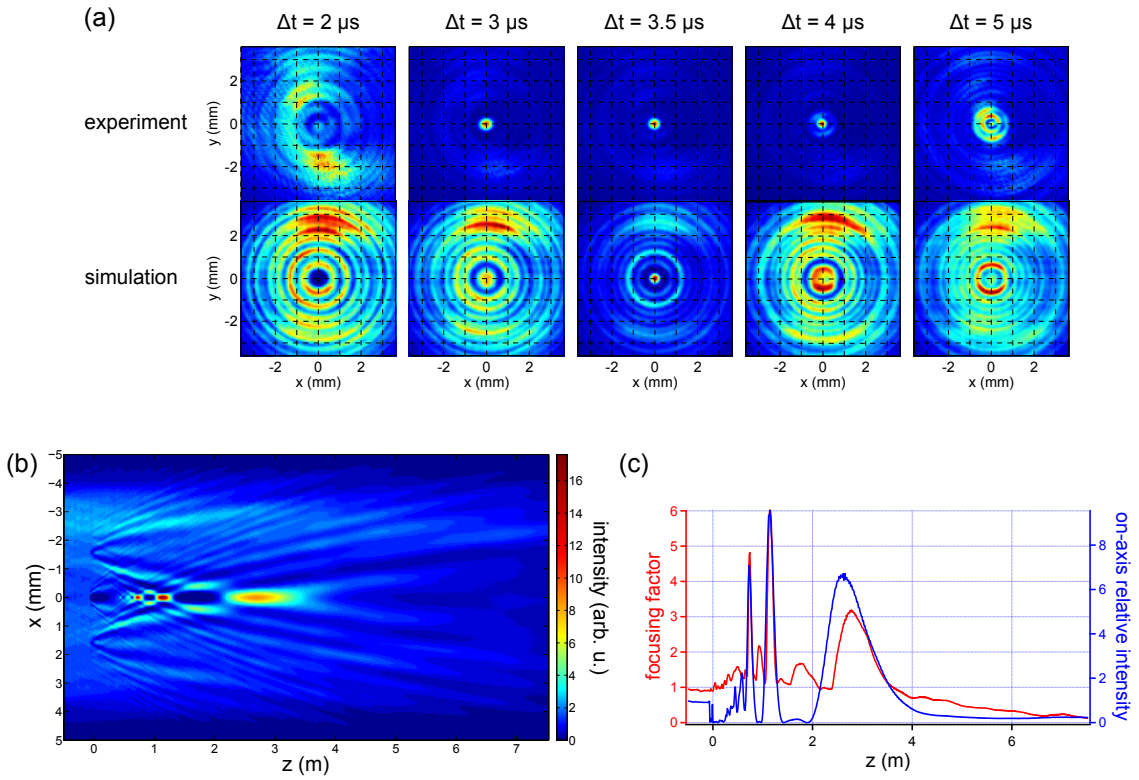

Figure 3.16: (a): comparison between experimental and simulated probe intensity spatial profiles taken at position $D = 2.12$ m for five different delays Δt. Filamentation was generated by a 5 mJ, 50 fs pulse at 800 nm focused at $f/55$. (b): simulated probe intensity distribution in the (x,$y = 0$,z) plane at delay $\Delta t = 4$ μs. (c): axial evolution of the focusing factor (red) and of the on-axis relative intensity (blue).

Figure 3.16-(a) compares experimental and simulated probe intensity profiles at a fixed position $D = 2.12$ m and different delays Δt. The overall agreement is good: an on-axis maximum appears and disappears simultaneously in both cases with a strong maximum reached at 3.5 μs. Moreover, accordance between ring shape and diameter is excellent. The only major discrepancy comes from a different intensity distribution between the rings, energy being much more focused at the center in the experiment than in the simulation, despite the fact that the real probe beam spatial profile was used as the input profile. It could come from a wrong estimate of the position of the filament with respect to the probe spatial profile, which does not have a cylindrical symmetry (see, e. g., the spatial profiles without filament in figure 3.15), but also from the total lack of information about the initial phase of the beam.

Figure 3.16-(b) gives the full simulated intensity profile for the probe in the (x,$y = 0$,z) plane over more than 7 m. Such a profile brings very interesting information: right after interacting with the filamentation-induced structure, the probe forms a characteristic ringed profile with a central hole, all the light having been expelled from the center by the underdense air channel. Meanwhile, light that interacted with the hydrodynamic wave around $x = \pm 1.5$ mm is focused back to the axis.

Interference between this refocused light and the expelled light gives birth to the complex measured probe profiles, with the appearance of several on-axis maxima. In this case, the final one, which is also the weakest, spans more than 1 m up to $D \approx 3.5$ m before leaving a central dark spot.

To assert the strength and quality of light focusing by the virtual axicon, we designed two parameters. The first one, called the focusing factor, corresponds to the ratio at a given z position between the maximum intensity in the (x,y,z) plane in presence of the filament and the maximum intensity in the same plane without filament (i. e. after propagation in free air). The second parameter, called on-axis relative intensity, is defined as the quotient of on-axis intensity in presence of a filament over on-axis intensity when no filament was formed. These two parameters are plotted in figure 3.16-(c). Before the filament ($z < -7$ cm), both parameters are equal to 1. After interacting with the filament-induced structure, the probe yields a global focusing factor > 1, meaning that peak intensity is higher in presence of the filament, with the presence of marked focusing regions with a maximum reached focusing factor equal to 6. As for the on-axis relative intensity, it globally remains below 1, that is even if an increase in intensity is witnessed, it does not occur at the center. We however see that the three marked focusing factor maxima also correspond to on-axis relative intensity maxima, meaning that optimum focusing is observed on the propagation axis. It is worth mentioning that even using a stronger focusing for filament generation ($f/55$ instead of $f/80$), the maximum observed focusing factor only increased from 4 (figure 3.15) to 6. Our virtual axicon can therefore be described as *weakly-focusing*.

To conclude on our filamentation-generated virtual axicon, it presents the two qualities described at the beginning of this section, that is it can be remotely-generated at arbitrary distances, and is also long-lived, with a typical optimal temporal window of several microseconds. However, it is for now only able to weakly focus, with only an order of magnitude higher intensity at the output. Though promising, this technology asks for an optimization of experimental parameters.

3.2.2 Multiple-filament structures

A hydrodynamic structure from a single filament is only able to provide waveguiding for peculiar eigenmodes with a doughnut shape. This is a serious limitation for any applications. A way to overcome this problem is to arrange several filaments in a layout that will provide an appropriate guiding effect for any spatial profile. This was recently demonstrated by Jhajj *et al.* using a four-filament structure [22].

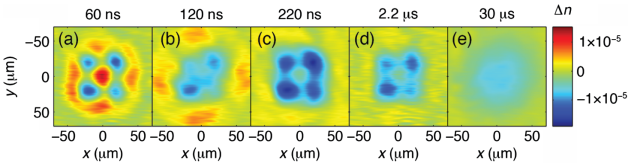

Figure 3.17: Interferometrically-recorded air refractive index profiles in the case of a four-filament structure, showing two different waveguiding structures. At short times (a), intersecting sound waves from each single filament form an on-axis refractive index maximum and provides guiding in the so-called *acoustic guide regime*. At longer times ((c) and (d)), underdense channels from each filament form a "moat" surrounding a central spot with normal air density, a structure that can persist for microseconds. This is called the *thermal guide regime*. From Jhajj *et al.* [22].

Starting from a Gaussian femtosecond beam, the authors used a double half-pellicle system

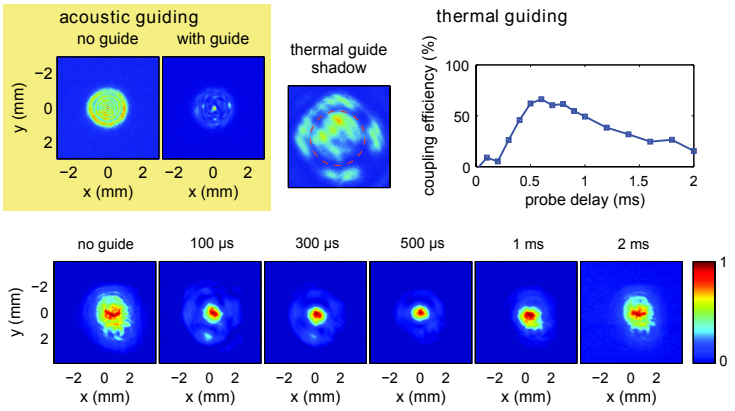

Figure 3.18: Demonstration of guiding of 7 ns, 532 nm pulses in 70 cm-long acoustic and thermal air waveguides produced by a four-filament. The panel in the upper left shows the probe beam, which is imaged after the filamentation region, with and without the filament. The time delay of the probe was 200 ns, which is in the acoustic guiding regime. The effect of the thermal waveguide, the shadow of which can be seen in the image in the top center (with a red dashed circle showing the position of the lower-density moat), is shown in the bottom row, where the probe beam is imaged after the exit location of the air waveguide with and without the filamenting beam. The coupling efficiency vs injected pulse delay is shown in the upper right. Peak energy guided was 110 mJ. From Jhajj *et al.* [22].

to generate a Hermite-Gauss TEM_{11} mode presenting four characteristic lobes symmetric with respect to the center of the beam. Focusing this beam yielded a four-filament structure with well controlled spacing. This in turn generated a characteristic air hydrodynamic response highlighting two potential waveguide regimes (figure 3.17): a short-lived acoustic regime occurring early after filamentation, and a long-lived thermal regime, of which lifetime is determined by the thermal diffusion time of the underdense channels and can therefore last up to milliseconds.

Injecting a probe pulse from a frequency-doubled, ns Nd:YAG laser in this air structure results in the guiding of the beam. Waveguiding effect over 70 cm was demonstrated both in the acoustic and thermal regime (figure 3.18). The authors report a single mode guiding with peak efficiency of over 50 %. Moreover, this virtual waveguide was shown to provide guiding of large average power beams well below the appearance of detrimental nonlinear effects such as self-focusing or stimulated Raman scattering. It is also resilient with respect to thermal blooming. It is worth mentioning that the same group also demonstrated eight-lobed filament structures using a Laguerre-Gauss LG_{04} spatial mode for their femtosecond laser pulse [2].

Conclusion

Concluding on energy deposition in air from single filamentation, we showed that actual deposited energy strongly depends on experimental parameters. Optimizing energy deposition by use of an initial high-energy laser pulse which is strongly focused leads to initial air heating in excess of 1000 K, giving birth to cylindrical shock waves instead of sound waves, and to significantly deeper underdense air channels that can last for more than 90 ms. Applications for such single-filamentation induced air structures revolve around remotely generated and long-lived optical structures for light control. Single-filamentation itself behaves as a waveguide of which eigenmodes are annular. This guiding effect is only supported by the sound/shock wave resulting from energy deposition [19]. It was also shown to result in the formation of very peculiar, ringed spatial profiles far after the interaction region. These profiles exhibit several on-axis intensity maxima that span several meters, and with a typical maximum intensity ~ 10 times higher than in absence of the filamentary structure. This *virtual axicon* is currently under development at LOA. Finally, a potential and promising application for our high-energy filamentation-induced hydrodynamics would be to use them in more traditional waveguides using multi-filament structures, particularly four and eight-lobed femtosecond beams using a Hermite Gauss TEM_{11} and a Laguerre-Gauss LG_{04} spatial mode, respectively, as demonstrated by the Milchberg research group.

Bibliography

[1] K. Lim, M. Durand, M. Baudelet, and M. Richardson, Scientific Reports **4**, 7217 (2014).

[2] J. K. Wahlstrand, N. Jhajj, E. W. Rosenthal, S. Zahedpour, and H. M. Milchberg, Optics Letters **39**, 1290 (2014).

[3] E. W. Rosenthal, J. P. Palastro, N. Jhajj, S. Zahedpour, J. K. Wahlstrand, and H. M. Milchberg, Journal of Physics B **48**, 094011 (2015).

[4] Y.-H. Cheng, J. K. Wahlstrand, N. Jhajj, and H. M. Milchberg, Optics Express **21**, 4740 (2013).

[5] E. F. Toro, *Riemann Solvers and Numerical Methods for Fluid Dynamics* (Springer, Berlin, Heidelberg, Germany, 2009).

[6] F. Théberge, W. Liu, P. T. Simard, A. Becker, and S. L. Chin, Physical Review E **74**, 036406 (2006).

[7] D. G. Papazoglou and S. Tzortzakis, Applied Physics Letters **93**, 041120 (2008).

[8] P. P. Kiran, S. Bagchi, C. L. Arnold, S. R. Krishnan, G. R. Kumar, and A. Couairon, Optics Express **18**, 21504 (2010).

[9] M. Kolesik, J. V. Moloney, and E. M. Wright, Physical Review E **64**, 046607 (2001).

[10] G. Fibich and B. Ilan, Physical Review E **67**, 036622 (2003).

[11] J.-C. Diels, J. Yeak, D. Mirell, R. Fuentes, S. Rostami, D. Faccio, and P. di Trapani, Laser Physics **20**, 1101 (2010).

[12] S. Petit, A. Talebpour, A. Proulx, and S. L. Chin, Optics Communications **175**, 323 (2000).

[13] B. Zhou, A. Houard, Y. Liu, B. Prade, A. Mysyrowicz, A. Couairon, P. Mora, C. Smeenk, L. Arissian, and P. Corkum, Physical Review Letters **106**, 255002 (2011).

[14] S. Mitryukovskiy, Y. Liu, P. Ding, A. Houard, and A. Mysyrowicz, Optics Express **22**, 12750 (2014).

[15] Z. Zhang, X. Lu, T.-T. Xi, W.-X. Liang, Z.-Q. Hao, Y. Zhang, M.-L. Zhou, Z.-H. Wang, and J. Zhang, Applied Physics B **97**, 207 (2009).

[16] J. Wu, H. Cai, H. M. Milchberg, and H. Zeng, Physical Review A **82**, 043431 (2010).

[17] M. Durand, A. Houard, B. Prade, A. Mysyrowicz, A. Durécu, B. Moreau, D. Fleury, O. Vasseur, H. Borchert, K. Diener, R. Schmitt, F. Théberge, M. Chateauneuf, J.-F. Daigle, and J. Dubois, Optics Express **21**, 26836 (2013).

[18] O. Lahav, L. Levi, I. Orr, R. A. Nemirovsky, J. Nemirovsky, I. Kaminer, M. Segev, and O. Cohen, Physical Review A **90**, 021801 (2014).

[19] N. Jhajj, J. K. Wahlstrand, and H. M. Milchberg, Optics Letters **39**, 6312 (2014).

[20] L. Levi, O. Lahav, R. A. Nemirovsky, J. Nemirovsky, I. Orr, I. Kaminer, M. Segev, and O. Cohen, Arxiv:1307.3588 (2013).

[21] M. D. Feit and J. A. Fleck, Applied Optics **17**, 3990 (1978).

[22] N. Jhajj, E. W. Rosenthal, R. Birnbaum, J. K. Wahlstrand, and H. M. Milchberg, Physical Review X **4**, 011027 (2014).

Chapter 4

Energy deposition in the multifilamentation regime

Contents

Introduction

This Chapter is dedicated to the study of energy deposition in the high-energy regime, giving birth to multifilamentation. In this high-energy limit, the beam breaks up into many co-propagating filaments early during propagation, and therefore results in laser energy being lost over a large distance and in an uncontrolled way, since multifilamentation is essentially a stochastic process (see Chapter 1, section 1.3.3.5). Optimizing energy deposition in a well defined area therefore asks for the study of the multifilamentation regime to somehow control multifilamentation spatial distribution. The first part of this Chapter focuses on this study in the very-high energy limit ($P \sim 100P_{cr}$) using moderate focusing ($f/165$). Energy deposition in this regime is then thoroughly studied by means of the diagnostics described in Chapter 2 and already implemented on high-energy single filaments (Chapter 3).

4.1 Study of multifilamentation in the high energy regime

Studied multifilament bundles were generated by a 200 mJ laser pulse at 800 nm using the Ti:sapphire laser chain "ENSTAmobile" (cf. Annex B). Due to constraints put on optical elements, pulse duration was adjusted to 175 fs, yielding a peak power $P = 1.1$ TW $\approx 230 P_{cr}$. We used a 5 m focusing lens which, in our case, corresponds to a $f/165$ focusing, that is a relatively weak one. Resulting multifilamentation spans roughly 4 m, starting $\sim$ 2.5 m after the lens. We first investigated the structure of the filament bundle, and later used a spectroscopic study for laser-induced plasma characterization. Finally, numerical simulations of the propagation of the pulse were done, yielding good agreement with experimental results.

4.1.1 Structure of the multifilament bundle

The main diagnostic used for characterization of the spatial distribution of the multifilament bundle is single-shot darkening of photographic plates. This simple technique consists in impacting a single laser pulse undergoing filamentation at a given z-position on a pre-insolated photographic paper (in our case a Fujifilm Fujibro WP FM2 black and white paper) to record the transverse intensity distribution of the pulse. Typically, the photographic paper has a high reaction intensity threshold, meaning that only the most intense parts of the laser pulse are actually captured. However, as shown by Méchain *et al.* [1], this threshold lies under air ionization threshold since filaments leave a characteristic circular burn pattern on the paper (see figure 4.1-(a)). Therefore this diagnostic enables us to track the appearance of filaments. We recorded such imprints every 2 cm along the beam propagation direction z, $z = 0$ defining the lens position. We could then build a 3-D reconstruction of the beam undergoing multifilamentation. A longitudinal projection of this reconstruction in the $(x = 0, y, z)$ plane is displayed in figure 4.1-(b).

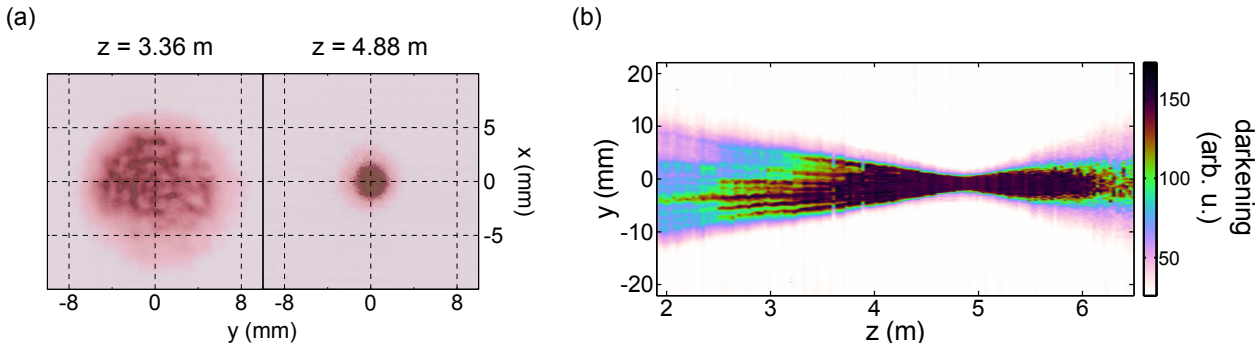

Figure 4.1: Experimental investigation of the structure of the multifilament bundle. (a): examples of laser impacts on photographic papers at two different propagation distances, showing burn patterns characteristic of filaments. (b): reconstructed intensity map in the $(x = 0, y, z)$ plane using these impacts. Here, the position $z = 0$ corresponds to the position of the lens.

As seen in this figure, the first filaments (appearing as dark channels) appear around $z = 2.5$ m. They multiply and converge under the focusing action of the lens. It is worth mentioning that short scale filaments can clearly be identified although imprints were recorded in the single-shot regime. This proves that in our case the appearance of multifilaments is a deterministic process, and not a stochastic one. We explain this phenomenon by the fixed amplitude and phase distortions imparted to the pulse spatial profile in the laser chain itself. A major shortcoming of this first diagnostic

comes from its low intensity saturation threshold. As multifilaments converge and get closer to each other when propagating towards the lens focus, it becomes impossible to distinguish them individually, yielding an homogeneously burned central spot surrounded by a lower intensity region (see the impact taken at $z = 4.88$ m in figure 4.1-(a)). This occurs after $z = 4.15$ m, where 45 filaments could be recorded. Consequently, we were unable to resolve any structure in the focal zone because of the saturation of photographic paper.

To address this problem, we shifted to another diagnostic: space-resolved pictures of plasma luminescence by means of a time-gated intensified CCD camera (model PI-MAX from Princeton Instruments). The camera was equipped with a 4× microscope objective, bringing its spatial resolution to 5 µm, together with a Schott BG39 colored filter meant to isolate plasma luminescence spectrum between 300 and 450 nm. Thus equipped, we recorded single-shot, transverse pictures of the multifilament bundle in the focal zone with a field of view on the order of 1 mm (see figure 4.2).

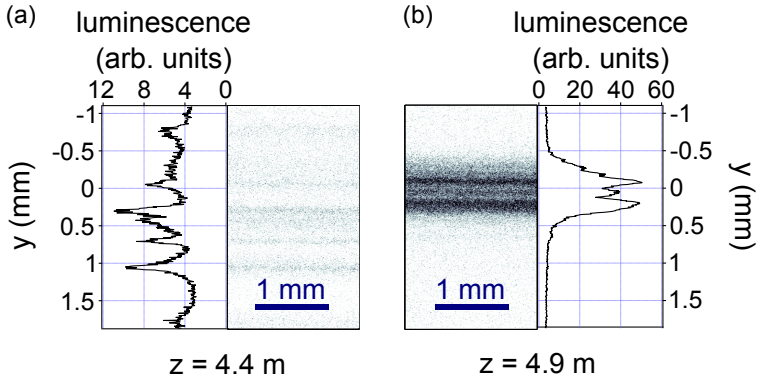

Figure 4.2: Side-view iCCD pictures of the plasma filaments centered at $z = 4.4$ m (a) and $z = 4.9$ m (b). Corresponding 1-D luminescence profiles are obtained by integrating 2-D pictures along z.

On the picture taken at $z = 4.4$ m (figure 4.2-(a)), that is beyond the point where photographic paper saturates, we can clearly see short-scale filaments distinct from each other, with a FWHM on the order of 70 µm. This size corresponds well to filaments generated with a $\sim f/150$ focusing (see figure 3.8 in Chapter 3). We therefore expect these multifilaments to have an accordingly standard electron density, that is around 10^{22} m^{-3} in these focusing conditions.

The picture is clearly different at $z = 4.9$ m (cf. figure 4.2-(b)). At this point, the well-differentiated short-scale filaments have been replaced by a large channel with a 540 µm FWHM. Still, this channel exhibits an internal structure with, in this case, three distinct luminescence maxima. As luminescence is related to ionization, plasma in the focal zone is more akin to a large ionized region with localized, denser areas than distinct ionized channels as it was the case before the focal region. Moreover, peak luminescence is recorded to be almost an order of magnitude higher in the focal region than in short-scale filaments.

4.1.2 Laser-induced plasma characteristics

A major drawback of the iCCD diagnostic we implemented is its lack of spectral resolution, preventing us from linking directly luminescence to plasma parameters. We consequently shifted to a spectroscopic analysis of the laser-induced plasma. Since we are now in the high-energy multifilament regime, we cannot straightforwardly use the diagnostic described in Chapter 2 (section 2.3.4), particularly because we do not know yet if the plasma emission spectrum in the focal zone

is similar to that of single filaments. To this purpose, we recorded this spectrum at $z = 4.9$ m with a ~ 1.5 nm resolution. This spectrum is plotted in figure 4.3.

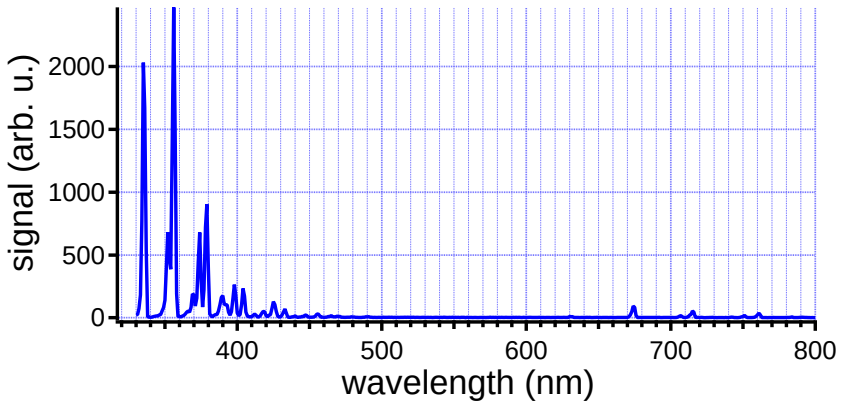

Figure 4.3: Emission spectrum of the laser-induced plasma in the focal zone ($z = 4.9$ m).

As seen on the previous figure, the spectrum is dominated by emission lines from the second positive system of N_2 and the first negative system of N_2^+, that already characterized emission from single filaments [2]. It also exhibits a negligible continuum contribution, proving that even in the focal zone, the plasma is relatively cold. From this analysis we conclude that emission from the first negative system of N_2^+ can still be used as a plasma diagnostic in our case. However, we have to be careful in interpreting the results because we are now in the multifilament regime. Luminescence signal L and electron density are linked by the integral relation:

$$L(z) \propto \int_{\mathbb{R}^2} n_e(r,\theta,z)\ r\mathrm{d}r\mathrm{d}\theta. \tag{4.1}$$

Now, since the number of filaments evolves in z, we can no longer assume a constant plasma transverse size, which previously enabled us to link $L(z)$ and the peak electron density $n_{e,max}(z)$.

We can overcome this difficulty by extracting plasma transverse section from impacts on photographic plates using an appropriate cutoff gray level, since this diagnostic reliably indicates the occurrence of ionization. It then becomes possible to evaluate a surface-averaged plasma density defined as:

$$\overline{n_e}(z) = \frac{1}{S(z)} \int_{\mathbb{R}^2} n_e(r,\theta,z)\ r\mathrm{d}r\mathrm{d}\theta \propto \frac{L(z)}{S(z)}, \tag{4.2}$$

$S(z)$ being the plasma section at position z. Recording luminescence signal from the first negative system of N_2^+, in our case at 428 nm, along z therefore enables us to extract the axial evolution of $\overline{n_e}$. These results are plotted in figure 4.4.

Three distinct regions can be defined from the graph displaying $\overline{n_e}(z)$ (figure 4.4-(b)). The first one, up to $z \sim 4.5$ m, is characterized by a very slow rise of electron density. This behavior can be explained by the clamping of intensity inside short-scale filaments that are sufficiently far one from another to be considered as independent. iCCD pictures confirm this is still the case at $z = 4.4$ m (figure 4.2-(a)). The second zone sees the quick rise of $\overline{n_e}$, reaching a maximum value around $z = 4.9$ m. This position lies within 5 % of the collapse distance given by the Marburger formula in the case of a Gaussian pulse (equation (1.69)). Although this formula is not really accurate in the multifilamentation regime, it gives an estimate of the position where most of the laser energy

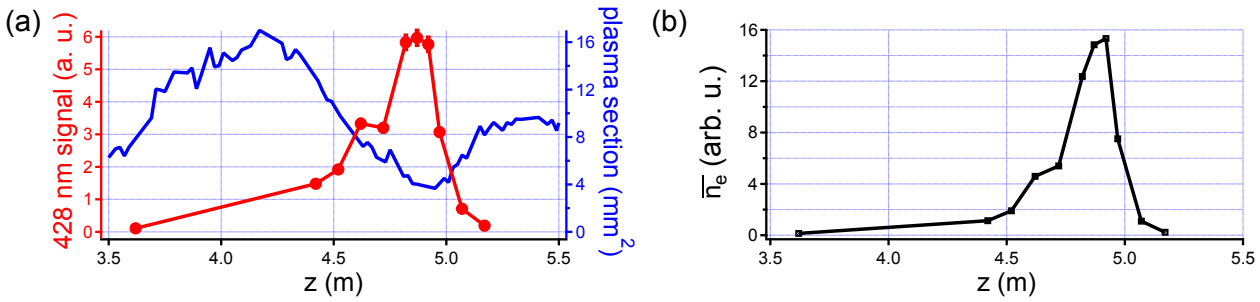

Figure 4.4: (a): evolution of plasma luminescence from the first negative system of N_2^+ (red circles) and of plasma transverse surface (blue squares) with z. (b): evolution of the surface-averaged electron density $\overline{n_e}$ along z.

will tend to concentrate during a full beam collapse process. The maximum average plasma density culminates at about 15 times the plateau level of the previous region. Finally, once the linear focus at $z = 5$ m is reached, the L/S ratio quickly falls, marking the end of the dense plasma region.

We therefore showed that there is a ~ 50 cm long region where $\overline{n_e}$ is significantly higher than in short-scale filaments. We measured the laser focal spot in the linear regime to be 112 µm. It corresponds to a Rayleigh length of 4.9 cm, ~ 10 times shorter than the dense plasma region. Assuming such an average density in multifilaments to lie between 10^{21} and 10^{22} m^{-3}, that is the expected density at moderate focusing $f/150$ (see figure 3.8), then the reached peak density is on the order of 10^{23} m^{-3}, a value that is normally recorded only using tighter focusing. This high-density plasma takes the form of an uniformly-ionized area presenting few structures displaying an even higher density, as evidenced by figure 4.2-(b). These structures are called *superfilaments* [3] because of the properties they share with standard filaments while resulting in a plasma significantly denser.

4.1.3 Numerical simulations

We simulated the propagation of our laser pulse to extract more information about *superfilaments*. As we are now in the multifilament regime, the beam no longer has a cylindrical symmetry, meaning that the full characterization of the propagation can only rigorously be recorded using a full 3-D plus time simulation, which is particularly cumbersome and time-intensive. To this purpose, a special time-independent fast code was developed by Vytautas Jukna, enabling us to run several simulations with different input parameters to try to get the best match with experimental data. Starting back from the equation system (1.124), we start to neglect any contribution from group velocity and group velocity dispersion, since we consider a time-independent configuration. Likewise, Raman contribution to the nonlinear refractive index is neglected. Finally, the propagation equation for the electric field envelope $\mathcal{E}$ is given by:

$$\begin{aligned}\partial_z \mathcal{E}(\vec{r}) =& \frac{i}{2k_0}\Delta_\perp \mathcal{E}(\vec{r}) + ik_0 n_2(\vec{r})|\mathcal{E}(\vec{r})|^2\mathcal{E}(\vec{r}) \\ &- \left(\frac{\beta_K}{2}|\mathcal{E}(\vec{r})|^{2K+1} + \frac{\sigma_{iB}(\omega_0)n_e(\vec{r})}{2}\left(1 + i\frac{\omega_0}{2\pi\nu_c}\right)\right)\mathcal{E}(\vec{r}).\end{aligned} \tag{4.3}$$

In this equation, we used a reduced electric field envelope expression so that the intensity $I = |\mathcal{E}|^2$. We chose $K = 8$, corresponding to the multiphoton absorption ionization regime in the case

of molecular oxygen. We used $n_2 = 2 \times 10^{-23}$ m$^2 \cdot$ W^{-1}, $\beta_8 = 8 \times 10^{-124}$ m$^{13} \cdot$ W^{-7}, $\sigma_{iB} = 5.6 \times 10^{-24}$ m^2 and $1/2\pi\nu_c = 350$ fs.

Equation (4.3) was solved by means of a split-step technique [4]. It involves a first step performed in the Fourier spatial frequency space (k_x,k_y) to account only for diffraction. A second step in the direct (x,y) space, accounts for amplitude and phase changes due to nonlinear terms. Because of the absence of temporal dynamics in our modeling, the presence of plasma is accounted for by mapping the intensity to the electron density generated by optical field ionization and avalanche at the temporal center of a 175 fs Gaussian pulse with peak intensity I. Simulations are initialized with noise levels of 10 % in intensity and 0.2 % in phase with a Gaussian spatial distribution, mimicking experimental input beam irregularities, triggering modulational instability and the subsequent multifilamentation. The spatial resolution was 6.2 µm in the transverse plane and 2.5 mm along z, which is sufficient to resolve short-scale filamentary structures in a reasonable computational time.

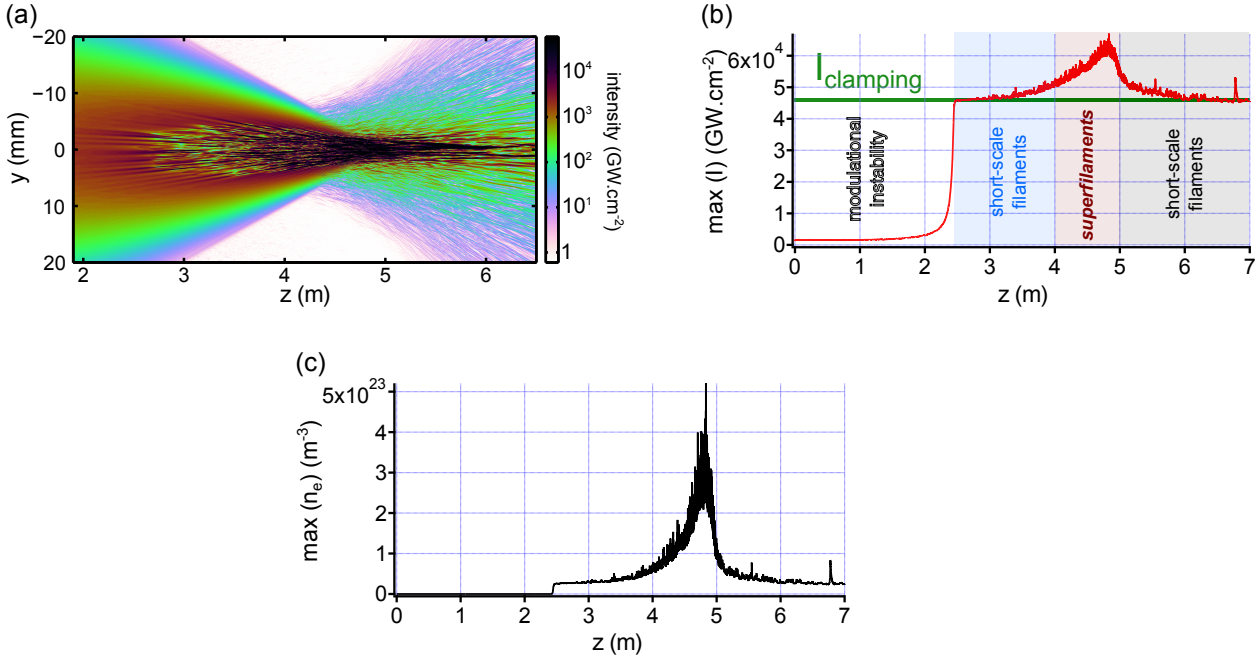

Figure 4.5: Simulated evolution of the multifilament bundle. (a): side view of the intensity map in the ($x = 0$,y,z) plane. (b): evolution of the maximum intensity in the transverse (x,y) plane along z. (c): same as (b) for the electron density.

Results of simulations are presented in figure 4.5. Figure 4.5-(a) displays the same intensity side view as figure 4.1-(b). A logarithmic color scale was chosen to mimic the response of the photographic paper. Even without taking a saturation effect into account, simulation and experiment show good agreement with respect to the beam shape, waist at the nonlinear focus, and the observation of only few filaments past $z = 6$ m.

Figures 4.5-(b) and 4.5-(c) give, respectively, the simulated maximum intensity and electron density recorded in the transverse (x,y) plane. Both values are very low before the onset of multifilamentation, which takes place around $z = 2.5$ m, similarly to the experiment. These short-scale filaments present typical intensity and plasma density clamping values ($I \sim 4.5 \times 10^{17}$ W $\cdot$ m^{-2} and $n_e \sim 2.5 \times 10^{22}$ m^{-3}). From $z = 3.5$ m, peak intensity and electron density start to rise slowly, eventually reaching maximum values of $I = 6.2 \times 10^{17}$ W $\cdot$ m^{-2} and $n_e = 4 \times 10^{23}$ m^{-3}. These

results correspond, respectively, to 1.4 and 16 times the clamping values. More specifically, figure 4.5-(c) compares well with the experimental curve (figure 4.4-(b)).

Therefore, numerical simulations give results that are in excellent agreement with experimental data, both qualitatively and quantitatively, confirming the existence of a ~ 50 cm long zone where filamentation results in significantly denser plasma channels.

4.1.4 Physical mechanisms involved

This study showed that moderately focusing a very powerful laser pulse leads first to the formation of short-scale filaments before the full beam could collapse. This breaking down mechanism results from strong noise initially present in our laser beam, but could also result from modulational instability. As in our case the peak power is above $200P_{cr}$, the appearance of such multifilaments was expected because we are clearly above the threshold of $\sim 100P_{cr}$ identified by Fibich *et al.* for the transition between initial multifilamentation and full beam collapse [5]. These multifilaments are initially widely spread but converge under the spherical phase imposed by the lens. This leads to multiple inter-filament interaction. Such interaction in the case of two filaments was shown to give rise to spectacular effects such as fusion, repulsion, energy redistribution or spiral motion of filaments, depending on their relative optical phase [6, 7, 8]. Bringing together several tens of filaments in the focal zone then must result in a complete redistribution of intensity in the transverse plane. It also leads to a decreased plasma defocusing effect because the local electron density gradients are reduced, smoothed by the large number of filaments close one to the others. Finally, the focusing action of the lens brings a lot of energy from the periphery to the propagation axis. This excess energy cannot be efficiently balanced by nonlinear losses and, therefore, results in the rise of intensity. All these factors lead to the emergence of *superfilaments* in the focal zone, that is few filamentary structures generating dense plasma.

The two main factors leading to the generation of *superfilaments* are, on the one hand, a pulse peak power high enough to promote the initial beam breakdown into many short-scale filaments and, on the other hand, a focusing strong enough to ensure a sufficient energy input in the focal zone. This would still result in an dense plasma region larger than the Rayleigh length, even in the case of extreme focusing conditions [9]. In this case however, the superfilamentary area will be limited to a mm-scale. For practical reasons, it is better to use weaker focusing, yielding a slightly less dense plasma, but significantly longer, as in our case where *superfilaments* spanned 50 cm. We will now study this propagation regime more thoroughly in terms of energy deposition.

4.2 Characterization of energy deposition in the multifilament regime

In this section, we study energy deposition in air from filamentation at the 100 mJ level, with peak powers in excess of $300P_{cr}$. Focusing conditions are typically tighter than the $f/165$ one used in the previous section, leading to energy deposition occurring within a smaller volume, yielding higher energy densities and eventually stronger hydrodynamic reactions. We first look at the influence of various experimental parameters on the global energy deposition in order to select the best conditions for optimum energy transfer. Then, we systematically investigate the mechanisms and effects of this energy transfer in these conditions.

4.2.1 Optimization of energy deposition

4.2.1.1 Influence of the laser pulse energy

We start in the same focusing conditions as we already used in Chapter 3, that is a relatively strong focusing at $f/30$ which, in our case, corresponds to a 1 m focal length. We first study the evolution of energy deposition with input energy using a Joule meter (see Chapter 2, section 2.3.1). We could use up to 165 mJ in this experimental configuration, with a pulse duration set at the minimum (50 fs), meaning we could reach a maximum peak power $P = 330P_{cr}$. Results are displayed in figure 4.6.

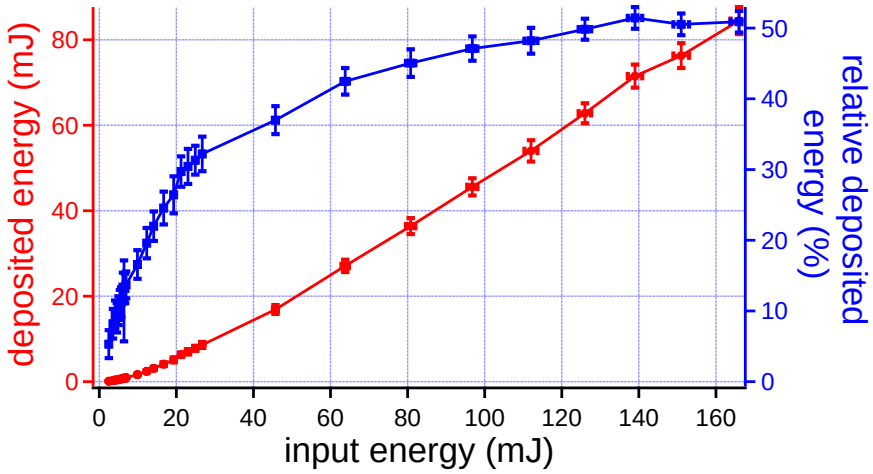

Figure 4.6: Evolution of the measured deposited laser energy (red circles) and of relative deposited energy E_{dep}/E_{in} (blue squares) with input laser energy. Filamentation was generated by a 50 fs laser pulse at 800 nm focused at $f/30$. Error bars correspond to a confidence interval of one standard deviation evaluated over 500 shots.

In this figure, we can see that deposited energy logically increases with an increasing input energy. This evolution becomes quasi linear at higher laser energies. More interesting, we also plotted the evolution of the relative deposited energy, that is the ratio of the deposited energy E_{dep} over the input energy E_{in}. This graph can be roughly divided in three parts: the first one, up to $E_{in} \approx 20$ mJ, is characterized by a very steep increase in relative deposited energy, which already reaches more than 25 % at this point. Past this input energy, relative deposited energy still increases, but much more slowly. Eventually, beyond $E_{in} \approx 140$ mJ, relative deposited energy saturates slightly above 50 %. The transition observed around 20 mJ, that is a peak power $P \approx 40P_{cr}$, could be linked to the threshold between full beam collapse and generation of multifilaments before the nonlinear focus described by Fibich *et al.* [5]. It would means that as soon as the beam breaks up into short-scale filaments before the focal zone, increasing input energy leads to a redistribution of this energy over many competing filaments, only slightly increasing the deposed energy for each of them. Conversely, as long as only one filament is concerned, any increase in energy will be channeled through this single structure and lead to a dramatically stronger energy deposition. Above 140 mJ, the saturation of the relative deposited energy means that roughly half of the laser energy will be absorbed and eventually converted into heat, an impressive conversion factor in itself.

4.2.1.2 Influence of the pulse duration

Influence of the laser pulse duration, that is of the peak power, on energy deposition was investigated by fixing input energy and focusing conditions and by misaligning the laser compressor, imparting temporal chirp to the pulse. The compressor was previously calibrated by means of auto-correlation techniques, enabling us to know precisely to which pulse duration corresponds the position of one of the gratings in the compressor. Deposited energy could then be measured using our Joule meter for different values of the pulse duration.

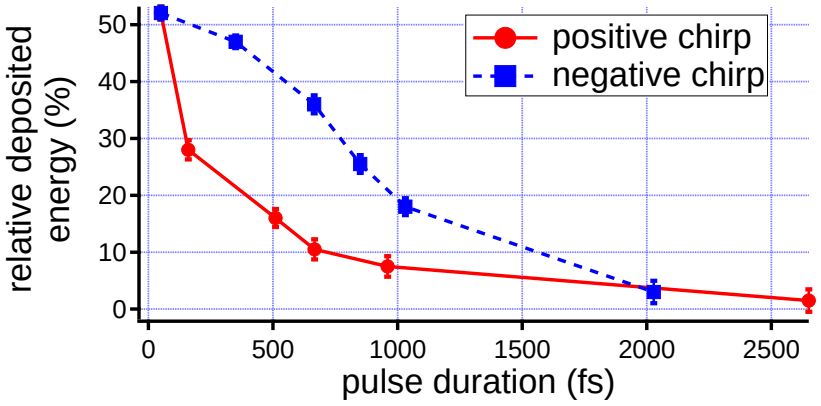

Figure 4.7: Evolution of the measured relative deposited laser energy with pulse duration in the case of a positive (red circles) or negative chirp (blue squares). Filamentation was generated by a 200 mJ, 50 fs laser pulse at 800 nm focused at $f/30$. Error bars correspond to a confidence interval of one standard deviation evaluated over 500 shots.

Results displayed in figure 4.7 are unambiguous: pulse duration seems to be a very sensitive parameter. As soon as it deviates from the minimum value of 50 fs, that is a maximum peak power, deposited energy quickly falls, being reduced from more than 50 % to less than 20 % at 1 ps. There is also a slight dependence of the deposited energy on the sign of the chirp, a negative chirp (that is, blue frequencies in front of the pulse) yielding better results than a positive chirp. This is due to the influence of the group velocity dispersion of air, which tends to temporally compress negatively chirped pulses, but also to a stronger plasma absorption and defocusing effect taking place for longer wavelengths [10], which tends to decrease intensity for positively chirped pulses.

One could think that as some energy transfer channels, like avalanche ionization, are favored by longer pulses, it could positively affect global energy deposition. Such behavior has indeed been observed during filamentation in fused silica [11] and water [12]. Conversely, it seems that maximum intensity gives the best results, because it promotes a more efficient nonlinear ionization and Raman absorption.

4.2.1.3 Influence of focusing conditions

Influence of focusing conditions was also investigated by comparing two cases: the $f/30$ case, that has been used in most experiments until now, and the extreme $f/3$ case, that corresponds to the quasi-breakdown regime described by Kiran *et al.* [9]. Results are given in figure 4.8.

Here, energy deposition in the $f/3$ case clearly dominates from the very beginning. Its evolution is quite similar to that of the $f/30$ focusing, with an initial quick rise followed by a gentler phase

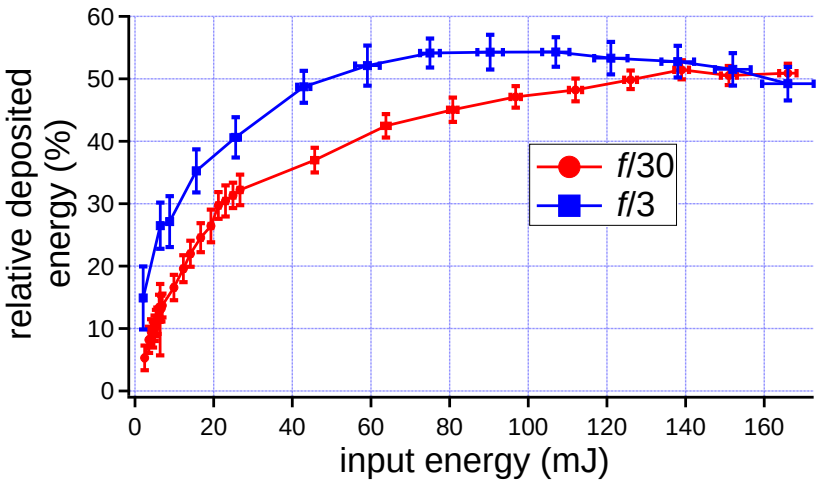

Figure 4.8: Evolution of the measured relative deposited laser energy with input energy using a $f/30$ (red circles) and a $f/3$ focusing (blue squares). Filamentation was generated by a 50 fs laser pulse at 800 nm. Error bars correspond to a confidence interval of one standard deviation evaluated over 500 shots.

until finally reaching a saturation plateau as early as $E_{in} = 75$ mJ at a level of 55 %. However, if input energy continues to rise, relative deposited energy eventually starts to *decrease*, but at a very slow rate, so that it goes below 50 % at 165 mJ. This behavior might be explained by the fact that at a given point, plasma density becomes high enough as to promote plasma defocusing, leading to an intensity decrease and, therefore, to a less efficient energy absorption. Also, strong focusing and high energies lead to the emergence of a large number of short-scale filaments, which decreases the beam quality and prevents an efficient energy focusing. Even though this decrease is modest, it results in energy deposition with $f/3$ focusing to be lower than energy deposition in the $f/30$ case at high input energy.

It is also possible that at even higher input energy, relative energy deposition in the $f/30$ case would start to decrease as well. Still, as far as we are concerned, such input energy values cannot be reached and the question remains open.

4.2.1.4 Conclusion on experimental conditions

From the previous study, we can deduce optimal experimental conditions to get the best laser energy deposition in air. First, of course, input energy should be as high as possible. Second, the pulse duration should be as short as possible. These two conditions result in the maximum available peak power and therefore, intensity. Finally, at such energy levels, strongest focusing conditions surprisingly do not result in the optimal energy deposition. A slightly weaker focusing indeed yields a better energy absorption. Quantitatively speaking, we found in our case the best experimental conditions to be an input energy of 165 mJ, a pulse duration of 50 fs and a $f/30$ focusing.

4.2.2 Experimental description of energy deposition

This section focuses on the characterization of filamentation-induced air hydrodynamics by means of the various diagnostics described in Chapter 2. We here use the experimental conditions described

in the previous section, that is 165 mJ, 50 fs laser pulses focused at $f/30$.

4.2.2.1 Time evolution of air density and channel symmetrization

Channel symmetrization We first made use of transverse interferometry to characterize the time evolution of air density following filamentation of the energetic laser pulse. However, a difficulty arises here related to this diagnostic, as precise as it may be. A fundamental prerequisite for density profiles extraction from interferometry using Abel inversion is to have a cylindrically-symmetric refractive index profile, which was the case for single filamentation (as described in Chapter 3). In the case of powerful laser pulses, a multifilamentary structure is typically encountered, such as those described in the previous section (for instance, in the figure 4.2). Consequently, it is highly unlikely for the cylindrical symmetry hypothesis to be fulfilled in this case.

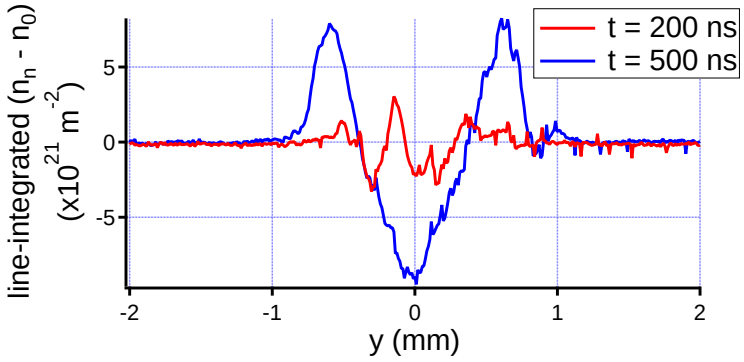

Figure 4.9: Line-integrated air density profiles at $z = 1$ m after the focusing lens (linear focus) and for two different delays. Filamentation was generated by a 165 mJ, 50 fs laser pulse focused at $f/30$.

Still, interferometry was used in this case to yield at least qualitative information about the evolution of air hydrodynamics, even though Abel inversion was not applicable. It was found that in the focal zone after a given delay, air density spontaneously evolved from a highly disorganized state, reminiscent of multifilamentation, to a cylindrically-symmetric state, as displayed in figure 4.9.

In this last figure are plotted two line-integrated air density profiles taken at the linear focus position. At delay 200 ns (red curve), several structures can be seen at the center of the profile, very similar to those seen in plasma luminescence profiles in the case of *superfilamentation* (figure 4.2-(b)), with approximately a same transverse size of ~ 1 mm. However, at delay 500 ns (blue curve), this line-integrated profile deeply transformed into a much more organized state, with a central density depletion and lateral density ridges. Even more interesting, the profile is now almost symmetric, meaning the initial density profile is cylindrically-symmetric. Therefore, Abel inversion can now be implemented to retrieve true air density radial profiles.

Air density profiles at $z = 1$ m were recorded using this method at times ≥ 500 ns and are displayed in figure 4.10-(a). They are characterized by an outward-propagating cylindrical shock wave that leaves a central underdense channel, much in the same way as single filamentation (see figure 3.5-(a) in Chapter 3). In the present case however, the shock wave is broader and its amplitude is higher than for a single filament. As for the underdense channel, it has approximately the same depth as before (approximately 30 % of normal air density), but is significantly larger,

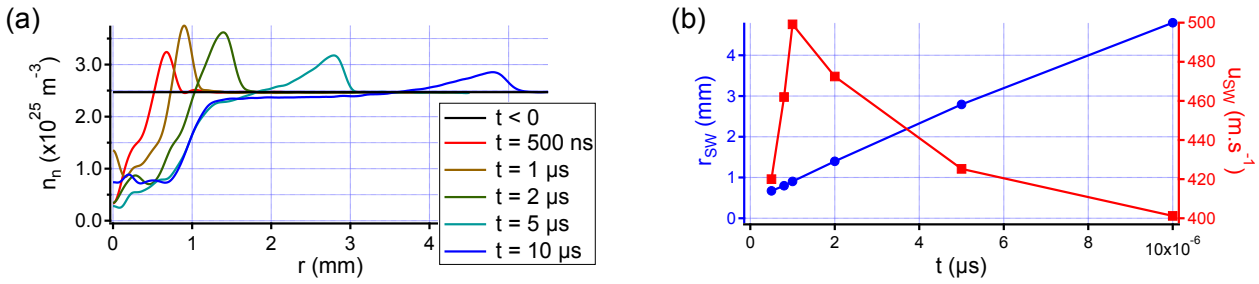

Figure 4.10: (a): air density profiles at various times after the filamentation of a 165 mJ, 50 fs laser pulse focused at $f/30$ taken at $z = 1$ m. (b): time evolution of the shock wave radius r_{SW} (blue circles) and of the shock wave speed u_{SW} (red squares).

reaching a FWHM of almost 2 mm after 10 µs. Shock wave speed u_{SW} was evaluated using shock wave radial position r_{SW} and plotted in figure 4.10-(b). It exhibits a steep initial increase up to $\sim 500\ \mathrm{m} \cdot \mathrm{s}^{-1}$ during the first microsecond, followed by a slower, gentle decrease at subsequent times, still propagating with a supersonic speed after 10 µs.

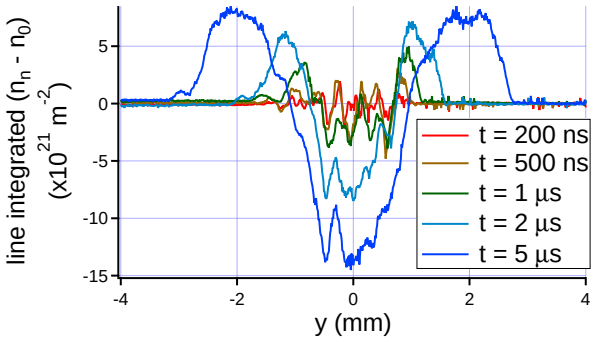

Figure 4.11: Line-integrated air density profiles at $z = 0.96$ m after the focusing lens (linear focus) and for two different delays. Filamentation was generated by a 165 mJ, 50 fs laser pulse focused at $f/30$.

The symmetrization process is highly dependent on the position along the filamentation area and, therefore, on the local profile of energy deposition. For instance, if we look at the evolution of the line-integrated air density with time at position $z = 96$ cm (figure 4.11), we can see that in this case, symmetrization takes a much longer time than at $z = 1$ m and remains incomplete even after 10 µs. This gives a clue about the origin of the symmetrization. We explain it as follows: multifilamentation results in an inhomogeneous energy deposition, which occurs in several separated channels. Each filament forms a hydrodynamic wave and the associated underdense air channel. If filaments are initially close enough one to the other (as it is typically the case in the focal zone), individual shock waves quickly interfere constructively, leading to the generation of a single, large shock wave. The time interval during which u_{SW} increases (figure 4.10-(b)) can be seen as a sign of this interference process during which the fastest components from the strongest filaments catch up with the slowest components and eventually take the lead. Since in the focal zone, filaments in the form of *superfilaments* are distributed in a much more symmetric fashion than in standard short-scale filamentation areas (see, e. g., figures 4.2-(b) and 4.5-(a)), this resulting

shock also exhibits an almost perfect cylindrical symmetry. As this shock is responsible for the formation of the central underdense channel by ejecting matter from the center, this channel shares the symmetry of the shock wave.

Hydrodynamic evolution in the focal zone Since full interferometric process can now be used in the focal zone to extract air density profiles, because of the symmetrization process we described, we can look at the evolution of air density both in space and time in this region. Figure 4.12 displays such 1-D density profiles recorded at various z positions and at delay 5 µs (a) and 10 µs (b).

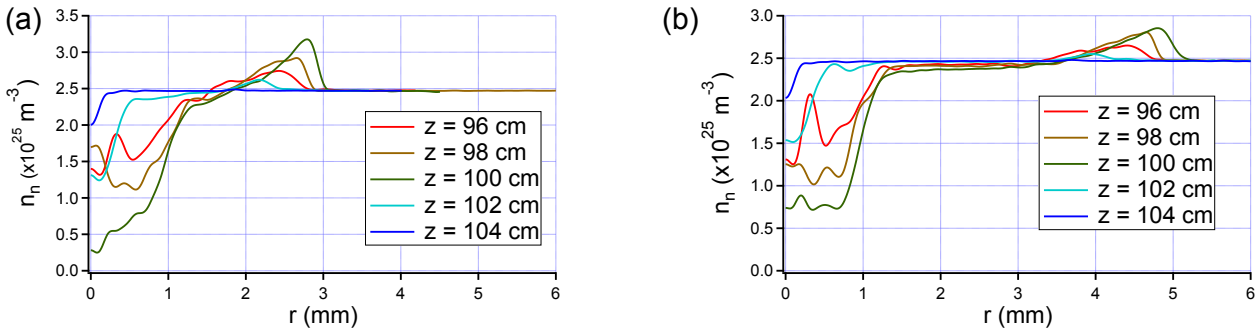

Figure 4.12: Air density profiles following filamentation of a 165 mJ, 50 fs laser pulse focused at $f/30$ at different z positions and delay 5 µs (a) and 10 µs (b).

These profiles are characterized by a strong evolution of the shock wave and the associated underdense channel in z. Starting before the linear focus, we progressively see this channel deepening and broadening until it reaches a maximum around $z = 1$ m. As for the shock wave, its speed and amplitude increase in the same fashion. After the linear focus, the shock speed and amplitude and channel depth decrease dramatically, quickly disappearing beyond $z = 105$ cm. The time evolution results in the shock propagating further and, consequently, decreasing in amplitude while the underdense channel starts to resorb. Therefore, energy deposition mainly occurs before the linear focus and is quickly suppressed beyond, which corresponds to what was recorded in the same focusing conditions but with a far lower energy (see Chapter 3, section 3.1.1.2).

Assuming that pressure equilibrium is reached at the delays studied here, we can deduce air temperature profiles from air density profiles through the ideal gas law. This gives, for instance, a maximum air temperature of $\sim$ 1800 K at 5 µs and $\sim$ 1000 K at 10 µs. The typical temperature reached in the case of multifilamentation is therefore comparable to the one observed in the single filamentation regime. The principal difference between the two regimes lies in the heated volume, which is considerably more important here: at 10 µs, the underdense channel in the multifilament regime has a $\sim$ 2 mm FWHM. It was only $\sim$ 450 µm for a 5 mJ pulse energy, that is a corresponding surface $\sim$ 16 times smaller. Therefore, we can evaluate the initial maximum lineic deposited energy to be 16 times the maximum value measured at 5 mJ, that is 16×400 µJ $\cdot$ cm^{-1} $\approx$ 6 mJ $\cdot$ cm^{-1} (Chapter 3, figure 3.2).

Generation of a continuous underdense channel at 10 Hz Since underdense channels generated by high-energy single filamentation were already very long-lived as to reach a lifetime of more than 100 ms (see Chapter 3), this effect should be even more pronounced in the multifilamentation

regime. We verified this hypothesis by recording phase shift profiles at the maximum delay we could reach (96.9 ms), yielding the curve displayed in figure 4.13-(a). By this time, the channel is still present but has become so large that it affects the whole field of view of the camera, preventing us from using a phase reference. As seen in this figure, the resulting profile is also not symmetrical, so that it would not be possible to extract a density anyway.

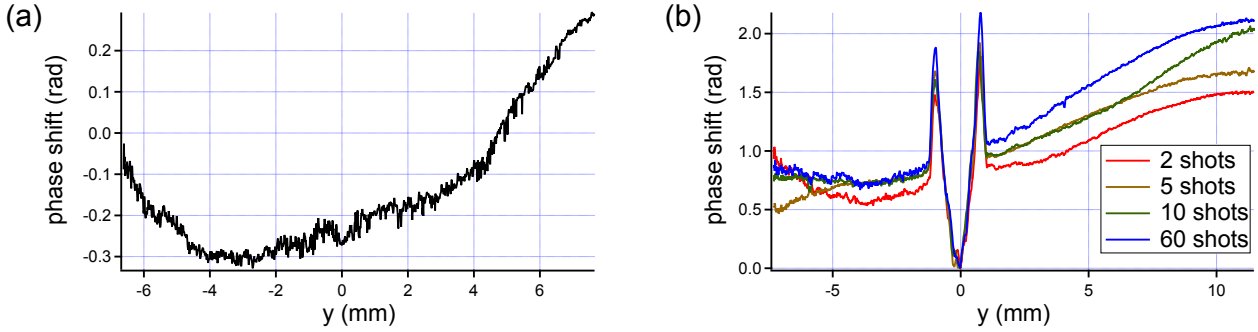

Figure 4.13: (a): phase shift profile recorded at $z = 1$ m and delay 96.9 ms after the filamentation of a 165 mJ, 50 fs laser pulse focused at $f/30$. (b): phase shift profiles recorded at a 10 Hz repetition rate and 10 µs after the passage of the N^{th} laser pulse using the same experimental conditions.

To look at a possible cumulative effect at 10 Hz, we used our laser in burst mode with a repetition rate of 10 Hz and looked at the phase shift profile 10 µs after the filamentation of a given N^{th} laser pulse. Corresponding results are plotted in figure 4.13-(b). This last figure displays the shock wave-underdense channel structure characteristic of filamentation, superimposed over the broad remains of the channels generated by previous pulses. However, this broad underdense channel does not deepens nor is significantly affected by the number of such pulses.

This study therefore shows that a permanent shallow underdense channel is indeed generated in the multifilamentation regime, but the 10 Hz repetition rate is too low to result in a significant deepening of this channel with more laser pulses. By the time the next laser pulse arrives, the underdense channel from the previous one has already strongly diffused and resorbed so that it is insignificantly affected by the new filament.

4.2.2.2 Microphone measurements

We also made use of microphone measurements to try to extract quantitative information about energy deposition in air. However, in this high-energy experimental conditions, the generated acoustic signal can cover more than 4 orders of magnitude, and such measurement therefore requires a very important dynamic range. To this purpose, we made use of a dual microphone configuration described in Chapter 2 (section 2.3.3). Results from this measurement are plotted in figure 4.14.

As displayed in this figure, there is a good agreement between the two sensors used, enabling us to extract a microphone scan over the whole filamentation region. We can here see that sound generation occurs mainly in an area close to the linear focus, with a typical length ~ 10 cm, and quickly drops beyond $z = 1$ m, which corresponds to what was found using interferometry. Knowing that this focal region exhibits the symmetrization effect described earlier in this section, and that, according to interferometry, channel width does not vary significantly shortly before the linear focus, we make the same assumption as in the single filamentation regime, that is the maximum pressure recorded at z is proportional to the local lineic deposited energy following equation (2.42).

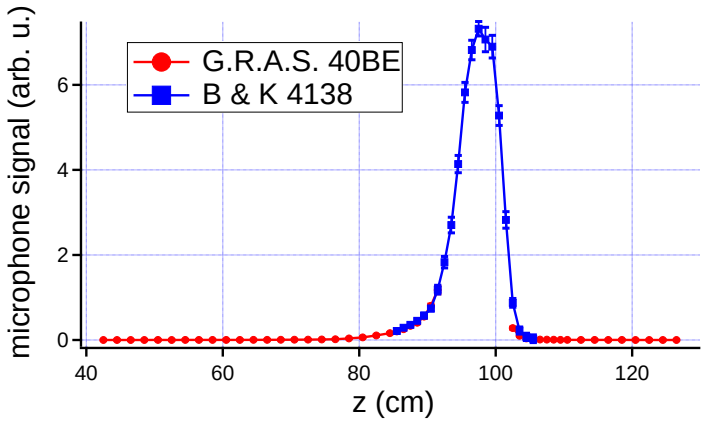

Figure 4.14: Microphone scans along z to investigate energy deposition from a 165 mJ, 50 fs laser pulse focused at $f/30$. Two different microphones with distinct sensitivities were used to cover the maximum dynamic range. Data is averaged over 200 shots.

Although this is not true outside the focal zone, microphone signal is so weak in this region that it is negligible, yielding a small error.

Consequently, we identified the integral of the microphone scan with the total measured deposited energy, as we already did in Chapter 3. This yields the figure 4.15. This graph exhibits interesting features: first, the maximum lineic deposited energy is 10 mJ $\cdot$ cm^{-1}. This value is very close to the one that was estimated in the previous section (6 mJ $\cdot$ cm^{-1}). Second, deposited energy rises slowly during the laser pulse propagation, ranging typically from 1 to 100 µJ $\cdot$ cm^{-1}, that is values recorded in the case of single filamentation (see previous Chapter).

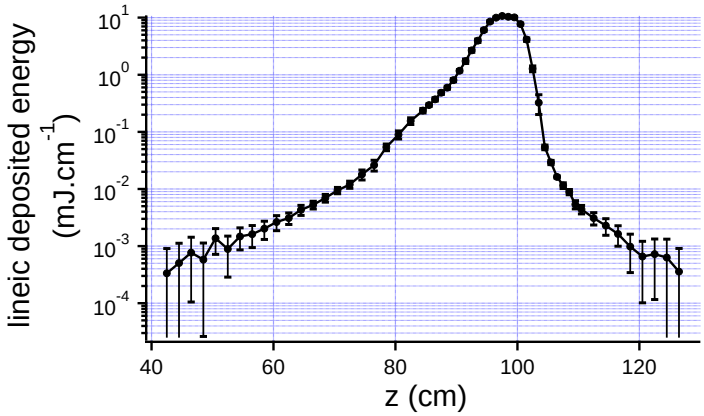

Figure 4.15: United microphone scan graph obtained from concatenation of the graphs displayed in figure 4.14. Results have been translated in terms of deposited energy using the measured value for ΔU.

4.2.2.3 Plasma luminescence measurements

Finally, we implemented the spectroscopic diagnostic on the laser-induced plasma luminescence as described in Chapter 2 (section 2.3.4). However here arises the same problem as for microphone

measurements, that is plasma radius can no longer be considered as constant. This is an even stronger constraint on plasma density since it remains in a disorganized, unsymmetrical state, unlike air density profiles that experience symmetrization and can therefore be considered as originating from such a symmetric energy deposition spatial profile. Consequently, no quantitative information can be here retrieved from this analysis, but it can still bring useful qualitative information. A complete analysis could be performed similarly to what was done in the study of *superfilaments*, with the plasma transverse surface being evaluated by means of impacts on photographic paper. However, we lacked time to perform such an experiment.

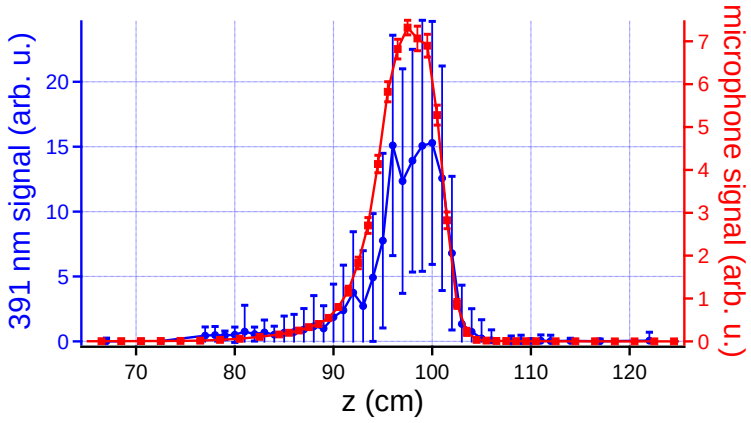

Figure 4.16: Evolution of the 391 nm plasma luminescence signal (blue circles) and of the microphone signal (red squares) with z following the filamentation of a 165 mJ, 50 fs laser pulse focused at $f/30$. Data is averaged over 200 shots.

Figure 4.16 displays the evolution of plasma luminescence from the first negative system of N_2^+ with z. On this graph is also plotted the microphone scan from the previous section as a reference. As in the case of single filamentation (figure 3.3), microphone signal starts to rise before luminescence, which is an evidence for the rise of Raman absorption before ionization occurs on a large scale. However, after the linear focus both parameters closely follow each other, marking the end of ionization and the rapid fall of intensity.

4.2.3 Conclusions

To conclude on the study of multifilamentation in the high-energy, strong focusing limit, we found that optimal energy deposition resulted from the most energetic and the shortest possible laser pulse. Surprisingly, an even stronger focusing did result in a slightly less important energy deposition, undoubtedly due to a strong plasma defocusing effect on the pulse. The full characterization of the resulting hydrodynamics gave interesting results, such as the self-symmetrization of air structures in the focal zone and the generation of very strong shock waves, coupled to wide underdense channels, of which depth is approximately the same as in the single filamentation case. Such air structures could be employed in the same applications as those based on single filamentation-induced hydrodynamics described in Chapter 3. However, a major difficulty in the case of multifilaments comes from the inhomogeneity of the whole beam. For instance, even though symmetrization occurs in the focal zone, it does not before this area, resulting in poor quality optical structures. Still, the far steeper shock and longer-lived underdense channel present advantages

interesting enough in this respect to keep going in this direction.

Conclusion

To conclude on energy deposition from laser pulses undergoing multifilamentation in air, we first study the multifilamentation process in the case of moderate focusing. We witnessed a propagation regime transition in the focal zone, shifting from standard short-scale filaments to larger, denser filamentary structures emerging from a background of weakly ionized plasma. These structures were called *superfilaments* because of the properties they share with filaments, while being an order of magnitude denser.

In a second part, we focused on the optimization of energy deposition in air in case of strong focusing. Best results were obtained using an energetic, short laser pulse with a strong, but not extreme, focusing. We characterized laser-induced hydrodynamics and witnessed a similar reaction as in the single filamentation regime, but with significantly stronger parameter values, such as shock wave amplitude or underdense channel width. Harnessing this deposited energy would undoubtedly result in a revolution of laser-induced optical structures that were studied at the end of Chapter 3.

Bibliography

[1] G. Méchain, C. D'Amico, Y.-B. André, S. Tzortzakis, M. Franco, B. Prade, A. Mysyrowicz, A. Couairon, E. Salmon, and R. Sauerbrey, Optics Communications **247**, 171 (2005).

[2] A. Talebpour, M. Abdel-Fattah, A. D. Bandrauk, and S. L. Chin, Laser Physics **11**, 68 (2001).

[3] G. Point, Y. Brelet, A. Houard, V. Jukna, C. Milián, J. Carbonnel, Y. Liu, A. Couairon, and A. Mysyrowicz, Physical Review Letters **112**, 223902 (2014).

[4] G. P. Agrawal, *Nonlinear Fiber Optics*, 4^{th} ed. (Academic Press, New York, NY, USA, 2007).

[5] G. Fibich, S. Eisenmann, B. Ilan, Y. Erlich, M. Fraenkel, Z. Henis, A. Gaeta, and A. Zigler, Optics Express **13**, 5897 (2005).

[6] T.-T. Xi, X. Lu, and J. Zhang, Physical Review Letters **96**, 025003 (2006).

[7] S. Varma, Y.-H. Chen, and H. M. Milchberg, Physical Review Letters **101**, 205001 (2008).

[8] B. Shim, S. E. Schrauth, C. J. Hensley, L. T. Vuong, P. Hui, A. A. Ishaaya, and A. L. Gaeta, Physical Review A **81**, 061803 (2010).

[9] P. P. Kiran, S. Bagchi, C. L. Arnold, S. R. Krishnan, G. R. Kumar, and A. Couairon, Optics Express **18**, 21504 (2010).

[10] Y. P. Raizer, Soviet Physics Uspekhi **8**, 650 (1966).

[11] A. Mermillod-Blondin, C. Mauclair, A. Rosenfeld, J. Bonse, I. V. Hertel, E. Audouard, and R. Stoian, Applied Physics Letters **93**, 021921 (2008).

[12] Y. Brelet, A. Jarnac, J. Carbonnel, Y.-B. André, A. Mysyrowicz, A. Houard, D. Fattaccioli, R. Guillermin, and J.-P. Sessarego, The Journal of the Acoustical Society of America **137**, 288 (2015).

Part III

Guiding of spark discharges using energy deposition from filamentation in air: applications

Chapter 5

Filamentation-guided discharges in air - principles and applications

Contents

Introduction

Triggering and guiding electric discharges using lasers is not a novel idea. The main motivation behind this use of lasers was to trigger lightning, a destructive and harmful natural phenomenon. It has been estimated that in the United States alone, thunderstorms are responsible for ten fatalities and for $\sim$ \$ 150 million in damage cost per year on average [1]. If the famous lightning rod, designed by Benjamin Franklin during the 18^{th} century, can deviate the path of lightning and offer some protection to buildings, it cannot trigger lightning. To this purpose, specially designed rockets trailing a long metallic cable are launched into thunderclouds [2]. However, this technique is expensive and has a success rate of only 60 %. Moreover, it is a single-shot method that requires a precise monitoring of the ambient electric field for maximum efficiency [3].

With the advent of powerful lasers in the 1960s, such as Q-switched Nd:YAG and CO_2 lasers in the MW peak power range, and the possibility to induce optical breakdown of air, the idea of an all-optical lightning trigger emerged. The major drawback of these lasers, despite the impressive energy they are able to deliver, comes from the mechanism they use to achieve ionization of air: avalanche ionization. Since this process does not saturate, free electrons are multiplied by the laser pulse in an exponential fashion until the plasma becomes opaque at the laser wavelength. In this case, the laser-induced plasma takes the form of discrete bubbles of strongly ionized medium along the laser propagation axis, with a strong inhomogeneity. Consequently, no significant results were obtained using long laser pulses [4, 5].

The advent of filamentation in air in the 1990s, brought about by the generalization of solid-state Ti:sapphire femtosecond lasers using the chirped pulse amplification technique, opened up new perspectives in the field of laser-triggered lightning. Indeed, filamentation can generate a continuous column of weakly-ionized plasma over $\sim$ 100 m distances, and is therefore a much more efficient way to create a conductive channel in air than, e. g., CO_2 lasers. Until now, filaments proved to be able to trigger sparks with a length of several meters, and even to deviate discharges from their natural path [6]. Work is still ongoing in the filamentation community to improve triggering and guiding of long sparks using femtosecond lasers.

The laser lightning rod is not the only application for filamentation-guided discharges. Filamentation-triggered spark gaps proved to be very robust and reliable [7, 8]. They offer an efficient way to transfer high current and/or voltage in a contactless way with an excellent timing accuracy. In the 1980s was also suggested to use the plasma column from Nd:YAG laser-guided electric discharges in air as a radiofrequency antenna. This idea was successfully demonstrated by Dwyer *et al.*, showing that such virtual antennas compare very favorably with standard copper antennas [9]. Later, our group at LOA showed the use of filamentation-guided discharge present superior trigger timing accuracy and also demonstrated the feasibility of such plasma antennas over 1 m [10].

This Chapter first introduces the physical mechanisms involved in the breakdown of air, and then focuses on the triggering and guiding effect of femtosecond filamentation.

5.1 Mechanisms for the electric breakdown of air

5.1.1 Avalanche mechanism and Townsend discharge

5.1.1.1 Description of the process - Paschen's law

The most basic mechanism for the electric breakdown of air was developed by Townsend at the beginning of the 20^{th} century [11]. This mechanism relies on an avalanche process quite similar to avalanche ionization due to a long laser pulse, as described in Chapter 1 (section 1.3.2.3). We here consider the situation described in figure 5.1, that is a gap of length L in which the electric field is constant and equal to $E = U/L$, U being the voltage between the two planar electrodes. Assuming at least one seed electron is initially present in the gap, due to cosmic rays for instance, this electron will be accelerated in the electric field, gaining kinetic energy. If this energy is high enough (typically on the order of 10 eV), the electron will be able to ionize a neutral gas molecule by an inelastic collision process, yielding a new electron. The two electrons will resume their drift in the electric field, gaining energy until they are able to produce a ionizing collision, giving four electrons, then eight, and so on.

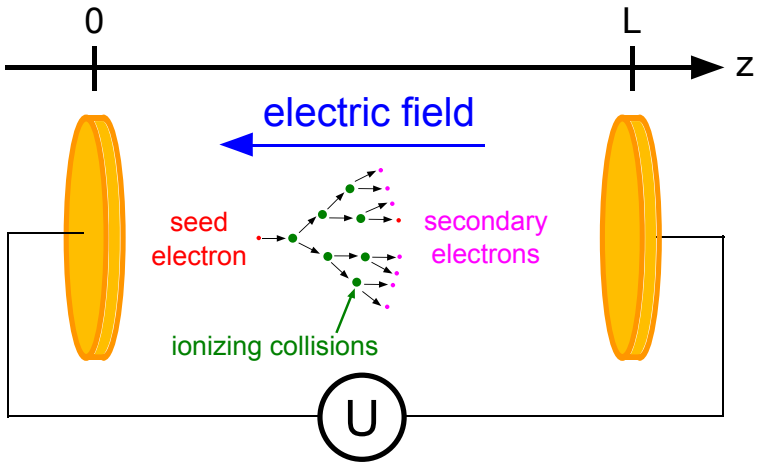

Figure 5.1: Schematic description of the development of a Townsend discharge.

The avalanche speed is quantified by the parameter α called first Townsend coefficient. This coefficient gives the number of electrons produced by the avalanche process by unit length, yielding the following equation for the evolution of the number of electrons in the gap, N_e:

$$\mathrm{d}N_e(\vec{r}) = \alpha(E,p)N_e(\vec{r})\ \mathrm{d}z. \tag{5.1}$$

where p denotes the gas pressure. Supposing the seed electron was generated at $z = 0$, then the number of electrons is given by:

$$N_e(z) = \exp(\alpha(E,p)z) \tag{5.2}$$

Over the propagation of electrons in the gap towards the anode, $\exp(\alpha(E,p)L) - 1$ new electrons and positive ions were generated. Townsend introduced a second coefficient to take into account the fact that heavy ions reaching the cathode can actually knock new electrons out of the electrode. Therefore the total number of free electrons left in the gap after the completion of this avalanche is given by:

$$N_{e,final} = \gamma\left(\mathrm{e}^{\alpha(E,p)L} - 1\right), \tag{5.3}$$

where γ is the dimensionless second Townsend coefficient. The breakdown condition in the case of a Townsend discharge, that is the condition for which the gap medium becomes conducting, is given by $N_{e,final} \geq 1$, that is:

$$\gamma \left(\mathrm{e}^{\alpha(E,p)L} - 1 \right) \geq 1. \tag{5.4}$$

The first Townsend coefficient α was shown by Townsend to obey the semi-empirical formula:

$$\alpha(E,p) = Ap \exp(-Bp/E), \tag{5.5}$$

where A and B are constants evaluated from experimental data. Therefore equation (5.4) can be rewritten to extract the value of the breakdown voltage U_{bd}:

$$U_{bd} = \frac{BpL}{\ln(ApL) - \ln\left(\ln\left(\frac{1+\gamma}{\gamma}\right)\right)}. \tag{5.6}$$

This last relation between the breakdown voltage, the gas pressure and the gap length had already been derived empirically by Paschen at the end of the 19^{th} century when Townsend discovered it independently. It is consequently named the Paschen's law [12].

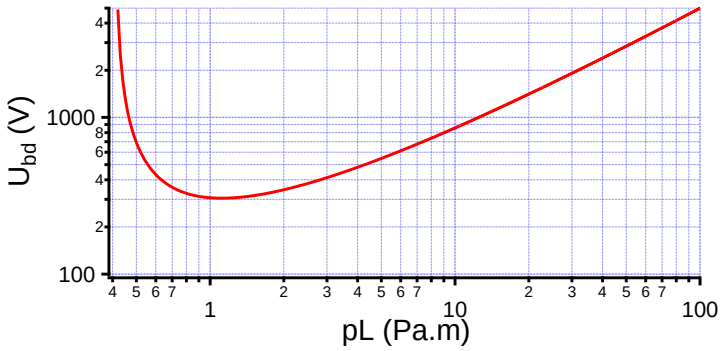

Figure 5.2: Evolution of the breakdown voltage with the product pL for air following the Paschen's law (equation (5.6)). Following values from reference [13] were used: $A = 11.25\ \mathrm{Pa}^{-1} \cdot \mathrm{m}^{-1}$, $B = 273.75\ \mathrm{V} \cdot \mathrm{Pa}^{-1} \cdot \mathrm{m}^{-1}$ and $\gamma = 10^{-2}$.

The breakdown voltage following the Paschen's law in case of air is plotted in figure 5.2. This graph was obtained using numerical values given by Bazelyan and Raizer [13]. It can be qualitatively explained as follows: if the mean free path of an electron in the gap is on the order of the gap length, then the probability of ionizing collisions in the gap decreases, asking for an increased electric field to optimize each collision. This corresponds to the strong divergence of U_{bd} on the left side of the curve. Conversely, when the pL product is increased, then a free electron experiences a lot of collisions in the gap so that it has less time to extract energy from the electric field. Reaching breakdown therefore necessitates a stronger field. This is precisely what happens on the right side of the curve.

Paschen's law was developed for gaps at standard temperature. A correction is needed when simultaneous pressure and temperature variations are encountered. One of the most used is called the Peek correction, that relates the gap breakdown voltage at a given (p,T) condition to the breakdown voltage at a reference point (p_0,T_0):

$$U_{bd}(p,T) = \frac{n_n}{n_0} U_{bd}(p_0,T_0), \tag{5.7}$$

where n_0 is the gas density at the reference point (p_0,T_0) [14]. If we take $p_0 = 1013$ hPa and $T_0 = 300$ K, we find back $n_0 = 2.47 \times 10^{25}$ m^{-3}. This correction accounts for the fact that the general relevant gas parameter for breakdown occurrence is density, and not pressure. Although empirical, it can be shown that this correction is indeed meaningful at sufficiently high reduced electric field E/n_n [15].

5.1.1.2 Limits to the Townsend discharge

The model developed by Townsend was the first to really describe the formation of an electric discharge. It also had the major advantage of linking the breakdown voltage and the product pL characteristic of the discharge gap instead of p on the one hand, and L on the other hand, allowing the use of a scaling law. However, this formalism has several drawbacks.

The first one comes from the semi-empirical character of the model, requiring experimental data to get a precise evaluation of the A and B parameters. Usually, these are precisely known only for a given range of pressure and electric field. This is not to mention the fact that the γ parameter is almost impossible to determine in a fixed set of experimental conditions, because it is extremely sensitive to them (for instance, the electrode material, which unavoidably varies from one piece to the other).

The second major drawback lies in the need for an electric field high enough to promote ionizing collisions, and is therefore unable to explain the propagation of a discharge in nonhomogeneous electric fields where the field strength can locally decrease below this limit.

Finally, the discharge behavior predicted by the Townsend formalism starts to deviate significantly from reality when pL increases above $\sim$ 250 Pa $\cdot$ m, and becomes completely erroneous above 1300 Pa $\cdot$ m, measured breakdown voltages U_{bd} for large gaps being significantly lower than estimates given by the Paschen's law.

5.1.2 Streamer discharge

In the 1930s, the need for a new theory of gas breakdown was crucial. Many experimental results strongly disagreed with the mechanism developed by Townsend at the beginning of the century, notably concerning high pressure discharges and discharges occurring in strongly asymmetric gaps. This problem was solved by the introduction of the concept of streamer discharge in the 1940s independently by Loeb and Meek [16] and by Raether [17]. This process became the foundation of all subsequent theories of gas breakdown.

5.1.2.1 Inception of a streamer discharge

Let us imagine a discharge gap with two asymmetric electrodes. As a consequence, the generated electric field will also be strongly inhomogeneous in the gap. The field strength will be noticeably larger near the electrode with the smaller curvature radius, which will result in the discharge initiation in the vicinity of this electrode. For the sake of simplicity, we will consider this electrode to be the negative electrode.

When a seed electron appears near the cathode, due to any random process, it will immediately accelerate in the electric field and start an avalanche process (see figure 5.3-(a)). Since electron mobility is far higher than ion mobility, free electrons quickly leave the formed plasma, propagating against the external field. This is responsible for the generation of a space charge electric field, that can be well approximated by a dipolar electric field (figure 5.3-(b)). This secondary field

enhances the total field experienced by the electrons at the tip of the avalanche and at the back of the ionic area, and screens the external field between the negatively charged avalanche head and the positively charged avalanche tail.

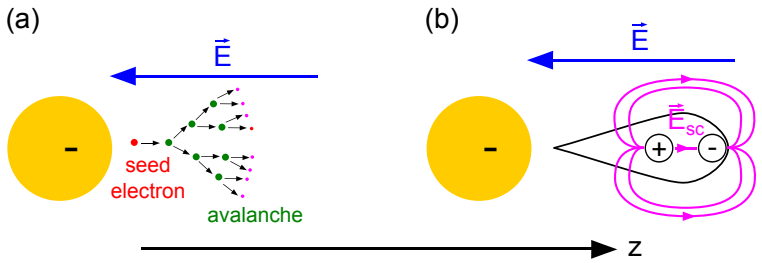

Figure 5.3: Inception of a streamer discharge. (a): illustration of the generation of an avalanche process near the cathode. (b): equivalent representation with the resulting dipolar space charge electric field.

Two processes can then occur: if the space charge field is not able to compensate the external field because of an insufficiently intense avalanche process, the latter will continue to propagate in the external field until it is unable to sustain ionizing collisions. Therefore, the generated plasma remains confined in the vicinity of the electrode, and typically takes the form of a corona discharge. Conversely, if the space charge field becomes so strong as to significantly distort the external field, the avalanche process will spontaneously evolve towards a streamer process: the total field at the tip of the avalanche, that is where free electrons are accelerated and are involved in ionizing collisions, is then intense enough to promote the further propagation of ionization in the gap, even though the external field alone might not be sufficient to sustain this process. Ionization can be further enhanced at the front of the avalanche by the release of energetic photons at the back of the streamer during radiative electron-ion recombination. This condition is called the Meek breakdown condition and yields:

$$E_{sc} \sim \frac{e}{4\pi\epsilon_0 r_a^2} \exp\left(\alpha(E,p)L\right) \sim E \tag{5.8}$$

where E_{sc} is the space-charge field amplitude, L is the gap length and r_a the avalanche head radius. Usually, this last parameter is estimated as $r_a \sim 1/\alpha(E,p)$ [13], which leads to:

$$\alpha(E,p)L \gtrsim 20. \tag{5.9}$$

In the end, an ionization wave forms in the form of filamentary structures and propagates towards the anode: a streamer discharge is born.

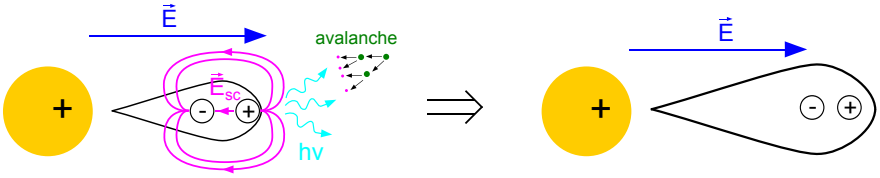

Figure 5.4: Evolution and growth of a positive streamer discharge, showing how photoionization ahead of the streamer head results in secondary avalanches in the enhanced electric field of the streamer head.

If we now investigate the case where the avalanche originates from the vicinity of the anode, the picture is quite similar to that of an anode-directed, or negative, streamer. Indeed, the external field will accelerate electrons towards the anode, yielding a space charge field that will also enhance the total electric field at the tip of the avalanche region, which is positively charged in this case, and screen the external field in the avalanche area. In this case, the role of photoionization is very important because it will generate new seed electrons ahead of the streamer head which will cause it to propagate forward while experiencing secondary avalanches (as detailed in figure 5.4). Examples of positive streamer propagation pictures are given in figure 5.5.

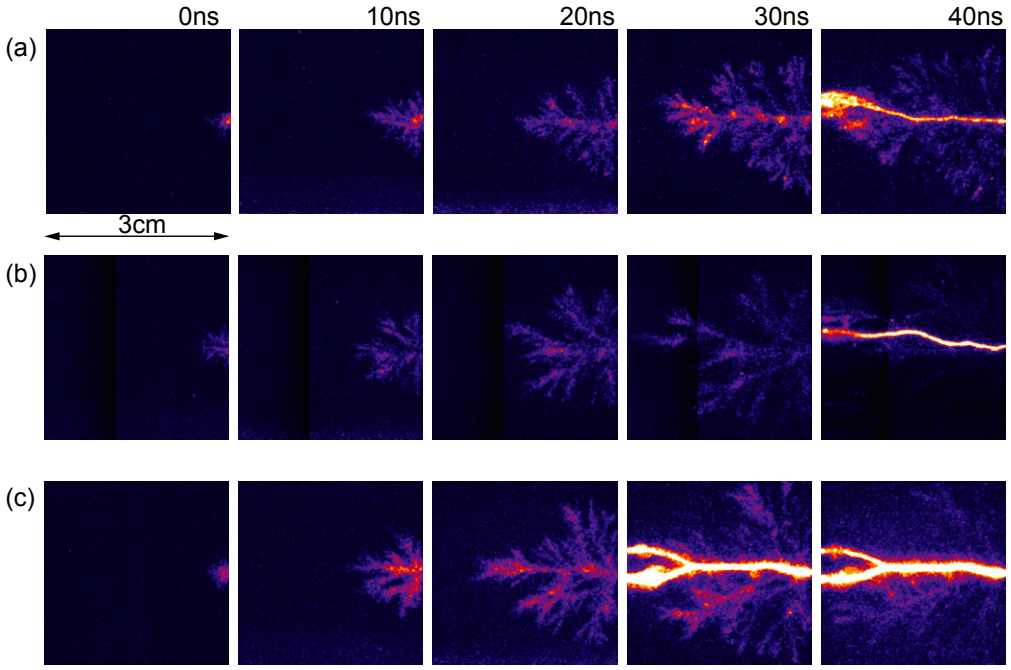

Figure 5.5: Pictures of positive streamers propagating in argon gas taken using an ultrafast ICCD camera. Applied gap voltage was 18 (a), 20 (b) or 22 kV (c). From Takahashi *et al.* [18].

5.1.2.2 Physical properties of streamers, streamer breakdown

Streamers are typically made of a low-density and cold plasma. The electron density in the ionized channels is on the order of 10^{19} m^{-3}, that is a ionization degree of 10^{-6}. This plasma disappears quickly with a ns characteristic time through recombination and, in air, attachment of free electrons to electronegative molecular oxygen. The streamer as an ionization wave propagates at an impressive speed of 10^7 to 10^8 $m \cdot s^{-1}$ [13]. Typical currents drained by a single streamer channel are on the order of 0.1 A [19].

From these parameters, it can be assessed if a pure streamer breakdown can be observed. The main condition here is that streamers must close the gap quickly enough so that their conductivity, which is already low at the moment of their initiation, remains high to promote current circulation once the gap is bridged. If the external field in the gap is also strong and/or exhibits a steep voltage rise in case of pulsed excitation, it can heat the medium by Joule effect and delay the plasma decay. According to Bazelyan and Raizer, the two main conditions to observe a pure streamer breakdown are consequently [13]:

- a short gap with typical length < 10 cm in air;
- a pulsed voltage excitation with a steep rising front and high amplitude on the order of 1 MV $\cdot$ ns^{-1} [13].

It is therefore extremely difficult to observe such breakdowns in atmospheric air because the required experimental conditions are usually not satisfied.

5.1.3 Leader phenomenon and breakdown of long gaps

If streamers are not able to support the development of sparks in large gaps, how is it possible to explain that such sparks can exist? As written in the previous section, one of the major problem of the streamers is their low conductivity and short lifetime. To ensure that long gaps can be effectively bridged to result in a breakdown, it is therefore crucial that electron density remains as high as possible in the precursor channels. In fact, this condition can be fulfilled due by the Joule heating of these channels.

We saw in the previous section that a single streamer channel drains a very weak current of ~ 100 mA. Such a current can be estimated to result in a channel heating of ~ 100 K, which is not enough to counterbalance plasma recombination and attachment. However, several streamers usually start simultaneously at the same location, usually near the electrode with the smallest radius of curvature. As these independent streamers share the same root, a significantly larger current goes through this stem, typically ~ 1 A. This current can raise the plasma temperature as high as 1500 K [19]. This temperature level is able to prevent electron attachment to molecular oxygen, preserving the channel conductivity. As a consequence, the effective electric field in this hot stem drops, and the potential of the electrode is projected to its extremity inside the gap, strengthening the field through the gap. The stem then elongates, absorbing the concatenated tails of the streamers, and starts to form what is called a leader canal. In a continuous process, streamers form from the tip of the leader canal, draining enough current to promote its growth and propagation in the gap. This leader tip behaves as an extension of the electrode, projecting the high-voltage potential deep into the gap and ensuring streamer formation far from the electrodes (see figure 5.6). Its propagation speed is several orders of magnitude lower than that of streamers, between 10^4 and 10^5 m $\cdot$ s^{-1}. Once the leader-streamer system approaches the second electrode and starts to feel an increased external field, it experiences a final jump marked by a sudden acceleration, effectively bridging the gap by a conductive channel that inevitably results in a spark discharge.

The streamer-leader model can be used for any gap in excess of 10 cm to explain the formation of long spark discharges, up to the kilometer distances encountered in lightning.

5.1.4 Conclusions

We saw that the electric breakdown of air results from different mechanisms depending on the gap length. Breakdown process always starts by the formation of streamers, usually near the electrode presenting the smaller curvature radius. This process results from a Townsend-like avalanche ionization in the strong local electric field, and generates a space charge that will eventually distort the external field. If the gap is small enough ($1 - 10$ cm in atmospheric air, depending on the applied voltage), streamers can bridge it quickly enough so that the conductivity remains sufficiently high as to allow the current to flow and the spark to occur. If not, the cumulative current drained by

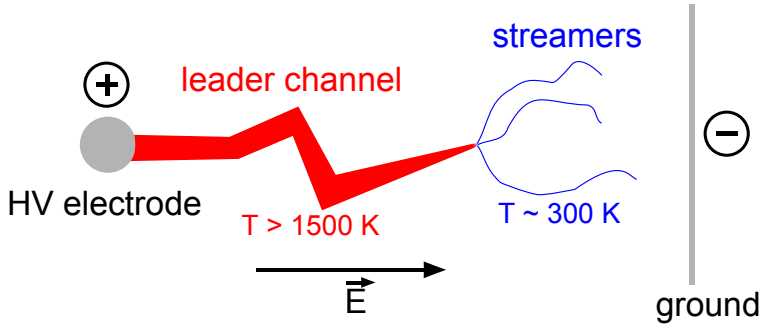

Figure 5.6: Schematic depiction of the propagation of a positive leader channel in a long discharge gap.

all the streamers near the electrode result in the heating of their common stem, giving birth to a leader channel. This leader channel is made up of a relatively hot and conductive plasma and acts as an extension of the electrode, projecting the potential deep in the gap and promoting the generation of streamers at its extremity. Eventually, the leader-streamer system will cross the gap and inevitably result in a spark discharge.

5.2 Triggering and guiding effect of filamentation on spark discharges

The previous section presented the mechanisms of the formation of spark discharges in air. We now investigate the effects of laser filamentation on these processes. Indeed, filamentation is known for triggering sparks at gap voltages that can be far lower than the breakdown voltage in atmospheric air [20, 21, 22]. Such filamentation-triggered sparks are also guided along the initial laser path, a clue that these phenomena are intrinsically linked.

5.2.1 Filament as a conductor in the gap

The most intuitive and natural way to consider that filamentation can trigger an electric discharge is to consider it as a straight conductor inserted in the discharge gap, linking the two electrodes. A first consideration must be here taken into account: because its fast decay, the filament-induced plasma column has actually a finite length L_{fil} given by:

$$L_{fil} = c\tau_{fil} \approx 3 \times 10^8.10^{-9} \text{ m} = 30 \text{ cm}. \tag{5.10}$$

The picture will then be different if the gap is larger or smaller than L_{fil}.

5.2.1.1 Short gaps

In the case of short gaps with $L < L_{fil}$, the plasma filament is able to span the whole gap and to directly link the two electrodes, thereby closing the electric circuit (figure 5.7). The plasma impedance is mainly resistive and is denoted R_{fil}. Using the classical plasma conductivity σ_p:

$$\sigma_p = \frac{n_e e^2}{m_e \nu_c}, \tag{5.11}$$

and using typical values for the plasma filament parameters (electron density $n_e \sim 10^{22}$ m^{-3}, filament radius $r_{fil} \sim 50$ µm), we find a typical lineic plasma resistance:

$$R_{fil,l} = 900 \text{ k}\Omega \cdot \text{m}^{-1}. \tag{5.12}$$

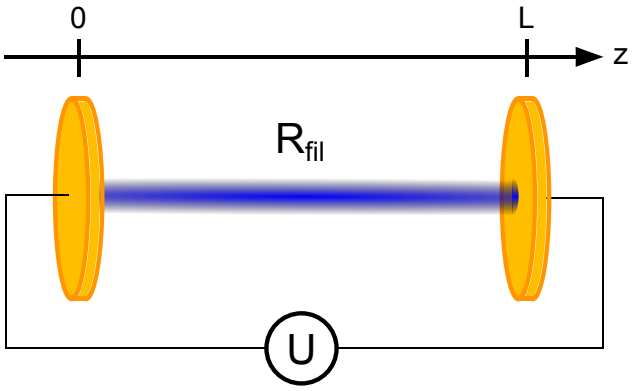

Figure 5.7: Representation of a plasma filament closing the electric circuit in the case of a short gap.

We use as the discharge development condition the same as for the formation of a leader: the gas temperature must be raised at least to 1500 K to prevent electron attachment to molecular oxygen, leading to a suppressed plasma decay and an increased plasma conductivity, leading to the initiation of a positive feedback loop that will result in the breakdown. We can link the Joule heating occurring during the filament initial lifetime τ_{fil} to the current I in a similar way as equation (3.5) describing air heating from filamentation:

$$R_{fil} I^2 \tau_{fil} \approx \frac{5}{2} k_B n_0 \Delta T \pi r_{fil}^2 L. \tag{5.13}$$

This yields:

$$I \approx 3 \text{ A}, \tag{5.14}$$

that is the same order of magnitude as the current typically drained by leaders. The needed electric field E_{crit} to achieve breakdown is therefore given by:

$$E_{crit} = R_{fil,l} I = 27 \text{ kV} \cdot \text{cm}^{-1}. \tag{5.15}$$

This critical field is almost equivalent to the electric field needed to achieve a breakdown in atmospheric air (~ 30 kV $\cdot$ cm^{-1}). The plasma filament is therefore unable to have the strong impact on the breakdown voltage that is observed in discharge guiding experiments. Even though free electrons remain in the gap with a reduced density for microseconds, they can only serve as seed for streamer inception. Discharge guiding must be attributable to a different mechanism.

Since filamentation usually results in impressive breakdown voltage reduction, the involved mechanism must be different than this one.

5.2.1.2 Long gaps

The picture is very different in the case of a long gap such as $L > L_{fil}$. Indeed, in this case, the plasma effectively covers only a part of the gap next to one of the electrodes in a way similar to

figure 5.8. The equivalent electric circuit therefore consists of the filament plasma resistance and of a capacitor between the tip of the filament and the second electrode. This capacitance can be expressed as [13]:

$$C_{fil} \approx \frac{2\pi\epsilon_0 L_{fil}}{\ln(L_{fil}/r_{fil})}. \tag{5.16}$$

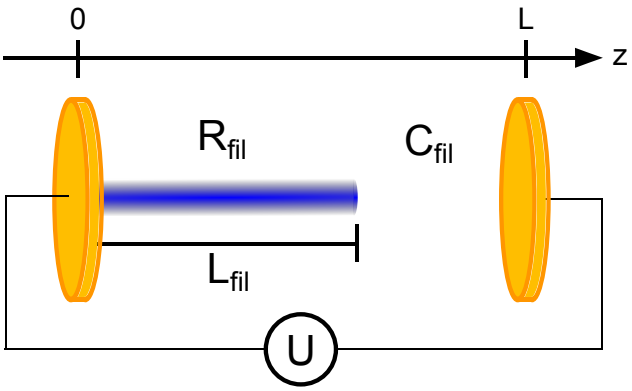

Figure 5.8: Representation of a plasma filament closing the electric circuit in the case of a long gap.

Discharge occurrence is strongly related to the time needed for the voltage at the tip of the filament to reach the potential of the electrode it touches. If this process occurs quickly enough, then the plasma behaves as a perfectly conducting rod projected deep in the gap, effectively increasing the electric field. The order of magnitude of this polarization time is given by the time constant of the relative RC circuit:

$$\tau_{pol} = R_{fil}C_{fil} = \frac{2\pi\epsilon_0 R_{fil,l} L_{fil}^2}{\ln(L_{fil}/r_{fil})} \approx 500 \text{ ns}. \tag{5.17}$$

This value is far higher than the plasma natural lifetime τ_{fil}. It is therefore highly unlikely that any polarization would be noticeable before plasma recombination, and that this effect can positively affect the development of a spark. For this purpose, it is first necessary to increase the plasma lifetime by means of alternative techniques. Several research groups attempted to make use of a long and energetic secondary laser pulse [23, 24]. The best results were achieved by Scheller *et al.* with an order of magnitude reduction of the breakdown voltage using a 3 J laser pulse with ns duration focused by an axicon lens over 5 cm [25]. More recently, Clerici *et al.* also demonstrated similar results using a femtosecond laser pulse only, strongly focused by an axicon lens with a 10° opening angle [26].

5.2.2 Filamentation as a heat source

The first part of this Thesis (Chapters 2 to 4) focused on energy deposition by femtosecond filamentation in air. We saw that filamentation results in important energy losses from the laser pulse, and that this energy is eventually converted into neutral thermal energy. As the heated volume is typically very small (that is a volume similar to that of the actual filament), thermal energy density is high and results in the formation of a cylindrical sound or shock wave that expels matter from the center of the filament, leaving a central underdense air channel (figure 5.9-(b)).

Such hydrodynamics induced by energy deposition had already been recorded in the early 2000s by Tzortzakis and co-authors at LOA. Using time-resolved diffractometry, they were able to record

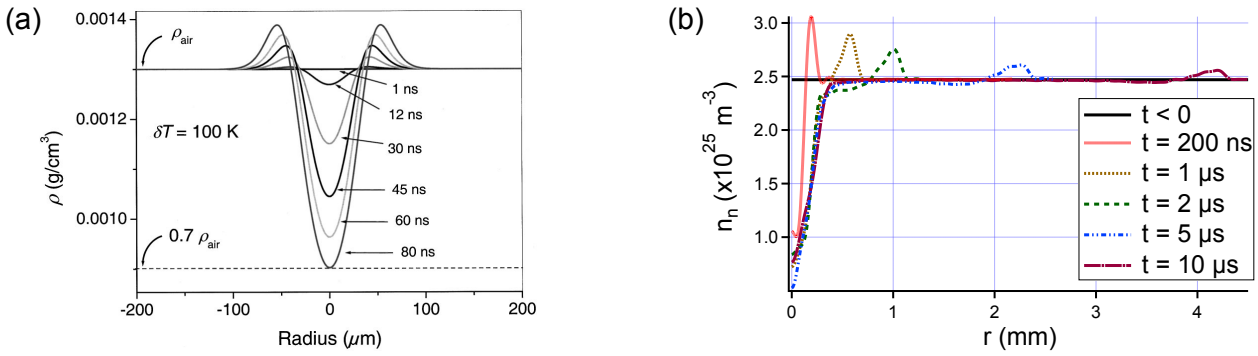

Figure 5.9: (a): simulated air density profiles following the generation of a plasma filament in a 18.5 kV · cm^{-1} external electric field. From Tzortzakis *et al.* [22]. (b): measured air density profiles recorded after the filamentation of a 5 mJ, 50 fs laser pulse focused at $f/30$.

the evolution of the channel formation following filamentation occurring in a strong external field of 18.5 kV · cm^{-1} [22]. They then made use of hydrodynamic simulations fitting experimental data to extract the initial gas temperature, estimated at 400 K (figure 5.9-(a)). The triggering effect of filamentation was explained by the formation of this underdense channel. As density drops in the center, so does the breakdown voltage, according to the Peek correction to the Paschen's law (equation (5.7)). Consequently, streamers and/or leaders can develop in the discharge gap despite the fact the external field is too low to support them in atmospheric air. Since this reduction of breakdown voltage occurs along a definite path, which is that of the laser pulse, the resulting spark is also guided. Tzortzakis *et al.* also observed a good agreement between the measured breakdown delay (80 ns) and the time needed for air to reach the low-density level at which the breakdown voltage given by the Paschen's law is equal to the gap voltage.

It should be noted however that the authors attributed the initial energy deposition mostly to energy deposited by the external field through Joule heating of the plasma filament before its recombination. We know now very well that filamentation itself can result, even with modest pulse energy and focusing, to a similar heating of air, and can yield even more extreme temperature if the pulse energy and the focusing are increased. It is then probable that the contribution of the external field in the deposited energy is very low, if not negligible. This opens wide perspectives in the field of filamentation-triggered and guided discharges, since laser characteristics appear as the only true limiting factor to reach a desired breakdown threshold over distances that can span hundreds of meters.

Conclusion

To conclude, we investigated the various mechanisms responsible for the generation of long spark discharges in atmospheric air. They are characterized by the appearance of streamers, or ionization waves driven by avalanche processes, in the region of maximum electric field in the gap. These streamers are most of times unable to result in a breakdown because of their low conductivity. However, after some time, the total current drained by all streamers will heat their common stem sufficiently so that a hot and conductive plasma region will start to form and propagate in the gap: a leader channel. This leader effectively projects one of the electrodes deep in the gap, giving birth to streamers at its tip that will promote its growth. Finally, the leader will close the gap and inevitably result in a breakdown.

Laser filamentation is well known for being able to trigger spark discharges at voltages far lower than the natural breakdown voltage of atmospheric air. We showed that this triggering effect is undoubtedly due to the generation of a low density transient channel subsequent to the heating of air following filamentation (as detailed in the first part of this Thesis). Indeed, the plasma filament itself is only weakly conductive and is unable to result in a breakdown unless experiencing a very high electric field.

Bibliography

[1] "National Lightning Safety Institute website." .

[2] V. A. Rakov and M. A. Uman, *Lightning: Physics and Effects* (Cambridge University Press, Cambridge, UK, 2003).

[3] R. Fieux, C. Gary, and P. Hubert, Nature **257**, 212 (1975).

[4] D. W. Koopman and T. D. Wilkerson, Journal of Applied Physics **42**, 1883 (1971).

[5] M. Miki, T. Shindo, and Y. Aihara, Journal of Physics D **29**, 1984 (1996).

[6] B. Forestier, A. Houard, I. Revel, M. Durand, Y.-B. André, B. Prade, A. Jarnac, J. Carbonnel, M. Le Nevé, J. C. de Miscault, B. Esmiller, D. Chapuis, and A. Mysyrowicz, AIP Advances **2**, 012151 (2012).

[7] P. Rambo, J. Schwarz, and J.-C. Diels, Journal of Optics A **3**, 146 (2001).

[8] L. Arantchouk, A. Houard, Y. Brelet, J. Carbonnel, J. Larour, Y.-B. André, and A. Mysyrowicz, Applied Physics Letters **102**, 163502 (2013).

[9] T. Dwyer, J. Greig, D. Murphy, J. Perin, R. Pechacek, and M. Raleigh, IEEE Transactions on Antennas and Propagation **32**, 141 (1984).

[10] Y. Brelet, A. Houard, G. Point, B. Prade, L. Arantchouk, J. Carbonnel, Y.-B. André, M. Pellet, and A. Mysyrowicz, Applied Physics Letters **101**, 264106 (2012).

[11] J. S. Townsend, *Electricity in Gases* (Oxford University Press, Oxford, UK, 1915).

[12] F. Paschen, Annalen der Physik **273**, 69 (1889).

[13] E. M. Bazelyan and Y. P. Raizer, *Spark Discharge* (CRC Press, Boca Raton, FL, USA, 1998).

[14] E. Sili, F. Koliatene, and J. P. Cambronne, in *Conference on Electrical Insulation and Dielectric Phenomena (CEIDP)* (2011) pp. 464–467.

[15] Y. I. Davydov, IEEE Transactions on Nuclear Science **53**, 2931 (2006).

[16] L. B. Loeb and J. M. Meek, *The Mechanism of Electric Spark* (Clarendon Press, Oxford, UK, 1941).

[17] H. Raether, *Electron Avalanches and Breakdown in Gases* (Butterworths, London, UK, 1964).

[18] E. Takahashi, S. Kato, H. Furutani, A. Sasaki, Y. Kishimoto, K. Takada, S. Matsumura, and H. Sasaki, Journal of Physics D **44**, 302001 (2011).

[19] A. Bondiou and I. Gallimberti, Journal of Physics D **27**, 1252 (1994).

[20] X. M. Zhao, J.-C. Diels, C. Y. Wang, and J. M. Elizondo, IEEE Journal of Quantum Electronics **31**, 599 (1995).

[21] D. Comtois, C. Y. Chien, A. Desparois, F. Génin, G. Jarry, T. W. Johnston, J.-C. Kieffer, B. La Fontaine, F. Martin, R. Mawassi, H. Pépin, F. A. M. Rizk, F. Vidal, P. Couture, H. P. Mercure, C. Potvin, A. Bondiou-Clergerie, and I. Gallimberti, Applied Physics Letters **76**, 819 (2000).

[22] S. Tzortzakis, B. Prade, M. Franco, A. Mysyrowicz, S. Hüller, and P. Mora, Physical Review E **64**, 057401 (2001).

[23] G. Méjean, R. Ackermann, J. Kasparian, E. Salmon, J. Yu, J.-P. Wolf, K. Rethmeier, W. Kalkner, P. Rohwetter, K. Stelmaszczyk, and L. Wöste, Applied Physics Letters **88**, 021101 (2006).

[24] B. Zhou, S. Akturk, B. Prade, Y.-B. André, A. Houard, Y. Liu, M. Franco, C. D'Amico, E. Salmon, Z.-Q. Hao, N. Lascoux, and A. Mysyrowicz, Optics Express **17**, 11450 (2009).

[25] M. Scheller, N. Born, W. Cheng, and P. Polynkin, Optica **1**, 125 (2014).

[26] M. Clerici, Y. Hu, P. Lassonde, C. Milián, A. Couairon, D. N. Christodoulides, Z. Chen, L. Razzari, F. Vidal, F. Légaré, D. Faccio, and R. Morandotti, Science Advances **1** (2015).

Chapter 6

Two-color interferometer for the study of filamentation-guided sparks

Contents

Introduction

A crucial point in the development of applications for filamentation-guided sparks is to have a precise knowledge of the plasma parameters in the discharge. This asks for an accurate plasma diagnostic able, among other things, to give a precise estimate of the plasma lifetime. A natural choice is to choose electron density as the recorded parameter, since the very notion of plasma is intrinsically linked to the existence of free electrons in the medium.

Electron density is a parameter that can be measured using a wide range of plasma diagnostics, from the diffusion of electromagnetic waves on the plasma to the study of plasma luminescence. However, one of the most widespread technique is based on the measurement of the plasma refractive index using all optical methods such as reflectometry, Schlieren imaging or interferometry. This last diagnostic was chosen because of its high accuracy, its ability to give an absolute density measurement and because of its adaptability to various experimental conditions [1].

This Chapter first deals with basics of interferometry for the measurement of a refractive index spatial profile. In a second part, the plasma refractive index is linked to electron density. Finally, the experimental setup and interferogram processing are presented, and the performance of the interferometer is assessed.

6.1 Interferometry as a refractive index measurement method

6.1.1 Principles of interferometry

Interferometry is a very efficient optical method to measure a refractive index spatial profile. It is based on the combination of two weakly dephased electromagnetic waves, the corresponding phase shift being due to different optical paths for the two beams. For instance, considering two harmonic electromagnetic plane waves meeting at a given position M, and assuming a similar polarization state for the two waves, we can write the total electric field in M as:

$$E(M,t) = E_1 \cos(\omega t + \varphi_1(t)) + E_2 \cos(\omega t + \varphi_2(t)). \tag{6.1}$$

The resulting intensity, as recorded by a detector of characteristic response time τ, is given by:

$$I(M) = \left\langle \left|\left| \vec{S}(M,t) \right|\right| \right\rangle_\tau = \frac{\epsilon_0 c n(M)}{2} \left\langle \left|\left| E(M,t)^2 \right|\right| \right\rangle_\tau , \tag{6.2}$$

$\vec{S}$ being the Poynting vector and $\langle\rangle_\tau$ corresponds to the time averaging operator during a time τ. We can rewrite this expression as:

$$\begin{aligned} I(M) =& \frac{\epsilon_0 c n(M)}{2} \left(E_1^2 \left\langle \cos^2\left(\omega t + \varphi_1(M,t)\right) \right\rangle_\tau + E_2^2 \left\langle \cos^2\left(\omega t + \varphi_2(M,t)\right) \right\rangle_\tau \right. \\ & \left. + 2E_1 E_2 \left\langle \cos\left(\varphi_2(M,t) - \varphi_1(M,t)\right) \right\rangle_\tau \right). \end{aligned} \tag{6.3}$$

If $\tau \gg 2\pi/\omega$, then:

$$\left\langle \cos^2\left(\omega t + \varphi_{1,2}(M,t)\right) \right\rangle_\tau = \frac{1}{\tau} \int_0^\tau \cos^2\left(\omega t + \varphi_{1,2}(M,t)\right) \, \mathrm{d}t \approx \frac{1}{2}. \tag{6.4}$$

In the visible/near infrared range that we use in our diagnostic, $\omega \sim 10^{15}$ rad $\cdot$ s^{-1}, meaning $2\pi/\omega \sim 10$ fs. Therefore we can always simplify the time average in this way. Finally equation (6.3) yields:

$$I(M) = \frac{\epsilon_0 c n(M)}{2} \left(\frac{E_1^2}{2} + \frac{E_2^2}{2} + E_1 E_2 \left\langle \cos\left(\varphi_2(M,t) - \varphi_1(M,t)\right) \right\rangle_\tau \right). \tag{6.5}$$

If the two interfering electromagnetic waves are coherent, i. e. the time variation of the relative phase $\varphi_2(M,t) - \varphi_1(M,t)$ occurs over times far larger than τ, then they will give birth to interference: the total intensity in M will no longer be given by the sum of the two independent waves, but will be modulated by a factor which depends on the relative phase between these waves. This corresponds to the working principle of interferometry: the refractive index of a medium can be determined from the interaction of an electromagnetic wave propagating through this medium (the probe beam) with another wave propagating only in a reference medium with a known refractive index n_{ref} (the reference beam). Measuring the variation of the total intensity at the interaction point, one can extract the value of the phase shift, which is linked to the refractive index following:

$$\varphi_2(M,t) - \varphi_1(M,t) = \Delta\varphi(M,t) = \frac{2\pi}{\lambda} \int_{s_1}^{s_2} \left(n(\vec{r}) - n_{ref}(\vec{r}) \right) \mathrm{d}s, \tag{6.6}$$

where s is the curvilinear coordinate along the propagation of the probe beam. Since lasers have a coherence time important enough so that any detector (including the naked eye) is able to detect this interference effect, their use as a light source in interferometric setups is widespread.

6.1.2 Interferometric setup

6.1.2.1 Various interferometers

Many interferometric setups exist, and can be broadly split in two categories: wavefront division interferometers and amplitude division interferometers. The first category relies on a physical splitting of the initial beam to generate the probe beam and the reference beam, for instance Lloyd's mirror or Fresnel's mirrors. The second category results in two beams sharing the whole wavefront of the incident beam, but with a weaker intensity by means of beam splitters.

The interferometer I decided to use is an amplitude division interferometer: the Mach-Zehnder interferometer.

6.1.2.2 The Mach-Zehnder interferometer

The major strength of the Mach-Zehnder interferometer lies in its ability to be adapted to virtually any experimental configuration. As displayed in figure 6.1, the initial beam is separated in two distinct paths, or arms, by means of a beam splitter. The object to be studied is placed in one of the arms (probe arm) while the other arm (reference arm) must remain unperturbed. The two beams are recombined at the output of the interferometer using a second beam splitter, generating an interference pattern. An imaging system (the most common being a single positive lens) generates the image of the studied object on a detector.

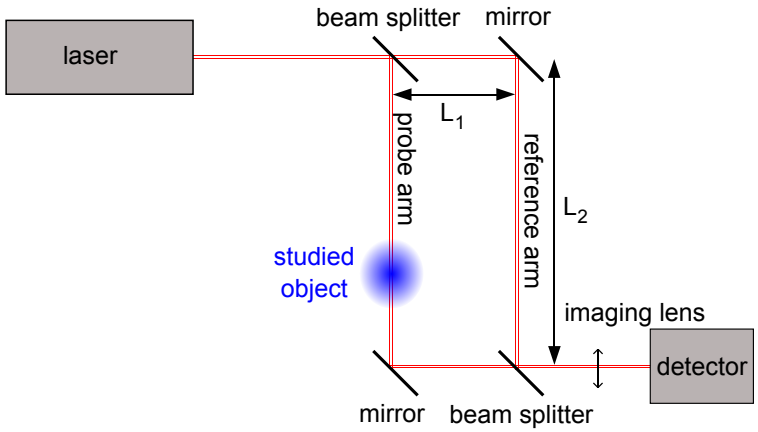

Figure 6.1: Schematic representation of a Mach-Zehnder interferometer.

Using a highly coherent source, such as a laser, with a perfectly aligned Mach-Zehnder interferometer with the same arm length does not yield any interference pattern since the two output beam are in phase at all times. Still, it is more useful for a refractive index measurement to register the deformation of an interference pattern when the probe object is added in the probe arm, rather than its appearance. To this purpose, the interferometer is first slightly misaligned so that interference fringes appear at its output, for instance by tilting one of the two mirrors by an angle α, meaning that the beam in the concerned arm will have an incidence angle of $\pi/4 + \alpha$ on optics. The equivalent configuration of the interferometer is represented in figure 6.2, dubbed *air wedge* configuration.

Supposing the input beam is a plane wave, the difference of optical paths followed by the green

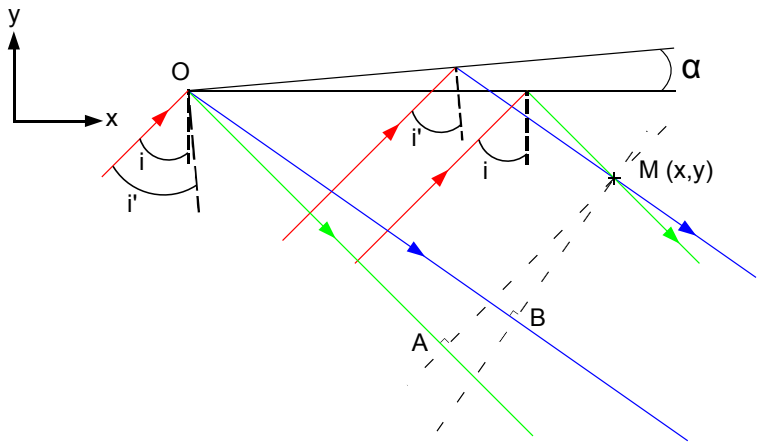

Figure 6.2: Schematic drawing of light rays in the equivalent representation of a Mach-Zehnder interferometer in an air wedge configuration. The incident beam (red) generates two non-parallel beams due to the angle α.

and blue rays at point M, $\delta(M)$, is geometrically given as:

$$\begin{aligned}\delta(M) = \delta(x,y) &= n_{ref}(OB - OA)\\ &= n_{ref}OM\left(\cos\left(\widehat{BOM}\right) - \cos\left(\widehat{AOM}\right)\right)\\ &= n_{ref}\sqrt{x^2+y^2}\left(\cos\left(\frac{\pi}{2} - \left(i + 2\alpha + \left(\vec{e_x},\overrightarrow{OM}\right)\right)\right) - \cos\left(\frac{\pi}{2} - \left(i + \left(\vec{e_x},\overrightarrow{OM}\right)\right)\right)\right)\\ &= -2n_{ref}\left(x\cos(i+\alpha)\sin(\alpha) + y\sin(i+\alpha)\sin(\alpha)\right). \end{aligned} \tag{6.7}$$

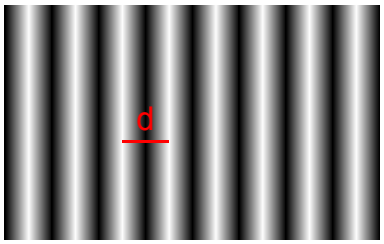

Figure 6.3: Rectilinear interference fringes from an air wedge.

Interference will be constructive if $\delta(M) = m\lambda, m \in \mathbb{Z}$, which defines a family of planes orthogonal to the (x,y) plane satisfying the following equations:

$$y = -\frac{x}{\tan(i+\alpha)} - \frac{m\lambda}{2\sin(i+\alpha)\sin(\alpha)}. \tag{6.8}$$

These planes are separated one from the other by a distance d, called fringe spacing, which is equal to:

$$d = \frac{\lambda}{2\sin(\alpha)}. \tag{6.9}$$

The interference pattern therefore consists of several fringes alternatively bright and dark parallel to the z axis (figure 6.3). This pattern in not localized in space and appears in the whole area where the two recombined beams interact.

When a phase object is placed in the probe beam, the interference pattern at the output will be modified. If this object is characterized by a discontinuous refractive index profile (a piece of glass placed in air, for instance), this discontinuity will be recorded on the fringe pattern. In this case, it is impossible to deduce the absolute phase shift induced by the object (see figure 6.4-(a)). Conversely, if the refractive index profile is continuous, fringes will also distort in a continuous way, which will enable one to measure the absolute phase shift if the probe beam is larger than the probed object (figure 6.4-(b)). This condition is crucial because it ensures that unperturbed areas will still be present in the fringe pattern, defining the phase reference necessary to extract the absolute phase shift.

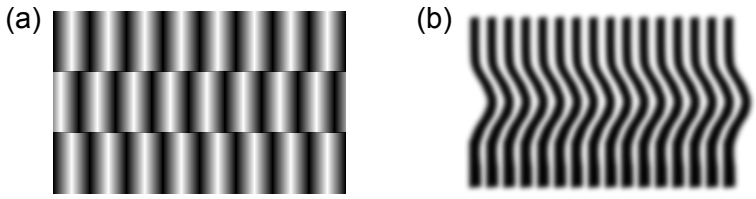

Figure 6.4: Fringe pattern from an air wedge recorded when a phase object is introduced in the probe arm. (a): the object is characterized by a discontinuous refractive index profile. (b): the object has a continuous refractive index profile.

6.1.3 Evaluation of the refractive index spatial profile

We have just seen that interferometry gives access to the absolute phase shift induced by a phase object. But extracting the refractive index spatial profile from this measurement is not obvious, because the two functions are linked through the integral relation of equation (6.6). If this step is immediate in the case of a constant refractive index, it is much more complicated if the corresponding spatial profile is an arbitrary function. Actually, no general solution to this problem exists. In the case of very complex geometries, one can multiply measurement chords to yield an approximated, reconstructed index profile, that is tomography [1]. However, there is a special case for which an exact solution is known: a cylindrically-symmetric refractive index spatial profile probed orthogonally to the symmetry axis, as represented in figure 6.5. This case is important in plasma physics, especially in the field of electric discharges, because such discharge plasmas exhibit this symmetry.

Considering that the phase shift $\Delta\varphi(y,z)$ recorded by the detector is integrated along the whole probe arm of the interferometer, we can write:

$$\Delta\varphi(y,z) = \frac{2\pi}{\lambda}\int_{x_1}^{x_2}(n(x,y,z) - n_{air})\,\mathrm{d}x. \tag{6.10}$$

Since $n(x,y,z) = n(r,z)$, and changing x for r under the integral we find:

$$\Delta\varphi(y,z) = \frac{2\pi}{\lambda}\left(\int_y^{\sqrt{x_1^2+y^2}}\frac{r(n(r,z) - n_{air})}{\sqrt{r^2-y^2}}\,\mathrm{d}r + \int_y^{\sqrt{x_2^2+y^2}}\frac{r(n(r,z) - n_{air})}{\sqrt{r^2-y^2}}\,\mathrm{d}r\right). \tag{6.11}$$

If x_1 and x_2 are large enough with respect to the object size, i. e. $\forall(y,z) \in \mathbb{R}^2, n(x_1,y,z) \approx n(x_2,y,z) \approx n_{air}$, then:

$$\Delta\varphi(y,z) = \frac{4\pi}{\lambda}\int_y^{+\infty}\frac{r(n(r,z) - n_{air})}{\sqrt{r^2-y^2}}\,\mathrm{d}r. \tag{6.12}$$

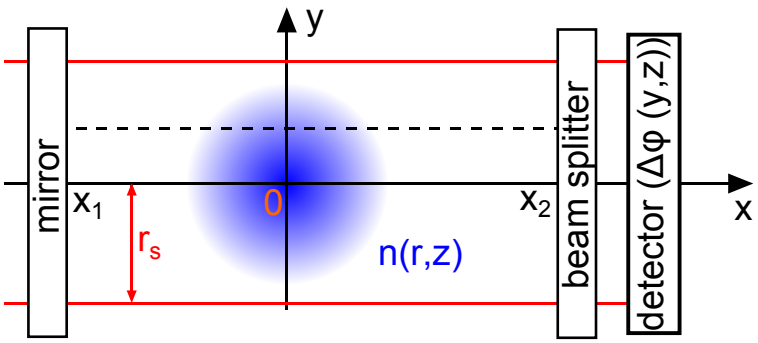

Figure 6.5: Schematic depiction of the probe arm of the interferometer, with a cylindrically-symmetric probed object.

This operation is proportional to the Abel transform of the function $n - n_{air}$. The Abel transform of a given function f is defined as:

$$\mathcal{A}(f)(x) = 2\int_x^{+\infty} \frac{yf(y)}{\sqrt{y^2 - x^2}}\,\mathrm{d}y. \tag{6.13}$$

If the function $n - n_{air}$ satisfies:

$$\forall z \in \mathbb{R}, \lim_{r\to+\infty} r(n(r,z) - n_{air}) = 0, \tag{6.14}$$

then its inverse Abel transform is defined and can be used to retrieve $n(r,z)$ from $\Delta\varphi(y,z)$:

$$n(r,z) = n_{air} - \frac{\lambda}{2\pi^2}\int_r^{+\infty} \frac{\partial\Delta\varphi}{\partial y}(y,z)\frac{\mathrm{d}r}{\sqrt{y^2 - r^2}}. \tag{6.15}$$

This last step is meaningful only if $\forall z, \Delta\varphi(y = \pm r_s,z) \approx 0$, that is if the probe beam is large enough with respect to the probe object so that some areas in the interference pattern are left undisturbed.

6.1.4 Summary

To summarize, interferometry is a technique enabling one to measure an optical phase shift with a precision easily able to reach 100 mrad. This corresponds to the characterization of the phase front of the probe beam with a $\sim \lambda/100$ accuracy. Since the phase shift is proportional to the line-integrated optical index of the probed object, it is impossible to find back the refractive index spatial profile on a general basis. However this becomes possible in at least two cases: that of a constant refractive index, and that of a cylindrically-symmetric refractive index profile. In this last case, the restitution procedure is made possible by the use of the inverse Abel transform.

6.2 Plasma two-color interferometry

The goal of plasma interferometry is to find the electron density spatial profile from a refractive index measurement. To this purpose, electron density must therefore be linked to the plasma refractive index first.

6.2.1 Modeling the plasma refractive index

Plasma is a medium consisting of free electrons, ions and neutrals. Each species reacts differently to the electromagnetic excitation from the probe beam in the interferometer. Moreover, in the case of heavy species, two contributions arise from bound electrons and nuclei, respectively. The total plasma polarization therefore reads:

$$\vec{P} = \vec{P}_e + \vec{P}_{i,e} + \vec{P}_{i,n} + \vec{P}_{n,e} + \vec{P}_{n,n}, \tag{6.16}$$

where $\vec{P}_e$ corresponds to the free electronic response, $\vec{P}_{i,e}$ and $\vec{P}_{i,n}$ to the ion-bound electronic response and the ionic nuclear response, respectively, and $\vec{P}_{n,e}$ and $\vec{P}_{n,n}$ to the neutral-bound electronic response and the neutral nuclear response, respectively. A first approximation can be made at this point. Since nuclei are far heavier than electrons ($m_{nuc}/m_e > 10^3$), they have such an inertia at optical frequencies that their contribution can be neglected [2]. Plasma polarization is reduced to:

$$\vec{P} = \vec{P}_e + \vec{P}_{i,e} + \vec{P}_{n,e}. \tag{6.17}$$

It is now necessary to model each term of this last equation. Because we make use of a weak probe laser (energy ~ 100 µJ, pulse duration ~ 10 ns), no nonlinear effects from the plasma are expected and the plasma polarization can be estimated in the linear regime.

6.2.1.1 Free electronic polarization

The free electronic polarization is already calculated in Chapter 1 (section 1.3.2.3). The calculation is based on the classical Drude model, in which the movement of a free electron in a cold, non-magnetized plasma and in the probe beam electric field is determined by the following equation:

$$m_e \frac{\mathrm{d}^2 \vec{r}}{\mathrm{d}t^2} = -e\vec{E} - 2\pi m_e \nu_c \frac{\mathrm{d}\vec{r}}{\mathrm{d}t}. \tag{6.18}$$

Considering the probe beam as a monochromatic wave of angular frequency ω, and taking the Fourier transform of the last equation, the electron position reads:

$$\vec{r}(\omega) = \frac{e\vec{E}/m_e\omega^2}{1 - i2\pi\nu_c/\omega}. \tag{6.19}$$

Since we supposed the plasma to be cold, ions keep a fixed position and the free electronic polarization is given by $\vec{P}_e = -en_e\vec{r}$, giving:

$$\vec{P}_e(\vec{r},\omega) = -\epsilon_0 \frac{\omega_p^2(\vec{r})}{\omega^2(1 - i2\pi\nu_c/\omega)} \vec{E}(\vec{r}), \tag{6.20}$$

where $\omega_p = \sqrt{n_e e^2/\epsilon_0 m_e}$ is the plasma frequency. In our case, the probe beam is either visible or in the near infrared so $\omega \sim 10^{15}$ rad $\cdot$ s^{-1}. The collision frequency was estimated in Chapter 1 as $\nu_c \approx 2$ THz so that $\omega \gg 2\pi\nu_c$. Equation (6.20) can then be simplified:

$$\vec{P}_e(\vec{r},\omega) = -\epsilon_0 \frac{\omega_p^2(\vec{r})}{\omega^2} \vec{E} = -\epsilon_0 \frac{4\pi c^2 r_e}{\omega^2} n_e(\vec{r})\vec{E}, \tag{6.21}$$

where the classical electron radius $r_e = e^2/4\pi\epsilon_0 m_e c^2$ was introduced.

6.2.1.2 Bound electronic polarization

The calculation of the bound electronic polarization is quite similar to the evaluation of the linear dielectric response performed in Chapter 1 (section 1.2.1.1). In this computation, we saw that a classical estimation using the Lorentz model (elastically-bound electrons) and a full quantum mechanical estimation yielded almost the same expression for the linear susceptibility. For a given species a in the plasma, the corresponding polarization due to a-bound electrons reads:

$$\vec{P}_a(\vec{r},\omega) = \sum_{k=1}^{N_a} f_{k,g} \frac{n_a(\vec{r})e^2/m_e}{\omega_{k,g}^2 - \omega^2 - 2i\omega\gamma_{k,g}} \vec{E}. \tag{6.22}$$

In this equation, $|g\rangle$ denotes the ground state of a, which is supposed to be the initial state of all a molecules, n_a is the density of species a, $\omega_{k,g}$ and $\gamma_{k,g}$ are respectively the characteristic frequency and damping factor of a given $|g\rangle \rightarrow |k\rangle$ transition, and $f_{k,g}$ is the oscillator strength associated to that transition. Oscillator strengths obey the following sum rule:

$$\sum_{k=1}^{N_a} f_{k,g} = N_e, \tag{6.23}$$

N_e being the total number of bound electrons in a. Since our probe wavelengths are far from any characteristic resonance of the probed species, we neglect the damping factor for all transitions. Finally, in the most general way, the total bound electronic polarization can be written as:

$$\vec{P}_{i,e}(\vec{r},\omega) + \vec{P}_{n,e}(\vec{r},\omega) = \frac{e^2}{m_e} \left(\sum_{l=1}^{N_i} n_{i,l}(\vec{r}) \sum_{k_l=1}^{N_l} \frac{f_{k_l}}{\omega_{k_l}^2 - \omega^2} + \sum_{m=1}^{N_n} n_{n,m}(\vec{r}) \sum_{k_m=1}^{N_m} \frac{f_{k_m}}{\omega_{k_m}^2 - \omega^2} \right) \vec{E}, \tag{6.24}$$

where N_i is the total number of ionic species and N_n that of neutral species in the plasma.

We will make several approximations at this point to simplify equation (6.24). First, we will neglect the contribution from ion-bound electrons. This can be justified by the fact that our studied sparks are only partially ionized, with an ionization degree never exceeding 20 %. However, this approximation is not enough since the expression of the neutral-bound electronic polarization remains very complex. An accurate evaluation of this term would ask for a precise knowledge of air chemistry during the discharge, which is particularly complex with the formation of new species, molecular dissociation, etc. Alpher and White experimentally demonstrated that for air, the refractivity at standard pressure and temperature can be used at least up to 5000 K in interferometric measurements. They showed that molecular oxygen is the first molecule to dissociate when temperature is raised, but since the polarizability ratio between O_2 and O is 2.11, this effect is almost negligible on the whole gas refractivity [3]. This becomes more problematic when N_2 dissociates because the polarizability ratio for nitrogen is equal to 1.55. We consequently adopt this formalism and consider the neutral-bound electronic response to yield the same response as air molecules:

$$\begin{aligned} \vec{P}_{n,e}(\vec{r},\omega) &= \frac{e^2}{m_e} \sum_{m=\mathrm{O_2},\mathrm{N_2}} n_{n,m}(\vec{r}) \sum_{k_m=1}^{N_m} \frac{f_{k_m}}{\omega_{k_m}^2 - \omega^2} \vec{E} \\ &= \frac{e^2 n_n(\vec{r})}{m_e} \left(0.2 \sum_{k_{\mathrm{O_2}}=1}^{N_{\mathrm{O_2}}} \frac{f_{k_{\mathrm{O_2}}}}{\omega_{k_{\mathrm{O_2}}}^2 - \omega^2} + 0.8 \sum_{k_{\mathrm{N_2}}=1}^{N_{\mathrm{N_2}}} \frac{f_{k_{\mathrm{N_2}}}}{\omega_{k_{\mathrm{N_2}}}^2 - \omega^2} \right) \vec{E}, \end{aligned} \tag{6.25}$$

where n_n is total air density. This expression is a slow varying function of ω and can be considered constant in the visible-near infrared frequency range that we use. Usually, polarization is written

following the Gladstone-Dale law:

$$\vec{P}_{n,e}(\vec{r}) = 2\frac{\beta}{n_0} n_n(\vec{r}), \tag{6.26}$$

where β is the Gladstone-Dale constant and n_0 a reference neutral density. The couple (β,n_0) defines the value of air refractive index in given thermodynamic conditions when no plasma is present following:

$$n_{air} = 1 + \beta. \tag{6.27}$$

The reference point in our case is taken as $p = 1.013 \times 10^5$ Pa and $T = 300$ K, for which $n_0 = 2.47 \times 10^{25}$ m^{-3}. Using the empirical Ciddor equation [4], which links the air refractive index to pressure, temperature and humidity level, to have a precise estimation of air refractive index in the visible/near infrared range, we find:

$$\beta = 2.7 \times 10^{-4}. \tag{6.28}$$

6.2.1.3 Plasma refractive index

The probe beam does not result in nonlinear effects in the plasma because of its low intensity. Moreover, studied plasmas are not magnetized, and can therefore be locally considered as linear and isotropic:

$$\vec{P} = \epsilon_0(\epsilon_p - 1)\vec{E}, \tag{6.29}$$

where the plasma dielectric permittivity in linked to the plasma refractive index by:

$$\epsilon_p = n_p^2. \tag{6.30}$$

The plasma refractive index then yields:

$$n_p(\vec{r},t) = \sqrt{1 - \frac{r_e\lambda^2}{\pi} n_e(\vec{r},t) + 2\frac{\beta}{n_0} n_n(\vec{r},t)}. \tag{6.31}$$

As $|n_p^2 - 1| \sim 10^{-4}$, we can derive a Taylor expansion of this expression to finally derive the plasma index:

$$n_p(\vec{r},t) = 1 - \frac{r_e\lambda^2}{2\pi} n_e(\vec{r},t) + \frac{\beta}{n_0} n_n(\vec{r},t). \tag{6.32}$$

6.2.2 Two-color interferometry

Equation (6.32) indicates that the plasma refractive index depends on two independent parameters, namely free electron density and neutral density. In several situations, this dependence on neutral density can be forgotten because the density is equal in the probe arm and in the reference arm. This is of course not the case for the discharges we investigated. We saw in Chapters 2, 3 and 4 that filamentation itself generated a strong hydrodynamic reaction in air because of the deposited laser energy. Sparks discharges are expected to bring even more energy into air, and therefore to give birth to a shock wave and an underdense channel over a ~ 100 ns timescale. As a consequence, neglecting the contribution of bound electrons to the refractive index would result in erroneous or even unphysical measurements with negative electron densities [5].

A solution to discriminate the contribution of free electrons and the contribution of bound electrons to the refractive index is to record the plasma index simultaneously at two different

wavelengths. Indeed, this yields a system of two equations with two unknowns that can be readily solved to give the following solution:

$$\begin{cases} \displaystyle\int_{s_1}^{s_2} n_e(s)\ \mathrm{d}s = \frac{\lambda_1\Delta\varphi(\lambda_1) - \lambda_2\Delta\varphi(\lambda_2)}{r_e(\lambda_2^2 - \lambda_1^2)} \\ \displaystyle\int_{s_1}^{s_2} (n_n(s) - n_0)\ \mathrm{d}s = \frac{n_0}{2\pi\beta}\frac{\lambda_2\Delta\varphi(\lambda_1) - \lambda_1\Delta\varphi(\lambda_2)}{\frac{\lambda_2}{\lambda_1} - \frac{\lambda_1}{\lambda_2}}. \end{cases} \tag{6.33}$$

This method, called two-color interferometry, was proposed at the end of the 1950s by Alpher and White [6]. Since then it has been successfully implemented by several groups [7, 8, 9, 10]. Using this technique, it becomes possible to isolate the free electron density, and to record neutral density as well. Two-color interferometry has also been used to make vibration-insensitive electron density measurements on large experiments, where such effects can become significant [11, 12, 13]. This application is very similar to ours, consisting in discriminating between two different contributions to the phase shift, one of them being independent of the wavelength. In the simpler case where the recorded phase shift only depends on the free electron density, dual-wavelength interferometry can also be used to extend the available dynamic range of the diagnostic, using a short wavelength to probe high-density areas, and shifting to a longer wavelength for low-density regions [14].

6.2.3 Summary

I developed a model for the determination of the plasma refractive index, which turns out to depend mostly on two independent parameters: the free electron density and the neutral density. If neutral density is balanced between the probe arm and the reference arm, then it does not contribute to the measured phase shift. This case corresponds to the standard plasma interferometry, requiring the use of a single wavelength. Conversely, the plasmas we study are generated by electric sparks that give birth to very strong hydrodynamic phenomena, strongly affecting the neutral density in the plasma. In this case, neutral-bound electrons can significantly contribute to the phase shift, making the use of two wavelengths compulsory in order to separate the contribution of free electrons from that of bound electrons.

6.3 Experimental setup for the two-color interferometer

The interferometer is built in a standard Mach-Zehnder configuration (cf. figure 6.6). The probe laser (Quanta Ray GCR-290-10 from Spectra Physics) is a Nd:YAG Q-switched, frequency doubled pulsed laser delivering $\sim$ 100 µJ, 8 ns FWHM light pulses at both 532 and 1064 nm. The probe beam is spatially cleaned and magnified using a beam expander and a 100 µm pinhole, yielding a pseudo-Gaussian collimated beam with a 7.2 mm FWHM at 532 nm and 8.3 mm FWHM at 1064 nm. The delay between the two probe pulses due to the propagation through optical materials is evaluated to a few ps, which is negligible with respect to the duration of laser pulses. The whole interferometer is built on a 60×60 cm^2 breadboard mounted on mechanic isolation feet to reduce vibrations, and entirely enclosed to limit the influence of air turbulence on measurements.

An ultrashort laser pulse from the Ti:sapphire chirped pulse amplification laser chain ENSTAmobile is used to form a filament in the discharge gap, triggering the studied spark. The resulting discharge plasma is generated in one of the arms of the interferometer, perpendicularly to the probe beam. The probe laser is synchronized with the ENSTAmobile using the latter's internal clock, enabling us to precisely adjust the temporal delay between the laser pulses between 0 and 100 ms

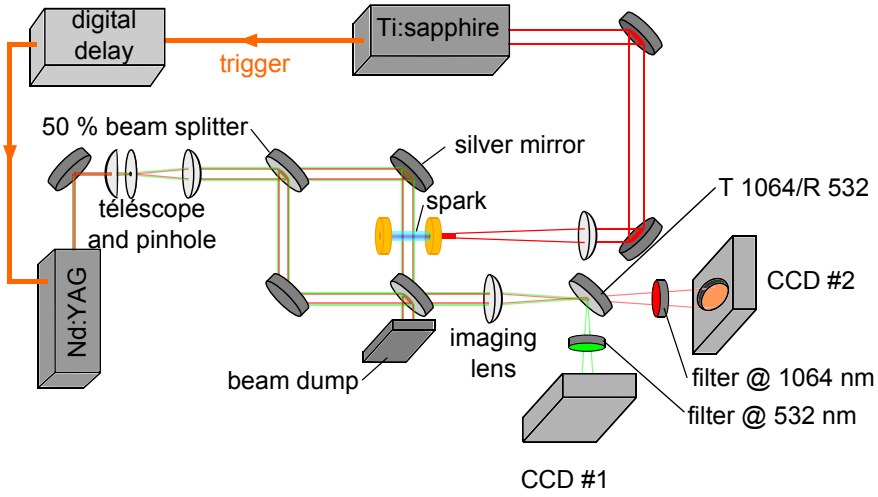

Figure 6.6: Schematic description of the two-color interferometric setup.

with a ns precision and a 1.5 ns jitter. Interferograms are recorded by means of two CCD cameras (TaperCamD-UCD12 from DataRay, Inc.) with a (1360 × 1024) pixel matrix and a 10.5 µm pixel size. Probe wavelengths are separated using a dichroic mirror (T1064/R532). Adapted bandpass filters with < 10 nm bandwidth suppress remaining broadband emission from the plasma. Typically, imaging is done using a $2f/2f$ configuration with a 75 mm focusing lens, but it is also possible to get an arbitrary magnification on the CCD cameras. The interferometer is slightly misaligned so that $\sim 10/20$ fringes (depending on the wavelength) appear on the detectors in absence of plasma in the probing arm.

6.4 Interferogram processing

The advent of computers was a true revolution in the field of plasma diagnostics as a whole, and especially for interferometry. Until then, phase shifts were evaluated directly on photographs of fringe patterns. The accuracy of this method is intrinsically mediocre, but nonetheless used to be the standard. The development of automated numerical data processing resulted in a dramatic increase in sensitivity for interferometers. Since the seminal paper of Takeda *et al.*, in which the authors detail the first rapid phase extraction algorithm based on the fast Fourier transform (FFT) [15], dozens of data processing algorithm applied to interferometry have been published every year, giving access to even faster and more accurate tools.

The use of fast and efficient data processing algorithms is crucial in the development of an interferometric diagnostic. Since the full interferogram processing involves many steps, each implemented algorithm must introduce errors and noise as small as possible to avoid error propagation and amplification. We chose to stick to algorithms that were developed a few years ago, but that were shown to be robust and efficient.

6.4.1 Phase extraction algorithm

Once the interferogram is recorded and discretized by the CCD matrix, the first step in the data processing procedure is to evaluate the relative phase of the fringe signal on the whole plane. To this purpose, I use an algorithm based on a 1-D *continuous wavelet transform* (CWT). Indeed, this

kind of algorithm offers superior reliability and noise-immunity with respect to the routines using the FFT, particularly when the signal to noise ratio is low, when contrast is mediocre or in the case of very localized and noisy areas [16, 17]. We first introduce the CWT and then detail working principles of the algorithm.

6.4.1.1 The continuous wavelet transform

Introduction to the continuous wavelet transform The continuous wavelet transform is a mathematical integral transform consisting in projecting a given function on a base of functions $\psi_{a,b}$, called *wavelets*. These wavelets are obtained by translation and dilatation of a mother wavelet ψ and are then called daughter wavelets. Supposing that ψ is defined over $\mathbb{R}$, then daughter wavelets are defined by:

$$\forall (a,b) \in \mathbb{R}_+^* \times \mathbb{R}, \forall x \in \mathbb{R}, \psi_{a,b}(x) = \frac{1}{\sqrt{a}} \psi \left(\frac{x-b}{a} \right). \tag{6.34}$$

Any function $\psi \in \mathrm{L}^2(\mathbb{R})$ such as:

$$\begin{cases} \displaystyle\int_{\mathbb{R}} \psi(x) \, \mathrm{d}x = 0 \\ \displaystyle\int_{\mathbb{R}} |\psi(x)|^2 \, \mathrm{d}x = 1, \end{cases} \tag{6.35}$$

that is with a zero average value and normalized to 1, can be used as a mother wavelet. Let f be a function in $\mathrm{L}^2(\mathbb{R})$. Then the CWT of f is given by the dot product of f and the daughter wavelet of parameters a and b:

$$f_{CWT}(a,b) = \langle f | \psi_{a,b} \rangle (a,b) = \int_{\mathbb{R}} f(x) \psi_{a,b}^*(x) \, \mathrm{d}x = \frac{1}{\sqrt{a}} \int_{\mathbb{R}} f(x) \psi^* \left(\frac{x-b}{a} \right) \, \mathrm{d}x. \tag{6.36}$$

The inverse continuous wavelet transform is defined only if the mother wavelet satisfies:

$$C_\psi = \int_0^{+\infty} \frac{\left| \hat{\psi}(k) \right|^2}{k} \, \mathrm{d}k < +\infty, \tag{6.37}$$

where $\hat{\psi}$ is the Fourier transform of ψ. In this case, f can be retrieved from its CWT following:

$$f(x) = \frac{2}{C_\psi} R_e \left(\int_0^{+\infty} \int_{\mathbb{R}} \frac{1}{a^2} f_{CWT}(a,b) \psi \left(\frac{x-b}{a} \right) \, \mathrm{d}b \mathrm{d}a \right). \tag{6.38}$$

This result is the theorem of Calderón, Grossmann and Morlet [18].

The mother wavelet is typically a function which is well localized both in direct space and Fourier space, that is which is approximately zero everywhere except on a small interval. It should also share some properties of the signal to study. For instance, if f is a periodic signal, the natural choice for ψ would be an oscillating wavelet. For a given value of a, the spatial extension of $\psi_{a,b}$ is fixed, and the CWT operation evaluates the cross correlation between the daughter wavelet and the signal f along b. The function f_{CWT} is found by repeating continuously this operation along a. This function is defined over a 2-D spatio-spectral space. Indeed, the parameter a defines the extension of $\psi_{a,b}$ in both the direct and Fourier space, and can directly be related to the Fourier frequency, while the b parameter corresponds to the variable in the direct space over which f is defined. If the mother wavelet ψ is a real function defined over $\mathbb{R}$, then f_{CWT} is also real and only gives information about the amplitude of f. To get phase information about f as well, ψ must

be extended to the complex space. The most natural way to perform this step is to consider the analytic signal ψ_{anl} corresponding to ψ:

$$\forall x \in \mathbb{R}, \psi_{anl}(x) = \psi(x) + i\mathcal{H}(\psi)(x), \tag{6.39}$$

where $\mathcal{H}$ is the Hilbert transform. Therefore ψ can be immediately retrieved from the real part of ψ_{anl}. This signal has the very interesting property that its Fourier transform has no negative frequency component. As a simple example, if $\psi(x) = \cos(x)$, the corresponding analytic signal is e^{ix}.

The complex CWT of a signal f with a well-defined instantaneous frequency yields a modulus plane and a phase plane defined over (a,b). The modulus plane is characterized by a parametric curve $a = g(b)$ following the maximum value of $|f_{CWT}|^2$ (spatio-spectral energy density). This curve is called the *ridge* of the CWT and gives, b being fixed, the value of a that results in $\psi_{a,b}$ being as close as possible to $f(b)$ in terms of amplitude and phase. Therefore, along the ridge, the instantaneous frequencies of f and f_{CWT} are the same.

Considering the mother wavelet is centered at $x = 0$:

$$\int_{\mathbb{R}} x|\psi(x)|^2 \, \mathrm{d}x = 0, \tag{6.40}$$

then any daughter wavelet of parameters (a,b) will be centered on $x = b$:

$$\int_{\mathbb{R}} x|\psi_{a,b}(x)|^2 \, \mathrm{d}x = \frac{1}{a}\int_{\mathbb{R}} x \left|\psi\left(\frac{x-b}{a}\right)\right|^2 \, \mathrm{d}x = \int_{\mathbb{R}} (y+b)|\psi(y)|^2 \, \mathrm{d}y = b. \tag{6.41}$$

Its secondmoment spatial extension $\sigma_x^{a,b}$ is:

$$\sigma_x^{a,b} = \sqrt{\int_{\mathbb{R}} x^2|\psi_{a,b}(x)|^2 \, \mathrm{d}x} = a\sqrt{\int_{\mathbb{R}} x^2|\psi(x)|^2 \, \mathrm{d}x} = a\sigma_x. \tag{6.42}$$

As the Plancherel theorem reads:

$$\int_{\mathbb{R}} |\psi(x)|^2 \, \mathrm{d}x = \frac{1}{2\pi}\int_{\mathbb{R}} |\hat{\psi}(k)|^2 \, \mathrm{d}k, \tag{6.43}$$

then the second moment spectral extension of the daughter wavelet is given by:

$$\sigma_k^{a,b} = \sqrt{\frac{1}{2\pi}\int_{\mathbb{R}} \left(k - \frac{k_0}{a}\right)\left|\hat{\psi}_{a,b}(k)\right|^2 \, \mathrm{d}k} = \frac{1}{a}\sqrt{\frac{1}{2\pi}\int_{\mathbb{R}} (k-k_0)\left|\hat{\psi}(k)\right|^2 \, \mathrm{d}k} = \frac{\sigma_k}{a}. \tag{6.44}$$

Finally we have:

$$\sigma_x^{a,b}\sigma_k^{a,b} = \sigma_x\sigma_k, \tag{6.45}$$

that is the volume occupied by the mother wavelet in the spatio-spectral space is the same as that occupied by any daughter wavelet. However the larger the scale parameter a, the wider $\psi_{a,b}$ in the direct space and, as a consequence, the narrower $\hat{\psi}_{a,b}$ in the Fourier space. Also, the fact that the central wavelet frequency of the daughter wavelet $k_0^{a,b}$ makes the CWT intrinsically more sensitive to low frequencies than to high frequencies. This behavior is completely different from that of the Fourier transform, for which the spatial spread of the "daughter wavelet" is infinite (trigonometric polynomials), meaning that any local information about the signal is lost. Conversely, the spectral spread is zero (Dirac distribution), which gives an absolute precision in the Fourier space. The CWT corresponds to a tradeoff between the spatial precision and the spectral precision, enabling it to give a simultaneous representation in both spaces.

The intimate relation linking the scale parameter a to the Fourier frequency still remains non-trivial. Indeed, the fact the daughter wavelet is centered on k_0/a does not necessarily implies that the spatio-spectral energy density $|f_{CWT}(a,b)|^2$ is maximum at this frequency. The rigorous way to find the Fourier frequency corresponding to the a parameter is to compute the CWT of a harmonic function of defined frequency $f(x) = \mathrm{e}^{2i\pi f_x x}$. The scale parameter corresponding to the frequency f_x is found by solving the following equation system:

$$\forall b \in \mathbb{R}, \begin{cases} \dfrac{\partial |f_{CWT}|^2}{\partial a}(a_0,b) = 0 \\ \dfrac{\partial^2 |f_{CWT}|^2}{\partial a^2}(a_0,b) < 0, \end{cases} \tag{6.46}$$

which corresponds to locating the ridge position. This method has been suggested by Meyers *et al.* [19] and applied to commonly used wavelets by Torrence and Compo [20]. Even if it can lead to complex calculations, it is the only way to precisely link f_x and a_0.

The Morlet wavelet The mother wavelet we use in our phase extraction algorithm is the Morlet wavelet, from Jean Morlet, a french geophysicist who pioneered work in the field of wavelet analysis in the 1970s. It is widely used because of its excellent localization both in the direct and Fourier space, but also because it is well adapted to the study of periodical signals [21]. The Morlet wavelet is a complex valued function constituted of a Gaussian window and an oscillating harmonic function:

$$\forall x \in \mathbb{R}, \forall s \in \mathbb{R}, \psi_s(x) = A_s \left(\mathrm{e}^{isx} + B_s \right) \mathrm{e}^{-x^2/2}. \tag{6.47}$$

The parameter s enables one to find a tradeoff between the wavelet spatial and spectral resolution by limiting the number of oscillations in the Gaussian window. Constants A_s and B_s are constrained by the conditions the wavelet must fulfill to be used as a mother wavelet (equation (6.35)). Thus:

$$\begin{cases} A_s = \pi^{-1/4} \left(1 + \mathrm{e}^{-s^2} - 2\mathrm{e}^{-3s^2/4} \right)^{-1/2} \\ B_s = -\mathrm{e}^{-s^2/2}. \end{cases} \tag{6.48}$$

The Morlet wavelet of parameter $s = 3$ is represented in figure 6.7. The Fourier transform of the Morlet wavelet is given by:

$$\begin{cases} \hat{\psi}_s(k) = A_s \left(\mathrm{e}^{-(s-k)^2/2} + B_s \mathrm{e}^{-k^2/2} \right), k \geq 0 \\ \hat{\psi}_s(k) = 0, k < 0. \end{cases} \tag{6.49}$$

It consists of a sum of two Gaussian functions, of which the major component is centered on $k = s$ (figure 6.7-(b)).

When s becomes large enough (typically $s \geq 5$), the Morlet wavelet can be simplified in the following way:

$$\begin{cases} \psi_s(x) = \frac{1}{\sqrt[4]{\pi}} \mathrm{e}^{isx} \mathrm{e}^{-x^2/2} \\ \hat{\psi}_s(k) = \frac{1}{\sqrt[4]{\pi}} \mathrm{e}^{-(s-k)^2/2}, k \geq 0 \\ \hat{\psi}_s(k) = 0, k < 0. \end{cases} \tag{6.50}$$

From now on, we will only use values of s so that this approximation is valid.

We can explicit the link between the scale parameter a and the Fourier frequency in the case of the Morlet wavelet, that is solving the equation system (6.46). To this purpose, we first have to calculate the spatio-spectral energy density $g(a,b)$ of a complex exponential of known frequency f_x:

$$g(a,b) = \left| \frac{1}{\sqrt[4]{\pi}} \int_{\mathbb{R}} \mathrm{e}^{i2\pi f_x x} \psi_s^* \left(\frac{x-b}{a} \right) \mathrm{d}x \right|^2 = \frac{a}{\sqrt{\pi}} \mathrm{e}^{-(s-2\pi f_x a)^2/2}. \tag{6.51}$$

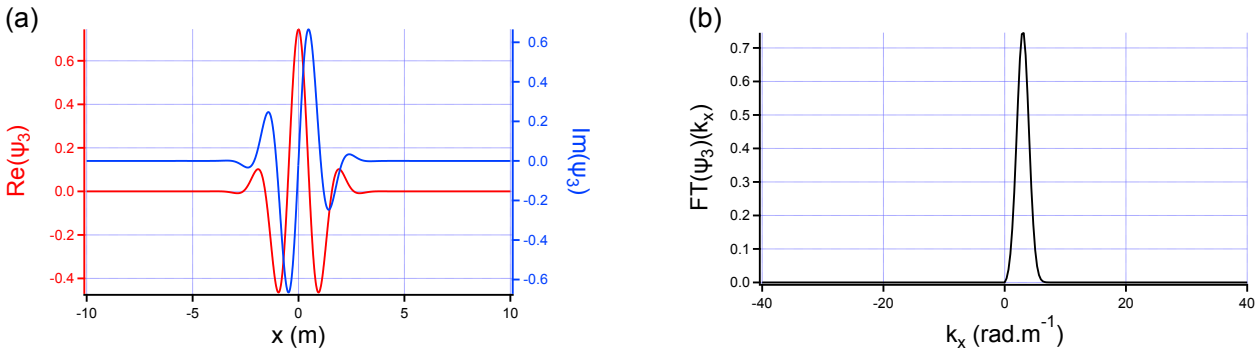

Figure 6.7: (a): representation of the complex Morlet wavelet for $s = 3$. (b): Fourier transform of the same wavelet.

Then we have to find the roots of the following equation:

$$\frac{\partial g}{\partial a}(a_0,b) = \frac{1}{\sqrt{\pi}} \mathrm{e}^{-(s-2\pi f_x a)^2/2}(1 - 4\pi a_0 f_x(2\pi a_0 f_x - s)) = 0. \tag{6.52}$$

This is a polynomial of degree 2 with two real roots, of which only one is positive. Since the scale parameter a is defined over $\mathbb{R}_+^*$, only this root is kept:

$$a_0^+ = \frac{s + \sqrt{2 + s^2}}{4\pi f_x}. \tag{6.53}$$

The last step to perform is to check that a_0^+ is indeed a local maximum of g. A tedious calculation finally leads to:

$$\frac{\partial^2 g}{\partial a^2}(a_0^+,b) < 0. \tag{6.54}$$

For the Morlet wavelet, the scale parameter and the Fourier frequency are therefore linked through:

$$f = \frac{s + \sqrt{2 + s^2}}{4\pi a}. \tag{6.55}$$

We are now able to perform quantitative time/frequency analysis. For instance, let us consider the following test function:

$$f_{test}(x) = \cos(2\pi(5 + 0.075x)x). \tag{6.56}$$

It is characterized by a frequency chirp, that is the instantaneous frequency of the signal evolves in space.

We evaluated the Fourier transform of f_{test} by means of a FFT algorithm. We first had to choose a window for the study, in this case the interval [0,100 m]. The corresponding spectral energy density is plotted in figure 6.8-(a). This spectral energy density is equal to 0 everywhere except in the $\pm$[5,20 m^{-1}] frequency interval. These frequency boundaries actually correspond to the signal instantaneous frequency at $x = 0$ and $x = 100$ m. At best, the Fourier transform is therefore only able to show the values that the instantaneous frequency can take during propagation, but cannot correlate these value with the spatial dimension. If we now perform the Morlet CWT of f_{test} and look at the resultant spatio-spectral energy density plane (figure 6.8-(b)), we can clearly see the ridge of the wavelet transform, that indicates the evolution of the instantaneous frequency of f_{test} in space.

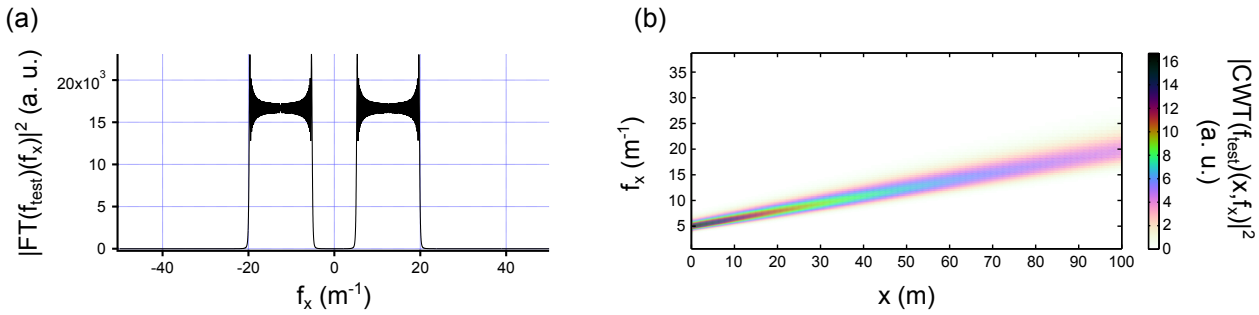

Figure 6.8: (a): spectral energy density from the Fourier transform of f_{test}. (b): spatio-spectral energy density from the CWT of f_{test}.

The CWT is therefore an incredible tool for time/frequency analysis, which is able to extract information about a signal amplitude and phase at the *local scale*, while the Fourier transform can only perform *global scale* analysis.

6.4.1.2 Description of the algorithm

CWT algorithm The core of the phase extraction algorithm is a 1-D fast Morlet CWT routine. It works similarly to the one detailed by Torrence and Compo [20]. It simply re-expresses the CWT as defined in equation (6.36) as a convolution product between f and the daughter wavelet:

$$f_{CWT}(a,b) = \frac{1}{\sqrt{a}} \int_{\mathbb{R}} f(x)\psi^* \left(\frac{x-b}{a} \right) \, \mathrm{d}x = \int_{\mathbb{R}} f(x) g_a(b-x) \, \mathrm{d}x = \sqrt{2\pi} f * g(b), \tag{6.57}$$

where $g_a(x) = \psi^*(-x/a)/\sqrt{a}$. Immediately, f_{CWT} can be rewritten following:

$$f_{CWT}(a,b) = \sqrt{2\pi}\mathcal{F}^{-1}(\hat{f}\hat{g}_a)(a,b) = \int_{\mathbb{R}} \hat{f}(k)\hat{g}_a(k)\mathrm{e}^{ikb} \, \mathrm{d}k. \tag{6.58}$$

The Fourier transform of g_a, $\hat{g}_a$, is given by:

$$\hat{g}_a(k) = \frac{1}{\sqrt{2\pi a}} \int_{\mathbb{R}} \psi^* \left(-\frac{x}{a} \right) \mathrm{e}^{-ikx} \, \mathrm{d}x = -\sqrt{\frac{a}{2\pi}} \hat{\psi}^*(ak). \tag{6.59}$$

The algorithm therefore works by fixing a value for a, computing the function $\hat{g}_a$, and finally evaluating the inverse Fourier transform of $\hat{f}\hat{g}_a$, taking advantage of the speed of FFT routines. Typically, the scale parameter a is discretized in a logarithmic way. This scale is all the more adapted to the CWT because the wavelet transform has more sensitivity at low frequencies than at high frequencies. In our case, a is discretized using 12 points per octave, which corresponds to the musical frequency sampling introduced by J. S. Bach.

Phase extraction algorithm The phase extraction algorithm works as follows: each line of the interferogram is selected one after the other (see figure 6.9-(a) for an example of recorded interferogram). The 1-D Morlet CWT routine is then applied to this signal, yielding a complex plane that is split into a modulus plane (figure 6.9-(b)) and a phase plane (figure 6.9-(c)).

The next step consists in retrieving the true wavelet ridge position from the CWT modulus map. Here, *true ridge* means the ridge resulting from the periodic interference fringes. Indeed, noise can also generate local maxima on the CWT modulus map, and the amplitude of such parasite peaks

can even dwarf the true ridge if contrast and/or signal to noise ratio are low. The most basic ridge extraction routines, which simply look for the global maxima on the CWT modulus map, can therefore be tricked quite easily and yield a wrong phase reconstruction.

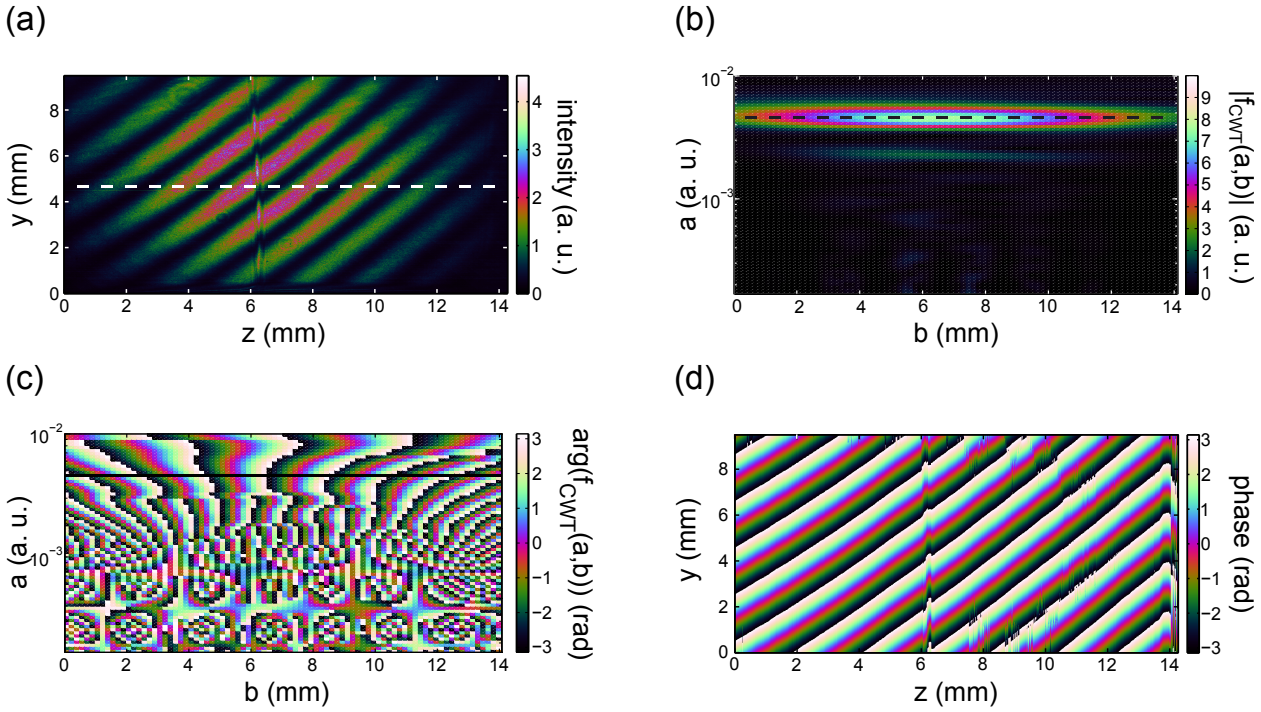

Figure 6.9: Illustration of working principles of the phase extraction algorithm. (a): example of recorded interferogram to deconvoluate. The test line is represented by the white dashed line. (b): modulus of the CWT of the test line. The wavelet ridge is highlighted by the black dashed line. (c): phase of the CWT of the test line. The wavelet ridge position was reported here, yielding the phase of the test line. (d): once all the lines of the interferogram are processed, the phase for the full image is extracted.

A way to overcome this and to enhance the robustness of the algorithm with respect to noise is to add a criterion for the ridge selection other than looking for the curve of maximum modulus. As the fringe frequency is relatively stable in space, unlike that of the noise, the true ridge should not present too pronounced steps along the scale parameter a. The ridge extraction routine then must be able to discard candidate ridges according to this characteristic. This operation is performed as an optimization problem, the routine looking for the parametric curve $a = g(b)$ minimizing a cost function C defined as:

$$C(g(b),b) = -A_1 \int_{-\infty}^{b} |f_{CWT}(g(b'),b')|^2 \, \mathrm{d}b' + A_2 \int_{-\infty}^{b} \left| \frac{\mathrm{d}g}{\mathrm{d}b'}(b') \right|^2 \, \mathrm{d}b'. \tag{6.60}$$

The first term tends to decrease the cost of a candidate ridge if its amplitude is strong, while the second term tends to increase it if this candidate is experiencing strong variations along a. The weighting coefficients A_1 and A_2 allow to balance each contribution to the cost. The choice of these parameters is usually done as follows. First, a simple, direct maximum ridge extraction routine is performed on the test line of the interferogram. If large errors in phase restoration occur, A_1 and A_2 are adjusted so that the cost of the false ridge becomes higher than that of the true ridge.

This cost function ridge extraction algorithm, initially published by Liu and co-authors [17], is a formidable tool to recover the true signal, even in case of mediocre contrast and signal to noise ratio. However, it suffers from a computing time much more important than direct-maximum based routines [22].

Once the ridge position for the test line has been determined, the corresponding parametric curve is reported on the phase plane of the CWT (figure 6.9-(c)). Since along the ridge, the instantaneous frequencies of the signal and of its CWT are equal, this operation immediately gives the phase of the test line. Repeating the treatment over all the lines of the interferogram yield the corresponding full phase map (figure 6.9-(d)).

6.4.2 Phase unwrapping algorithm

6.4.2.1 Brief description of existing algorithms

As seen in figure 6.9-(d), the phase extraction algorithm yields the *wrapped* phase of the interferogram, characterized by 2π discontinuities. This comes from the use of the arctangent function for phase evaluation, returning the principal value of the phase in the $[-\pi,\pi[$ interval. The next step therefore consists in unwrapping phase planes.

If the wrapped phase map does not present any noise or irregularities, unwrapping is a trivial operation, merely implying integration of phase spatial gradients and is independent of the chosen path. In reality, a low signal to noise ratio or undersampling problems make unwrapping a delicate step. Even worse, it is common that the resulting unwrapped phase map depends on the chosen path for the unwrapping operation.

In a general way, phase unwrapping algorithms can be divided in two broad categories [23]:

- *local* algorithms, that integrate the phase gradient $\vec{g}_\varphi$ estimated from the wrapped phase along a definite path. The unwrapped phase φ_u can therefore be defined as:

$$\varphi_u(\vec{r}) = \varphi_u(s_0) + \int_{s_0}^{s(\vec{r})} \vec{g}_\varphi(s).\mathrm{d}\vec{s}. \tag{6.61}$$

  This kind of algorithm can be further divided in two different types: the first type selects the unwrapping path by defining a reliability function and propagating on the phase plane following the decrease of this function. The reliability function can be defined from many different parameters [24]. The second type of routine first try to identify noisy regions, called residuals, in the wrapped phase map, and to isolate them by branch cuts through which the unwrapping path cannot propagate. If branch cuts are correctly positioned, then unwrapping becomes effectively path-independent [25].

- *global* algorithms, which try to minimize the difference between the estimated phase gradient $\vec{g}_\varphi$ and the true, unknown phase gradient $\vec{\nabla}\varphi$, that is the function:

$$\min_{\vec{r}\in\mathbb{R}^2} \left|\left| p(\vec{r})\vec{g}_\varphi(\vec{r}) - p(\vec{r})\vec{\nabla}\varphi(\vec{r}) \right|\right|^n, \tag{6.62}$$

  where p is a weighting function in [0,1] that can be used to exclude noisy regions from the operation [26]. Many algorithms take $n = 2$ and $p = 1$, that is least-square algorithms without weighting [27]. More advanced routines can consider an arbitrary value for n [26]. Generally global algorithms are robust but more time-consuming than local algorithms.

The phase unwrapping algorithm we use is a quality-guided local algorithm, using a reliability function computed from the inverse of squared phase gradients computed for each pixel of wrapped phase planes. Published by Arevallilo Herráez *et al.*, it proved to be robust and fast [28].

6.4.2.2 Description of the phase unwrapping algorithm

Our algorithm works as follows. The first step is to compute the reliability on the whole phase map in order to define the unwrapping path. For each pixel (i,j) not belonging to the edge of the map, the reliability function R is computed:

$$R(i,j) = \frac{1}{\sqrt{H(i,j)^2 + V(i,j)^2 + D_1(i,j)^2 + D_2(i,j)^2}}, \tag{6.63}$$

where:

$$\begin{cases} H(i,j) = w(\varphi(i,j-1) - \varphi(i,j)) - w(\varphi(i,j) - \varphi(i,j+1)) \\ V(i,j) = w(\varphi(i-1,j) - \varphi(i,j)) - w(\varphi(i,j) - \varphi(i+1,j)) \\ D_1(i,j) = w(\varphi(i-1,j-1) - \varphi(i,j)) - w(\varphi(i,j) - \varphi(i+1,j+1)) \\ D_2(i,j) = w(\varphi(i+1,j-1) - \varphi(i,j)) - w(\varphi(i,j) - \varphi(i-1,j+1)) \end{cases} \tag{6.64}$$

Here w is the phase wrapping operator that returns the principal value of an angle. Once the reliability has been computed for each pixel, it is possible to define the reliability of pixel edges, either vertical or horizontal, by merely adding the reliability value of two adjacent pixels. Edges are then sorted by decreasing reliability, defining the non-continuous unwrapping path.

The two pixels separated by the most reliable edge are first unwrapped one with respect to the other, and joined together in a group. Afterwards, in the case of a given pixel edge, several configurations can be encountered:

- if the two involved pixels do not belong to any group, the most reliable pixel is unwrapped with respect to the other and they form a new group.
- if one of the pixel is in a group and the other is alone, the latter is unwrapped with respect to the former and joined to the group.
- if the two pixels are in two different groups, the smaller group is unwrapped with respect to the larger one and the two groups are fused together.

Once all edges have been processed, boundaries are unwrapped with respect to the rest of the phase plane. By sorting pixels by decreasing reliability, one ensures that noise-generating areas will be unwrapped at the end of the process, and always with respect to more reliable pixels. Thus, noise is effectively confined to small regions and cannot corrupt the rest of the phase plane.

As an example, we can start back from the wrapped phase plane displayed in figure 6.9-(d). Implementing the phase unwrapping algorithm on this plane yields the map of figure 6.10. We can clearly see that phase noise initially present on the right of the wrapped phase map did not propagate during the unwrapping process, preserving experimental data.

6.4.3 Phase shift evaluation

Information is carried by interferograms in the form of phase shift. Until now, we have just extracted the total phase of the fringe pattern. To yield this information, phase from the spatial carrier (that is from the undisturbed fringe pattern) must be subtracted. To this purpose, several

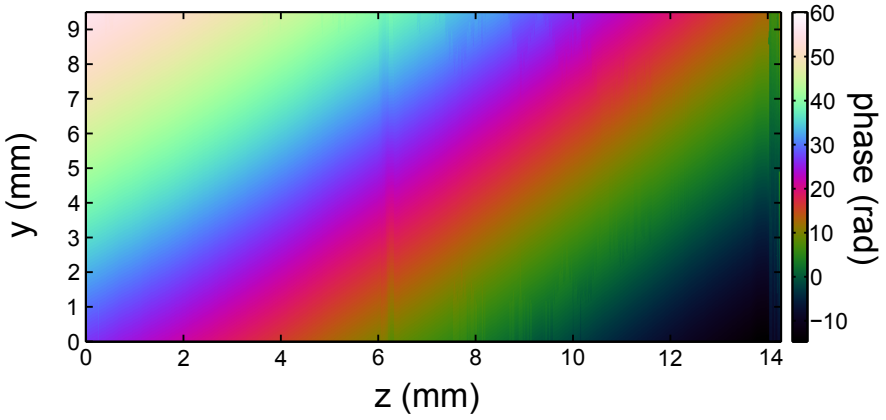

Figure 6.10: Unwrapped phase plane obtained after implementation of the algorithm on the wrapped phase plane of figure 6.9-(d).

blank interferograms (meaning without plasma in the probe arm) are recorded and corresponding unwrapped phase maps are computed. For each working interferogram, for which a discharge occurred, a very simple routine looks for the phase reference map that will minimize the function σ:

$$\sigma(\varphi) = \sqrt{\langle(\varphi - \varphi_{ref})^2\rangle - (\langle\varphi - \varphi_{ref}\rangle)^2}, \tag{6.65}$$

which is the spatial standard deviation of the difference between the working phase map and the reference phase map. Once the best reference candidate is found, it is subtracted from the informative phase plane. Usually, a phase offset persists after this step. To correct this, the average phase outside the plasma-affected region is computed and removed from the whole phase map, giving a globally null phase shift out of the plasma. For instance, the interferogram displayed in figure 6.10 results in the phase shift map of figure 6.11 using an appropriate reference phase map. Phase noise can also be evaluated as the phase standard deviation over the undisturbed region. We typically find a limiting value of 30 mrad RMS at 532 nm, which results, for a probed object of size ~ 200 µm, in a density resolution of 4×10^{22} m^{-3} for free electrons and of 10^{24} m^{-3} for neutrals.

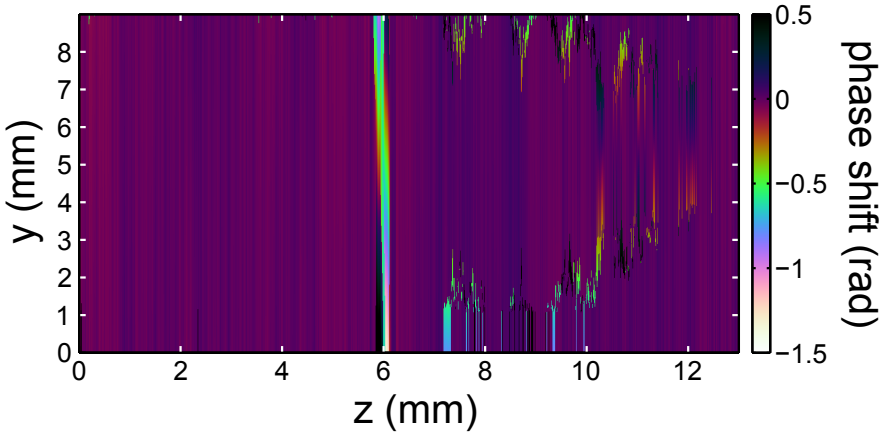

Figure 6.11: Phase shift map obtained from the informative unwrapped phase plane of figure 6.10.

This technique also allows to compensate for front phase distortions induced by optical elements

in the interferometer. Phase shift maps can then be used directly to estimate line-integrated electron and neutral densities following equation system (6.33).

6.4.4 Inverse Abel transform algorithm

The very last step in data processing is to recover density spatial profiles from line-integrated densities estimated from the linear combination of phase shift maps, as presented in section 6.1.3. As a reminder, if ρ denotes either n_e or $n_n - n_0$ and f the corresponding line-integrated density, we have to solve the following equation:

$$\rho(r,z) = -\frac{1}{\pi}\int_r^{+\infty} \frac{\partial f}{\partial y}(y,z)\frac{\mathrm{d}y}{\sqrt{y^2-r^2}}, \tag{6.66}$$

that is the inverse Abel transform of f.

The most straightforward way to implement an inverse Abel transform algorithm is to discretize equation (6.66). To get rid of the pole $y = r$, the numerator is slightly modified:

$$\rho(r_i,z_j) = -\frac{1}{\pi}\sum_{k=1}^{N-1} \frac{f(y_{k+1},z_j) - f(y_k,z_j)}{\sqrt{\left(y_k + \frac{\Delta y}{2}\right)^2 - r_i^2}}. \tag{6.67}$$

However this translation does not bear any physical justification. Moreover the presence of a spatial derivative is intrinsically bound to amplify experimental noise. This is not to mention that possible undersampling of f will be exacerbated by this algorithm [29].

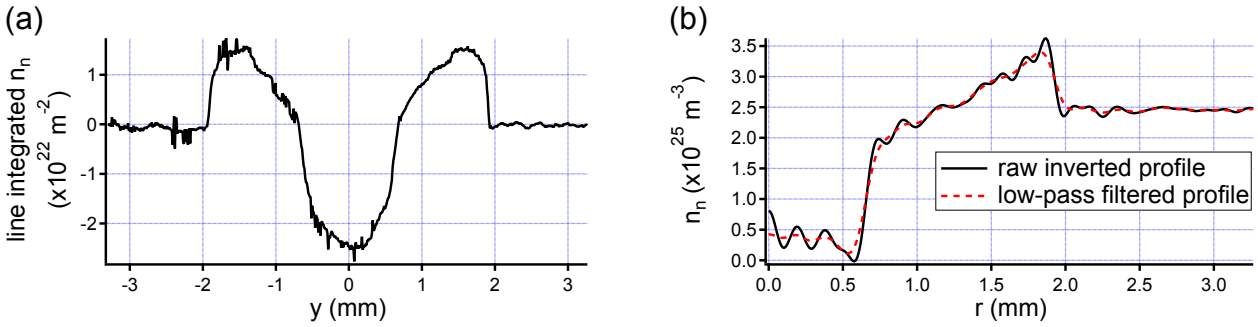

Figure 6.12: (a): example of experimental line-integrated neutral density profile. (b): corresponding neutral density profile obtained using our Fourier-Hankel inverse Abel algorithm without (black solid) and with low-pass data filtering (red dashed).

It is possible to avoid most problems by going to the Fourier space. Indeed Abel transform $\mathcal{A}$ belongs to the FHA cycle, meaning that it can be written as:

$$\mathcal{A} = \mathcal{F}^{-1}\mathcal{H}_0, \tag{6.68}$$

where $\mathcal{H}_0$ is the Hankel transform of order 0 [30, 31]. The inverse Abel transform therefore yields:

$$\rho(r,z) = \mathcal{A}^{-1}(f)(r,z) = \frac{1}{2\pi}\int_{\mathbb{R}^+}\left(\int_{\mathbb{R}} f(y,z)\mathrm{e}^{-iky}\,\mathrm{d}y\right) kJ_0(kr)\,\mathrm{d}k, \tag{6.69}$$

where J_0 is the Bessel function of the first kind of order 0. In this form, the inverse Abel transform no longer exhibits the pole $y = r$, nor the spatial derivative term. It is now possible to discretize

equation (6.69):

$$\rho(r_i,z_j) = \frac{\Delta k \Delta y}{2\pi} \sum_{l=0}^{N} k_l J_0(r_i k_l) \sum_{m=-N}^{N} f(y_m,z_j) \mathrm{e}^{-ik_l y_m}. \tag{6.70}$$

Because of the possible use of a FFT routine, this Fourier-Hankel algorithm is also particularly fast.

The inverse Abel transform can be performed under the hypothesis that f is an y even function, since ρ is cylindrically-symmetrical. However experimental data never verifies this hypothesis scrupulously (see for instance the line integrated density profile displayed in figure 6.12-(a)). Therefore our algorithm works as follows: first, the symmetry axis is selected by minimizing a symmetry indicator. Function f is then cut in two pieces with respect to this symmetry center, and each half of f is symmetrized to yield two perfectly even functions f_{left} and f_{right}. The Fourier-Hankel routine is then applied to these two functions, yielding two density profiles ρ_{left} and ρ_{right}. Finally, the density profile ρ corresponding to f is taken as:

$$\rho = \frac{\rho_{left} + \rho_{right}}{2}. \tag{6.71}$$

This procedure works well when experimental data only slightly deviate from an ideal symmetry, which is our case.

Even though the Fourier-Hankel algorithm is extremely efficient and fast, it can also result in the appearance of noise in the form of high-frequency oscillations (see the raw inverted profile in figure 6.12-(b)). This can be corrected by implementing a low-pass filtering during the Abel inversion process. Indeed, the Fourier-Hankel algorithm involves two steps. The first one is to implement the Fourier transform of f. Once in the Fourier space, high frequencies can be directly filtered using an adapted window (in our case a Hann window). Then the inverse Hankel transform is performed to yield the filtered density profile. This method is very easy to implement and yields good results by effectively smoothing raw data very accurately (see the red dashed profile in figure 6.12-(b)).

6.4.5 Summary

To conclude on interferogram processing, we have at hand very efficient and robust algorithms to accurately extract phase shift from interference patterns and then compute density profiles. More important, they are extremely resilient to noise and also prevent error propagation from one step to the other.

Conclusion

To conclude, I built a plasma diagnostic for the study of filamentation-guided sparks based on interferometry. Because of the strong hydrodynamic effects generated by the studied sparks, neutral and ion-bound electrons result in a significant contribution to the plasma refractive index. To separate this contribution from that of free electrons, it is necessary to record the plasma index simultaneously at two different wavelengths. The experimental setup makes use of a Mach-Zehnder interferometer in transverse geometry and of a Q-switched Nd:YAG probe laser, yielding a temporal resolution of 8 ns. Output imaging system enables to change the spatial resolution at will but is used most of times with no magnification, giving a resolution of 10.5 µm, that is the pixel size of detectors. Interferogram processing starts with a phase extraction algorithm based on a 1-D continuous wavelet transform algorithm coupled to a cost function ridge extraction routine. Phase is then unwrapped by means of a local, quality guided phase unwrapping algorithm. Once line-integrated densities have been retrieved, density profiles are evaluated using a Fourier-Hankel inverse Abel transform algorithm. The best achieved phase noise at 532 nm was 30 mrad which, for a typical plasma transverse size of 200 µm, gives an electron density resolution of 4×10^{22} m^{-3} and a neutral density resolution of 10^{24} m^{-3}.

Bibliography

[1] I. H. Hutchinson, *Principles of Plasma Diagnostics*, 2^{nd} ed. (Cambridge University Press, Cambridge, UK, 2002).

[2] M. Born and E. Wolf, *Principles of Optics*, 7^{th} ed. (Cambridge University Press, Cambridge, UK, 1999).

[3] R. A. Alpher and D. R. White, Physics of Fluids **2**, 153 (1959).

[4] P. E. Ciddor, Applied Optics **35**, 1566 (1996).

[5] J. Filevich, J. J. Rocca, M. C. Marconi, S. J. Moon, J. Nilsen, J. H. Scofield, J. Dunn, R. F. Smith, R. Keenan, J. R. Hunter, and V. N. Shlyaptsev, Physical Review Letters **94**, 035005 (2005).

[6] R. A. Alpher and D. R. White, Physics of Fluids **2**, 162 (1959).

[7] A. J. Alcock and S. A. Ramsden, Applied Physics Letters **8**, 187 (1966).

[8] C. D. David, Applied Physics Letters **11**, 394 (1967).

[9] B. V. Weber and S. F. Fulghum, Review of Scientific Instruments **68**, 1227 (1997).

[10] R. Sanginés de Castro, H. Sobral, C. Sánchez-Aké, and M. Villagrán-Muniz, Physics Letters A **357**, 351 (2006).

[11] T. Lehecka, W. A. Peebles, N. C. Luhmann, and T. N. Carlstrom, Review of Scientific Instruments **59**, 1580 (1988).

[12] K. Kawahata, K. Tanaka, Y. Ito, A. Ejiri, and R. J. Wylde, Review of Scientific Instruments **70**, 695 (1999).

[13] K. Tanaka, A. L. Sanin, L. N. Vyacheslavov, T. Akiyama, K. Kawahata, T. Tokuzawa, Y. Ito, and S. Okajima, Review of Scientific Instruments **75**, 3429 (2004).

[14] A. Sagisaka, A. S. Pirozhkov, H. Daido, A. Fukumi, Z. Li, K. Ogura, A. Yogo, Y. Oishi, T. Nayuki, T. Fujii, K. Nemoto, S. Orimo, M. Nishiuchi, Y. Hayashi, M. Mori, M. Kado, S. Nakamura, A. Noda, I. W. Choi, J. H. Sung, D.-K. Ko, and J. Lee, Applied Physics B **84**, 415 (2006).

[15] M. Takeda, H. Ina, and S. Kobayashi, Journal of the Optical Society of America **72**, 156 (1982).

[16] P. Tomassini, A. Giulietti, L. A. Gizzi, M. Galimberti, D. Giulietti, M. Borghesi, and O. Willi, Applied Optics **40**, 6561 (2001).

[17] H. Liu, A. N. Cartwright, and C. Basaran, Applied Optics **43**, 850 (2004).

[18] S. Mallat, *A wavelet tour of signal processing - The sparse way*, 3^{rd} ed. (Academic Press, New York, NY, USA, 2009).

[19] S. D. Meyers, B. G. Kelly, and J. J. O'Brien, Monthly Weather Review **121**, 2858 (1993).

[20] C. Torrence and G. P. Compo, Bulletin of the American Meteorological Society **79**, 61 (1998).

[21] M. A. Gdeisat, D. R. Burton, and M. J. Lalor, Applied Optics **45**, 8722 (2006).

[22] A. Z. Abid, M. A. Gdeisat, D. R. Burton, and M. J. Lalor, Journal of Physics: Conference Series **76**, 012045 (2007).

[23] G. Fornaro, G. Franceschetti, R. Lanari, E. Sansosti, and M. Tesauro, Journal of the Optical Society of America A **14**, 2702 (1997).

[24] X. Su and W. Chen, Optics and Lasers in Engineering **42**, 245 (2004).

[25] B. Gutmann and H. Weber, Applied Optics **39**, 4802 (2000).

[26] D. C. Ghiglia and M. D. Pritt, *Two-dimensional phase unwrapping: theory, algorithms and software* (John Wiley and Sons, Hoboken, NJ, USA, 1998).

[27] B. R. Hunt, Journal of the Optical Society of America **69**, 393 (1979).

[28] M. A. Herráez, D. R. Burton, M. J. Lalor, and M. A. Gdeisat, Applied Optics **41**, 7437 (2002).

[29] R. Álvarez, A. Rodero, and M. C. Quintero, Spectrochimica Acta Part B: Atomic Spectroscopy **57**, 1665 (2002).

[30] L. Montgomery Smith, D. R. Keefer, and S. Sudharsanan, Journal of Quantitative Spectroscopy and Radiative Transfer **39**, 367 (1988).

[31] R. N. Bracewell, Science **248**, 697 (1990).

Chapter 7

Filamentation-triggered spark gap: characterization and application

Contents

Introduction

One of the main applications for filamentation-triggered electric discharges is the design of laser-triggered spark gaps. The concept of the use of a laser to close a high-voltage switch is almost as old as the laser [1]. Such contactless switches indeed offer many advantages over other spark gap designs such as trigatrons, for which the trigger consists in a secondary spark discharge from a third electrode. They were shown to have a very low triggering jitter and response time, granting them a great stability. They can work in a wide voltage range, either close or far from the self-breakdown voltage, and can be used with various gap widths. Since they use an optical triggering, which is not coupled to the high voltage system, the risk of accidental closure of the switch is greatly reduced. These qualities can explain the quick spreading of laser triggering in the field of pulsed power, as evidenced by the review paper from Guenther and Bettis [2], and from Dougal and Williams [3]. Using nanosecond laser pulses, the best reported performances typically give a jitter on the order of 1 ns for a switched voltage of ~ 100 kV [4, 5, 6]. The jitter can be effectively reduced down to ~ 100 ps by using SF_6 gas as dielectric [7]. The use of femtosecond lasers and of filaments was shown to yield much better results than longer pulses. Thus, a ~ 10 ps jitter was achieved in the case of an atmospheric air spark gap, but with significantly lower operating voltage (4.5 kV) and with a mm wide gap [8]. Such a jitter was also demonstrated by Luther and co-authors using a high-pressure ($p > 150$ kPa) air-filled switches [9].

A filamentation-triggered spark gap was designed and tested at LOA by Leonid Arantchouk. It is basically an atmospheric air-filled, longitudinal spark gap consisting of two drilled electrodes separated by a ~ 1 cm gap. Using a 250 mJ, 700 fs triggering laser pulse at 800 nm focused at $f/165$ and a pulsed voltage operation, we were able to reach a jitter down to ~ 100 ps for a switched current in excess of 10 kA [10]. The presentation of this spark gap makes up the first part of the present Chapter. In a second part, the discharge plasma in the gap is investigated using the two-color interferometer presented in Chapter 6 in order to elucidate the on-state dynamics of the device. Finally, the last part concentrates on an application of our filamentation-triggered spark gap: a Marx generator entirely triggered by laser.

7.1 Characteristics of the compact spark gap

7.1.1 Technical description

The gap switch consists of two cylindrical electrodes in copper/tungsten alloy with face diameter 36 mm. Holes of diameter 3 mm are drilled in the center of each electrode so that 90 % of laser energy can pass through the whole system. This hole diameter was chosen to optimize the contact between the laser-induced plasma and the electrodes and, therefore, the performance of the spark gap. The electrodes are mounted in a Plexiglas casing holed with transverse ~ 1 cm wide ports for discharge visualization and probing. One of the electrodes can be screwed and fastened at a given position, enabling us to adjust the gap width at will up to 2 cm. The switch relies on atmospheric air for electrical insulation. A photograph of the setup is given in figure 7.1.

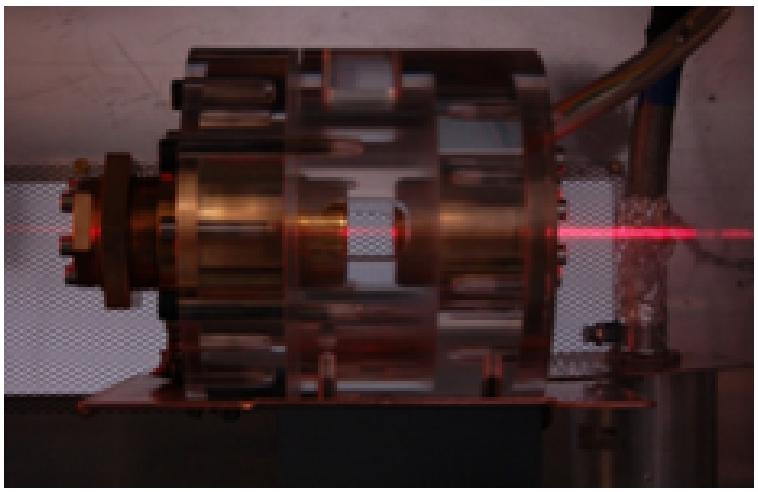

Figure 7.1: Photograph of the gap switch designed at LOA by Leonid Arantchouk. The red light comes from the scattered supercontinuum emission from laser filaments.

The spark gap has been operated for thousands of shots with peak currents in excess of 10 kA without any obvious deterioration of its characteristics, proving its sturdiness and its reliability.

7.1.2 Operational characteristics in the pulsed regime

The spark gap characteristics were first investigated in the pulsed voltage regime, for which a voltage pulse is triggered on the gap a few hundred nanoseconds before a filament is launched in the inter-electrode space. In this regime, the self-breakdown voltage of the gap is raised by 20 to 28 % with respect to the breakdown threshold given by the Paschen's law in the static regime, U_{cr}. Pulsed operation therefore enables us to explore an voltage operating range exceeding this critical value.

The electric circuit used to bring the switch in this regime is schematically represented in figure 7.2-(a). A capacitor C = 360 nF is first charged up to $U_0 \leq 30$ kV through a resistor R = 50 Ω placed in parallel with the spark gap. Voltage is applied to the gap by means of a conventional trigatron switch made up of three electrodes: the two main electrodes on which is applied the voltage to switch, and a third electrode in the form of a spark plug that triggers the switch by ionizing the medium, thereby reducing its dielectric strength and leading to breakdown and closure of the switch. Gap voltage takes the form of a pulse with a (10-90 %) risetime of 50 ns decaying

exponentially with a characteristic time RC = 14 µs. Inductance L originates from the circuit self-inductance. A filament is generated in the spark gap at the beginning of the voltage pulse, resulting in the closure of the switch after a delay on the order of ∼ 10 ns. The capacitor therefore discharges through the low resistance spark thus formed, yielding exponentially-damped current oscillations characteristic of the LC circuit (figure 7.2-(b)).

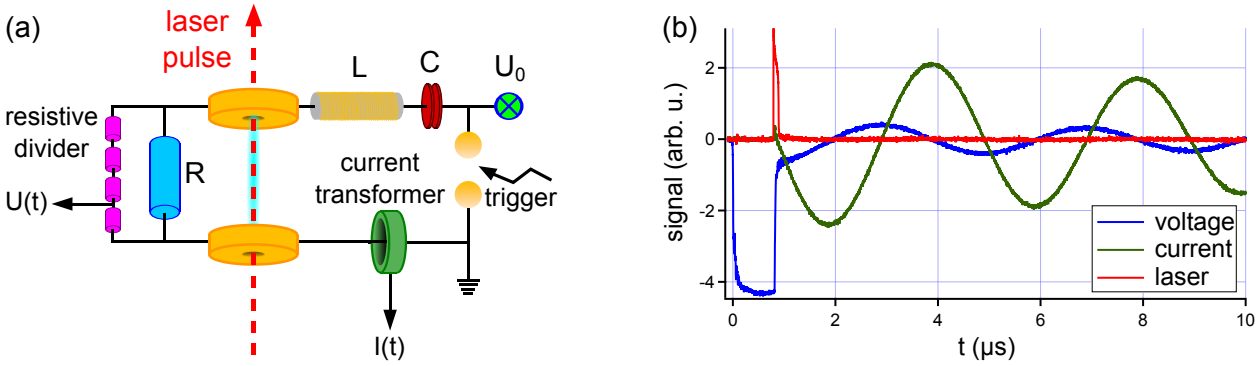

Figure 7.2: (a): schematic description of the electric circuit used to operate the gap switch in the pulsed regime. (b): typical example of current and voltage signals during pulsed spark gap operation. Voltage is triggered by the conventional switch at $t = 0$, producing a slow-decaying voltage pulse. Laser is sent later, resulting in the quasi-immediate gap closure.

Current was monitored by means of a pulse current transformer (Stangenes 0.5-0.01), while a resistive divider allowed us to follow the evolution of the gap voltage. As the spark resistance is typically on the order of 1 Ω, maximum reached current is in excess of 10 kA depending on charging voltage U_0. Influence of the laser arrival time on the gap switching characteristics was shown to be negligible over the range 250-1200 ns.

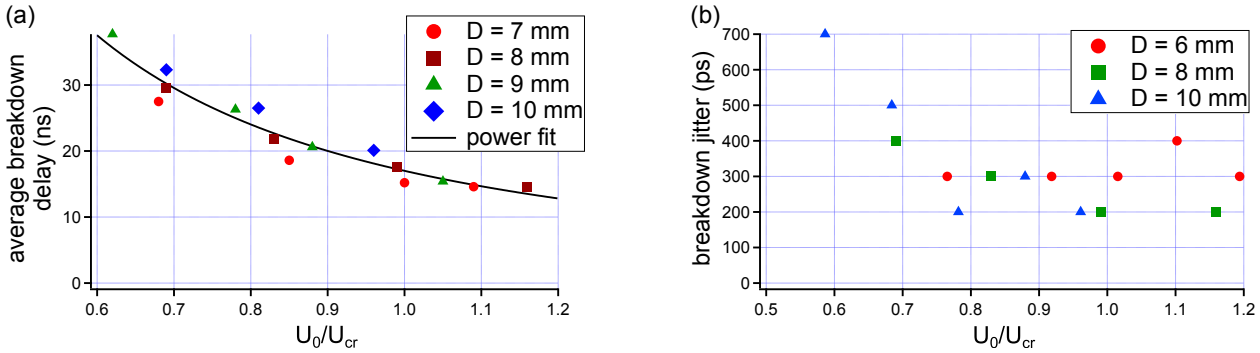

Figure 7.3: (a): average delay between the laser arrival and the breakdown as a function of the gap relative voltage for four different gap widths. (b): evolution of the corresponding jitter with gap relative voltage.

The evolution of the delay between filament formation in the gap and breakdown occurrence with the gap voltage is displayed in figure 7.3-(a). Plotted data was averaged over 10 shots. Different gap widths were tested, ranging from $D = 7$ mm to $D = 10$ mm. As seen on this graph, breakdown delay decreases with gap voltage, and shorter gaps tend to yield shorter delays than longer gaps for the same applied relative voltage. The whole dataset is well fitted by a power law

$f(t)[\text{ns}] = 17(U/U_{cr})^{-1.55}$. Study of the breakdown delay gives also access to the gap jitter, which is one of the most important characteristics of a gap switch. We can see in figure 7.3-(b) that if voltage is raised above $0.8U_{cr}$, jitter remains more or less stable and low. The lowest recorded value was 200 ps, which is an excellent performance for an atmospheric air-filled switch.

7.1.3 Operational characteristics in the static regime

The spark gap was also operated in the static regime, that is when voltage is permanently applied to the gap. The corresponding electric circuit is displayed in figure 7.4-(a). A high-voltage power supply is used to charge a 2 nF capacitor C with a voltage $U_0 \leq 30$ kV. When a filament is formed in the gap, it closes after a given delay, allowing the capacitor to discharge through the ballast resistance R. Current is now measured by means of a current viewing resistor or shunt R_s with a 50 mΩ nominal resistance and a 2 GHz bandwidth (SDN-414-05 from T & M Research Products).

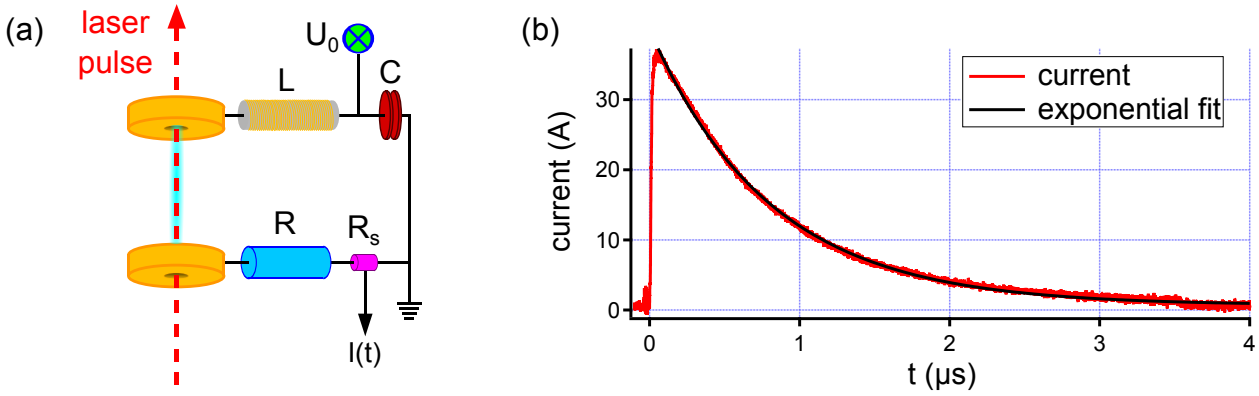

Figure 7.4: (a): schematic description of the electrical circuit used to operate the spark gap in the static regime. (b): example of current time trace for a ballast resistance R = 400 Ω and exponential fit.

The self-inductance L of the circuit is estimated around 1 µH. Therefore the discharge current waveform will depend on the ballast. If $R \gtrsim 45\ \Omega$, current will be exponentially damped with a characteristic time $\approx$ RC. An example is given in figure 7.4-(b), which was recorded with R = 400 Ω. On the contrary, if R is lower than this value, the circuit enters in the oscillatory regime, with exponentially damped sinusoidal oscillations. In our case, the gap width was fixed at 1 cm, yielding a critical voltage $U_{cr} = 30.7$ kV according to the Paschen's law.

In that configuration, we found that spark gap characteristics were significantly worse than in the pulsed regime. For a relative voltage $U_0/U_{cr} = 0.49$, we find the average laser/discharge delay over 40 shots to be 46 ns, which corresponds more or less to what was found in the pulsed regime. However the corresponding jitter is now equal to 5.7 ns, that is an order of magnitude higher than before. The picture remains the same at higher voltage. Indeed for $U_0/U_{cr} = 0.65$ we measured a jitter equal to 8.4 ns.

This significant degradation of the gap characteristics in the static regime could be explained by the fact that the constantly applied voltage can lead to the formation of corona discharges around the electrodes. As this phenomenon is random, its coupling to filamentation can either hasten or slow breakdown occurrence in an unpredictable way, dramatically increasing discharge jitter.

7.1.4 Conclusion

The gap switch designed at LOA proved to be very simple, reliable and sturdy. Using atmospheric air as a dielectric insulator, it can reach a jitter down to 200 ps, which corresponds to a significant improvement with respect to air-filled switches triggered by nanosecond lasers. However, such a jitter was obtained in the pulsed voltage regime only, which involves a much complex electric circuit than the free running, static regime.

7.2 Spark gap on-state dynamics

The characterization of the spark gap switching properties is not enough for a precise knowledge of its operation. It is also crucial to study its on-state dynamics with respect to the discharge current waveform in order to understand how the plasma disappears and how the switch goes back to the off-state. To this purpose we use the two-color interferometric plasma diagnostic described in Chapter 6 to perform a space and time-resolved study of the switch plasma for various current waveforms. The electric circuit adopted in this section is the one described in figure 7.4-(a). Indeed, the electric circuit in the static regime is much simpler and even though this regime brings a much higher jitter, resulting discharge plasmas are exactly the same as in the pulsed voltage regime given electric components have the same value.

7.2.1 Discharge-induced dynamics

We first study discharge-induced dynamics using a 400 Ω ballast resistance. In this case, the discharge generates a current pulse similar to the one displayed in figure 7.4-(b), with a peak intensity of 39 A and a characteristic 1/e damping time of 800 ns. Such a low-current spark can also be used to estimate the performance of the interferometric diagnostic since electron density is expected to be low in this case.

7.2.1.1 Electron density

Examples of radial profiles for electron density are given in figure 7.5-(a). These profiles are taken in the middle of the gap and averaged over a 210 µm length along z. They are characterized by a central main peak, the amplitude of which is at most 6.8×10^{23} m^{-3} and with a FWHM of $\sim$ 200 µm, flanked by a secondary ring with a comparable width. As time goes on both peaks decrease in amplitude, with the ring flattening much faster and propagating outwards with an average speed of about 700 m · s^{-1}, while keeping a constant width. After 2.5 µs, that is more than three times the current 1/e damping time, it is still possible to record a peak electron density around 10^{23} m^{-3}. Past this point, n_e drops below our detection limit, that was estimated at 4×10^{22} m^{-3} in the previous Chapter.

Figure 7.5-(b) displays the evolution of on-axis electron density and of discharge current with time. Each data point represents an average taken over five shots, and the error bars corresponds to ±1 standard deviation. In this figure it is possible to witness the decreasing trend of n_e in time, which loosely follows the exponential decay of the current. This behavior can be explained by the fact that the central density peak does not widen significantly with time as shown in figure 7.5-(a). As a consequence maximum electron density should indeed follow the current time evolution.

The occurrence of an electronic side peak propagating outwards is linked to the formation of a shock wave resulting from energy deposition in the center of the channel. Even though this

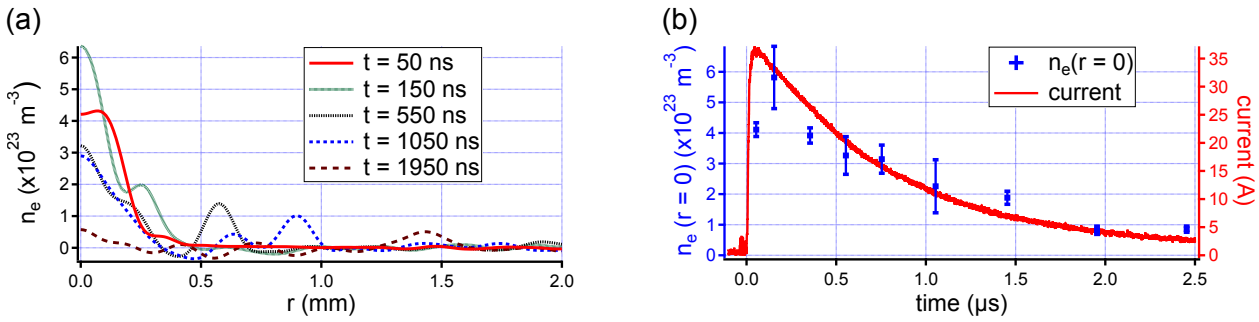

Figure 7.5: (a): electron density profiles recorded at different probe delays. (b): time evolution of on-axis electron density (blue circles) and of discharge current (red solid line).

phenomenon is much more flagrant when studying neutral density profiles (cf. section 7.2.1.2), it appears that a significant portion of the initial plasma is carried away by this hydrodynamic wave.

The maximum encountered electron density can be compared to an estimated value using the discharge current following:

$$I = \iint_S \vec{j}.\mathrm{d}\vec{S} = -e \iint_S n_e(\vec{r})\vec{v}(\vec{r}).\mathrm{d}\vec{S}. \tag{7.1}$$

Once steady state is reached, any inertial term in the fluid equations for the evolution of momentum for plasma species can be neglected, so electron drift speed is given by:

$$\vec{v} = \mu_e \vec{E} - D_e \left(\frac{\vec{\nabla} T_e}{T_e} + \frac{\vec{\nabla} n_e}{n_e} \right), \tag{7.2}$$

where $\mu_e = -e/m_e\nu_c$ is the electron mobility and $D_e = k_B T_e/m_e\nu_c$ is the electron diffusion coefficient. We can estimate the relative weight of diffusion with respect to mobility following:

$$\left| \frac{\mu_e E}{D_e \left(\frac{\vec{\nabla} T_e}{T_e} + \frac{\vec{\nabla} n_e}{n_e} \right)} \right| \approx \frac{eEL}{k_B T_e}, \tag{7.3}$$

where L is the characteristic length of electron density/temperature gradients. In our case $L \sim 100$ µm, and T_e is on the order of a few eV. As for the electric field, it can be seen in figure 7.3-(b) that as soon as breakdown occurs, voltage drops by $\sim 85\%$ across the plasma, which gives $E \sim 220$ kV $\cdot$ m^{-1}, so finally we find:

$$10 > \left| \frac{\mu_e E}{D_e \left(\frac{\vec{\nabla} T_e}{T_e} + \frac{\vec{\nabla} n_e}{n_e} \right)} \right| > 1, \tag{7.4}$$

that is electron motion is weakly dominated by mobility. We therefore discard diffusion, which is all the more justified because we want to estimate the initial electron density. Equation (7.1) can be rewritten as:

$$I = \frac{e^2}{m_e\nu_c} \iint_S n_e(\vec{r})\vec{E}.\mathrm{d}\vec{S} \approx \frac{e^2 E \pi r_0^2}{m_e\nu_c} n_e(r=0), \tag{7.5}$$

where r_0 is the half-width of the electron density profile. As $I_{max} = 39$ A, and using $r_0 = 100$ µm, $\nu_c = 2$ THz and $E = 220$ kV $\cdot$ m^{-1} we have:

$$n_{e,max}(r=0) \approx 4 \times 10^{23}\ \mathrm{m}^{-3}, \tag{7.6}$$

which is in excellent agreement with the measured value of 4.1×10^{23} m^{-3} at $t = 50$ ns, given that this is only a rough estimate.

7.2.1.2 Neutral density

As seen in figure 7.6-(a), neutral density profiles are characterized by a central, low-density region where n_n is typically less than 10 % of the reference neutral density n_0, surrounded by a high-density ring. With time, the central density hole widens while the high-density peak increases in amplitude at first, and then decreases and enlarges. After a few microseconds, hole FWHM stabilizes around 1.5 mm. This behavior is typical of the formation of a blast wave following a quick and important energy deposition in air with the formation of an outward-propagating shock wave, much in the same way filamentation can generate underdense air channels.

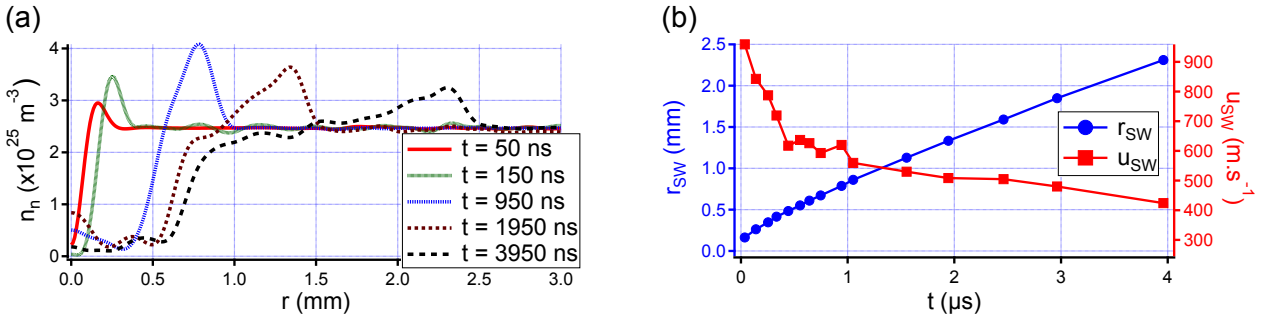

Figure 7.6: (a): measured neutral density profiles at various times. (b): radial position of the shock wave r_{SW} (blue circles) and corresponding shock speed u_{SW} (red squares).

Figure 7.6-(b) represents the time evolution of the shock wave radius r_{SW}, taken as the position of maximum density. Using this data, we can estimate the shock wave speed u_{SW} by means of finite differences. As seen in the same figure, the velocity remains well above the speed of sound in air in standard pressure and temperature conditions $c_s = 343$ m $\cdot$ s^{-1}, up to the maximum probed time, beyond which measurements cannot be reliably done because r_{SW} exceeds the field of view of cameras. Starting at nearly 1 km $\cdot$ s^{-1}, u_{SW} falls abruptly during the first 500 ns then gently decreases to about 400 m $\cdot$ s^{-1} after 4 µs.

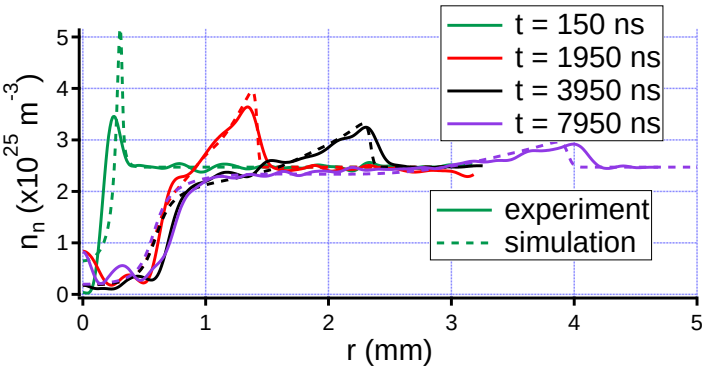

Figure 7.7: Comparison between experimental (solid lines) and simulated (dashed lines) neutral density profiles.

We also performed hydrodynamic simulations of the time evolution of neutral density profiles in order to have an estimate of the initial temperature profile leading to the formation of the shock wave. To this purpose we used the same Eulerian code that we used in Chapter 3 to find back the

air temperature profile following filamentation (section 3.1.1.4). The best fit overall is displayed in figure 7.7. This numerical study was initialized with a Gaussian temperature profile with a 10 kK amplitude and a 140 µm standard deviation. There are discrepancies however, especially concerning the initial shock amplitude and channel depth. This can be explained by the fact that energy deposition can no longer be considered as instantaneous for discharges because current flows through the plasma during several 100s ns, unlike filamentation. Getting a perfect description would require to implement a Joule heating term in the hydrodynamic code and to use the current time trace as another input. Still, as we are here only interested in an order of magnitude for the temperature, we used our basic version of the code.

7.2.1.3 Interferometer probe deflection by the plasma

In the previous Chapter, we did not mention an effect that can seriously affect interferometric measurements: since the diagnostic is probing a phase gradient object, this means that probe beams can be deflected by the plasma, resulting in a loss of contrast and a blurring of the image on the detectors. We therefore performed a test to estimate the importance of this effect by using a recorded plasma refractive index profile at $\lambda = 1064$ nm and $t = 150$ ns, that is when refractive index gradients and, consequently, probe deflection are maximum (figure 7.8-(b)). In the framework of geometrical optics, the deflection angle profile can be deduced from the refractive index profile following:

$$\alpha(y) = \pi - 2y(1+\beta)\int_{r_0}^{+\infty} \frac{\mathrm{d}r}{r\sqrt{r^2 n_p(r)^2 - y^2(1+\beta)^2}}, \tag{7.7}$$

where r_0 is the radius solution of the equation $r_0 n_p(r_0) = y(1+\beta)$ [11]. From the refractive index profile plotted in figure 7.8-(b), we find the maximum deviation angle to be less than 0.8 mrad.

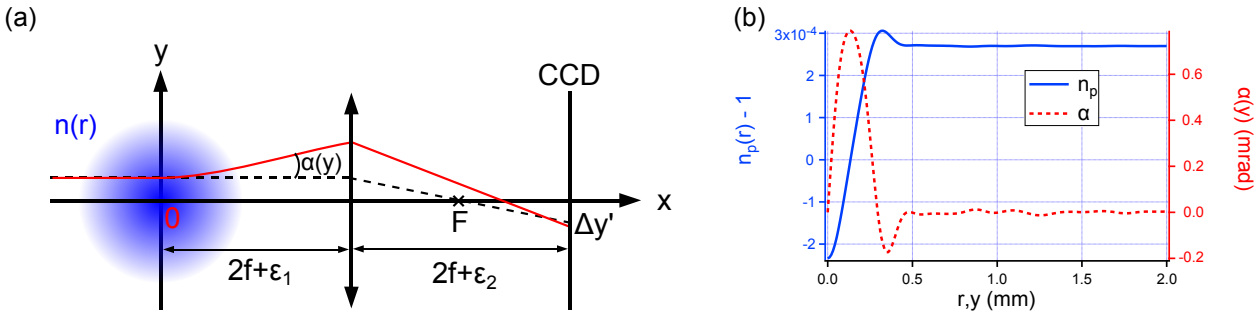

Figure 7.8: (a): scheme for the probe beam deflection scenario in the case of a $2f/2f$ imaging system. (b): experimentally recorded refractive index profile for $\lambda = 1064$ nm and $t = 150$ ns (blue solid line) and corresponding deviation angle profile (red dashed line).

Using the schematic representation of figure 7.8-(a) in the case of a $2f/2f$ imaging system, which is what we used in the experiment, we can evaluate the position difference $\Delta y'$ on the CCD array between the deflected beam and a hypothetical undeviated beam (red solid ray and black dashed ray, respectively). From geometrical calculation we find:

$$\Delta y'(y) = \left(\epsilon_1 + \epsilon_2 + \frac{\epsilon_1 \epsilon_2}{f}\right)\tan(\alpha(y)). \tag{7.8}$$

Here $2f + \epsilon_1$ is the distance between the imaging lens and the point where the two beams start to separate, inside the plasma. $2f + \epsilon_2$ corresponds to the distance between the lens and the CCD

array. ϵ_1 originates from the misalignment of the imaging system and from the spatial extension of the plasma, while ϵ_2 arises solely from a misplacement of the lens and/or the CCD array.

For $\Delta y'$ to be as large as one pixel size, the factor in parentheses in equation (7.8) must be on the order of 1 cm. As the plasma has a typical transverse size of 200 µm, the only significant contribution to ϵ_1 comes from a misalignment of the imaging system, much like ϵ_2. As a consequence, even a slight misalignment of a few millimeters cannot result in a detectable probe deflection effect in this experiment.

7.2.1.4 Summary

Discharge-induced dynamics are characterized by the generation of an on-axis plasma column, initial density of which can be well correlated to the discharge current. This column becomes less and less dense in time as current decreases and becomes unable to sustain it. The intense heating resulting from deposited energy in air over a large volume is responsible for the generation of a strong shock wave initially propagating with a speed > 1 km $\cdot$ s^{-1}, blasting matter away from the center and leaving a quasi vacuum channel. We estimated the initial air temperature due to Joule heating to be ~ 10 kK.

7.2.2 Influence of the current waveform on plasma parameters: monopolar regime

The first study we performed was to look at the influence of the current pulse width and amplitude on the spark gap plasma. To this purpose, we fixed our electric energy by keeping charging voltage fixed at 15 kV, yielding a stored energy of 220 mJ. The ballast resistance was then varied between 400 Ω and 25 Ω, giving monopolar current pulses of constant charge but with an amplitude ranging from 39 to 352 A and a temporal width from 4 µs to 100 ns (cf. figure 7.9). We then made use of the two-color interferometer to characterize the temporal evolution of the plasma for each experimental configuration.

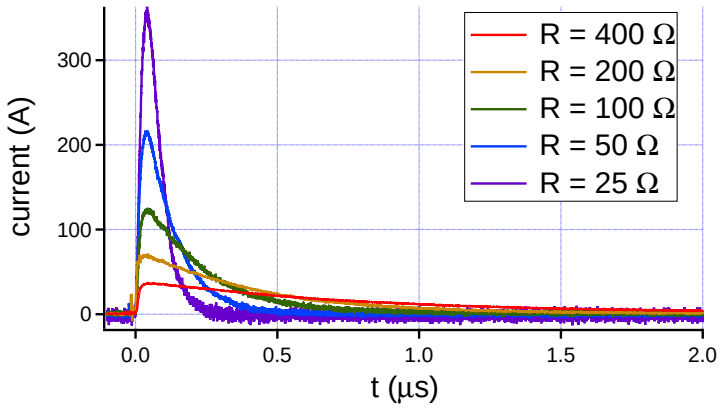

Figure 7.9: Different monopolar current pulses generated during the study.

7.2.2.1 Electron density

The most important parameter to monitor in this study is electron density, because its time evolution enables one to estimate the plasma lifetime, that is the on-state time of the gap switch.

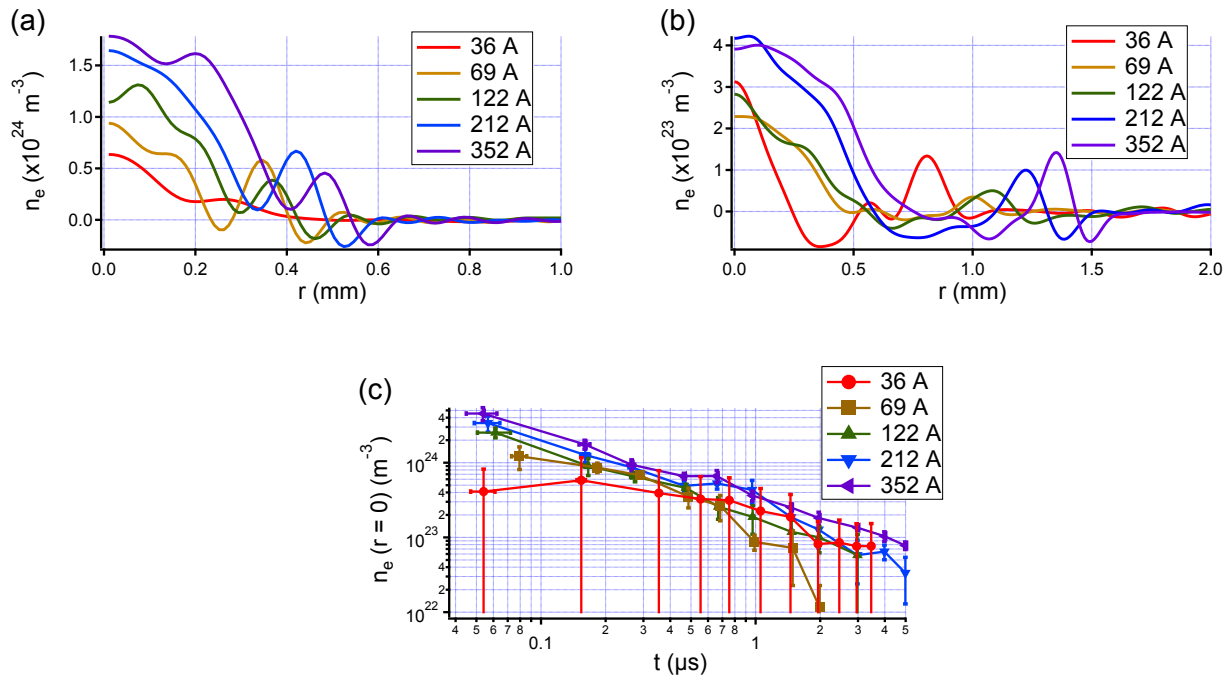

Figure 7.10: Electron density profiles for the different current waveforms recorded at delay 150 ns (a) and 950 ns (b) midway of the discharge. (c): time evolution of on-axis electron density for the different experimental configurations. Error bars correspond to ±1 standard deviation over a 5 shot statistics.

Figure 7.10-(a) and (b) presents electron density profiles measured at delay 150 and 950 ns after the onset of the discharge. All these profiles are characterized by a central electron density peak, in the same way as presented in section 7.2.1. At short times, the amplitude and width of this peak is well ordered with respect to the current pulse amplitude, that is the more intense the pulse, the higher and wider the electron density profile. This ordering is no longer respected by 950 ns. Indeed by this time, plasma columns generated by intermediate current pulses collapsed and decreased below the profile obtained with 39 A. All the profiles also enlarged significantly, as to reach a 1 mm for the 352 A pulse.

To get a clearer picture, we investigated the time evolution of the on-axis electron density for all current pulses. Results are plotted in figure 7.10-(c). These curve clearly exhibit the initial ordering of n_e with the peak current. However, it is clear that the 39 A pulse yields the slowest density decay, while the 69 A pulse has the fastest decrease. Above $\sim$ 100 A, decay occurs at an approximately constant rate, with more intense pulses resulting in a plasma with a longer duration. There is consequently a clear regime transition for the plasma decay around a critical intensity value of $\sim$ 100 A.

If we look more carefully to the damping of electron density for the 69 A current pulse, we can see it can be perfectly fitted by an exponential decrease with the same characteristic time as the current waveform (figure 7.11-(a)).

As for the 122 A current pulse, such an exponential fit no longer matches electron density damping (see figure 7.11-(b)). Density decreases notably faster, and is actually perfectly fitted by a hyperbolic function. This behavior is characteristic of a plasma evolution dominated by recombination. Indeed, if we consider an isolated plasma, the evolution of the electron density will

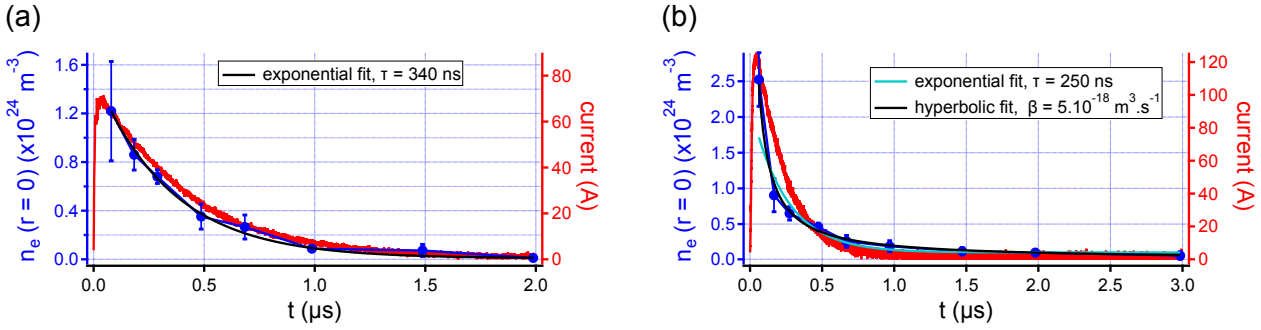

Figure 7.11: (a): time evolution of on-axis electron density and of discharge current for the 69 A current pulse, and exponential fit. (b): time evolution of on-axis electron density and of discharge current for the 122 A current pulse, with exponential and hyperbolic fits.

be given by equation (1.112) from Chapter 1:

$$\partial_t n_e(\vec{r},t) - D_a(\vec{r},t)\Delta n_e(\vec{r},t) = -\beta_{eff} n_e(\vec{r},t)^2, \tag{7.9}$$

where D_a is the ambipolar diffusion coefficient for the plasma, and β_{eff} the effective recombination rate taking into account different processes. Here the approximation $n_i \approx n_e$ was done since the Debye length of discharge plasmas is far smaller than the plasma characteristic size. The diffusion term can actually be neglected in our case. Indeed the ambipolar diffusion coefficient is given by:

$$D_a = D_i\left(1+\frac{T_e}{T_i}\right) = \frac{k_B T_i}{m_i \nu_i}\left(1+\frac{T_e}{T_i}\right) \approx 2\frac{k_B T_i}{m_i \nu_i}, \tag{7.10}$$

because the spark plasma is typically a thermal plasma. The dominant collision frequency term for ions comes from electron-ion collisions. The corresponding frequency averaged over a Maxwellian distribution yields [12]:

$$\nu_{ei}[\mathrm{Hz}] \approx \frac{5\times 10^{-11} n_e[\mathrm{m}^{-3}] Z_i}{T_e[\mathrm{eV}]^{3/2}} \frac{\ln\Lambda}{17}, \tag{7.11}$$

where Z_i is the average ionization factor and $\ln\Lambda$ is the Coulomb logarithm with $\Lambda = 4\pi n_e \lambda_{De}^3$, λ_{De} being the electronic Debye length. Using $n_e \sim 10^{24}$ m^{-3}, $Z_i \sim 1$ and $T_e \sim 5$ eV we find $\nu_{ei} \sim 1$ THz and, eventually, $D_a \sim 10^{-5}$ m$^2 \cdot$ s^{-1}. Therefore:

$$\frac{\partial_t n_e}{D_a \Delta n_e} \sim \frac{L^2}{T D_a}, \tag{7.12}$$

where L and T are characteristic variation length and time for n_e, respectively. From the experiment we have $L \sim 100$ μm and $T \sim 100$ ns meaning:

$$\frac{\partial_t n_e}{D_a \Delta n_e} \sim 10^4. \tag{7.13}$$

Diffusion is consequently completely negligible at our timescales and the time evolution of electron density is given by:

$$n_e(t) = \frac{n_e(0)}{1+\beta_{eff} n_e(0) t}, \tag{7.14}$$

that is a hyperbola.

This observed regime transition between a plasma supported by current and a quasi-free evolving plasma can be explained the following way. For long and low-intensity current pulses, an initially moderately dense plasma is formed. In this case even a low input current is able to sustain this plasma, resulting in electron density closely following the current waveform over a long time. Conversely for short and intense pulses, the initially generated plasma is denser (above 2×10^{24} m^{-3}) so that it needs a high permanent current to be sustained. Instead current falls rather quickly because of the constant charge of the current pulse, so that the plasma is left in a free evolution state as if no current was actually flowing in the discharge. Moreover, fitting the time evolution of on-axis electron density allows to retrieve recombination coefficients for different current pulses:

$$\begin{cases} \beta_{eff}(122\text{ A}) = 5.0 \times 10^{-18}\text{ m}^3 \cdot \text{s}^{-1} \\ \beta_{eff}(212\text{ A}) = 3.9 \times 10^{-18}\text{ m}^3 \cdot \text{s}^{-1} \\ \beta_{eff}(352\text{ A}) = 2.6 \times 10^{-18}\text{ m}^3 \cdot \text{s}^{-1} \end{cases} \tag{7.15}$$

Therefore as the initial current increases, plasma not only becomes denser but also recombines more slowly, so that higher currents should be linked to higher electron temperatures as well.

7.2.2.2 Neutral density

Two-color interferometry also grants the possibility to record neutral density profiles. We saw in the previous section (7.2.1) that the initial energy deposition resulting from the initiation of the spark leads to the formation of a shock wave that ejects matter from the center and eventually separates from the associated underdense channel after ~ 2 µs.

Figure 7.12-(a) displays neutral density profiles recorded at delay 150 ns after the spark onset for the different current pulses. They are all sharing the same characteristics with a cylindrical outward-propagating shock wave which is, at this time, still linked to the underdense channel it creates during its propagation. However it appears that if the shock wave amplitude does not vary significantly from one configuration to the other, higher currents result in a greater shock speed and a larger underdense channel.

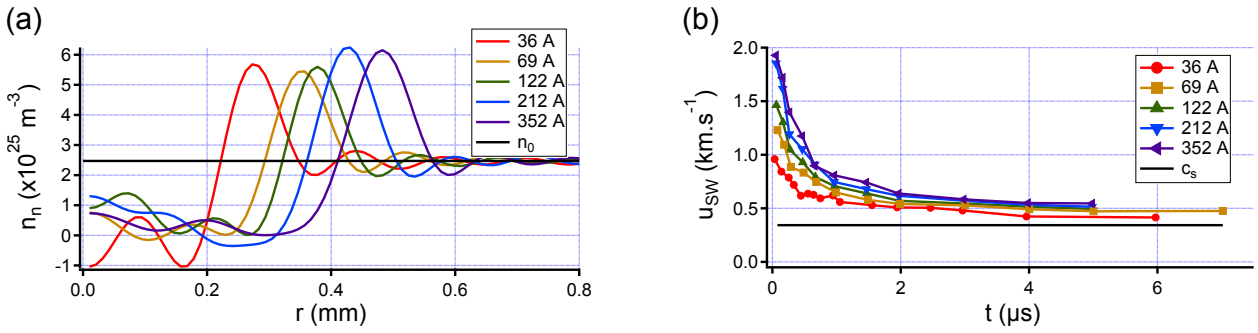

Figure 7.12: (a): neutral density profiles measured at delay $t = 150$ ns and for the different monopolar current pulses. (b): time evolution of the shock wave speed u_{SW} extracted from neutral density profiles for the different experimental configurations.

We can study this parameter more in detail by recording the shock wave position in time using neutral density profiles and estimate the propagation speed. Results are plotted in figure 7.12-(b). This graph shows that when increasing peak current from 36 to 350 A, the initial shock speed goes from 1 to 2 km $\cdot$ s^{-1}. Still, all current waveforms give approximately the same behavior with a

quick decrease for u_{SW} during the first 500 ns followed by a much more slower relaxation. The wave remains supersonic in all cases after it exits the field of view of cameras.

Using the Rankine-Hugoniot equation for an ideal gas, it is possible to evaluate the peak pressure found at the shock front [13]:

$$\frac{p_{max}}{p_0} = \frac{n_{n,max}(\gamma+1) - n_0(\gamma-1)}{n_0(\gamma+1) - n_{n,max}(\gamma-1)}, \tag{7.16}$$

where $p_0 = 1.013 \times 10^5$ Pa is the pressure of ambient air and $\gamma = 1.4$ is the heat capacity ratio for air at 20 °C. As $n_{n,max} \approx 5.5 \times 10^{25}$ m^{-3} (figure 7.12-(a)), we find a peak pressure of:

$$p_{max} \sim 0.3 \text{ MPa}. \tag{7.17}$$

Such a pressure level is the same as the one recorded 1.7 m away from a 1 kg TNT charge exploding in atmospheric air [14].

We can estimate the energy carried away from the system as shock kinetic energy. Knowing that the shock wave results in the formation of a quasi-vacuum density channel with half-width $r_0 \sim 1$ mm and propagates with a speed ~ 1 km $\cdot$ s^{-1}, then the shock kinetic energy is given as:

$$K_{SW} \approx \frac{1}{2} n_0 L \pi r_0^2 m_{air} u_{SW}^2, \tag{7.18}$$

where $L = 1$ cm is the length of the discharge and m_{air} the average mass of an air molecule. We find:

$$K_{SW} \sim 10 \text{ mJ}. \tag{7.19}$$

The initial thermal energy can also be evaluated using the heating found from hydrodynamic simulations in section 7.2.1 and the first law of thermodynamics. Using a temperature profile with 10 kK amplitude and 100 µm half-width, we find:

$$\Delta U_{ini} \sim 3 \text{ mJ}. \tag{7.20}$$

This discrepancy, especially $\Delta U_{ini} < K_{SW}$, can be explained by the fact that the shock acquires kinetic energy as long as it does not separate from the underdense channel because energy is continuously deposited in the channel by the current. Still, these estimations show that the shock actually drains a considerable part of the energy deposited in the early stages of the discharge (up to a few hundred ns) and constitutes the most efficient dissipation channel for short and intense current pulses. As such, the shock wave is an excellent diagnostic for the initial energy deposition in air.

7.2.3 Influence of the current waveform on plasma parameters: alternative regime

We also investigated the temporal evolution of the spark gap plasma when it is used to switch an oscillating current. To this purpose, a 28 µH coil was inserted in the electric circuit described in figure 7.4-(a). The ballast resistor was reduced to R = 10 Ω to decrease current damping. Corresponding current waveform is plotted in figure 7.13.

This waveform is well fitted by an exponentially-damped sinusoidal function:

$$I(t) = A e^{-t/\tau} \sin(2\pi f_0 t + \varphi), \tag{7.21}$$

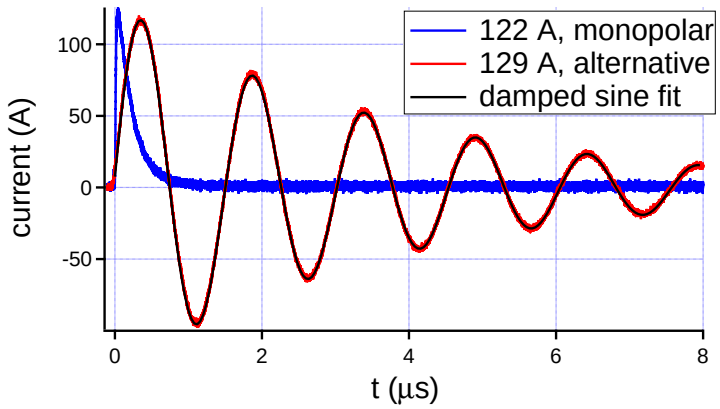

Figure 7.13: Current waveforms measured in the monopolar regime with a 100 Ω ballast (blue) and in the alternative regime (red), with corresponding exponentially-damped sinusoidal fit (black).

where $\tau = 2\mathrm{L}/\mathrm{R}$ is the characteristic damping time and $2\pi f_0 = \frac{1}{\sqrt{\mathrm{LC}}}\sqrt{1 - \frac{\mathrm{R}^2\mathrm{C}}{4\mathrm{L}}}$ is the circuit characteristic angular frequency. This fitting yields the following values for waveform parameters:

$$\begin{cases} A = 129 \text{ A} \\ \tau = 3.77 \text{ µs} \\ f_0 = 659 \text{ kHz}. \end{cases} \tag{7.22}$$

Using these figures and holding the value for the inductance L, we find:

$$\begin{cases} \mathrm{R} = 15.4 \ \Omega \\ \mathrm{C} = 2.0 \text{ nF}. \end{cases} \tag{7.23}$$

The value for the circuit resistance is 50 % higher than the ballast. This stray resistance could come either from the plasma itself, or from contact resistance in the plasma sheaths between the spark and the electrodes. Since the alternative current waveform yields a peak current close to that of one of the studied monopolar pulses (on average 122 A for a 100 Ω ballast), we can directly compare the results between these two cases.

7.2.3.1 Electron density

The time evolution of the on-axis electron density in the plasma for the oscillatory regime is plotted in figure 7.14 (red curve). These results are compared to those obtained using the 122 A monopolar current pulse studied in the previous section (blue curve).

As seen on this graph, the monopolar current pulse initially gives a much higher electron density than for the AC configuration but decreases quite rapidly, going under the density of the alternative case around 500 ns and becoming undetectable beyond 3 µs. Conversely, the density observed for the AC current remains very stable all along, staying at a few 10^{23} m^{-3} from the breakdown up to 6 µs before starting to decrease with a faster rate. This quasi-static evolution is well fitted by an exponential decrease using the damping characteristic time for the envelope of the current, $\tau = 3.77$ µs.

An important point to notice here is that for the oscillatory regime, the electron density does not evolve with the instantaneous current, but is rather sensitive to its envelope. Such a behavior

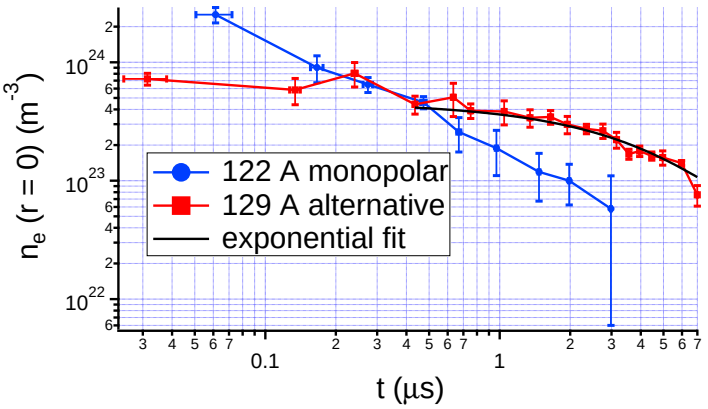

Figure 7.14: Temporal evolution of the on-axis electron density for the monopolar 122 A current pulse (blue circles) and for the 129 A alternative waveform (red squares). This last graph is fitted by an exponential decrease of characteristic time $\tau = 3.77$ µs.

must be highly dependent on the AC frequency f_0 and, more precisely, on the comparison between the plasma characteristic recombination time and $1/f_0$. We found for the 122 A monopolar current pulse that the recombination coefficient was $\beta_{eff} = 5 \times 10^{-18}$ m^3 · s^{-1}, so that the characteristic recombination time τ_{rec} for a plasma with density $n_e \approx 4 \times 10^{23}$ m^{-3} is:

$$\tau_{rec} = \frac{1}{\beta_{eff} n_e} \sim 500 \text{ ns}. \tag{7.24}$$

The half-period of current oscillations is:

$$\frac{T_I}{2} = 760 \text{ ns} \approx \tau_{rec}. \tag{7.25}$$

Recombination thus occurs over a timescale similar to that of current oscillations. As a consequence the plasma is mostly insensitive to these fast dynamics and is only affected by the global evolution of the current, which occurs at a timescale ~ 10 times longer. If the current frequency decreased so that $T_I/2 \gg \tau_{rec}$, electron density should follow current oscillations more closely because plasma would have time to recombine between the occurrence of two successive current extrema.

From this study, it is clear that current is crucial to sustain the plasma in the gap. Even though the two configurations use exactly the same electric charge and yield the same peak current, the monopolar current pulse feeds electrons in the plasma only once and therefore deposits energy only once. As for the oscillatory regime, it propagates current back and forth in the plasma for a much longer duration, eventually depositing much more energy in the plasma so that it can last longer.

7.2.3.2 Neutral density

Examples of radial neutral density profiles are plotted in figure 7.15. These graphs show unambiguously that the shock wave development is much slower in the oscillatory regime than in the monopolar regime, with a shock speed also slower for AC current.

We saw in the previous section that shock wave speed and/or underdense channel width are an excellent diagnostic of the initial energy deposition in the system, because in this process a large part of this energy is transferred to the shock kinetic energy. It is possible to link the trends

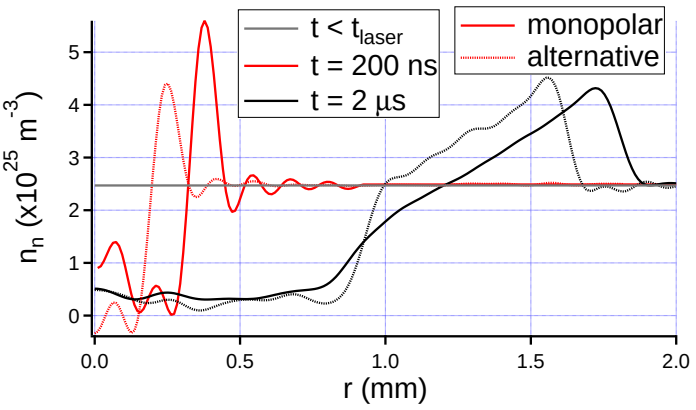

Figure 7.15: Neutral density profiles recorded at $t = 200$ ns (red) and $t = 2$ µs (black) for the monopolar (solid lines) and the oscillatory regime (dashed lines).

exhibited in figure 7.15 to current waveforms. In figure 7.13, we can see that the current slope in the AC regime is less steep than in the monopolar regime. Therefore, initial energy deposition due to the current in air will occur more slowly for the oscillatory current than for the monopolar pulse. Consequently, shock kinetic energy will be smaller and the shock will propagate more slowly.

7.2.4 Conclusion

To conclude on this study of the influence of current waveforms on the gap switch plasma, we saw that in the monopolar regime, current pulses with a peak intensity < 100 A generate moderately ionized plasmas that can be easily sustained by a low current. In this case, time evolution of the electron density closely follows that of the current. When peak current is increased, spark plasma is initially denser, which asks for higher currents to be sustained at this density level. As usually the current pulse maintains a high current value only for a short time, the plasma starts to evolve on its own, recombining more or less quickly depending on its initial density. Studying the oscillatory regime showed that the AC current can sustain the plasma for a much longer time than a simple monopolar pulse as free electrons are brought back and forth into the plasma. Depending on the current frequency, this can result in electron density following the current waveform at low frequency, or evolving according to the current envelope at high frequency.

Investigating current effects on neutral density profiles also brought useful information. We showed that the discharge-generated shock wave speed is an excellent diagnostic for initial energy deposition in air by the current, since most of this energy is used as shock kinetic energy. This said, the shock speed logically increases according to the peak current, but is also very sensitive to the slope of the current waveform. The steeper the slope, the higher the initial energy deposition and the faster the shock. This explains why the AC regime results in significantly slower shocks.

As long as plasma is still present in the gap, it can be considered as closed because current can easily flow through it, heating it and increasing its density back to its initial level. But even if plasma has recombined, the spark-generated underdense channel remains for a very long time. Since total energy deposition greatly exceeds that encountered in filamentation (see Chapters 3 and 4), the system takes a considerably longer time to get back to pressure equilibrium. For instance, it was simulated that on-axis pressure would stay below standard air pressure for ~ 100 µs after a spark breakdown with an exponentially-damped current waveform of amplitude 1 kA, frequency

100 kHz and damping time 100 ns, that is conditions close to ours [15]. In that case, according to the Paschen's law, breakdown voltage would be reduced in the gap and could result in a new breakdown occurring, if voltage is allowed to build-up quickly enough. Actually, it would take a considerably longer time to fully restore the dielectric strength of the gap, preventing a precise use of the switch with a high repetition rate.

7.3 Filamentation-triggered Marx generator

7.3.1 Motivation

The Marx generator was invented in 1924 by the German electrical engineer Erwin Otto Marx, and is now widely used in high-energy physics (pinch plasmas, electron and ion beam acceleration, etc.) and for pulsed power applications (industry, medical sector, etc.). This generator design consists of a set of capacitor stages charged in parallel under a given voltage U_0 and discharged in series by means of closing switches. This results in an output voltage pulse, amplitude of which is ideally given by the number of stages times the charging voltage.

Performances of the Marx generator are strongly dependent on those of the gap switches used between each stage. More specifically, it is crucial to have a triggering jitter as low as possible so that all stages could discharge almost simultaneously, yielding the steepest possible voltage pulse at the output of the generator. However in the traditional mode of operation, only the first switch is externally-triggered, with the following ones being driven by the resulting overvoltage. A sub-ns jitter was achieved in several publications using rather elaborate methods. Kusama and Yagi thus used dry air spark gaps with a 0.4 MPa pressure very close to their breakdown limit ($U_0/U_{cr} = 0.95$) [16]. A KrF excimer laser beam was then passed through a metallic mesh installed in the switch electrodes so that the produced photoelectrons would in turn trigger a discharge in two adjacent switches simultaneously. Another group made use of switches filled with a gas mixture containing SF_6 at 0.3 MPa triggered by a UV laser [17], yielding a sub-ns jitter, similarly to what was reported by Mayes *et al.* [18].

The first part of this Chapter was dedicated to the description of a simple, compact and robust gap switch triggered by laser filamentation. This switch was shown to be able to reach a 200 ps jitter in atmospheric air with a rather large gap spacing of 1 cm and even with a charging voltage as low as $0.7U_{cr}$. In the same conditions, the average delay between filamentation and breakdown was measured between 15 and 30 ns. This means that if filamentation spans several gap switches, they will close simultaneously. Leonid Arantchouk therefore designed and built a coaxial Marx generator, where all switches are triggered by the same multifilament bundle propagating through the whole generator assembly [19].

7.3.2 Description of the generator

Our Marx generator is composed of up to six stages, with a 250 mm diameter and a total length of 55 cm. It can generate an output voltage up to 180 kV.

Following the classification proposed by Martin *et al.* [20], it has a hybrid design because while its size corresponds to that of *ultra-compact* generators, its output voltage makes it more akin to *compact* generators. A single stage of our Marx generator (see figure 7.16) is composed of two parts. The first one is made up of six parallel 2 nF "door-knob" ceramic capacitors connected by two metal discs. The second part is a spark gap made of two 35 mm diameter cylindrical electrodes

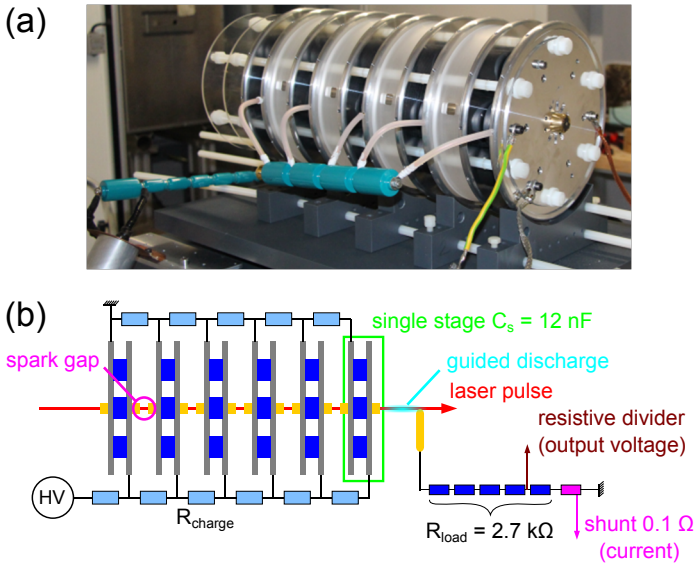

Figure 7.16: (a): photograph of the filamentation-triggered Marx generator in the 5-stage configuration. (b): schematic representation of the filamentation-triggered Marx generator consisting of 6 stages with 12 nF capacitance charged up to 30 kV. Once triggered, the generator produces a voltage pulse that results in a guided spark that discharges through the resistive load $R_{load} = 2.7$ kΩ.

with 5 mm radius curved border, similar to the switch described earlier in section 7.1. The laser beam enters and leaves the spark gap through 3 or 4.5 mm diameter holes drilled axially in the electrodes. Inter-electrode gap D is constrained by a Plexiglas ring which serves at the same time as a spacer between the Marx's stages. We worked with gap spacing D = 11.25 mm and 12 mm, corresponding to self-breakdown voltages $U_{cr} = 34$ kV and 36 kV respectively. A DC power supply charged each stage up to 30 kV, yielding an electric energy of up to 5.4 J per stage. The assembled stages were slid over six nylon all-threaded rods and tightened up with nuts. Our design allows arranging gap switch holes in an optical line of sight with a good precision so that the laser beam can pass through all stages.

A brass discharge electrode was placed 30 mm away from the generator output electrode and connected to a resistive load $R_{load} = 2.7$ kΩ. This ensured that the generator would always safely discharge its high energy through the load to the ground. The load itself was made up of high-voltage resistors forming a voltage divider enabling us to record the time evolution of the Marx's output voltage. A current viewing resistor or shunt with a 0.1 Ω resistance was also used to monitor the corresponding current.

7.3.3 Performance of the generator

7.3.3.1 General characterization of output voltage

An example of voltage pulse from the Marx generator is given in figure 7.17. This pulse was recorded for a 6-stage Marx charged to 27 kV, yielding a theoretical maximum voltage of 162 kV.

As seen in figure 7.17-(a), the laser arrival results in a clear voltage pulse that quickly damps by a few ns, followed ~ 30 ns later by the triggering of the Marx generator, which results in a very steep voltage pulse. The 10-90 % rising slope of this pulse was measured at 32 kV $\cdot$ ns^{-1}, with a

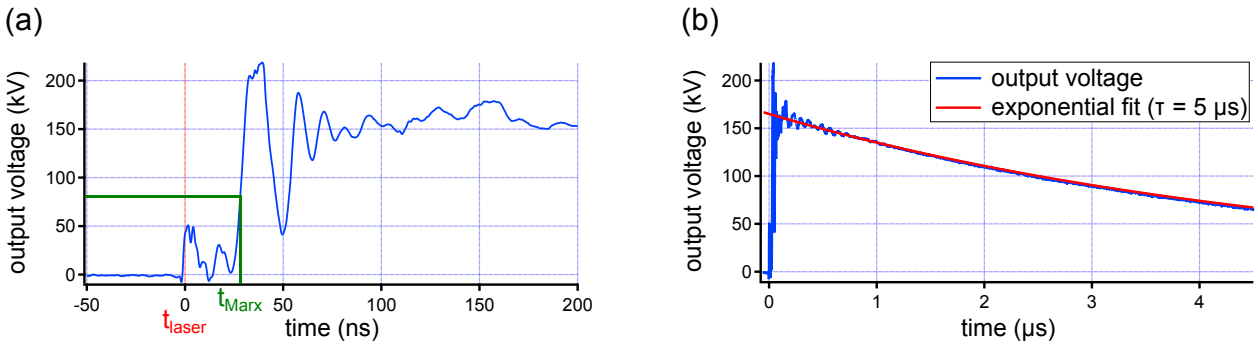

Figure 7.17: (a): rising edge of the voltage pulse from the Marx generator charged at $U_0 = 27$ kV. (b): long-time evolution of the same voltage pulse and exponential fit with a 5 µs damping time.

maximum voltage reached in ~ 5 ns. This risetime is limited by the inductance of the generator, a parameter that we did not try to optimize, which leaves room for improvement. After a transient regime of duration ~ 50 ns characterized by strong oscillations (probably due to noise), voltage stabilizes around 160 kV, which is within 5 % of the ideal output voltage amplitude (162 kV). The long-time evolution of the voltage pulse follows an exponential decay with a damping time of 5 µs (figure 7.17-(b)). This corresponds to the characteristic time $R_{load}C_{Marx} \approx 5.4$ µs.

We also checked that the triggering of the generator was due to filamentation. Indeed, if the first spark gap is undoubtedly closed by the action of filaments, the other switches could be triggered by a cascade process, in the same way as classical Marx generators. To this purpose, we occluded the third spark gap by inserting a plastic element in the generator so that the laser could not propagate past the second switch.

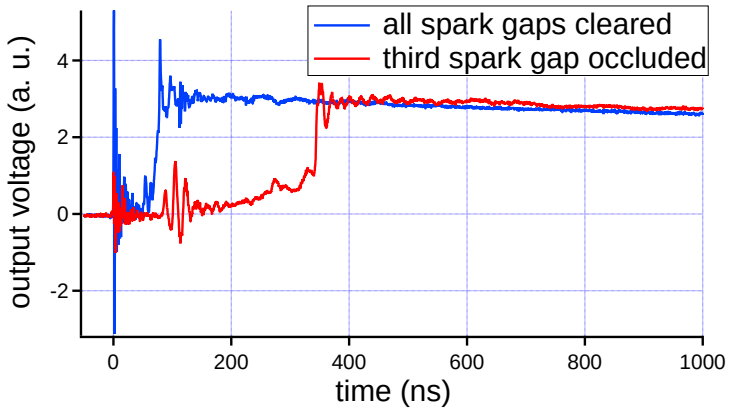

Figure 7.18: Time evolution of the Marx's output voltage with all spark gaps cleared (blue) and when the third spark gap is occluded.

Figure 7.18 presents the Marx's output voltage when the third spark gap is occulted, compared to the regular case with all spark gaps cleared. It is clear that the Marx performance is significantly degraded when filament-triggering of final gap switches is prevented. The 10-90 % risetime now reaches more than 150 ns, that is two orders of magnitude higher than before. Therefore we can say that if our Marx generator design is highly successful when properly triggered by laser filaments, its characteristics in the standard cascade triggering scheme are conversely very poor.

7.3.3.2 Triggering delay and jitter

Performance of the Marx generator can also be assessed with two other important parameters:

- first, the average delay between the laser pulse arrival and the breakdown of the generator. Breakdown time is taken as the time at which the output voltage reaches 50 % of the ideal maximum voltage output (that is the number of stages times U_0).
- second, the jitter of the laser/discharge delay.

The statistics presented in this section are based on 10 to 15 shots. We tested both positive and negative polarities to investigate a potential influence on the Marx's performance.

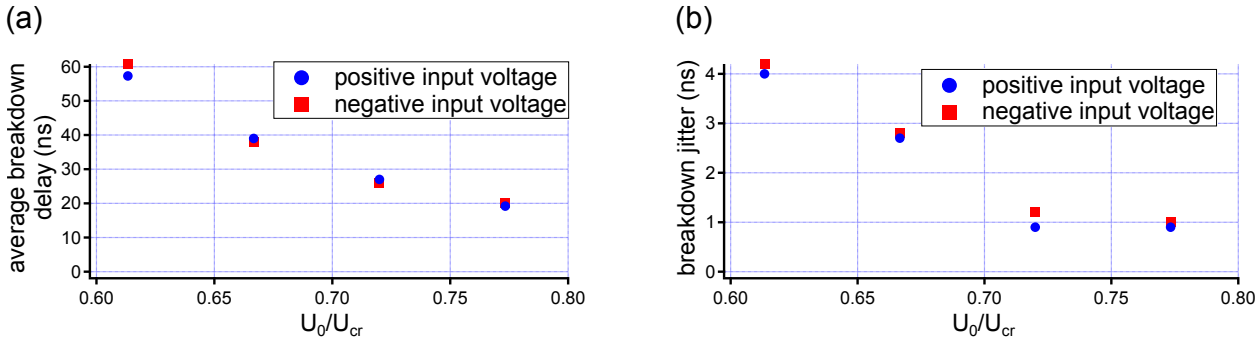

Figure 7.19: (a): evolution of the average laser/breakdown delay with the relative charging voltage of the Marx generator. (b): corresponding jitter evolution.

Figure 7.19-(a) displays the evolution of the average breakdown delay with the relative charging voltage. The delay appears to decrease as the charging voltage is increased, a trend that was already observed in the case of a single spark gap (figure 7.3-(a)). It is worth saying that the average breakdown delay for the whole Marx assembly is quite similar to that of a single spark gap, which constitutes a proof that the Marx output voltage pulse comes from the simultaneous triggering of all stages. Moreover the Marx's characteristics appear to be almost independent on the charging polarity.

As for the breakdown jitter (figure 7.19-(b)), it also decreases with the charging voltage and saturates past $U_0/U_{cr} = 0.7$, exactly like the jitter of a single gap switch (see figure 7.3-(b)). Of course, the jitter for the whole Marx generator is higher than for a single spark gap, because it should ideally be given by $\sqrt{N}\sigma_{SG}$, where N is the number of stages and σ_{SG} the jitter of a gap switch. Still a respectable value of $\sim$ 1 ns is reached, allowing for a very precise timing of the Marx's output voltage for applications. Here too, the charging voltage polarity has a negligible influence on the results.

Finally we tested the influence of laser parameters on the breakdown jitter to determine the minimum requirements in terms of laser resources. We found that with a charging voltage $U_0 =$ 27 kV, we were able to keep the same breakdown delay of $\sim$ 20 ns with a $\sim$ 1 ns jitter down to a laser energy of 30 mJ for a 900 fs pulse duration, or 6 mJ for a 100 fs pulse duration. This corresponds to a pulse peak power of $\sim$ 50 GW $\approx 10P_{cr}$, that is the upper limit for the single filamentation regime. Nowadays laser systems able to deliver such a peak power are widespread and have a relatively low cost, which make our filamentation-triggered Marx generator an affordable technology.

7.3.4 Conclusion

We built and demonstrated a Marx generator entirely triggered by laser filamentation. Based on the gap switch described in the first part of this Chapter, it is a compact, yet powerful instrument, able to deliver a voltage pulse up to 180 kV (or 30 kV per stage) with a risetime of $\sim$ 5 ns. The average delay between the laser arrival and the breakdown of the generator is $\sim$ 10 ns with a minimum jitter of $\sim$ 1 ns. The generator is able to work indifferently with a positive or negative polarity, operates in atmospheric air and is very reliable and sturdy, and quite easily adaptable to most experimental conditions by adjusting the number of stages and/or the charging voltage. It can also be triggered by a relatively weak laser pulse in the single-filamentation regime, which opens perspective for its widespread use given the high availability of low energy Ti:sapphire lasers.

Conclusion

This Chapter presented one of the main applications of laser filamentation-triggered and guided discharges: the contactless, remote switching of high currents and high voltages. In the first part was presented a simple and reliable air-filled gap switch able to reach down to a 200 ps jitter while switching currents in excess of 10 kA. In a second part, the on-state dynamics of this spark gap were systematically studied by means of the two-color interferometer presented in Chapter 6. We showed that when the gap is operated in the monopolar regime, characterized by a single current pulse, the switch plasma evolution was either governed by the current waveform for low-intensity pulses, or by recombination for high-intensity pulses. As for the alternative regime, it was shown to yield much longer plasma lifetimes than comparable monopolar pulses. In all cases however, a strong air hydrodynamic reaction takes place, that affects durably the gas pressure, density and temperature and significantly decreases the air dielectric strength for at least 100 µs even when the plasma has recombined. Finally we presented a compact and powerful Marx generator entirely triggered by laser filamentation. By closing all inter-stage gap switches simultaneously, it is able to generate a very steep voltage pulse with a total jitter of ~ 1 ns. Moreover it was shown that this generator can be triggered by a single filament with a femtosecond laser pulse of only $10P_{cr}$ peak power.

Bibliography

[1] W. K. Pendleton and A. H. Guenther, Review of Scientific Instruments **36**, 1546 (1965).

[2] A. H. Guenther and J. R. Bettis, Journal of Physics D **11**, 1577 (1978).

[3] R. A. Dougal and P. F. Williams, Journal of Physics D **17**, 903 (1984).

[4] J. R. Woodworth, R. G. Adams, and C. A. Frost, IEEE Transactions on Plasma Science **10**, 257 (1982).

[5] K. R. LeChien, M. E. Savage, V. Anaya, D. E. Bliss, W. T. Clark, J. P. Corley, G. Feltz, J. E. Garrity, D. W. Guthrie, K. C. Hodge, J. E. Maenchen, R. Maier, K. R. Prestwich, K. W. Struve, W. A. Stygar, T. Thompson, J. Van Den Avyle, P. E. Wakeland, Z. R. Wallace, and J. R. Woodworth, Physical Review Special Topics - Accelerators and Beams **11**, 060402 (2008).

[6] B. T. Hutsel, S. D. Kovaleski, D. L. Sullivan, and J. M. Gahl, IEEE Transactions on Dielectrics and Electrical Insulation **16**, 999 (2009).

[7] J. R. Woodworth, C. A. Frost, and T. A. Green, Journal of Applied Physics **53**, 4734 (1982).

[8] J. Hendriks, B. H. P. Broks, J. J. A. M. van der Mullen, and G. J. H. Brussaard, Journal of Applied Physics **98**, 043309 (2005).

[9] B. M. Luther, L. Furfaro, A. Klix, and J. J. Rocca, Applied Physics Letters **79**, 3248 (2001).

[10] L. Arantchouk, A. Houard, Y. Brelet, J. Carbonnel, J. Larour, Y.-B. André, and A. Mysyrowicz, Applied Physics Letters **102**, 163502 (2013).

[11] U. Kogelschatz and W. R. Schneider, Applied Optics **11**, 1822 (1972).

[12] J. A. Bittencourt, *Fundamentals of Plasma Physics*, 3rd ed. (Springer, New York, NY, USA, 2004).

[13] R. T. Beyer, *Nonlinear Acoustics* (U.S. Government Printing Office, Washington, DC, USA, 1974).

[14] G. F. Kinney and K. J. Graham, *Explosive Shocks in Air*, 2^{nd} ed. (Springer-Verlag, New York, NY, USA, 1985).

[15] M. N. Shneider, Physics of Plasmas **13**, 073501 (2006).

[16] H. Kusama and T. Yagi, IEEE Transactions on Plasma Science **25**, 1431 (1997).

[17] J. C. Kellogg, in *12th IEEE International Pulsed Power Conference*, Vol. 2 (1999) pp. 1175–1178.

[18] J. R. Mayes, W. J. Carey, W. C. Nunnally, and L. Altgilbers, in *IEEE Pulsed Power and Plasma Science Conference* (2001) p. 468.

[19] L. Arantchouk, G. Point, Y. Brelet, J. Larour, J. Carbonnel, Y.-B. André, A. Mysyrowicz, and A. Houard, Applied Physics Letters **104**, 103506 (2014).

[20] B. Martin, P. Raymond, and J. Wey, Review of Scientific Instruments **77**, 043505 (2006).

Chapter 8

Development of a long-lived radio-frequency plasma antenna

Contents

Introduction

Plasma radio-frequency (RF) antennas are apparatuses in which the traditional metallic emitter/receiver is replaced by a plasma column. The main advantages of this technology with respect to traditional antennas are very fast turn-on and turn-off times, reduced radar cross-section when non-operational, and the possibility to shape the plasma column to suit current needs at best. Until now most plasma antenna designs relied on solid dielectric vessels to confine the plasma. These vessels were filled with low-pressure noble gases ionized by means of an intense electric field [1, 2, 3, 4]. These plasma antenna designs proved to compare favorably with metallic antennas in terms of radiation strength and radiation pattern [1, 2, 3, 4, 5].

At the end of the 1960s, Gurgen Askar'yan already suggested to use laser-induced plasma to guide microwave radiation [6]. Later in the 1980s, a research team at the Naval Research Laboratory demonstrated the proof of principle of a fully virtual plasma antenna based on spark discharges triggered and guided by means of long Nd:YAG laser pulses [7]. Such plasma antennas have the great advantage to be vessel-free, further increasing their stealth capabilities. Later on, with the advent of femtosecond lasers and the emergence of filamentation as a research topic, attention turned to the possibility to use the long plasma columns generated by nonlinear ionization processes as waveguides, particularly for infrared [8] and microwave radiation [9, 10]. Naturally, one could expect this guiding effect to be valid in the RF range as well.

However a major drawback arising from the use of filamentation-generated plasma columns is their short lifetime. At $1 - 10$ ns, it is effectively too short for a practical use, especially in the prospect of radio communication. To this purpose, one must first increase the plasma lifetime by means of auxiliary techniques such as the use of a second, longer laser pulse to heat and densify the initial plasma [11], or the use of an external electric field to slow down the filament plasma decay [12]. Another related method is to use filamentation to trigger a guided spark discharge. Although this last technique does not prevent the laser-induced plasma from recombining, it results in a dense plasma column with a well controlled path. We decided to implement this last method in order to lengthen the lifetime of our plasma column.

This Chapter is made up of two parts: the first one is dedicated to the demonstration of a working virtual plasma antenna based on femtosecond filamentation. To this purpose, filamentation was used to guide meter-long sparks from a Tesla coil, in which were coupled RF signals with frequencies ranging from 500 MHz to 1.2 GHz. The second part focuses on the generation of plasma columns with a very long lifetime (~ 1 ms) using our filamentation-triggered Marx generator described in Chapter 7, so as to bring the plasma antenna one step closer to a working prototype.

8.1 Experimental demonstration of a virtual plasma antenna from filamentation-triggered Tesla coil spark discharges

We demonstrated a fully working virtual RF plasma antenna based on guided sparks from a Tesla coil. The choice of this kind of generator was dictated by the need for a power source able to deliver a very high voltage, yet compact. The Tesla coil proved to be able to routinely generate meter-long sparks, in which we coupled radio-frequency signals from a solid-state amplifier chain using a cylindrical cavity.

8.1.1 Guiding of long sparks from a Tesla coil

8.1.1.1 The Tesla coil

The Tesla coil is basically a high-gain voltage transformer made up of two resonant RLC circuits coupled magnetically, one coil of which is considerably larger than the other (figure 8.1-(a)). This enables one to obtain voltage AC bursts with peak amplitudes of several 100s kV [13, 14]. In our case, the primary capacitor C_1 is first charged up to a 12.5 kV DC voltage. The primary circuit is then closed by means of a closing switch, here a triggered trigatron with a $\sim$ 20 ns jitter. This initiates voltage and current oscillations in the primary circuit that are transferred to the secondary circuit through the mutual inductance M (figure 8.1-(b)). The capacitor C_2 is a combination of the self-capacitance of the secondary coil and of the capacitance between the output torus (see figure 8.1-(a)) and the ground. Our Tesla coil was built with the following component values: $C_1 = 40$ nF, $L_1 = 62$ µH, $C_2 \approx 49$ pF and $L_2 = 52.9$ mH, so that both circuits share the same resonance frequency:

$$f_1 \approx f_2 = \frac{1}{2\pi\sqrt{L_2 C_2}} = 101 \text{ kHz}. \tag{8.1}$$

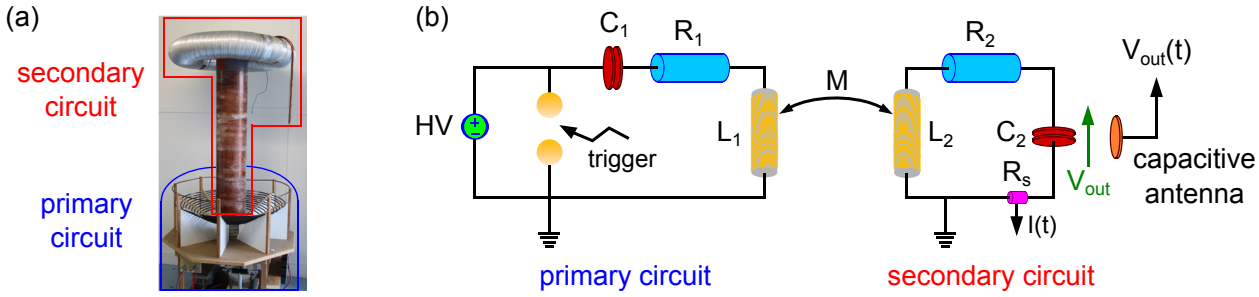

Figure 8.1: (a): photograph of the Tesla coil used in our experiments. (b): equivalent electric circuit, showing electric diagnostics (shunt R_s for the discharge current and capacitive antenna for the output voltage).

Currents in the primary and secondary circuits are solutions of the following equation system:

$$\begin{cases} \dfrac{1}{C_1} i_1(t) + R_1 \dfrac{di_1}{dt}(t) + L_1 \dfrac{d^2 i_1}{dt^2}(t) + M \dfrac{d^2 i_2}{dt^2}(t) = 0 \\ \dfrac{1}{C_2} i_2(t) + R_2 \dfrac{di_2}{dt}(t) + L_2 \dfrac{d^2 i_2}{dt^2}(t) + M \dfrac{d^2 i_1}{dt^2}(t) = 0. \end{cases} \tag{8.2}$$

The mutual inductance is given by $M = k\sqrt{L_1 L_2}$ where $k \approx 0.2$ is the coupling coefficient. Solving this equation system with appropriate initial conditions [13], one can find a solution consisting of

two damped sinusoidal oscillations of characteristic frequencies:

$$f_{\pm} = \frac{f_1}{\sqrt{1 \pm k^2}}, \tag{8.3}$$

forming a beating structure (figure 8.2). The corresponding high-frequency is $f_+ = 103.5$ kHz, that is a period equal to 9.66 µs.

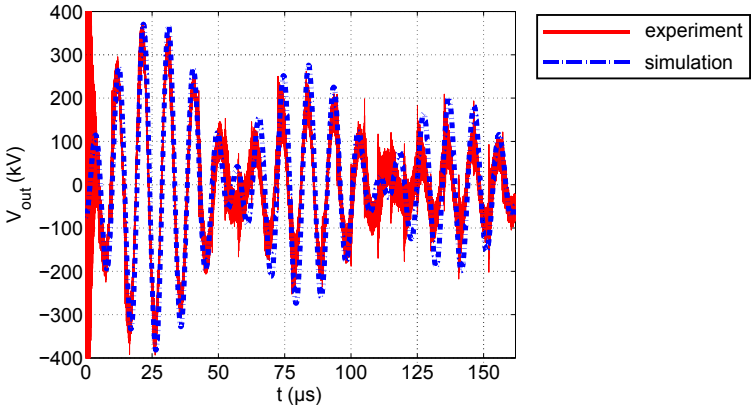

Figure 8.2: Measured (red solid) and simulated (blue dashed) output voltage from our Tesla coil.

To measure the time evolution of the output voltage of our Tesla coil, we made use of a remote capacitive antenna. This antenna, a 70 mm-wide copper disk, was directed towards the output torus of the Tesla coil and connected to a 1 MΩ oscilloscope channel using a 12.5 m coaxial cable, thus forming a capacitive divider. The high voltage part of this divider consists of the very small capacitor between the antenna and the Tesla coil. The low voltage part lies in the cable capacitance $C_{cable} = 1.25$ nF. This modeling is valid for timescales far smaller than 1.25 nF × 1 MΩ = 1.25 ms and can therefore be used to probe the evolution of voltage oscillations with 100 kHz frequency. The antenna was calibrated using a resistive divider made of twenty 18 kV high voltage resistances and by varying the supply voltage from 3 to 6 kV on the primary Tesla capacitor C_1. We thus measured a maximum output voltage amplitude of 365 kV (figure 8.2), yielding a gain $G = 28.9 \pm 1$, very close to the theoretical value $G_{th} = \sqrt{C_1/C_2} = 28.5$. Using this diagnostic we estimate the precision of voltage measurements to be better than 7 %. We also made use of a current viewing resistor installed in the grounded electrode to measure the discharge current.

8.1.1.2 Guided electric discharges from the Tesla coil

The Tesla coil in itself is able to generate impressive streamer and corona discharges from its output torus in the air, as depicted in figure 8.3-(a). To prevent such widespread spontaneous discharges, we attached a rod to the torus and fixed a brass spherical electrode with 10 mm diameter at its end. A similar electrode was grounded and placed at a distance D from the HV electrode, thus defining the length of the discharge gap. In this configuration, our Tesla coil was able to produce sparks up to 32 cm long (figure 8.3-(b)).

Using laser filaments to trigger spark discharges, it becomes possible to generate perfectly straight plasma columns linking the two electrodes (see figure 8.3-(b)). Actually, filamentation was shown to be able to increase the length of discharges by a factor 3 to 4 with respect to the maximum gap length for self-breakdown [15, 16, 17]. At LOA we even reached the record length of 1.8 m for

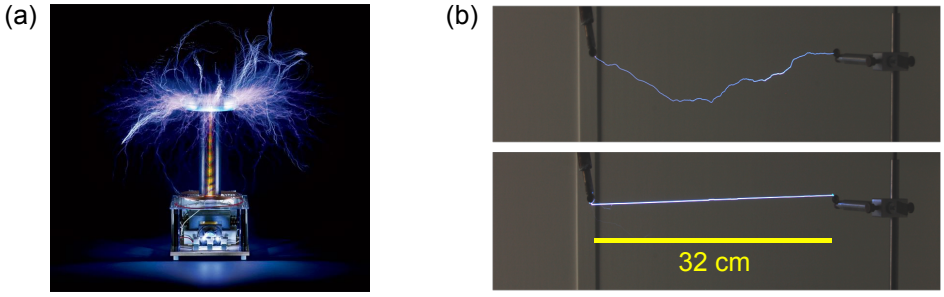

Figure 8.3: (a): photograph of natural discharges from the bare output tore of a Tesla coil (credit: Stan Musilek). (b): natural (top) and filament-guided (bottom) spark discharge from our Tesla coil. The laser propagates from left to right.

a guided discharge, although the corresponding triggering probability proved to be low [18]. This is much longer than what was observed for monopolar voltage sources: for instance, we only had a 320 % increase using the Marx generator described at the end of Chapter 7. This shows that AC voltage appears more favorable for discharge development than monopolar voltage.

The development of long gap, filamentation-guided spark discharges also appears very different from what was observed for centimeter-scale sparks (see Chapter 7). Figure 8.4 gives an example of antenna signal recorded during experiment. Tesla voltage oscillations are triggered at $t = 0$ by closing the trigatron switch (as shown in figure 8.1-(b)). The laser pulse is sent later, after a delay Δt we fixed by means of a digital delay generator (model DG535 from Stanford Research Systems).

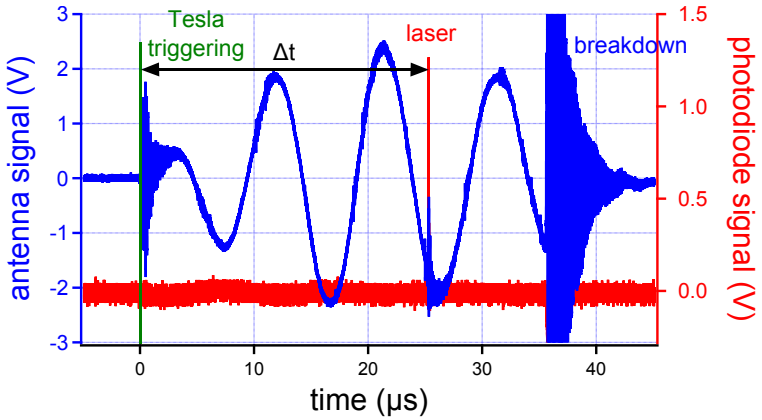

Figure 8.4: Examples of antenna (blue) and photodiode (red) signals recorded during discharge guiding experiments. The Tesla coil is triggered at $t = 0$ and the laser pulse is sent after a defined delay Δt. The discharge occurs later and is clearly visible as damped high-frequency oscillations on the antenna signal.

Then gap breakdown occurs after an incubation time, which in this case is about 10 µs. We even recorded sparks occurring almost 20 µs after filamentation. Assuming that discharge development starts as soon as filamentation takes place, the average propagation speed of discharge precursors is 10^5 m $\cdot$ s^{-1}. For centimeter-scale discharges, this speed was about 10 times higher, with a laser/discharge delay on the order of 10 ns.

The development of similar meter-scale laser-guided sparks from a Tesla coil was recorded by

means of a streak camera by a research group from the Canadian DRDC. The authors described the propagation of a hot plasma channel in the gap, luminescence of which closely followed voltage oscillations from the Tesla coil [17]. This precursor is undoubtedly akin to a leader channel (cf. Chapter 5), as evidenced by its moderate propagation speed.

Once breakdown occurs, current starts flowing through the plasma channel. Current signals are characterized by a main peak, which is quasi-symmetric (as in figure 8.5). Depending on the gap length, current can range from 60 to 350 A with a pulse duration varying between 30 and 100 ns. This current originates from the charge accumulated in capacitor C_2. The total charge evacuated through the plasma should therefore be given by $Q = C_2 U_{bd}$, where U_{bd} is the Tesla output voltage at the time of the breakdown. However we systematically found that the actual delivered charge is almost half of this theoretical charge. This is equivalent to defining a corrected output capacitor $C_{out} = 27 \pm 5$ pF. This charge leakage could originate from losses due to corona discharges and/or leader formation and propagation.

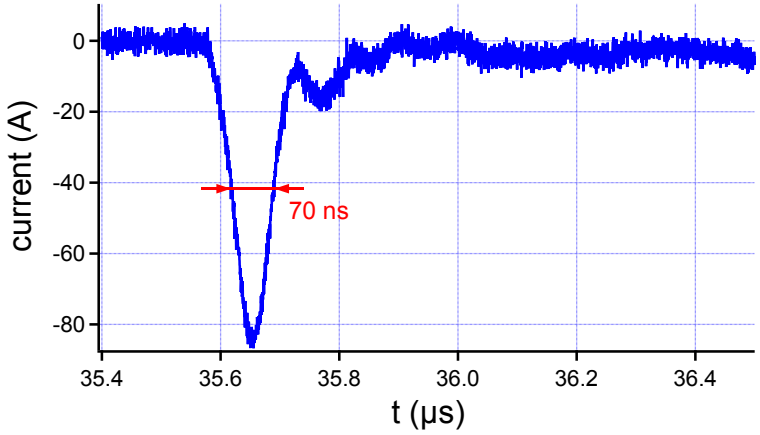

Figure 8.5: Discharge current measured during the the same discharge recorded in figure 8.4.

Since the antenna stops to give accurate voltage measurements during the discharge due to the strong breakdown-induced noise (as seen in figure 8.4), it is not possible to directly estimate the plasma resistance from the current waveform. Still, we can use our capacitor modeling to extract the time evolution of the output voltage of the Tesla coil during the spark:

$$V_{out} = U_{bd} - \frac{1}{C_{out}} \int_{t_{bd}}^{t} I(t')\ \mathrm{d}t'. \tag{8.4}$$

As $V_{out} = 0$ at the end of the discharge and since the current peak is roughly symmetric, the plasma resistance at the time of maximum current is given by:

$$R_{plasma}(t = t(I_{max})) = \frac{U_{bd}}{2I_{max}}. \tag{8.5}$$

Using experimental data for different gap lengths, we can see that this plasma resistance actually follows a linear trend with D (figure 8.6). A linear fit yields a lineic resistance $R_l = 8\ \Omega \cdot \mathrm{cm}^{-1}$. Assuming that the plasma column has approximately the same radius as for the centimeter-scale sparks studied in Chapter 7, that is 100 µm, we can estimate the plasma conductivity σ_p as:

$$\sigma_p = \frac{1}{R_l S} \approx 4 \times 10^4\ \mathrm{S} \cdot \mathrm{m}^{-1}, \tag{8.6}$$

that is 3 orders of magnitude below the conductivity of copper.

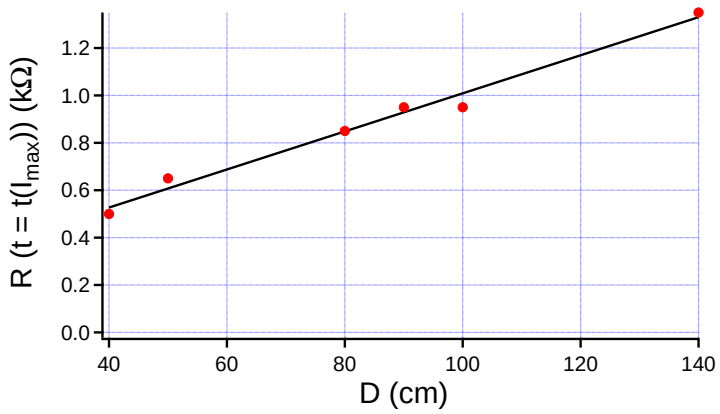

Figure 8.6: Evolution of the guided spark resistance at time of maximum current as a function of the gap length. The linear fit yields a lineic plasma resistance of 8 $\Omega \cdot \mathrm{cm}^{-1}$.

8.1.1.3 Optimization of filamentation-guided sparks from the Tesla coil

In order to use the plasma column from Tesla guided sparks as a RF antenna, experimental parameters first have to be optimized in order to yield the most favorable discharge conditions. Three of them are especially important:

- first, laser parameters for a discharge triggering and guiding effect as efficient as possible.
- second, the gap length, that is the length of the plasma column to be used in the RF coupling experiments.
- third, the delay Δt at which the laser in sent with respect to the triggering of the Tesla coil.

Laser parameters As seen in Chapter 5, the triggering of long gaps mostly relies on filamentation-induced hydrodynamic effects in air, and particularly on the transient air density reduction that occurs at the center of the filamentation channel and accordingly decreases breakdown voltage. To have an efficient spark triggering and guiding effect one therefore has to maximize filament energy deposition over the whole gap length. As the covered distance has to be on the order of 1 m, this asks for moderate focusing and input energy as high as possible. We decided to use $f/165$ focusing conditions with a laser energy of 300 mJ. Since the beam had to propagate for a few meters until reaching the lens due to practical reasons , we had to increase the pulse duration up to 900 fs so that the beam did not generate filaments inside the lens. We therefore used laser parameters close to those used for the generation of *superfilaments* (cf. section 4.1 in Chapter 4). As energy deposition is maximum shortly before the linear focus and quickly vanishes beyond, we positioned the linear focus of the lens very close to the furthermost electrode (in our case the grounded electrode) so that the maximum energy deposition occurred over the gap.

Gap length The choice of the gap length is important. Indeed shorter gaps yield better triggering probability and smaller plasma resistance (as seen in figure 8.6), meaning higher plasma conductivity and, therefore, better emitting properties. Of course this also means a shorter plasma length, which could negatively affect these same properties. Moreover, we noticed that very short gaps (down to $D = 40 - 50$ cm) often yield sparks that are only partially-guided, as in figure 8.7,

because the laser-induced path has to compete with naturally-generated paths from strong corona and streamer discharges originating from the HV electrode. This is also strongly detrimental to the plasma antenna since we are looking for a straight emitter.

Figure 8.7: Photograph of a partially-guided discharge recorded with a 32 cm gap.

A tradeoff must therefore be found to ensure that discharges could be reliably triggered, reasonably resistive and perfectly straight. To this purpose, we decided to use ~ 1 m long gaps.

Laser/voltage delay The final parameter to be adjusted is the delay between the laser arrival and the voltage triggering. To this purpose we scanned the value for Δt with a 1 µs step between 7 and 28 µs, recording the occurrence guided discharges. Probabilities were recorded over 10 to 20 shots and are plotted in figure 8.8.

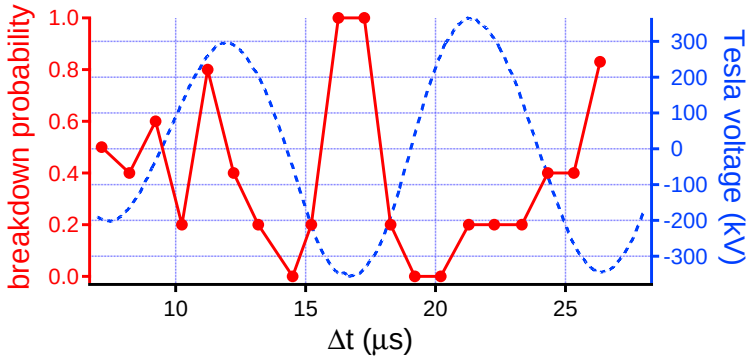

Figure 8.8: Evolution of the breakdown probability (red circles) with Δt for $D = 1$ m. Tesla output voltage (blue dashed curve) is also plotted as a convenience.

As seen in this last figure, spark probability goes to zero when the electric field in the gap is null. Moreover, it appears strongly dependent on the voltage polarity. Indeed, it becomes almost certain that breakdown would occur if filamentation happens when voltage is near a negative maximum. Probability is conversely much lower near voltage positive maxima. The most favorable delay then appears to lie around $\Delta t = 16$ µs, with a microsecond-wide window with a breakdown probability of 1. Moreover, at these delays, we recorded the discharge jitter to be around 440 ns, ensuring sparks develop always at the same time with respect to the period of voltage oscillations, and therefore yielding an optimal discharge reproducibility.

8.1.2 Coupling radio-frequency to plasma

Coupling RF current to the discharge plasma consists in generating an appropriate electromagnetic field by means of an adequate coupler so that this field will induce current in the plasma which

will in turn radiate at the same frequency as the excitation, much like a conventional wire antenna. These plasma-coupled electromagnetic fields are actually surface waves that remain confined on the air/plasma interface, as it will be shown in this section. This surface wave propagates along the plasma column and damps more or less rapidly depending on plasma parameters.

Dispersion equation for the surface waves The dispersion equation for the plasma-coupled electromagnetic modes is derived by considering the spark plasma as a long homogeneous cylinder of constant electron density n_e and of radius a generated in air. We are looking for an electromagnetic field that shares the cylindrical symmetry of the plasma, that is periodic functions of θ, but that also propagates along z. Decomposing the solution field in Fourier series we have:

$$\begin{cases} E_z(r,\theta,z) = \sum\limits_{n\in\mathbb{Z}} a_n E_z^n(r) \mathrm{e}^{i(n\theta+\beta z)} \\ B_z(r,\theta,z) = \sum\limits_{n\in\mathbb{Z}} b_n B_z^n(r) \mathrm{e}^{i(n\theta+\beta z)}, \end{cases} \tag{8.7}$$

where $\beta \in \mathbb{C}$ is the wavevector for the solution field and $(a_n,b_n) \in \mathbb{R}^2$. Full calculation is quite cumbersome and is given in Annex A. This leads to the following dispersion equation:

$$\left(\frac{a}{\kappa_p}\frac{I_n'(\kappa_p a)}{I_n(\kappa_p a)} - \frac{a}{\kappa_a}\frac{K_n'(\kappa_a a)}{K_n(\kappa_a a)}\right)\left(\frac{a}{\kappa_p}\frac{\omega\epsilon_p(\vec{r},\omega)}{c^2}\frac{I_n'(\kappa_p a)}{I_n(\kappa_p a)} - \frac{a}{\kappa_a}\frac{\omega\epsilon_a(\vec{r},\omega)}{c^2}\frac{K_n'(\kappa_a a)}{K_n(\kappa_a a)}\right) = n^2\beta^2\left(\frac{1}{\kappa_p^2} - \frac{1}{\kappa_a^2}\right)^2, \tag{8.8}$$

where I_n and K_n are modified Bessel functions of degree n of the first kind and of the second kind, respectively, ϵ_p and ϵ_a are the dielectric permittivities for the plasma and air, and the factors κ_p and κ_k are given by:

$$\begin{cases} \kappa_p = \sqrt{\beta^2 - \dfrac{\omega^2}{c^2}\epsilon_p} \\ \kappa_a = \sqrt{\beta^2 - \dfrac{\omega^2}{c^2}\epsilon_a}. \end{cases} \tag{8.9}$$

As modified Bessel functions are transcendental, the roots of this equation of unknown β form a twofold infinity. Thus, for each value of n there is a denumerable infinity of roots, any one of which can be denoted by the subscript m. A given mode is therefore defined by two subscripts (n,m).

$n = 0$ modes It can be shown that axially non-symmetric modes $n \neq 0$, if excited, damp so quickly that they do not play any role in the propagation of current along the plasma [19]. Therefore we will consider only cylindrically-symmetrical modes $n = 0$ for the rest of this study. In this case the dispersion equation (8.8) can be greatly simplified:

$$\left(\frac{a}{\kappa_p}\frac{I_0'(\kappa_p a)}{I_0(\kappa_p a)} - \frac{a}{\kappa_a}\frac{K_0'(\kappa_a a)}{K_0(\kappa_a a)}\right)\left(\frac{a}{\kappa_p}\frac{\omega\epsilon_p(\vec{r},\omega)}{c^2}\frac{I_0'(\kappa_p a)}{I_0(\kappa_p a)} - \frac{a}{\kappa_a}\frac{\omega\epsilon_a(\vec{r},\omega)}{c^2}\frac{K_0'(\kappa_a a)}{K_0(\kappa_a a)}\right) = 0. \tag{8.10}$$

In this precise case, we have a decoupling between $(a_0^p A_0, a_0^a B_0)$ and $(b_0^p C_0, b_0^a D_0)$. Each of this couple is solution of a system of two equations, the determinant of which is given by the first and second factor of equation (8.10), respectively. There are therefore two possible cases:

- if $\frac{a}{\kappa_p}\frac{I_0'(\kappa_p a)}{I_0(\kappa_p a)} - \frac{a}{\kappa_a}\frac{K_0'(\kappa_a a)}{K_0(\kappa_a a)} = 0$, then $(a_0^p A_0, a_0^a B_0) = (0,0)$, meaning the axial electric field $E_{z,0}$ is null in the whole space. This is a transverse electric (TE) mode.

- if $\frac{a}{\kappa_p}\frac{\omega\epsilon_p(\vec{r},\omega)}{c^2}\frac{I_0'(\kappa_p a)}{I_0(\kappa_p a)} - \frac{a}{\kappa_a}\frac{\omega\epsilon_a(\vec{r},\omega)}{c^2}\frac{K_0'(\kappa_a a)}{K_0(\kappa_a a)} = 0$, then $(b_0^p C_0, b_0^a D_0) = (0,0)$ and this time it is the axial magnetic field $B_{z,0}$ that vanishes everywhere, that is a transverse magnetic (TM) mode.

The most useful modes in our case are TM_{0m} modes because they generate an axial current along the z-axis, which corresponds to the case of a classical wire antenna. Accordingly, we designed our RF coupler to generate such TM modes, and particularly the first one (TM_{01}), which is also the least attenuated during its propagation along the plasma. This mode satisfies the following dispersion equation:

$$\frac{a}{\kappa_p}\frac{\omega\epsilon_p(\vec{r},\omega)}{c^2}\frac{I_0'(\kappa_p a)}{I_0(\kappa_p a)} - \frac{a}{\kappa_a}\frac{\omega\epsilon_a(\vec{r},\omega)}{c^2}\frac{K_0'(\kappa_a a)}{K_0(\kappa_a a)} = 0. \tag{8.11}$$

The TM_{01} mode To characterize the TM_{01} mode, one has first to find the corresponding wavevector β. To this purpose, we use the modeling that was presented in Chapters 1 and 6 for the plasma dielectric permittivity, based on the Drude model:

$$\epsilon_p(\vec{r},\omega) = 1 - \frac{\omega_p^2(\vec{r})/\omega^2}{1 - i\nu_c/\omega}. \tag{8.12}$$

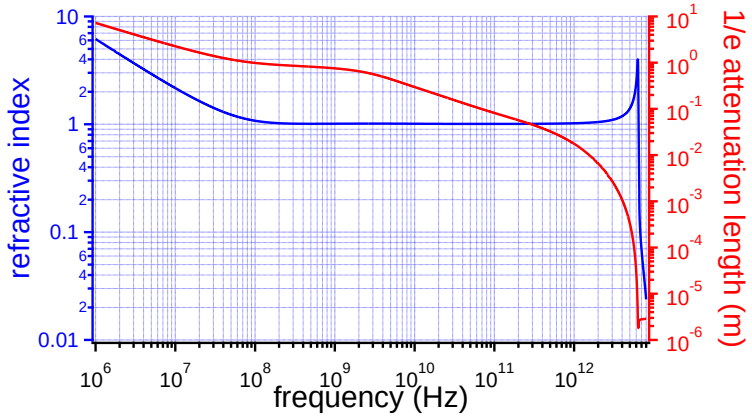

Figure 8.9: Computed evolution of the refractive index (blue) and of the 1/e attenuation length (red) for the TM_{01} mode with frequency.

We will here use orders of magnitude derived from the previous Chapter for plasma parameters for current pulses of the same amplitude as those from the Tesla coil: $n_e \sim 10^{24}$ m^{-3}, $T_e \sim 5$ eV yielding $\nu_c \sim 1$ THz. For air, we simply consider:

$$\epsilon_a(\vec{r},\omega) = 1. \tag{8.13}$$

The evolution of β with the field frequency, and more specifically of its normalized real part (refractive index) and imaginary part (1/e attenuation length), is plotted in figure 8.9. At low frequencies, the mode propagates rather slowly but is also weakly attenuated. From 100 MHz on, the refractive index stabilizes at 1. Attenuation starts to increase after a 1 GHz, and does so more and more rapidly as the frequency gets closer to the plasma frequency, eventually reaching ~ 10 µm beyond 1 THz. The most favorable frequency range therefore lies in between 100 MHz and 1 GHz because the field there propagates quite fast while attenuation is relatively low at ~ 1 m^{-1}.

We can also characterize the full electromagnetic field for the TM_{01} mode. In this case, the magnetic field is purely azimuthal, while the electric field has an on-axis component, but also a radial component. Figure 8.10 displays the spatial evolution of the absolute value of the total E and B fields at frequency 1 GHz. As seen in this figure, the electric field exhibits a strong discontinuity at the plasma boundary. This discontinuity only comes from the radial component of $\vec{E}$, which also proves to be much stronger than the axial field E_z. It can actually be shown that the amplitude of the discontinuity is proportional to the ratio of dielectric constants, which is on the order of 100 at this frequency. As for the axial electric field E_z, it is continuous at the boundary between plasma and air and is maximum at this radius value $r = a$. This behavior is shared by the magnetic field, which strongly peaks at the interface but quickly damps either in the plasma or in air.

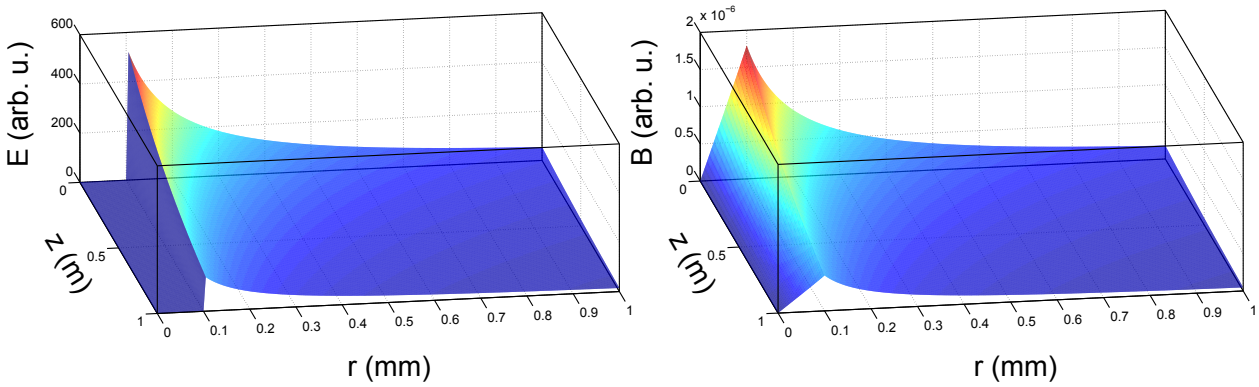

Figure 8.10: Spatial evolution of the total electric field (top) and of the total magnetic field (bottom) for a field frequency of 1 GHz. The plasma consists of an homogeneous column of radius $a = 100$ µm and density 10^{24} m^{-3}.

The TM_{01} mode is thus confined at the vicinity of the plasma/air boundary, quickly damping when the radius moves away from a. This behavior is characteristic of a surface wave. It also damps along z but at a much slower rate, allowing propagation over meter-long distances, which is particularly interesting in our case.

Limits of the model This modeling is rough in many ways. The most dubious hypothesis was to consider plasma as an homogeneous cylinder, which results in the appearance of a dielectric constant discontinuity. This discontinuity is then also present in the radial electric field. In reality, the transition from the plasma to the surrounding air is smooth and continuous, as it was shown in the previous Chapter during the study of spark plasmas. An adequate model would require using such a smooth electron density profile, but this would also result in the formation of a surface wave (see, e. g., reference [20]). Moreover, this would also render calculations even more cumbersome than they already are.

8.1.3 Coupling experiments: the virtual plasma RF antenna

8.1.3.1 The radio-frequency generation chain and the coupler

The radio-frequency coupler we decided to use in our experiments is a brass cylindrical cavity of 14 mm internal diameter, represented in figure 8.11-(a). This cavity is designed to emit an

electromagnetic wave with a transverse magnetic mode, corresponding precisely to our requirements as developed in the previous section. Electrically, it is equivalent to a RLC circuit, ideal response of which is represented in figure 8.11-(b). As seen in this last figure, the coupler is characterized by a broad resonance centered at 3.1 GHz but can work over a 10 GHz range, albeit with a mediocre gain. By construction, the metallic outer shell of the coupler is grounded and therefore acts as an excellent electromagnetic shielding. This point is especially relevant because discharge experiments are known for generating a broadband and intense noise.

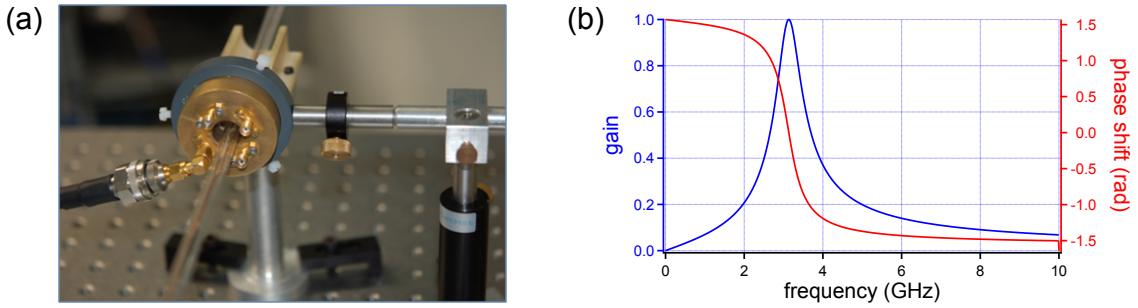

Figure 8.11: (a): photograph of the brass cylindrical cavity that we used as a RF coupler. (b): theoretical frequency and phase response of the coupler.

Our radio-frequency generation chain is depicted in figure 8.12. It consists of a signal generator with a 9 kHz - 3 GHz frequency range (model SMA 100A from Rohde & Schwarz). It is coupled to a solid-state 35 W amplifier with a 80 MHz - 1 GHz bandwidth (model BLWA 0810-30 from Bonn Elektronik). A bidirectional coupler at the output of the amplifier is connected to power sensors enabling us to record the power sent to and reflected by the end load. A 80 MHz - 1 GHz bandpass filter is used on the line to prevent discharge-induced current from going back to the RF generation chain. Finally, an impedance matching network consisting in a variable capacitor maximizes power transmission to the radio-frequency coupler.

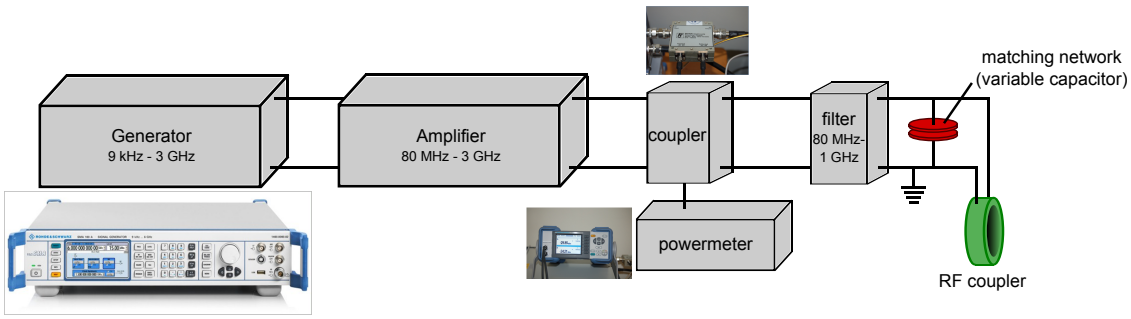

Figure 8.12: Schematic representation of the RF generation chain.

8.1.3.2 Experimental setup

The experimental setup used during coupling experiments on the discharge plasma is depicted in figure 8.13. Our Tesla coil is equipped with a spherical brass high-voltage electrode with 10 mm diameter. The second electrode consists of a simple copper wire. This choice was made to strengthen the electric field as much as possible at the grounded electrode so that the discharge would not

strike the RF coupler itself. The interelectrode gap is fixed at $D = 1.2$ m. To further reduce the risk of the discharge earthing through the RF coupler, we used a 30 cm long glass tube protruding from the coupler into the discharge gap. This tube proved not to reduce the electric field too much in the gap because we did not notice any reduction in breakdown probability.

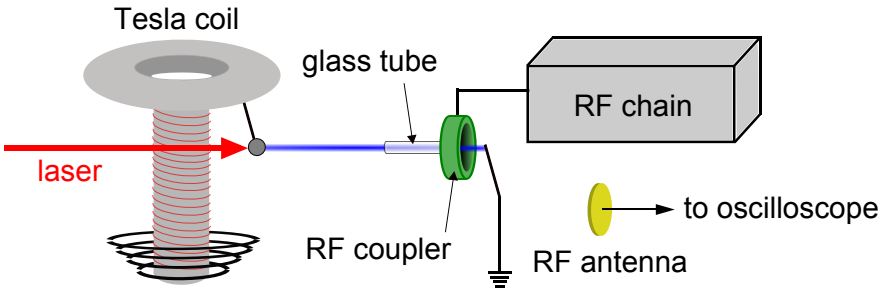

Figure 8.13: Experimental setup used during RF coupling experiments on the discharge plasma.

A patch antenna with a 100 MHz - 2 GHz bandwidth designed at the Laboratoire d'Electronique, Antennes et Télécommunications of Nice, France, is placed at ~ 2 m transversally from the plasma and detects any RF emission occurring in the room.

8.1.3.3 Experimental results

Using the experimental setup described in the previous section, we performed a frequency sweep with the RF generation chain every 10 MHz between 510 MHz and 1.2 GHz, recording a single discharge signal at each point. A typical antenna signal recorded for an excitation at 990 MHz is represented in figure 8.14-(a). Before the discharge occurrence, it exhibits a slowly varying behavior characteristic of the relatively low frequency voltage oscillations from the Tesla coil. The discharge itself results in a surge of RF emission that damps over a few microseconds, until the signal becomes flat.

Data processing is performed in the following way: we first identify the breakdown time, and then define two temporal windows with respect to this time: the first one starts at the beginning of the signal and lasts until the breakdown. The second one starts at the breakdown and covers the whole RF surge. These two windows have a similar duration so that they can be directly compared one to the other. Fourier transform is then performed on the signal limited to these two windows, yielding two different spectra that are plotted in figure 8.14-(b). As seen in this figure, injecting 990 MHz in the coupler results in no signal being detected before the discharge has occurred. However when plasma is generated through the RF coupler, a very strong emission peak at 990 MHz becomes visible. This result demonstrates that a RF field was successfully coupled to the spark plasma, and that in turn the plasma column behaved as an emitting RF antenna.

In order to characterize more thoroughly the emission properties of the plasma, we also computed the continuous wavelet transform of the signal from figure 8.14-(a) using a Morlet wavelet (cf. section 6.4.1.1 in Chapter 6). This powerful tool indeed gives access to a time-frequency signal representation, which is particularly useful in our case. The corresponding power density is displayed in figure 8.14-(c).

This scalogram shows that the discharge onset (around $t = 14.5$ µs) results in a broadband noise. More interesting, a clear signal centered on 990 MHz appears at this time and remains at a comparable level for the next 3 µs. This result can be interpreted as a sign that the discharge

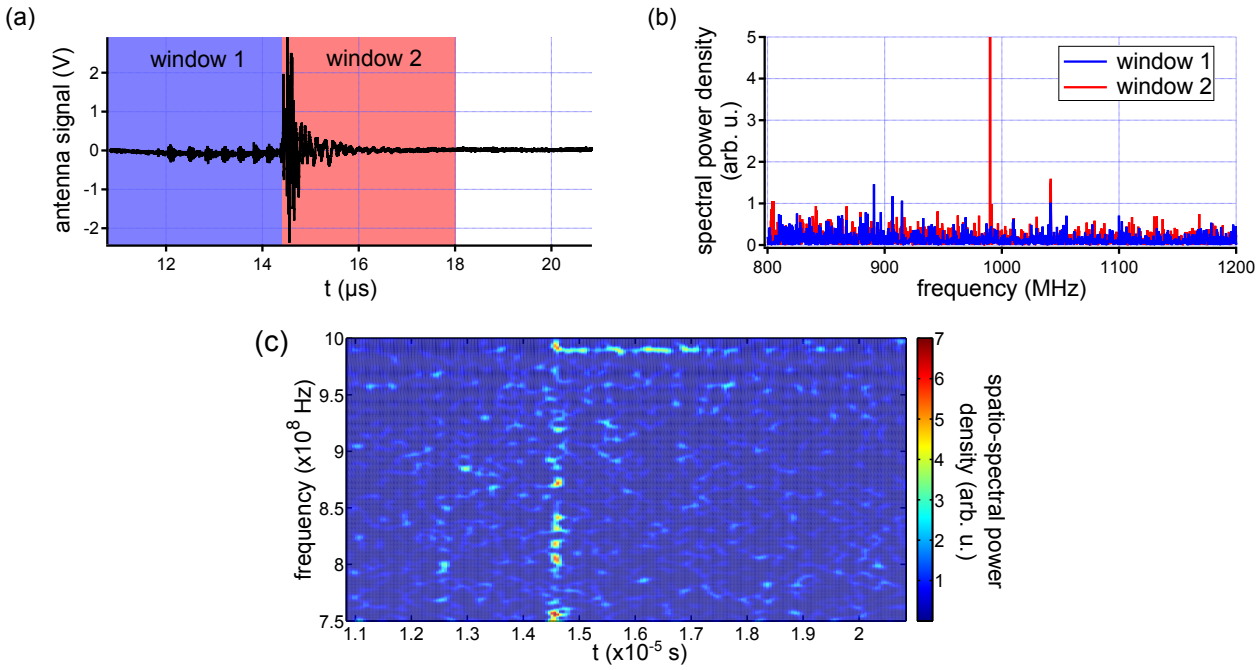

Figure 8.14: (a): raw antenna signal recorded during the discharge while exciting the RF coupler at 990 MHz. Two temporal windows with the same width are here defined: the first one lasts from the beginning of the recording up to the occurrence of the discharge. The second one starts at the beginning of the discharge. (b): corresponding Fourier spectra displaying a characteristic emission peak at 990 MHz when plasma is generated and proving RF coupling. (c): squared modulus of the Morlet continuous wavelet transform of the signal from figure 8.14-(a), displaying the appearance of a signal at 990 MHz from the discharge occurrence.

plasma remains conductive enough to emit radio-frequencies for much longer than the discharge current pulse. This is hardly surprising because we saw in Chapter 7 that short current pulses of duration $\sim$ 100 ns and amplitude $\sim$ 100 A generate a plasma that can keep a density above 10^{23} m^{-3} for several microseconds.

Figure 8.15 gives the evolution of two parameters with the excitation frequency: first, the signal strength, that is the spectral power density recorded in time window 2 at the excitation frequency weighted by the window duration. This corresponds to the raw coupled signal. Second, the signal to noise ratio (SNR), that is the ratio between the signal strength recorded in time window 2 and in time window 1.

In this last figure, we clearly see that the strongest emission is observed around 1 GHz, with the highest signal being recorded at 990 MHz.This frequency range appears well correlated to a high SNR as well, though for instance the SNR at 990 MHz is lower than at 980 MHz. This last frequency yielded the highest SNR at 59, which corresponds to a 35 dB gain.

Finally we compared emission characteristics of the plasma antenna with those of a standard wire antenna. To this purpose, a 5 mm diameter copper wire was installed linking the two electrodes through the RF coupler. We found that the spectral power density at 990 MHz in this case was 19.5 times higher than the one measured with the plasma antenna. To estimate the corresponding SNR, we simply divided the peak amplitude in the Fourier plane by that of the baseline and found it to be around 50 dB, about an order of magnitude higher than for the plasma.

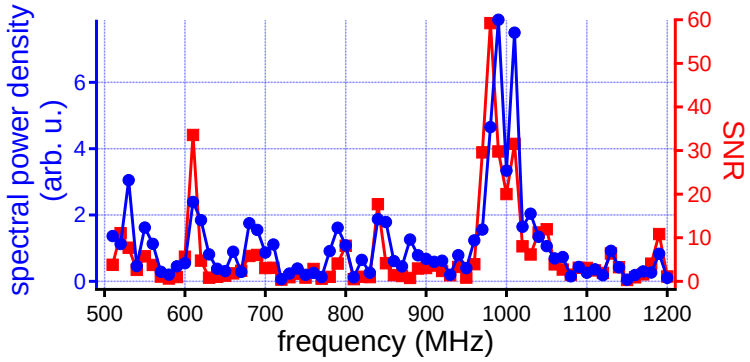

Figure 8.15: Evolution of the signal strength recorded in time window 2 at the exciting frequency (blue) and of the corresponding signal to noise ratio (red) with excitation frequency.

8.1.4 Conclusion

This section presented a proof of principle experiment for the use of a discharge plasma as an emitting radio-frequency antenna. This experiment relies on a Tesla coil as high-voltage generator. The main advantage of using such an AC voltage source is that it yields better results in terms of reduction of breakdown voltage when coupled to laser filaments, compared to monopolar voltage sources. After optimizing experimental parameters, we could achieve a 100 % breakdown probability with gaps up to 120 cm long, that is 3.8 times the maximum self-breakdown voltage. RF excitation was done by means of a cylindrical brass cavity linked to a 35 W solid-state RF generation chain with a 80 MHz - 1 GHz bandwidth. By forcing the spark discharge through the coupler, we successfully coupled the excitation frequency in the plasma, and the plasma then re-emitted at the same frequency. The best emission was achieved around 1 GHz while the top recorded SNR was equal to 35 dB. This compares well with a standard metallic wire antenna with an order of magnitude difference both in terms of signal strength and SNR, while the plasma conductivity is three orders of magnitude lower than that of copper. We also characterized the emission using the continuous wavelet transform and found that plasma radiated for several microseconds, which corresponds well to the decay of electron density in the spark plasma as studied in the previous Chapter. This microsecond lifetime is very short and is a serious limitation to the practical development of prototypes. We therefore focused on the generation of a plasma column with a lifetime as long as possible.

8.2 Lengthening the plasma lifetime

The method we chose to lengthen the discharge plasma lifetime is based on the results obtained from the study of our gap switch on-state dynamics (cf. Chapter 7). In this Chapter, we saw that the use of AC current with relatively low amplitude and moderate damping could significantly increase the plasma lifetime with respect to a monopolar current pulse with similar electric charge. Obviously it can also be asserted that the larger the electric charge, the longer the plasma will last. If it is possible, for a given generator, to bring it in the oscillatory regime by adjusting the load impedance, it is also much more difficult to increase its capacitance and/or its charging voltage. To this purpose we adopted a hybrid scheme: the high-voltage generator is only used to provide the necessary energy to achieve air breakdown and sustain the discharge plasma for a short time.

Then a secondary circuit with a large capacitor starts to discharge through the plasma over a much longer period.

This method was tested on the filamentation-triggered Marx generator described in Chapter 7. Using an adapted secondary circuit, we were able to achieve plasma lifetimes of more than 1 ms for 8.5 cm long spark discharges. Surprisingly the plasma column keeps a straight form up to these times. This represents a significant step towards the development of a working RF plasma antenna.

8.2.1 Experimental setup

The electric setup used in the experiments is displayed in figure 8.16. It consists of two entangled RLC circuits with different resonance frequencies: the first one is made up of the Marx generator, the coil L_2, the resistor R_2 and the capacitor C_2. In the second circuit, the coil L_1 takes the place of the Marx generator. The capacitor C_2 is charged up to $U_2 = -20$ kV from an external DC high-voltage power supply. For these experiments, the Marx generator was fitted with five stages charged up to -20 kV DC. In order to obtain optimal triggering characteristics (particularly jitter), we reduced the discharge gap to 8.5 cm.

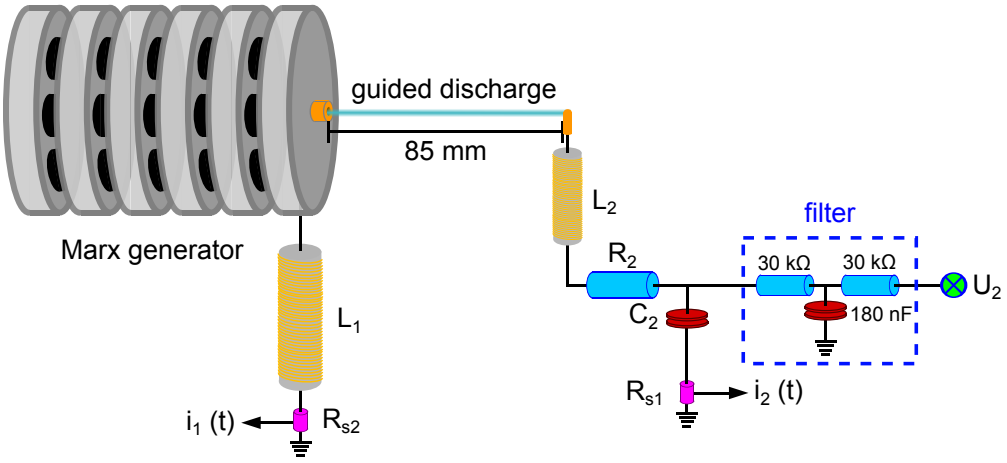

Figure 8.16: Schematic description of the electric setup used to lengthen the discharge lifetime. A filamentation-guided spark first occurs between the Marx generator and the other electrode, with the generator supplying the initial charge necessary to create and sustain the plasma at short times. Afterwards, the capacitor C_2 starts to discharge in the plasma through the two coils L_1 and L_2, significantly increasing its lifetime.

When gap breakdown occurs following filamentation, the Marx generator starts to discharge in the first ($R_2L_2C_2$) circuit at the condition that $L_2 \ll L_1$. It results in characteristic damped sinusoidal current oscillations at the high frequency f_{HF}:

$$f_{HF} = \frac{\sqrt{C_{Marx} + C_2}}{2\pi\sqrt{L_2 C_{Marx} C_2}}. \tag{8.14}$$

For the C_2 capacitor to withstand the high-frequency current oscillations, it has to be much larger than the Marx capacitance:

$$C_2 \gg C_{Marx}. \tag{8.15}$$

A RC filter placed between C_2 and the external power supply ensures that no return current could reach the DC generator.

Once the spark is established, C_2 starts to discharge through the plasma. By carefully choosing the value of L_1 with respect to the Marx's impedance, almost no return current goes to the Marx and most charges from C_2 effectively go through L_1. This secondary ($R_2L_1L_2C_2$) is characterized by current oscillations with a much lower frequency f_{LF}:

$$f_{LF} = \frac{1}{2\pi\sqrt{L_1L_2C_2}}. \tag{8.16}$$

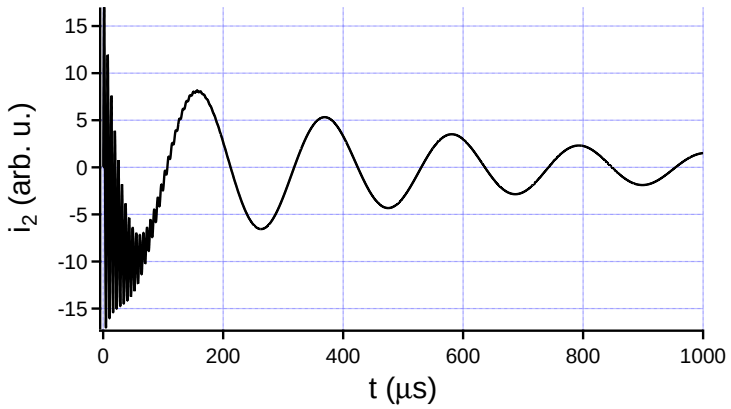

Figure 8.17: Simulated waveform of discharge current i_2 from the PSpice software.

To satisfy all these conditions and reach the millisecond timescale for the current we used the following component values: $C_2 = 180$ nF, $L_1 = 5.84$ mH and $L_2 = 454$ µH. To reduce damping at a reasonable level, the ballast resistor was fixed at $R_2 = 10\ \Omega$. In these conditions the two characteristic frequencies are equal to:

$$\begin{cases} f_{LF} = 4.70 \text{ kHz} \\ f_{HF} = 153 \text{ kHz}. \end{cases} \tag{8.17}$$

Two current viewing resistors R_{s1} and R_{s2} enable us to record the time evolution of the current through the first circuit and the second circuit, respectively.

We made simulations of the discharge current i_2 using the PSpice software. Results are plotted in figure 8.17, which shows two different regimes: at early times, current is characterized by a combination of a high frequency and a low frequency. At longer times, after ~ 100 µs, only the low frequency regime remains. A Fourier analysis gives the value of 5 kHz for the low frequency and 168 kHz for the high-frequency, which is close to the theoretical values of equation (8.17).

8.2.2 Experimental results

8.2.2.1 Discharge current

The time evolution of the discharge current recorded by the shunts R_{s1} and R_{s2} is displayed in figure 8.18. Figure 8.18-(a) shows current waveforms for short times up to 200 µs. In this temporal window, i_2 is characterized by a fast oscillating component with frequency 155.9 kHz superimposed over a slowly varying component with frequency 3.998 kHz. These two frequencies are in good agreement both with the theoretical values given in equation (8.17) and with the PSpice simulation displayed in figure 8.17. They correspond respectively to the Marx generator discharging through

the ($R_2L_2C_2$) circuit, and to the C_2 capacitor discharging through the ($R_2L_1L_2C_2$) circuit. We can see that after $\sim$ 70 µs the high-frequency disappears, marking the complete discharge of the Marx generator. From this point on, only C_2 is supplying charges to the circuit. As for i_1, it is almost free of the high-frequency regime, proving that it is well isolated from the first discharge circuit.

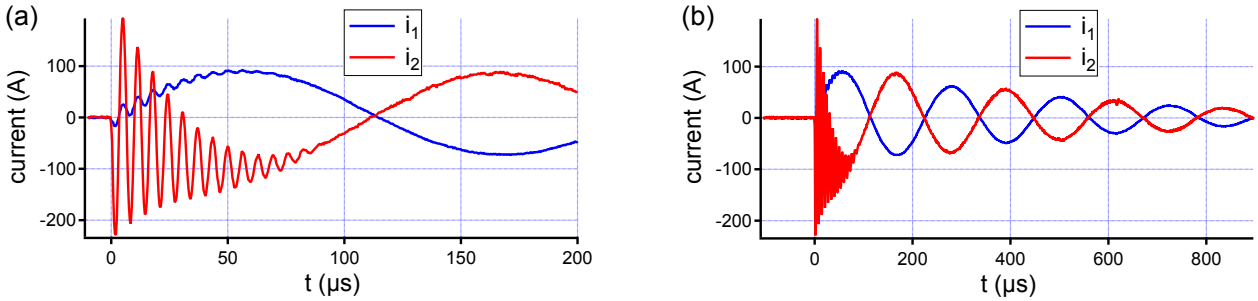

Figure 8.18: Time evolution of the discharge currents i_1 (blue) and i_2 (red) with experimental parameters described in the previous section. (a): short time window, displaying the high-frequency regime. (b): full waveform. $t = 0$ corresponds to the laser arrival time.

At longer times (figure 8.18-(b)), both currents evolve in the low frequency regime. The low damping enable them to reach a duration of more than 1 ms, proving that plasma exists at least up to this point, which is a remarkable result in itself. Still, other diagnostics need to be implemented on the discharges because current measurements do not give access to any plasma parameters while they are especially important in the development of the plasma antenna.

8.2.2.2 Plasma investigation: two-color interferometry

In order to assess the time evolution of plasma characteristics during the discharge, we used our interferometric diagnostic presented in Chapter 6. However its implementation on a setup such as the Marx generator asked for a completely new instrument. Indeed experimental conditions are much more hostile now than they were for the study of the gap switch, with voltages in excess of 100 kV and the risk that the discharge could strike optics or mounts. To this purpose we built a fully-integrated diagnostic using only Plexiglas parts, thereby strongly reducing the electric hazard (see figure 8.19).

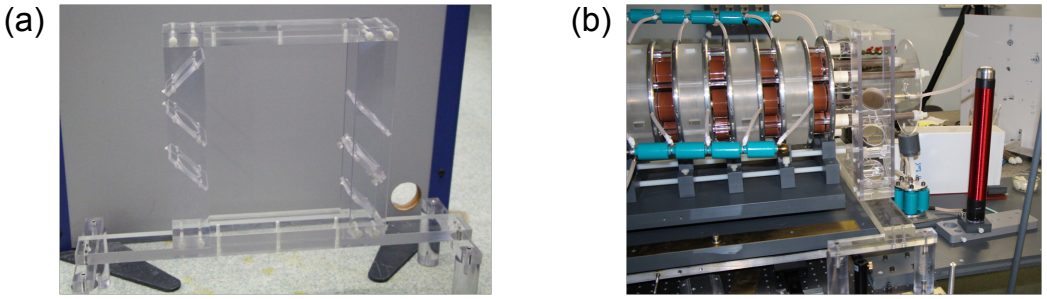

Figure 8.19: (a): photograph of the interferometer specifically built for the Marx generator. (b): photograph of the interferometer mounted on the Marx generator with the two-circuit discharge system.

However the new interferometer was built without any mechanical isolation or protection against air turbulence. Therefore its density resolution is undoubtedly lower than that of the instrument previously used in Chapters 3, 4 and 7.

Electron density We first studied the evolution of electron density in time. To this purpose we recorded electron density profiles in the middle of the spark discharge at various delays corresponding to extrema and zeros for the current waveform. Such profiles are plotted in figure 8.20-(a). As expected, these profiles are noisy, much more than those recorded with the gap switch for instance (see figure 7.10-(a) and (b)) because of the lack of noise damping devices on the instrument. Nevertheless they can still give access to useful information. They exhibit the same form as we previously encountered with cm-scale discharges, that is akin to a bell curve. We can see that after a delay of a few microseconds, electron density is at a level $\sim 10^{23}$ m^{-3}. Moreover, the density level does not vary much in time, only slowly damping. The full width at half maximum of the profile is on the order of 2 mm. This is much more important than in the case of the gap switch where the discharge FWHM was about 1 mm only. The fact that sparks from the Marx generator have a larger number of free electrons than discharges from Chapter 7 is not surprising because the Marx generator houses a much higher electric charge. However this does not result in a higher electron density but in a larger discharge channel. This can be explained as follows: we saw in the previous chapter that sustaining a plasma with a high electron density asks for an intense current bringing energy to the plasma. In other words, each current value corresponds to an electron density value that can be sustained. As in the case of sparks from the Marx generator and from the gap switch the current is approximately the same, then it is hardly surprising to find that spark plasmas share the same density.

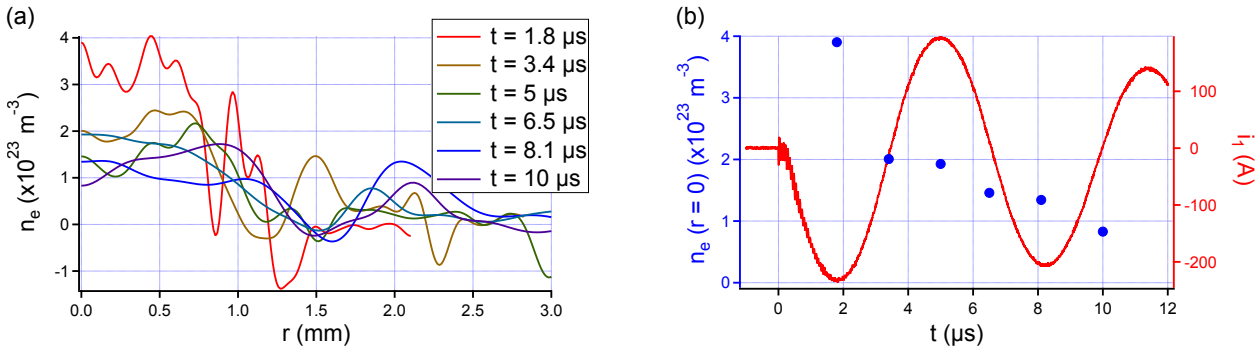

Figure 8.20: (a): radial electron density profiles recorded at early times in the high-frequency current regime in the middle of the spark discharge. (b): time evolution of the on-axis electron density (blue circles) and of the current i_1 (red solid).

Figure 8.20-(b) gives the evolution of the on-axis electron density with time, compared to that of the discharge current. We can see here that density remains very stable while current is oscillating. This steady-state has much in common with the one that was described for the gap switch in the AC regime (figure 7.14). In the former case the current frequency was ~ 500 kHz, about five times higher than f_{HF}. Still, it appears that f_{HF} is too high for the plasma to feel its influence.

At longer times in the low-frequency current regime, it becomes impossible to record electron density when the current is near zero. At current extrema, electron density profiles yield a peak density of $\sim 10^{23}$ m^{-3} (cf. figure 8.21), very similar to what was recorded at earlier times. It appears

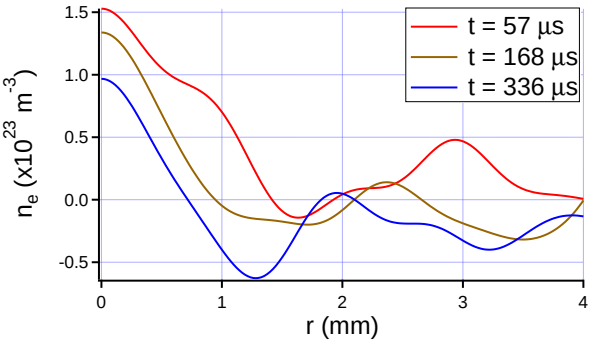

Figure 8.21: Radial electron density profiles recorded at long times in the low-frequency current regime in the middle of the spark discharge.

that with the low-frequency current, electron density behaves similarly to intensity, going below the detection threshold at low current and rising again at high current. This effect was predicted in the previous Chapter and expected to appear when the half-period of the current would become much larger than the plasma characteristic recombination time. We evaluated $\tau_{rec} \sim 500$ ns. Here with $f_{LF} = 4$ kHz, we have $T_I/2 = 125$ µs, which is indeed much higher than τ_{rec}. We could not record electron density past 350 µs because of the low detection threshold of the instrument. As a conclusion, we can say that plasma lasts *at least* up to the point current stops flowing, that is more than 1 ms. Since the recombination time of the remaining low-density plasma would be negligible with respect to this timescale anyway, we can identify the plasma lifetime with the current flowing time without introducing a large error.

Neutral density Hydrodynamic effects generated by the spark discharges were also studied using the two-color interferometer. Corresponding profiles exhibit the same phenomena as for cm-scale sparks, that is the formation of a shock wave blasting matter from the center, leaving a density hole with a residual density $< 0.1 n_0$ (see figure 8.22). The initial speed of the shock wave is estimated at 700 m $\cdot$ s^{-1}. This speed is much lower than the initial speed recorded in the case of far low intensity current pulses (for instance, for a 36 A current pulse, we had $u_{SW} \approx 1$ km $\cdot$ s^{-1}, see section 7.2.1.2 in Chapter 7). However we saw in Chapter 7 that shock wave speed is an excellent diagnostic for the initial energy deposition in air. This modest shock speed can then be explained by a lower energy deposition from the Marx sparks, due to the small current time derivative (even lower than when we investigated the AC regime with the gap switch in section 7.2.3.2, Chapter 7).

At longer times (figure 8.22-(b)), the shock disappeared, leaving the central underdense channel that continues to expand. However while expanding, it keeps its density level near 0, which does not correspond to a diffusive evolution. Actually, as long as current flows through the plasma, energy is deposited in the medium and brings heat to the system, and the channel will continue to expand while remaining saturated at zero density. Only when current stops will the channel start to evolve following thermal diffusion. Given the size the channel would have reached by this time (~ 2 cm FWHM), it could take longer than 1 s to disappear.

An interesting point to notice is that at all times, the neutral underdense channel is larger than the plasma channel, meaning that plasma remains somehow confined in the low density and low pressure region. This could be explained by a hydrodynamic confinement of the plasma heavy species in an area of minimum pressure, preventing free electrons from going away.

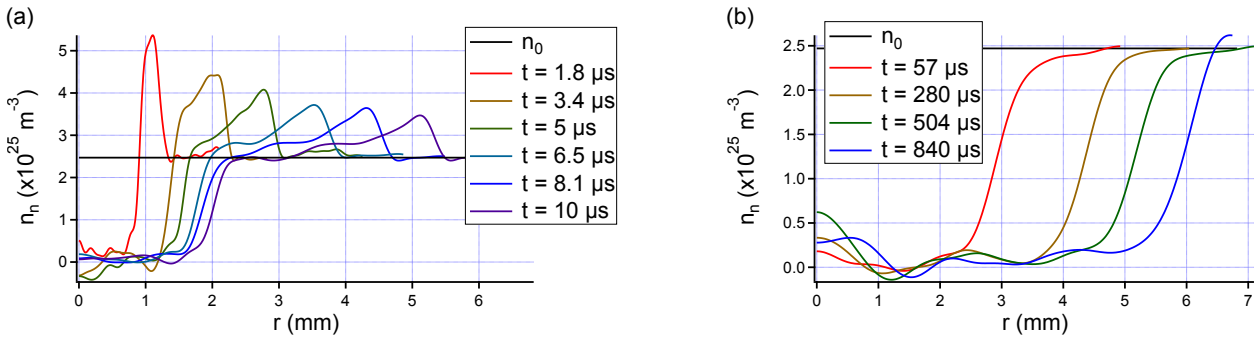

Figure 8.22: Radial neutral density profiles recorded in the middle of the spark discharge at early times in the high-frequency current regime (a) and at longer times in the low frequency current regime (b).

8.2.2.3 Discharge investigation: high-speed camera

To further investigate the spark plasma, we used a high-speed camera (Fastcam SA-X2 from Photron, Inc.) able to reach a repetition rate up to 1 MHz. In this experiment, it was fixed to 288 kHz, that is an image every 3.5 µs, with an exposure time of 300 ns.

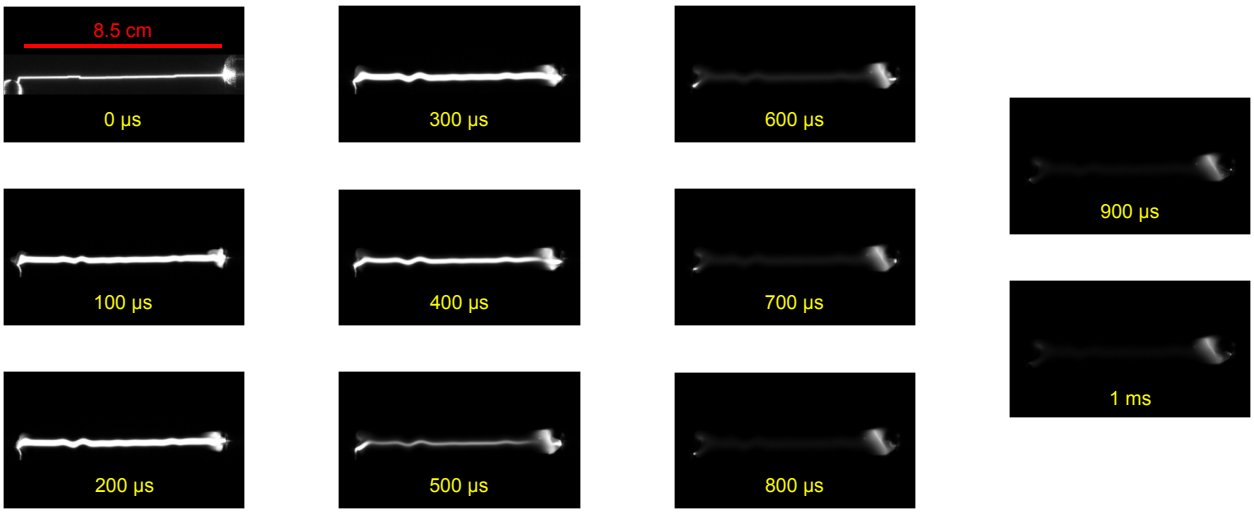

Figure 8.23: Selected pictures from a film of a single guided discharge from the Marx generator with the double electric circuit. Corresponding times are indicated on each picture.

Figure 8.23 gives examples of pictures from such a film, taken on a single guided discharge. From the onset of the discharge, a highly luminous channel forms and enlarges after 100 µs. Luminosity then slowly damps while the channel widens, and can still be seen after 1 ms. A striking characteristic of these pictures comes from the fact the discharge keeps a straight path all along. This finding is particularly important for the development of a long-lived plasma antenna because it ensures the antenna will keep stable emission characteristics like radiation pattern.

Figure 8.24-(a) displays the evolution of the discharge luminescence L in time using the high-speed camera. Results here are striking: we found that the luminescence oscillates at a frequency which is twice as high as that of the current. If we correlate these findings with results from

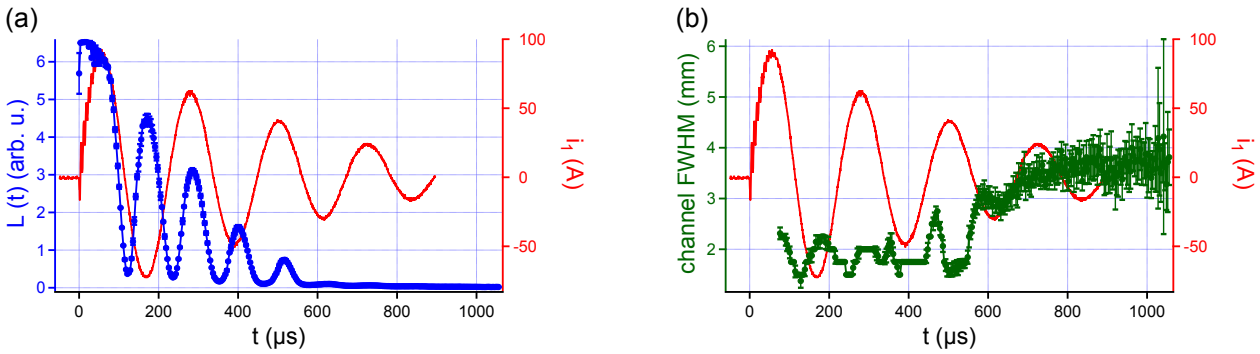

Figure 8.24: (a): time evolution of the space-averaged discharge luminescence as recorded by the high-speed camera. (b): evolution of the space-averaged luminescence profile FWHM with time. Current is also plotted as a convenience. Error bars correspond to a confidence interval of ± one standard deviation.

interferometry, we can see that in both cases the low-frequency current drives plasma dynamics, with either a non-detectable electron density and a very low luminescence near current zeros, and maximum values near current extrema. We can also see that a clear transition occurs shortly before 600 µs with the plasma becoming dark.

We also investigated the evolution of the luminous channel transverse size from the same images. In figure 8.24-(b) is plotted the channel FWHM time trace. It is characterized by an almost constant value around 2 mm during the first 600 µs. This value is in excellent agreement with the transverse size of electron density profiles measured by interferometry (figure 8.21). This proves that luminescence comes only from the plasma column at the center of the larger underdense air channel. There is also a transition beyond 600 µs with the channel width increasing progressively, stabilizing around 4 mm for the rest of the discharge, which should result in a strong decrease in electron density since current varies only slowly. This sudden increase in plasma volume must be linked to hydrodynamic effects, like a rapid evolution of pressure gradients at the center, and certainly not to hypothetical magnetic effects because of the very low current intensity.

8.2.3 Conclusion

We presented an original technique to increase the lifetime of discharge plasmas. It consists in using a double discharge circuit, the first one bringing the high-voltage needed to achieve breakdown, the second one bringing a large electric charge to slowly flow through the spark in order to sustain the plasma. This technique was tested using the filamentation-triggered Marx generator presented in Chapter 7. By using a relatively modest secondary capacitor of 180 nF, we were able to reach plasma lifetimes up to 1 ms, a considerable increase compared to the previously measured plasmas in Chapter 7. Using two-color interferometry and a high-speed camera, we were able to characterize the resulting sparks. They exhibit an oscillatory electron density and luminescence, which evolve at twice the current frequency, a behavior which was predicted for low-frequency currents in Chapter 7. A steady-state is quickly reached by a few tens of microseconds and lasts up to 600 µs. At this point, the plasma expands and its density decreases, but it nonetheless survives as long as current is flowing. More important, even though its transverse size is evolving, it keeps the straight shape it originally had, which is particularly important for the development of a reliable, long-lived plasma antenna. In the near future, the goal would be to implement this double circuit layout on the Tesla

coil in order to reach meter-long, millisecond guided sparks.

Conclusion

This Chapter presented results that were obtained for the development of a working RF plasma antenna. We first demonstrated that we could effectively use plasma from filamentation-guided sparks as a RF emitting medium. To this purpose we made use of a Tesla coil as high-voltage generator, first characterizing optimal experimental parameters to yield discharges with the best achievable quality. RF coupling experiment were then performed by placing a RF coupler around the discharge plasma and feeding it with a well defined frequency from a 35 W solid-state RF generation chain. Using an adapted antenna placed 2 m away from the plasma, we could clearly record a signal at the seeded frequency, but only when plasma was present, thus proving that coupling occurred and that plasma behaved as a wire antenna. The emission characteristics of the plasma antenna are within an order of magnitude to those of a standard copper wire antenna. We estimated the emission duration at a few microseconds, which is directly linked to the plasma lifetime. This duration is insufficient for our antenna to be of any practical use. We therefore designed a two-circuit scheme to be used with our high-voltage generators, that we tested on the filamentation-triggered Marx generator described in Chapter 7. Using this scheme, we were able to prolong the lifetime of 8.5 cm long sparks up to 1 ms. Characterization of these discharges showed that the plasma keeps its initial straight form until its recombination, ensuring this method can effectively be used for the improvement of our antenna design. The next step will be to implement the double circuit scheme on the Tesla coil to obtain meter-long sparks with a millisecond lifetime.

Bibliography

[1] G. G. Borg, J. H. Harris, D. G. Miljak, and N. M. Martin, Applied Physics Letters **74**, 3272 (1999).

[2] J. P. Rayner, A. P. Whichello, and A. D. Cheetham, IEEE Transactions on Plasma Science **32**, 269 (2004).

[3] I. Alexeff, T. Anderson, S. Parameswaran, E. P. Pradeep, J. Hulloli, and P. Hulloli, IEEE Transactions on Plasma Science **34**, 166 (2006).

[4] G. Cerri, R. De Leo, V. M. Primiani, and P. Russo, IEEE Transactions on Instrumentation and Measurement **57**, 242 (2008).

[5] E. N. Istomin, D. M. Karfidov, I. M. Minaev, A. A. Rukhadze, V. P. Tarakanov, K. F. Sergeichev, and A. Y. Trefilov, Plasma Physics Reports **32**, 388 (2006).

[6] G. A. Askar'yan, Soviet Physics JETP **28**, 1400 (1969).

[7] T. Dwyer, J. Greig, D. Murphy, J. Perin, R. Pechacek, and M. Raleigh, IEEE Transactions on Antennas and Propagation **32**, 141 (1984).

[8] M. Alshershby, Z. Hao, A. Camino, and J. Lin, Optics Communications **296**, 87 (2013).

[9] M. Châteauneuf, S. Payeur, J. Dubois, and J.-C. Kieffer, Applied Physics Letters **92**, 091104 (2008).

[10] Y. Ren, M. Alshershby, J. Qin, Z. Hao, and J. Lin, Journal of Applied Physics **113**, 094904 (2013).

[11] B. Zhou, S. Akturk, B. Prade, Y.-B. André, A. Houard, Y. Liu, M. Franco, C. D'Amico, E. Salmon, Z.-Q. Hao, N. Lascoux, and A. Mysyrowicz, Optics Express **17**, 11450 (2009).

[12] S. Bodrov, N. Aleksandrov, M. Tsarev, A. Murzanev, I. Kochetov, and A. Stepanov, Physical Review E **87**, 053101 (2013).

[13] D. G. Bruns, American Journal of Physics **60**, 797 (1992).

[14] K. D. Skeldon, A. I. Grant, and S. A. Scott, American Journal of Physics **65**, 744 (1997).

[15] Y. Brelet, A. Houard, G. Point, B. Prade, L. Arantchouk, J. Carbonnel, Y.-B. André, M. Pellet, and A. Mysyrowicz, Applied Physics Letters **101**, 264106 (2012).

[16] M. Henriksson, J.-F. Daigle, F. Théberge, M. Châteauneuf, and J. Dubois, Optics Express **20**, 12721 (2012).

[17] J.-F. Daigle, F. Théberge, P. Lassonde, J.-C. Kieffer, T. Fujii, J. Fortin, M. Châteauneuf, and J. Dubois, Applied Physics Letters **103**, 184101 (2013).

[18] L. Arantchouk, G. Point, Y. Brelet, B. Prade, J. Carbonnel, Y.-B. André, A. Mysyrowicz, and A. Houard, Journal of Applied Physics **116**, 013303 (2014).

[19] J. A. Stratton, *Electromagnetic Theory* (McGraw-Hill Book Company, New York, NY, USA, 1941).

[20] W. Zhijiang, Z. Guowei, X. Yuemin, L. Zhiwei, and X. Jie, Plasma Science and Technology **9**, 526 (2007).

Chapter 9

Towards a laser lightning rod

Contents

Introduction

Lightning is a fascinating and destructive phenomenon. Even though the probability of a lightning strike occurrence for a given area is low (on the order of 3 to 5 strikes per square kilometer per year in Europe [1]), it leads to several deaths and serious infrastructure damage on a regular basis. The protection offered by metallic lightning rods is relative, as sometimes lightning is known to take longer paths than expected, because of fluctuations of the local electric field. The protection of sensitive installations, like airfields for instance, asks for more elaborate and efficient lightning protection methods.

We saw in Chapter 5 that the use of specially-designed rockets trailing a metallic cable are able to trigger lightning [2]. This method, although useful, suffers from a relatively low triggering probability (60 %), and also works in the single shot regime. This is not enough since many lightning strikes are usually necessary to completely neutralize a storm cloud. An ideal discharge triggering method would be able to work at a high repetition rate and with a negligible cost for each shot. Powerful lasers able to ionize air are able to meet these requirements. Even though the use of nanosecond lasers proved not to bring any significant results [3, 4], the advent of femtosecond lasers and the emergence of filamentation in air revived the dream to be able to trigger lightning at will.

As early as 1995, that is the date of the founding paper of Braun on filamentation [5], Zhao and co-authors from the University of New Mexico demonstrated a dramatic reduction of air breakdown voltage over a 26 cm gap using a 200 μJ femtosecond laser pulse at 248 nm [6]. Later, the guiding effect of filamentation was proven over several meters using standard infrared femtosecond pulses [7, 8, 9, 10]. Still, full-scale outdoor experiments did not yield significant results. The most advanced work, up to now, was done by the Teramobile project when they recorded precursor signals of discharges spatially and temporally correlated with laser shots during a thunderstorm [11]. New generations of lasers might prove crucial in the development of this technology.

This Chapter first presents the mechanisms of lightning and how filamentation can be expected to trigger it. In a second part, we expose the results from experiments that were carried out at the DGA/TA facilities in Balma, France in collaboration with the Airbus Group.

9.1 Lightning mechanisms and realistic scenarii for filamentation-triggered lightning

9.1.1 Mechanisms for lightning development

Lightning is the name given to natural sparks originating from storm clouds. Even though the mechanism of electrostatic charging of clouds is not well elucidated, it is known that in 90 % of cases a storm cloud is charged negatively with respect to the ground. Lightning strikes can be divided in two categories: on the one hand, inter and intra-cloud discharges, that is sparks occurring either between different clouds or between two regions of a same cloud with opposite global charges, or cloud-cloud lightning. On the other hand, the storm cloud can also discharge to the ground, which is our case of interest. Typically cloud to ground sparks occur 2 to 3 times less frequently than cloud to cloud discharges. Altitude of thunder clouds is about 3 km on average, but lightning can originate from deep inside the cloud up to 10 km. In most situations storm clouds carry an important negative charge closest to the ground, with a few positive charges at the very bottom edge of the cloud. The resulting voltage drop between earth and storm clouds can reach 100 MV [12]. These characteristics are schematically displayed in figure 9.1.

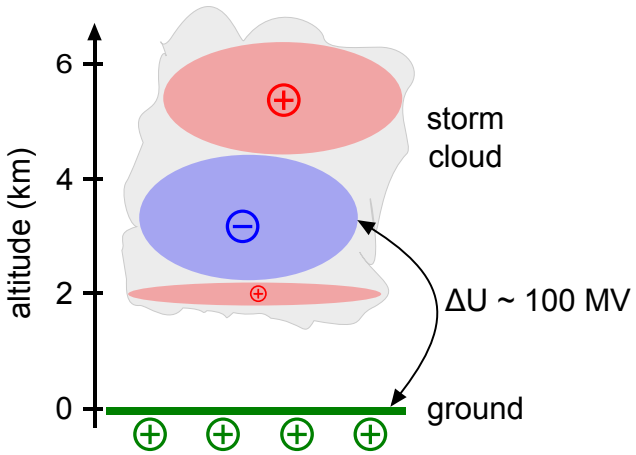

Figure 9.1: Schematic representation of a thunderstorm cloud displaying intra-cloud charge repartition with respect to altitude.

9.1.1.1 Initial lightning strike

The development of an initial lightning strike starts as streamer discharges between the strong negative region in the cloud and the weak positive region at its bottom edge. The required field is on the order of 3 MV $\cdot$ m^{-1}, that is the critical field for atmospheric air breakdown. These discharges quickly neutralize the weak positive region and the streamers proceed down in air between the storm cloud and the ground. They will eventually induce the generation of a leader channel, that is a channel of hot plasma. The leader formation comes from the strong Joule heating of air due to the combined streamer currents flowing from the cloud, rising the gas temperature above the threshold where electron attachment is largely negated, that is about 1500 K (cf. Chapter 5). Leader conductivity is high enough so that the voltage drop across it is small with respect to the cloud potential. As a consequence the leader “carries” the high-voltage potential of the storm cloud

further down into the gap, which promotes the formation of new streamers from its tip and allows the leader to extend progressively in space. The propagation of such a negative leader typically occurs in jumps with about 50 m length. This step-wise propagation is due to the time needed for the root of streamers at the leader tip to heat up and rise their conductivity high enough so that the leader channel can effectively propagate. The typical time needed to perform a step is on the order of several tens of microseconds while the step itself develops in ~ 1 µs, yielding an average propagation speed of $10^5 - 10^6$ m $\cdot$ s^{-1}. Depending on the local electric field distribution, the leader can branch several times during its propagation. Negative leader current was estimated at several hundreds of amperes, corresponding to a number of streamers at the leader tip in excess of 10^5.

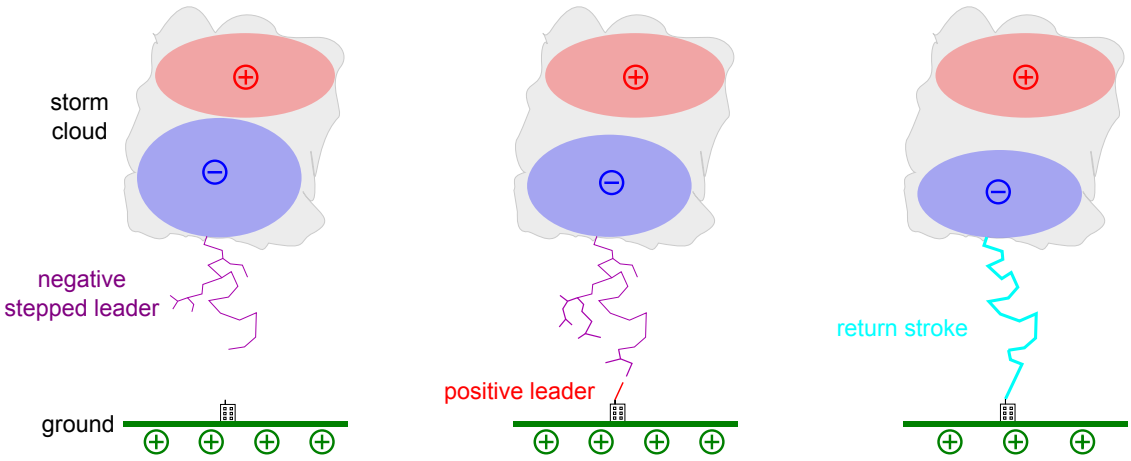

Figure 9.2: Inception of a lightning strike: a stepped negative leader forms from the storm cloud and proceeds down towards the ground with a typical speed $10^5 - 10^6$ m $\cdot$ s^{-1}, branching in many directions (left). While approaching the ground, this leader raises the electric field experienced by objects on the ground. This is sometimes sufficient to trigger a positive upward leader from regions of maximum electric field (center). Finally, positive and negative leaders connect, resulting in a high current pulse ($\sim$ 100 kA) propagating from the ground to the cloud: the return stroke (right).

When the stepped negative leader is less than $\sim$ 200 m from the ground, it raises the electric field so much that positive upward leaders can be triggered from ground objects, especially if they have a small radius of curvature and reinforce the field, like antennas for instance. Upward and downward leaders eventually connect, establishing a conducting channel over the whole length between the storm cloud and the ground. A current pulse then occurs, propagating from the ground to the cloud at almost the speed of light to neutralize its negative charge reservoir. This massive natural spark, which can carry currents in excess of 100 kA, is called the return stroke and is responsible for the sudden high-intensity glow of the lightning channel. Discharge processes can then stop here, resulting in the slow decay of the plasma and of lightning-generated hydrodynamic air structures. If enough charges are still available in the ground, they can also result in secondary lightning components.

9.1.1.2 Subsequent lightning components

Once the first return stroke has occurred, the resulting tremendous current flowing through air results in a strong hydrodynamic reaction, very similar to what we measured in the case of labora-

tory spark discharges (see Chapters 7 and 8). This reaction consists in the generation of an intense cylindrical shock wave which is the source of thunder. This shock ejects matter from the center of the channel, leaving a quasi null neutral density. This low-density channel extends over the whole cloud-ground gap and can greatly favor the development of subsequent discharge processes because of the resulting high reduced field E/n_n, given enough charges and voltage are available.

Secondary discharges can take different forms, depending on the associated current pulse. The most violent subsequent strike is associated with the formation of a *dart leader*, so called because of the absence of any branching during its propagation. Basically it is akin to a leader channel but propagating much faster in the low density channel generated by the first strike. Once the dart leader connects back the ground and the storm cloud with a conducting plasma channel, a new return stroke occurs shortly. Dart leaders only develop when current initially stopped flowing in the original conducting channel because no new precursor can form as long as plasma has not recombined [13].

Sometimes a background current of intensity $\sim$ 100 A continuously flows through the initial discharge channel, preventing plasma from recombining. In this case, current impulses can form and propagate from the cloud to the ground. One of the most studied of such impulses is the M-component, which was explained to originate from a high-altitude inter-cloud leader finding its way down to the old discharge channel from the first return stroke [14].

On average more than 10 discharge events can occur before the cloud charge is significantly depleted [13].

9.1.2 Realistic scenarii for filamentation-triggered lightning

Influence of filamentation on the triggering of high-voltage discharges has already been investigated in Chapter 5. The most basic approach is to think of the plasma filament as a conductor placed in the ground/storm cloud gap, resulting in a local reinforcement of the electric field. This is exactly the scheme detailed in the section 5.2.1.2, which relies on the polarization of the low-conducting plasma channel in the external field. We saw that the corresponding needed time was on the order of 500 ns, which is much higher than the plasma lifetime. A direct action of the filament plasma on the triggering of lightning is therefore highly unlikely to have any influence. This would require increasing the plasma lifetime by at least several orders of magnitude using alternative techniques.

Filamentation-induced air hydrodynamics appear more promising since they were shown to result in a dramatic decrease of air density, given enough laser energy is deposited. As filamentation can be generated at distances up to 1 km [15] and propagate over several hundred meters [16], it is theoretically possible to extend energy deposition up to such distances, but doing so in an efficient way would ask for very energetic and powerful laser pulses, although short pulse duration was shown to be detrimental on the length of filaments in long-range propagation [17]. This could be coupled to the use of a high repetition rate laser, typically at 1 kHz or more, so that cumulative effects similar to those discovered by Cheng *et al.* could be observed [18].

Given the current available technology, the most realistic scenario for lightning triggering using filamentation would be the initiation of upward positive leaders in order to intercept a natural downward negative leader, in the same way standard metallic lightning rods work (see figure 9.2). This would have the advantage to allow the use of a short pulse duration to maximize energy deposition over $\sim$ 100 m. An alternative scenario would be to generate filaments close to the storm cloud at distances up to 2 to 3 km to initiate a descending negative leader. This would ask for energy deposition concentrating at very long propagation distances, requiring controlling

multifilamentation despite strong air turbulence.

9.2 Large scale discharge experiments

Results that are presented in this section were obtained during an experimental campaign that took place in the facilities of the Direction Générale de l'Armement/Techniques Aéronautiques in Balma, France. This study was funded by the Airbus Group as a prospective work for the development of a laser lightning rod.

9.2.1 Experimental facilities and experimental setup

Experiments took place in a large hall with synthetic and wooden walls housing a 25 stage Marx generator from Haefely Hipotronics (see figure 9.3-(a)) able to deliver 2.9 MV voltage pulses. For our study we used a voltage waveform with a slow risetime in order to mimic the approach of a descending negative leader towards the ground. The need for a high charging resistor reduced the effective electrode voltage to 1.55 MV (see waveform in figure 9.3-(b)).

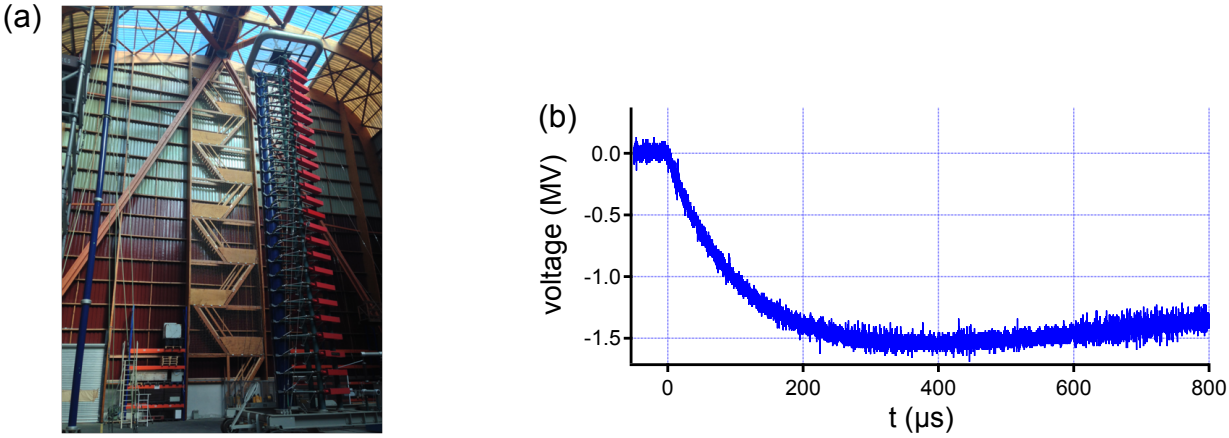

Figure 9.3: (a): photograph of the 25 stage Marx generator. (b): voltage waveform on the high voltage electrode.

The high-voltage electrode consisted in a large metallic plate several meters long placed at an adjustable height. The grounded electrode was a rod terminated by a metallic sphere with 10 cm diameter. Inter-electrode gap was fixed at 4 m. The femtosecond laser (Ti:sapphire laser chain "ENSTAmobile") was placed in a tent with air conditioning systems. A photograph of the whole setup is given in figure 9.4-(a).

Two different experimental configurations were tested: in the first one, laser filaments covered the whole discharge gap, skimming the ground electrode and continuing all the way up to the HV electrode. In this case, a $f/330$ focusing is used, corresponding to a 10 m lens. In the second configuration, filamentation only covers half of the gap using a focusing two times stronger at $f/165$ (figure 9.4-(b)).

In this study, we made use of different diagnostics. We had access to the evolution of the gap voltage given by a high-voltage resistive divider. A Rogowski coil enabled us to measure the current going to the grounded electrode up to 5 A. Two triggered Canon cameras recorded time-integrated pictures of discharges from two different points of view. Finally a fast photodiode allowed to

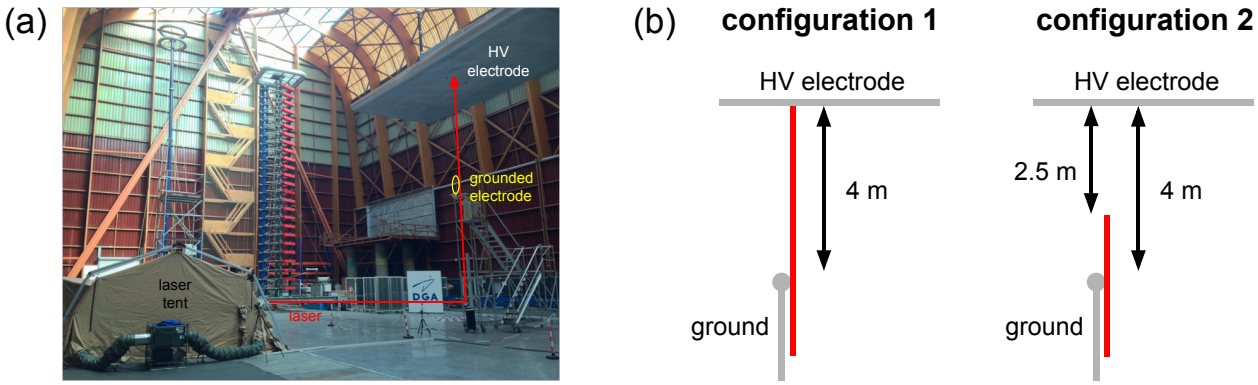

Figure 9.4: (a): photograph of the experimental setup displaying the Marx generator, electrodes and the laser path. (b): schematic description of the two investigated configurations.

precisely time the laser shot with respect to voltage.

9.2.2 Electrical phenomena during a natural discharge

We first investigate electrical phenomena occurring during natural discharges, that is discharges in absence of filamentation. Corresponding voltage and current waveforms are displayed in figure 9.5-(a).

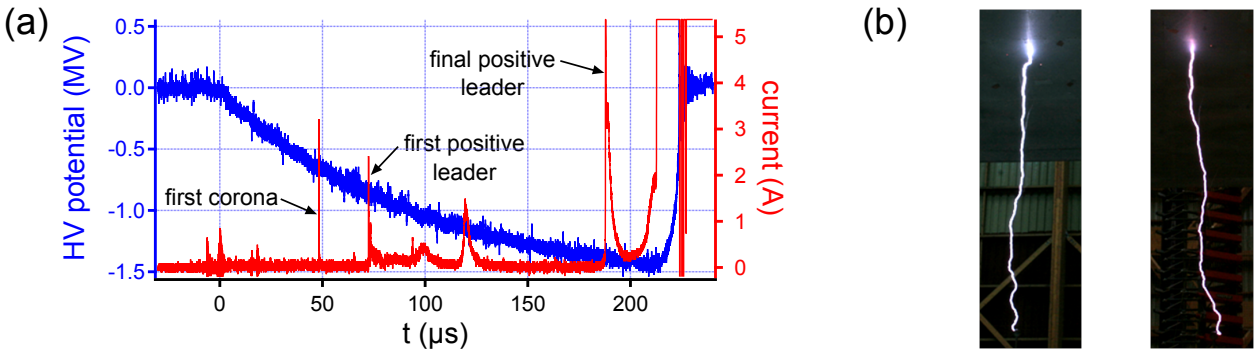

Figure 9.5: (a): voltage and current waveforms recorded during a natural discharge, showing successively the appearance of a corona discharge on the grounded electrode and the inception of a first upward positive leader followed by a second positive leader shortly before breakdown occurrence. (b): time-integrated pictures of the discharge taken from two different points of view.

The current waveform is characterized by a number of peaks with a ~ 1 A amplitude. The first one occurs shortly before 50 µs and is extremely brief, only lasting ~ 100 ns. This peak corresponds to the initiation of a corona discharge on the ground electrode when the electric field reaches the value of 30 kV $\cdot$ cm^{-1} necessary to trigger ionization (see figure 9.6). As this corona seeds the discharge gap with a net positive charge, it results in the shielding of the electric field, which quickly turns off any ionization process. During the following "dark period", which in this case lasts 20 µs, positive ions progressively drift towards the cathode where they recombine, which enables the electric field to recover while the energy deposited near the anode by the first corona discharge heats up the surrounding gas, increasing the effective electric field E/n_n [8]. At one point, a new

corona forms and quickly turns into an ascending positive leader that starts to propagate towards the cathode. The presence of a leader can be assessed by the recorded continuous background of ~ 200 mA on the anode current waveform.

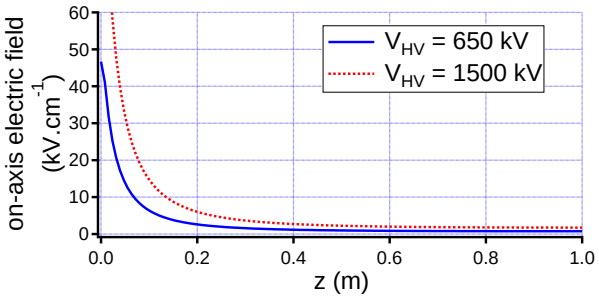

Figure 9.6: Calculated electric field along the symmetry axis of the ground electrode when the potential on the HV electrode is equal to 650 kV (blue solid curve) and to 1500 kV (red dashed curve). Position $z = 0$ corresponds to the spherical grounded electrode.

For the discharge presented in figure 9.5-(a), this first leader seems to have developed too early during the voltage rise because it eventually dies out before reaching the cathode. A new latency period takes place until a new positive corona forms after 60 µs, this time draining a much more important current. It generates a second leader channel, which seems to propagate much faster than the first one, perhaps because the latter left a preferential path of high E/n_n in the gap. After only 20 µs, the current starts to rise again significantly shortly before breakdown occurs, which can be explained by the positive leader entering into the high field zone near the cathode, leading to the leader final jump. Therefore it seems the discharge was triggered from the anode, even though no apparent directive branching is visible on time-integrated pictures (figure 9.5-(b)) to confirm it. This results from the anode having a much smaller radius of curvature than the HV electrode.

9.2.3 Configuration 1

9.2.3.1 Characterization of filamentation

The multifilament bundle used in the experiment is formed using a 250 mJ, 900 fs laser pulse focused at $f/330$ by a 10 m lens. Characterization of this bundle is done using single-shot impacts on photographic paper, as it has already been done in Chapter 4. Such impacts are displayed in figure 9.7.

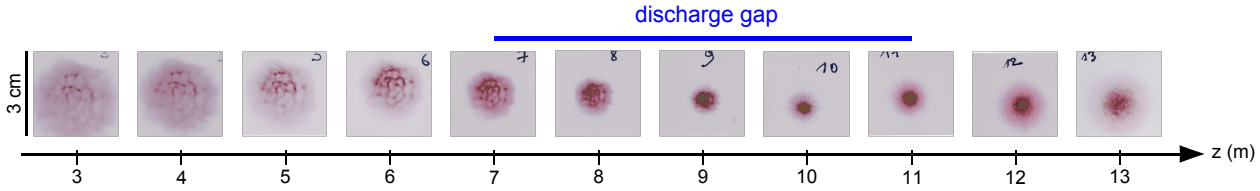

Figure 9.7: Impacts on photographic paper from a 250 mJ, 900 fs laser pulse focused at $f/330$. The discharge gap is placed between 7 and 11 m along the filament bundle.

Filaments appear after only 2 m of propagation and multiply as the beam focuses, eventually

leaving a homogeneous burn pattern between 9 and 11 m. As we saw in Chapters 3 and 4 that energy deposition quickly decreases past the linear focus, we decided to place the discharge gap between 7 and 11 m after the focusing lens, in the region where laser energy deposition is maximum.

9.2.3.2 Effect of filamentation

In this experimental configuration two main effects resulting from filamentation were witnessed. The first one corresponds to the data displayed in figure 9.8-(a). Here the laser was sent at a time when an upward positive leader was already propagating towards the cathode. However it seems that filamentation did not have much influence on this leader.

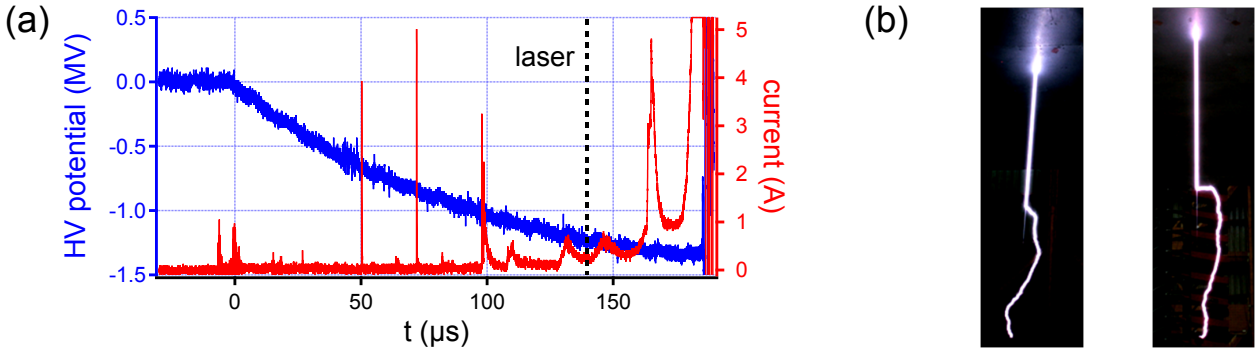

Figure 9.8: (a): voltage and current waveforms recorded during a guided discharge. The laser was sent 139 µs after the Marx triggering. (b): time-integrated pictures of the discharge taken from two different points of view.

On the other hand, as seen on the time-integrated pictures (figure 9.8-(b)), we can clearly see that the laser promoted the guiding of the spark upper half. A faint downward branching at the end of the guided portion even shows that this straight plasma comes from an anode-directed, negative leader that was undoubtedly both triggered and guided by filaments. This is the proof that filamentation is able to generate downward leaders if it can reach the area of strong electric field in altitude.

Another interesting phenomenon arising from filamentation is described in figure 9.9. Indeed in this case the laser apparently triggered an upward positive leader, according to the current waveform (figure 9.9-(a)). This leader was, however, preceded by two corona discharges that failed to fully develop. This could explain why a significant portion of the discharge path near the anode is not guided (figure 9.9-(b)). The positive leader would already have a prepared natural path competing with the one generated by the laser. It is also worth mentioning that filamentation could well have triggered a negative leader as well, as in the previous case.

To conclude on this configuration, we saw that filamentation was able to induce the formation of both a negative descending leader and of a positive ascending leader. However it appears difficult to observe the guiding from the anode surface, as corona discharges tend to form early in time and generate their own preferential path for leaders that compete with that of the laser.

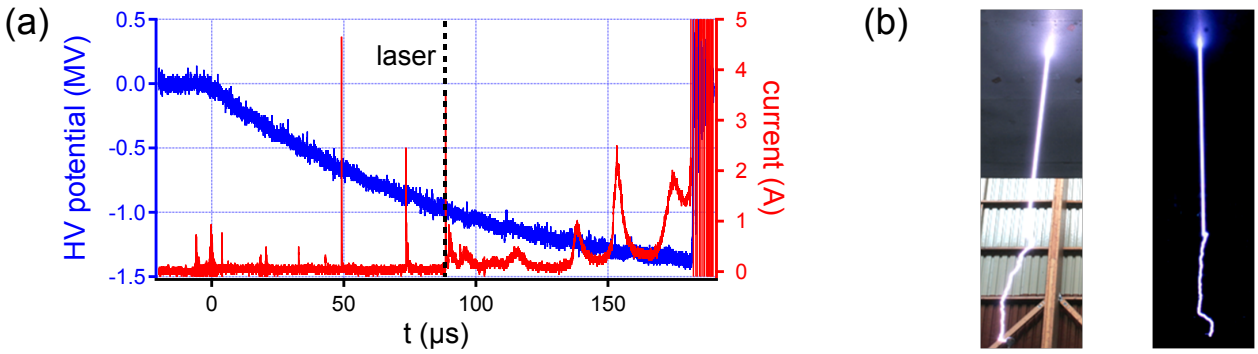

Figure 9.9: (a): voltage and current waveforms recorded during a guided discharge. The laser was sent 88 µs after the Marx triggering. (b): time-integrated pictures of the discharge taken from two different points of view.

9.2.4 Configuration 2

9.2.4.1 Characterization of filamentation

In the second configuration tested, the length of filaments had to be somehow limited so that they covered only part of the gap. This was done using a shorter focusing lens, thereby resulting in a shorter multifilament bundle. We consequently used a $f/165$ focusing (5 m lens) and an equivalent laser pulse (250 mJ, 900 fs).

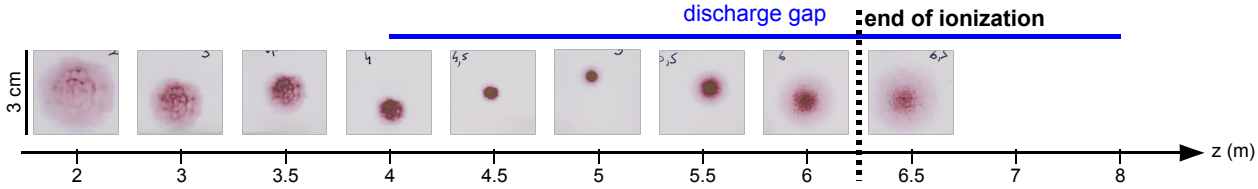

Figure 9.10: Impacts on photographic paper from a 250 mJ, 900 fs laser pulse focused at $f/165$. The discharge gap is placed between 4 and 8 m along the filament bundle, while ionization stops around 6.5 m.

As seen in figure 9.10, ionization starts around 2 m and occurs over ~ 4.5 m. Strong ionization, characterized by a central spot uniformly burned, stops earlier around 5.5 m. We took this point as the reference for the end of filamentation, knowing from Chapter 4 that even though filaments still exist beyond this point, no significant energy deposition actually takes place in this region. Since the ground electrode was placed at 4 m, it means that there is a gap portion of length ≈ 2.5 m not covered by filaments (cf. figure 9.4-(b)).

9.2.4.2 Effect of filamentation

Using this configuration, filamentation should no longer be able to trigger downward negative leaders since it stops well before reaching the HV electrode. By sending the laser early enough, that is before the inception of a natural positive corona, we were able to trigger immediately this first corona, that quickly developed into a leader, as seen in the current waveform of figure 9.11-(a).

Although the first leader died out after a few microseconds, followed by another unsuccessful

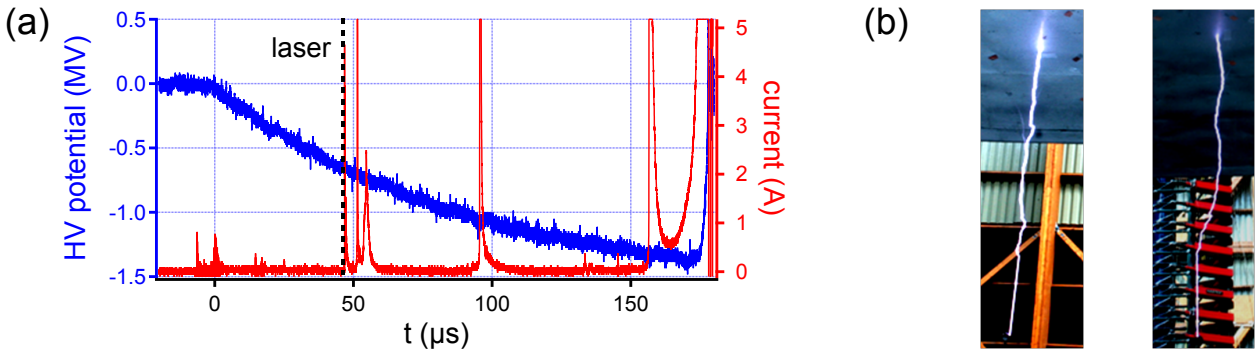

Figure 9.11: (a): voltage and current waveforms recorded during a guided discharge. The laser was sent 36 µs after the Marx triggering. (b): time-integrated pictures of the discharge taken from two different points of view.

one, time-integrated pictures clearly show that all the bottom part of the discharge is well guided down to the anode and up to the point filamentation stops. Moreover one can see upward branching of the spark near the HV electrode, meaning that it undoubtedly resulted from a purely positive leader. This point is very important because it corresponds precisely to the most credible scenario for a working laser lightning rod: the inception of an upward leader in the rising electric field brought by a descending negative leader.

9.2.5 Statistical analysis

We performed a simple statistical analysis over the whole recorded data in the case of natural discharges and for discharges that occurred in presence of filaments. We thus estimated the voltage on the HV electrode at specific instants, namely when the first corona started, when the first positive upward leader was generated, and when breakdown occurred. This data is given in table 9.1.

HV potential (kV)/configuration	natural discharges	discharges with laser
first corona	650 ± 17	649 ± 19
first positive leader	1308 ± 204	1191 ± 245
breakdown	1423 ± 60	1370 ± 80

Table 9.1: Average value ± one standard deviation of the HV potential at the occurrence time of different significant events in the case of natural discharges (9 shots) and for discharges with laser (29 shots).

As seen here, the occurrence of the first corona discharge is insensitive to the presence of filaments in the gap. This first point comes from the low number of shots where the laser was sent at early times, that is before the natural inception of the corona, although figure 9.11-(a) clearly shows that filamentation is able to promote the development of such coronas. A more detailed study is given in figure 9.12, which shows the evolution of the first corona voltage with the laser/Marx delay. This graph clearly shows that if the laser is sent before the HV potential reaches the value for natural corona generation, it can trigger this corona at a lower voltage. This effect has already been witnessed by Comtois *et al.* in the case of 5 m long discharges using a steeper voltage pulse

with 2 MV amplitude [19].

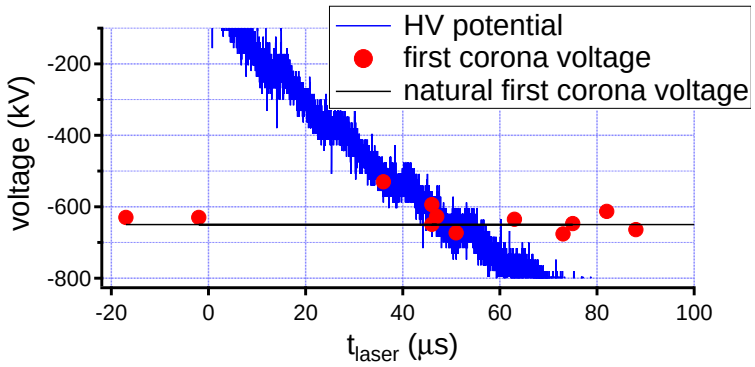

Figure 9.12: Evolution of the first corona voltage appearance with the laser/Marx delay. HV potential waveform and natural corona voltage appearance are given as a convenience. A slight laser effect can be witnessed shortly before 40 µs but the lack of statistics in this region prevents us to definitely conclude.

The effect of the laser is more important on the voltage threshold for the generation of the first upward positive leader. As seen in table 9.1, the needed voltage for positive leader inception is significantly lowered when using the laser, which proves that filaments have a beneficial effect on upward leader formation. This finding is very important for the development of a working laser lightning rod.

Finally, concerning breakdown voltage, it appears that filamentation has only a marginal effect. It should be noticed however that this effect was not the one which was looked for. This experimental campaign focused on filamentation effects on the generation of leaders in real conditions, that is with a very slow voltage pulse known to mimic the approach of a negative leader towards the ground. Significantly better results were recorded using a much faster voltage pulse or a positive polarity [20].

Conclusion

To conclude on this Chapter dedicated to the development of a laser lightning rod using filamentation, we saw in the first part that the most credible scenario for such a technology would be to induce a positive upward propagating leader from the ground in order to intercept a downward negative leader. Indeed we estimated that filamentation in itself could not have any influence on the electric field in the cloud/ground gap to result in dramatic effects such as those witnessed using rockets trailing metallic wires. In theory filamentation could also induce a downward negative leader near the bottom of storm clouds but this would ask for an important laser energy being deposited at altitudes up to 3 km, which barely foreseeable in the next few years.

Concentrating on the upward leader scenario, we organized an experimental campaign at the high-voltage facilities of the DGA/TA at Balma. During this campaign we simulated the approach of a negative leader towards the ground by applying a slow -1.5 MV voltage pulse on a large plate electrode. A spherical grounded electrode was placed 4 m below the HV electrode, and was skimmed by the laser-generated filament bundle. Two different configurations were used: in the first one filaments covered the whole discharge gap while in the second one they stopped at about one third of the gap. In the first configuration we were able to systematically trigger descending leaders, sometimes coupled to an ascending leader, resulting in guided discharges of impressive length (up to 3.6 m). In the second configuration, only positive ascending leaders were generated by filamentation, but in a very reliable way and with a much lower voltage than naturally needed. We were also able to trigger the first positive corona at a lower voltage than without filaments by carefully adjusting the laser time with respect to the voltage.

These results, however partial, give good hope that a working laser lightning rod could be developed in the next few years. Given the pace of current laser development, particularly concerning the steep rise of the available average power with new kilohertz laser at the ~ 100 mJ level, this objective is almost at hand.

Bibliography

[1] E. M. Bazelyan, Y. P. Raizer, and N. L. Aleksandrov, Plasma Sources Science and Technology **17**, 024015 (2008).

[2] V. A. Rakov and M. A. Uman, *Lightning: Physics and Effects* (Cambridge University Press, Cambridge, UK, 2003).

[3] D. W. Koopman and T. D. Wilkerson, Journal of Applied Physics **42**, 1883 (1971).

[4] M. Miki, T. Shindo, and Y. Aihara, Journal of Physics D **29**, 1984 (1996).

[5] A. Braun, G. Korn, X. Liu, D. Du, J. Squier, and G. Mourou, Optics Letters **20**, 73 (1995).

[6] X. M. Zhao, J.-C. Diels, C. Y. Wang, and J. M. Elizondo, IEEE Journal of Quantum Electronics **31**, 599 (1995).

[7] D. Comtois, C. Y. Chien, A. Desparois, F. Génin, G. Jarry, T. W. Johnston, J.-C. Kieffer, B. La Fontaine, F. Martin, R. Mawassi, H. Pépin, F. A. M. Rizk, F. Vidal, P. Couture, H. P. Mercure, C. Potvin, A. Bondiou-Clergerie, and I. Gallimberti, Applied Physics Letters **76**, 819 (2000).

[8] H. Pépin, D. Comtois, F. Vidal, C. Y. Chien, A. Desparois, T. W. Johnston, J. C. Kieffer, B. La Fontaine, F. Martin, F. A. M. Rizk, C. Potvin, P. Couture, H. P. Mercure, A. Bondiou-Clergerie, P. Lalande, and I. Gallimberti, Physics of Plasmas **8**, 2532 (2001).

[9] M. Rodriguez, R. Sauerbrey, H. Wille, L. Wöste, T. Fujii, Y.-B. André, A. Mysyrowicz, L. Klingbeil, K. Rethmeier, W. Kalkner, J. Kasparian, E. Salmon, J. Yu, and J.-P. Wolf, Optics Letters **27**, 772 (2002).

[10] R. Ackermann, K. Stelmaszczyk, P. Rohwetter, G. Méjean, E. Salmon, J. Yu, J. Kasparian, G. Méchain, V. Bergmann, S. Schaper, B. Weise, T. Kumm, K. Rethmeier, W. Kalkner, L. Wöste, and J.-P. Wolf, Applied Physics Letters **85**, 5781 (2004).

[11] J. Kasparian, R. Ackermann, Y.-B. André, G. Méchain, G. Méjean, B. Prade, P. Rohwetter, E. Salmon, K. Stelmaszczyk, J. Yu, A. Mysyrowicz, R. Sauerbrey, L. Wöste, and J.-P. Wolf, Optics Express **16**, 5757 (2008).

[12] E. M. Bazelyan and Y. P. Raizer, *Lightning Physics and Lightning Protection* (IOP Publishing, Bristol, UK, 2000).

[13] R. J. Fisher, G. H. Schnetzer, R. Thottappillil, V. A. Rakov, M. A. Uman, and J. D. Goldberg, Journal of Geophysical Research: Atmospheres **98**, 22887 (1993).

[14] V. A. Rakov, R. Thottappillil, M. A. Uman, and P. P. Barker, Journal of Geophysical Research: Atmospheres **100**, 25701 (1995).

[15] M. Durand, A. Houard, B. Prade, A. Mysyrowicz, A. Durécu, B. Moreau, D. Fleury, O. Vasseur, H. Borchert, K. Diener, R. Schmitt, F. Théberge, M. Chateauneuf, J.-F. Daigle, and J. Dubois, Optics Express **21**, 26836 (2013).

[16] G. Méchain, G. Méjean, R. Ackermann, P. Rohwetter, Y.-B. André, J. Kasparian, B. Prade, K. Stelmaszczyk, J. Yu, E. Salmon, W. Winn, L. A. (Vern) Schlie, A. Mysyrowicz, R. Sauerbrey, L. Wöste, and J.-P. Wolf, Applied Physics B **80**, 785 (2005).

[17] G. Méchain, C. D'Amico, Y.-B. André, S. Tzortzakis, M. Franco, B. Prade, A. Mysyrowicz, A. Couairon, E. Salmon, and R. Sauerbrey, Optics Communications **247**, 171 (2005).

[18] Y.-H. Cheng, J. K. Wahlstrand, N. Jhajj, and H. M. Milchberg, Optics Express **21**, 4740 (2013).

[19] D. Comtois, H. Pepin, F. Vidal, F. A. M. Rizk, C.-Y. Chien, T. W. Johnston, J. Kieffer, B. La Fontaine, F. Martin, C. Potvin, P. Couture, H. P. Mercure, A. Bondiou-Clergerie, P. Lalande, and I. Gallimberti, IEEE Transactions on Plasma Science **31**, 377 (2003).

[20] B. Forestier, A. Houard, I. Revel, M. Durand, Y.-B. André, B. Prade, A. Jarnac, J. Carbonnel, M. Le Nevé, J. C. de Miscault, B. Esmiller, D. Chapuis, and A. Mysyrowicz, AIP Advances **2**, 012151 (2012).

General conclusion

This Thesis was dedicated to the study of energy deposition from filamentation in air and its application to the triggering and guiding of spark discharges.

I investigated the influence of experimental parameters on deposited energy densities both in the case of a single filament, witnessing the transition from a low-energy regime characterized by the generation of sound waves to a high-energy regime resulting in shock waves. Peak temperatures are also one order of magnitude higher at ~ 1000 K, while the resulting low-density channels are deeper and last much longer. In the case of multifilaments, I characterized a new filamentation regime reached when a large number of filaments are brought together using strong enough focusing, yielding a large plasma volume and a few filamentary structures with high plasma density in the focal zone. A significant energy deposition is observed in this region, which results in the rapid coalescence of initially discrete underdense air channels into a larger one. The peak temperature is not much higher than for a single filament but the heated volume is much more important. Applications for such filamentation-induced hydrodynamics concern the remote generation of virtual air optical structures, which use the spatial modulation of the air density to create waveguides or axicons. Another interesting application would be to use the filament-heated air column at the front of a supersonic aircraft to break the induced shock wave and thereby significantly increase fuel efficiency. Finally, as filamentation can generate deep underdense air channels, it means that it is able to locally decrease the dielectric strength of air. This point serves as the basis for filamentation-triggered discharges, the study of which makes the last part of the Thesis.

In order to investigate filamentation-triggered sparks, I built a plasma diagnostic to have a space and time-resolved measurement of electron density in discharge plasmas. This diagnostic also enabled me to record neutral density profiles as well, which proved very useful to record the evolution of discharge-induced hydrodynamics. Thus equipped, I worked for the development of the three main applications to filamentation-guided sparks. First, I investigated the plasmas generated in a compact laser-triggered gap switch. This switch was then used to build a new kind of Marx generator, entirely triggered by filamentation. This design is very simple, robust and yields a very steep voltage front. It is also modular, giving the possibility to use an arbitrary number of stages and, therefore, output voltage. Second, I participated to the development of a virtual radio-frequency plasma antenna based on filamentation-guided sparks from a Tesla coil. A broadband emission in the 500 - 1200 MHz range was achieved but only lasted for a few microseconds, that is the plasma lifetime. In order to increase this lifetime, a technique based on a low amplitude AC current flowed through the plasma was designed and studied using the filamentation-triggered Marx generator. A maximum duration of ~ 1 ms was reached without any significant distortion of the plasma channel. The next step would be to implement this technique on the Tesla coil to

achieve both long lifetimes and long plasma columns. Finally I also participated to a prospective study aimed at the development of a laser lightning rod. Using the current laser technology, the most realistic scenario would be to initiate a positive upward leader channel from earth in order to intercept a downward negative leader descending from a storm cloud. During the experimental campaign carried at the DGA/TA high voltage facilities in Balma, France, it was shown that filamentation was well able to reach this goal, which opens favorable perspectives to the short term development of this technology.

Annexes

Annex A: calculation of the dispersion equation for the plasma surface wave

To derive the dispersion equation for the plasma-coupled electromagnetic modes, we will consider the spark plasma as a long homogeneous cylinder of constant electron density n_e and of radius a generated in air. We start back from the propagation equation for the electric field in the Fourier space (equation (1.12)):

$$\Delta\vec{E}(\vec{r},\omega) + \frac{\omega^2}{c^2}\epsilon_r(\vec{r},\omega)\vec{E}(\vec{r},\omega) = \vec{0}, \tag{A.1}$$

where ϵ_r is the relative dielectric permittivity of the considered propagation medium. Along z and using cylindrical coordinates, it can be rewritten as:

$$\frac{1}{r}\frac{\partial}{\partial r}\left(r\frac{\partial E_z}{\partial r}(\vec{r},\omega)\right) + \frac{1}{r^2}\frac{\partial^2 E_z}{\partial\theta^2}(\vec{r},\omega) + \frac{\partial^2 E_z}{\partial z^2}(\vec{r},\omega) + \frac{\omega^2}{c^2}\epsilon_r(\vec{r},\omega)E_z(\vec{r},\omega) = 0. \tag{A.2}$$

It is worth mentioning the axial component of the magnetic field B_z is also solution of this last equation.

We are looking for an electromagnetic field that shares the cylindrical symmetry of the plasma, that is periodic functions of θ, but that also propagates along z. Decomposing the solution field in Fourier series we have:

$$\begin{cases} E_z(r,\theta,z) = \sum\limits_{n\in\mathbb{Z}} a_n E_z^n(r)\mathrm{e}^{i(n\theta+\beta z)} \\ B_z(r,\theta,z) = \sum\limits_{n\in\mathbb{Z}} b_n B_z^n(r)\mathrm{e}^{i(n\theta+\beta z)}, \end{cases} \tag{A.3}$$

where $\beta \in \mathbb{C}$ is the wavevector for the solution field and $(a_n,b_n) \in \mathbb{R}^2$. Injecting this expression in equation (A.2), we find that:

$$\forall n \in \mathbb{Z}, \frac{\mathrm{d}^2 E_z^n}{\mathrm{d}r^2}(r) + \frac{1}{r}\frac{\mathrm{d}E_z^n}{\mathrm{d}r}(r) - \left(\frac{n^2}{r^2} + \beta^2 - \frac{\omega^2}{c^2}\epsilon_r(r)\right)E_z^n(r) = 0. \tag{A.4}$$

We define:

$$\rho^2 = r^2\left(\beta^2 - \frac{\omega^2}{c^2}\epsilon_r(r)\right) = r^2\kappa^2, \tag{A.5}$$

enabling us to rewrite equation A.4 as:

$$\forall n \in \mathbb{Z}, \rho^2\frac{\mathrm{d}^2 E_z^n}{\mathrm{d}\rho^2}(\rho) + \rho\frac{\mathrm{d}E_z^n}{\mathrm{d}\rho}(\rho) - (n^2+\rho^2)E_z^n(\rho) = 0. \tag{A.6}$$

This equation is a modified Bessel equation, solution of which is given by:

$$\forall n \in \mathbb{Z}, E_z^n(\rho) = A_n I_n(\rho) + B_n K_n(\rho), \tag{A.7}$$

where I_n and K_n are modified Bessel functions of degree n of the first kind and of the second kind, respectively. Knowing that:

$$\begin{cases} \lim\limits_{x\to+\infty} I_n(x) = +\infty \\ \lim\limits_{x\to 0} K_n(x) = +\infty \end{cases} \tag{A.8}$$

we can express E_z^n in the plasma and in air, respectively:

$$\begin{cases} E_z^n(r) = A_n I_n(\kappa_p r), r \in [0,a] \\ E_z^n(r) = B_n K_n(\kappa_a r), r \in]a, +\infty[, \end{cases} \tag{A.9}$$

where indexes p and a denote plasma and air parameters. The magnetic field can be expressed in the same way:

$$\begin{cases} B_z^n(r) = C_n I_n(\kappa_p r), r \in [0,a] \\ B_z^n(r) = D_n K_n(\kappa_a r), r \in]a, +\infty[. \end{cases} \tag{A.10}$$

Solving the problem as a whole requires finding all the components of the electromagnetic field and of their spatial derivatives and expressing them as functions of E_z^n and B_z^n. To this purpose, we can expand the Maxwell-Faraday equation projected on each axis in the cylindrical coordinate system:

$$\begin{cases} \frac{1}{r}\frac{\partial E_z}{\partial\theta}(\vec{r},\omega) - \frac{\partial E_\theta}{\partial z}(\vec{r},\omega) = -i\omega B_r(\vec{r},\omega) \\ \frac{\partial E_r}{\partial z}(\vec{r},\omega) - \frac{\partial E_z}{\partial r}(\vec{r},\omega) = -i\omega B_\theta(\vec{r},\omega) \\ \frac{1}{r}\left(\frac{\partial}{\partial r}(rE_\theta(\vec{r},\omega)) - \frac{\partial E_r}{\partial\theta}(\vec{r},\omega)\right) = -i\omega B_z(\vec{r},\omega). \end{cases} \tag{A.11}$$

We can do the same thing using the Maxwell-Ampere equation:

$$\begin{cases} \frac{1}{r}\frac{\partial B_z}{\partial\theta}(\vec{r},\omega) - \frac{\partial B_\theta}{\partial z}(\vec{r},\omega) = i\frac{\omega}{c^2}\epsilon_r(\vec{r},\omega)E_r(\vec{r},\omega) \\ \frac{\partial B_r}{\partial z}(\vec{r},\omega) - \frac{\partial B_z}{\partial r}(\vec{r},\omega) = i\frac{\omega}{c^2}\epsilon_r(\vec{r},\omega)E_\theta(\vec{r},\omega) \\ \frac{1}{r}\left(\frac{\partial}{\partial r}(rB_\theta(\vec{r},\omega)) - \frac{\partial B_r}{\partial\theta}(\vec{r},\omega)\right) = i\frac{\omega}{c^2}\epsilon_r(\vec{r},\omega)E_z(\vec{r},\omega). \end{cases} \tag{A.12}$$

Combining equation systems (A.11) and (A.12) we find:

$$\begin{cases} \frac{1}{r}\frac{\partial E_z}{\partial\theta}(\vec{r},\omega) + i\frac{c^2}{\omega\epsilon_r(\vec{r},\omega)}\frac{\partial}{\partial z}\left(\frac{\partial B_r}{\partial z}(\vec{r},\omega) - \frac{\partial B_z}{\partial r}(\vec{r},\omega)\right) = -i\omega B_r(\vec{r},\omega) \\ -i\frac{c^2}{\omega\epsilon_r(\vec{r},\omega)}\frac{\partial}{\partial z}\left(\frac{1}{r}\frac{\partial B_z}{\partial\theta}(\vec{r},\omega) - \frac{\partial B_\theta}{\partial z}(\vec{r},\omega)\right) - \frac{\partial E_z}{\partial r}(\vec{r},\omega) = -i\omega B_\theta(\vec{r},\omega) \\ \frac{1}{r}\frac{\partial B_z}{\partial\theta}(\vec{r},\omega) - i\frac{1}{\omega}\frac{\partial}{\partial z}\left(\frac{\partial E_r}{\partial z}(\vec{r},\omega) - \frac{\partial E_z}{\partial r}(\vec{r},\omega)\right) = i\frac{\omega}{c^2}\epsilon_r(\vec{r},\omega)E_r(\vec{r},\omega) \\ i\frac{1}{\omega}\frac{\partial}{\partial z}\left(\frac{1}{r}\frac{\partial E_z}{\partial\theta}(\vec{r},\omega) - \frac{\partial E_\theta}{\partial z}(\vec{r},\omega)\right) - \frac{\partial B_z}{\partial r}(\vec{r},\omega) = i\frac{\omega}{c^2}\epsilon_r(\vec{r},\omega)E_\theta(\vec{r},\omega) \end{cases} \tag{A.13}$$

We can now use the expressions for the E-field and the B-field from equations (A.9) and (A.10) in this system. For the total electromagnetic field in the plasma ($r \in [0,a]$) we find:

$$\begin{cases} E_r(\vec{r},\omega) = \sum\limits_{n\in\mathbb{Z}}\left(b_n^p C_n \frac{n\omega}{\rho_p^2 r} I_n(\rho_p) + ia_n^p A_n \frac{\beta r}{\rho_p} I_n'(\rho_p)\right) \mathrm{e}^{i(n\theta+\beta z)} \\ E_\theta(\vec{r},\omega) = -\sum\limits_{n\in\mathbb{Z}}\left(ib_n^p C_n \frac{\omega r}{\rho_p} I_n'(\rho_p) - a_n^p A_n \frac{n\beta r}{\rho_p^2} I_n(\rho_p)\right) \mathrm{e}^{i(n\theta+\beta z)} \\ E_z(\vec{r},\omega) = \sum\limits_{n\in\mathbb{Z}} a_n^p A_n I_n(\rho_p)\mathrm{e}^{i(n\theta+\beta z)} \end{cases} \tag{A.14}$$

for the electric field and:

$$\begin{cases} B_r(\vec{r},\omega) = \sum_{n\in\mathbb{Z}} \left(ib_n^p C_n \frac{\beta r}{\rho_p} I'_n(\rho_p) - a_n^p A_n \frac{nr\omega\epsilon_p(\vec{r},\omega)}{c^2\rho_p^2} I_n(\rho_p) \right) \mathrm{e}^{i(n\theta+\beta z)} \\ B_\theta(\vec{r},\omega) = \sum_{n\in\mathbb{Z}} \left(b_n^p C_n \frac{n\beta r}{\rho_p^2} I_n(\rho_p) + ia_n^p A_n \frac{r\omega\epsilon_p(\vec{r},\omega)}{c^2\rho_p} I'_n(\rho_p) \right) \mathrm{e}^{i(n\theta+\beta z)} \\ B_z(\vec{r},\omega) = \sum_{n\in\mathbb{Z}} b_n^p C_n I_n(\rho_p) \mathrm{e}^{i(n\theta+\beta z)} \end{cases} \tag{A.15}$$

for the magnetic field. In air ($r \in]a, +\infty[$), the electric field is given by:

$$\begin{cases} E_r(\vec{r},\omega) = \sum_{n\in\mathbb{Z}} \left(b_n^a D_n \frac{n\omega r}{\rho_a^2} K_n(\rho_a) + ia_n^a B_n \frac{\beta r}{\rho_a} K'_n(\rho_a) \right) \mathrm{e}^{i(n\theta+\beta z)} \\ E_\theta(\vec{r},\omega) = -\sum_{n\in\mathbb{Z}} \left(ib_a^p D_n \frac{\omega r}{\rho_a} K'_n(\rho_a) - a_n^a B_n \frac{n\beta r}{\rho_a^2} K_n(\rho_a) \right) \mathrm{e}^{i(n\theta+\beta z)} \\ E_z(\vec{r},\omega) = \sum_{n\in\mathbb{Z}} a_n^a B_n K_n(\rho_a) \mathrm{e}^{i(n\theta+\beta z)} \end{cases} \tag{A.16}$$

and the magnetic field by:

$$\begin{cases} B_r(\vec{r},\omega) = \sum_{n\in\mathbb{Z}} \left(ib_n^a D_n \frac{\beta r}{\rho_a} K'_n(\rho_a) - a_n^a B_n \frac{nr\omega\epsilon_a(\vec{r},\omega)}{c^2\rho_a^2} K_n(\rho_a) \right) \mathrm{e}^{i(n\theta+\beta z)} \\ B_\theta(\vec{r},\omega) = \sum_{n\in\mathbb{Z}} \left(b_n^a D_n \frac{n\beta r}{\rho_a^2} K_n(\rho_a) + ia_n^a B_n \frac{r\omega\epsilon_p(\vec{r},\omega)}{c^2\rho_a} K'_n(\rho_a) \right) \mathrm{e}^{i(n\theta+\beta z)} \\ B_z(\vec{r},\omega) = \sum_{n\in\mathbb{Z}} b_n^a D_n K_n(\rho_a) \mathrm{e}^{i(n\theta+\beta z)}. \end{cases} \tag{A.17}$$

The absence of surface current on the plasma shell at $r = a$ imposes the continuity of the tangential components of the electromagnetic field as boundary conditions so that we can relate air and plasma field components at this radius value:

$$\begin{cases} ib_n^p C_n \frac{\omega a}{\kappa_p} I'_n(\kappa_p a) - a_n^p A_n \frac{n\beta}{\kappa_p^2 a} I_n(\kappa_p a) = iB_n^a D_n \frac{\omega}{\kappa_a} K'_n(\kappa_a a) - a_n^a B_n \frac{n\beta}{\kappa_a^2 a} K_n(\kappa_a a) \\ a_n^p I_n(\kappa_p a) = a_n^a B_n K_n(\kappa_a a) \\ b_n^p C_n \frac{n\beta}{\kappa_p^2 a} I_n(\kappa_p a) + ia_n^p A_n \frac{\omega\epsilon_p(\vec{r},\omega)}{c^2\kappa_p} I'_n(\kappa_p a) = b_n^a D_n \frac{n\beta}{\kappa_a^2 a} K_n(\kappa_a a) + ia_n^a B_n \frac{\omega\epsilon_a(\vec{r},\omega)}{c^2\kappa_a} K'_n(\kappa_a a) \\ B_n^p C_n I_n(\kappa_p a) = B_n^a D_n K_n(\kappa_a a). \end{cases} \tag{A.18}$$

This last equation system can be rewritten in a matrix form:

$$M_n \times \begin{pmatrix} a_n^p A_n \\ a_n^a B_n \\ b_n^p C_n \\ b_n^a D_n \end{pmatrix} = 0, \tag{A.19}$$

with the matrix M_n being defined as:

$$M_n = \begin{pmatrix} -\frac{n\beta}{\kappa_p^2 a} I_n(\kappa_p a) & \frac{n\beta}{\kappa_a^2 a} K_n(\kappa_a a) & i\frac{\omega}{\kappa_p} I_n(\kappa_p a) & -i\frac{\omega}{\kappa_a} K_n(\kappa_a a) \\ I_n(\kappa_p a) & -K_n(\kappa_a a) & 0 & 0 \\ i\frac{\omega\epsilon_p(\vec{r},\omega)}{c^2\kappa_p} I'_n(\kappa_p a) & -i\frac{\omega\epsilon_a(\vec{r},\omega)}{c^2\kappa_a} K'_n(\kappa_a a) & \frac{n\beta}{\kappa_p^2 a} I_n(\kappa_p a) & -\frac{n\beta}{\kappa_a^2 a} K_n(\kappa_a a) \\ 0 & 0 & I_n(\kappa_p a) & -K_n(\kappa_a a). \end{pmatrix} \tag{A.20}$$

This equation has non-zero solutions only if $\det(M_n) = 0$, a condition which finally gives the dispersion equation for the mode n coupled to the plasma:

$$\left(\frac{a}{\kappa_p}\frac{I_n'(\kappa_p a)}{I_n(\kappa_p a)} - \frac{a}{\kappa_a}\frac{K_n'(\kappa_a a)}{K_n(\kappa_a a)}\right)\left(\frac{a}{\kappa_p}\frac{\omega\epsilon_p(\vec{r},\omega)}{c^2}\frac{I_n'(\kappa_p a)}{I_n(\kappa_p a)} - \frac{a}{\kappa_a}\frac{\omega\epsilon_a(\vec{r},\omega)}{c^2}\frac{K_n'(\kappa_a a)}{K_n(\kappa_a a)}\right) = n^2\beta^2\left(\frac{1}{\kappa_p^2} - \frac{1}{\kappa_a^2}\right)^2. \tag{A.21}$$

Annex B: the ENSTAmobile laser chain

All the experiments presented in this Thesis were done using the same Ti:sapphire laser chain: the ENSTAmobile. It consists in a chirped pulse amplification laser chain from Amplitude Technologies entirely integrated in a $\sim 3\ m^3$ wheeled container. Ultrashort laser pulses generated from a femtosource oscillator (Femtolasers GmbH) are amplified in three successive stages: first, a regenerative amplifier coupled to a multipass amplifier, pumped by a 130 mJ frequency-doubled Nd:YAG laser (CFR200 from Quantel Laser), followed by a second multipass amplifier pumped by a 2 J frequency-doubled Nd:YAG laser (PRO-PULSE+ from Amplitude Technologies). At the output the laser pulse has an energy of up to 200 mJ for a minimum duration of 50 fs and a 10 Hz repetition rate. Its spatial profile is close to a super-Gaussian with a 35 mm FWHM. A photograph of the laser is given in figure B.I while the full optical drawing is displayed in figure B.II.

Figure B.I: Photograph of the ENSTAmobile installed in the experiment room.

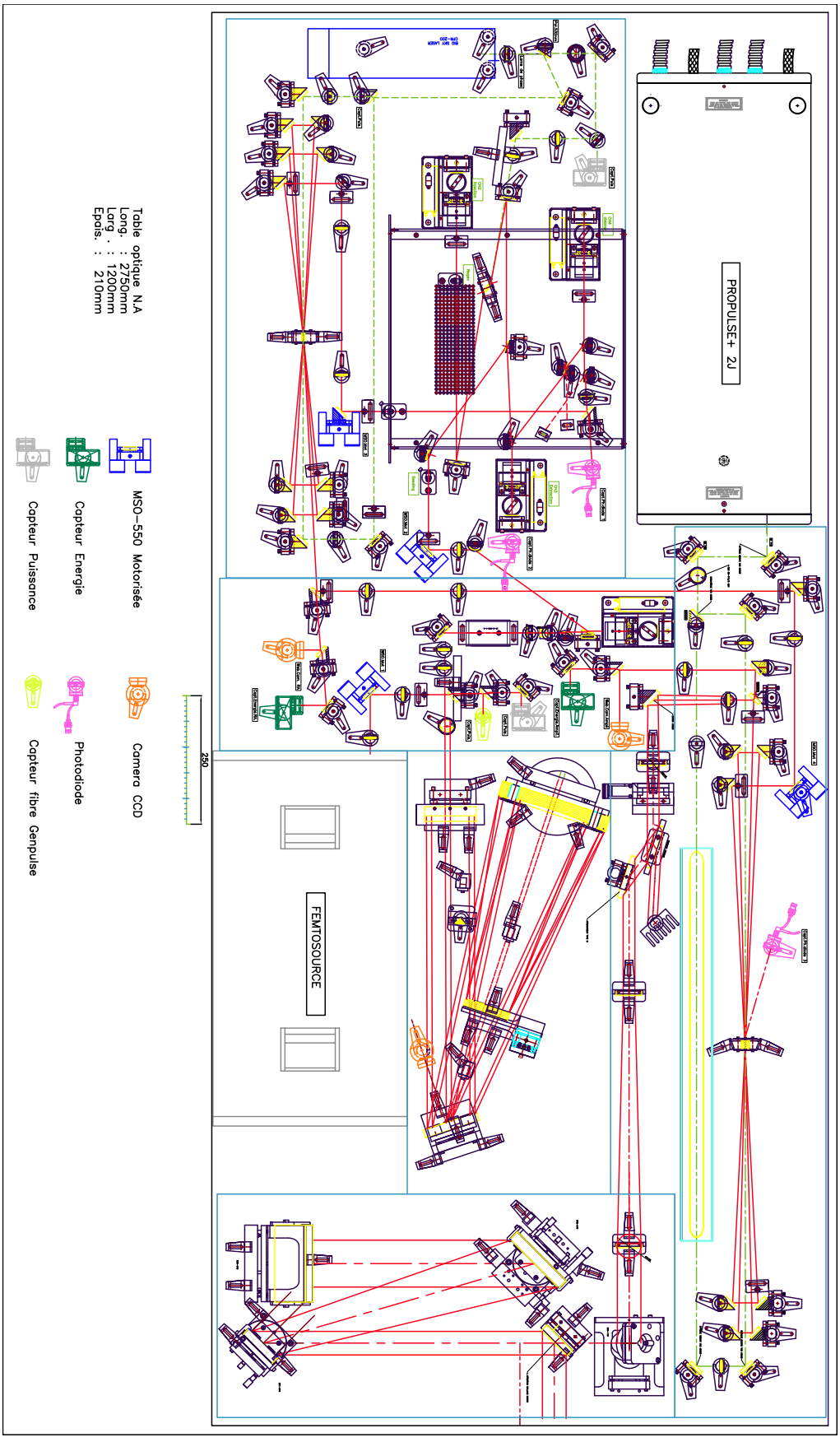

Figure B.II: Full optical drawing of the ENSTAmobile laser chain.

Annex C: list of publications and of attended conferences

Personal publications in peer-reviewed journals

[9] G. Point, C. Milián, A. Couairon, A. Mysyrowicz et A. Houard, "Generation of long-lived underdense channels using femtosecond filamentation in air", Journal of Physics B **48**, 094009 (2015).

[8] A. Murari, M. Gelfusa, E. Peluso, P. Gaudio, D. Mazon, N. Hawkes, G. Point, B. Alper, T. Eich and JET-EFDA contributors, "Improved equilibrium reconstructions by advanced statistical weighting of the internal magnetic measurements", Review of Scientific Instruments **85**, 123507 (2014).

[7] G. Point, Y. Brelet, L. Arantchouk, J. Carbonnel, B. Prade, A. Mysyrowicz et A. Houard, "Two-color interferometer for the study of laser filamentation triggered electric discharges in air", Review of Scientific Instruments **85**, 123101 (2014).

[6] L. Arantchouk, G. Point, Y. Brelet, B. Prade, J. Carbonnel, Y.-B. André, A. Mysyrowicz et A. Houard, "Large scale Tesla coil guided discharges initiated by femtosecond laser filamentation in air", Journal of Applied Physics **116**, 013303 (2014).

[5] G. Point, Y. Brelet, A. Houard, V. Jukna, C. Milián, J. Carbonnel, Y. Liu, A. Couairon et A. Mysyrowicz, "Superfilamentation in air", Physical Review Letters **112**, 223902 (2014).

[4] L. Arantchouk, G. Point, Y. Brelet, J. Larour, J. Carbonnel, Y.-B. André, A. Mysyrowicz et A. Houard, "Compact 180-kV Marx generator triggered in atmospheric air by femtosecond laser filaments", Applied Physics Letters **104**, 103506 (2014).

[3] G. Point, Y. Liu, Y. Brelet, A. Houard et A. Mysyrowicz "Lasing of ambient air with microjoule pulse energy pumped by a multi terawatt IR femtosecond laser", Optics Letters **39**, 1725 (2014).

[2] Y. Liu, Y. Brelet, G. Point, A. Houard et A. Mysyrowicz "Self-seeded lasing in ionized air pumped by 800 nm femtosecond laser pulses", Optics Express **21**, 22791 (2013).

[1] Y. Brelet, A. Houard, G. Point, B. Prade, L. Arantchouk, J. Carbonnel, Y.-B. André, M. Pellet et A. Mysyrowicz, "Radiofrequency plasma antenna generated by femtosecond laser filaments in air", Applied Physics Letters **101**, 264106 (2012).

Attended peer-reviewed international conferences

[10] G. Point, L. Arantchouk, Y. Brelet, J. Carbonnel, Y.-B. André, A. Mysyrowicz et A. Houard, "Space and time-resolved study of plasma columns generated by laser filamentation guided electric discharges", Conference on Lasers and Electro-Optics Europe (CLEO Europe 2015), oral contribution.

[9] G. Point, C. Milián, A. Couairon, A. Mysyrowicz et A. Houard, "Underdense channels generated in air by energetic femtosecond laser pulses", Conference on Lasers and Electro-Optics Europe (CLEO Europe 2015), poster.

[8] G. Point, Y. Brelet, L. Arantchouk, J. Carbonnel, B. Prade, A. Mysyrowicz et A. Houard, "Two-color interferometry for the study of laser filamentation triggered discharges in air", International Conference on Plasma Science (ICOPS 2015), oral contribution.

[7] G. Point, L. Arantchouk, J. Carbonnel, A. Mysyrowicz et A. Houard, "Evolution of a laser filamentation triggered electric discharge in air", International Conference on Plasma Science (ICOPS 2015), oral contribution.

[6] G. Point, Y. Brelet, L. Arantchouk, J. Carbonnel, B. Prade, A. Mysyrowicz et A. Houard, "Interferometric analysis of plasmas induced by filamentation guided electric discharges in air", 5^{th} Symposium on Filamentation (COFIL 2014), poster.

[5] G. Point, Y. Brelet, A. Houard, V. Jukna, C. Milián, J. Carbonnel, Y. Liu, A. Couairon et A. Mysyrowicz, "Study of the interaction between multiple filaments in air", Conference on Lasers and Electro-Optics (CLEO 2014), oral contribution.

[4] A. Houard, G. Point, Y. Brelet, J. Carbonnel, Y.-B. André, B. Prade, L. Arantchouk et A. Mysyrowicz, "Guiding of meter scale AC discharges by laser filamentation in air", Conference on Lasers and Electro-Optics (CLEO 2013), oral contribution.

[3] G. Point, Y. Brelet, A. Houard, J. Carbonnel, L. Arantchouk, B. Prade, Y.-B. André et A. Mysyrowicz, "Plasma column from laser filamentation in air as a virtual radio-frequency antenna", Conference on Lasers and Electro-Optics (CLEO 2013), poster.

[2] L. Arantchouk, A. Houard, G. Point, Y. Brelet, J. Larour, J. Carbonnel, Y.-B. André et A. Mysyrowicz, "Compact Marx generator triggered by femtosecond filaments in air", Pulsed Power and Plasma Science (PPPS 2013), oral contribution.

[1] G. Point, A. Houard, Y. Brelet, L. Arantchouk, J. Carbonnel, B. Prade, Y.-B. André and A. Mysyrowicz, "Laser induced plasma column heated by Tesla coil discharges as a radio-frequency antenna", Pulsed Power and Plasma Science (PPPS 2013), oral contribution.

Attended peer-reviewed national conferences

[1] G. Point, C. Milián, A. Couairon, A. Mysyrowicz et A. Houard, "Canaux sous-denses générés dans l'air par filamentation laser femtoseconde", Congrès Général de la Société Française de Physique 2015 (SFP 2015), oral contribution.

Abstract

Laser filamentation is a spectacular optical propagation regime appearing for pulses of which peak power exceeds a few GW in air. Filament forms due to the optical Kerr effect, which tends to self-focus the beam until intensity reaches the medium ionization threshold by multiphoton absorption. A complex dynamic competition is then established between the Kerr effect on the one hand, and diffraction, nonlinear absorption and plasma defocusing effect on the other hand. This results in a reorganization of the beam profile, characterized by a thin (100 μm) and intense (10^{18} W $\cdot$ m^{-2}) core able to propagate over a distance much longer than the Rayleigh length. When the initial pulse peak power largely exceeds filamentation threshold, several co-propagating filaments are formed in the same beam, with each of these multifilaments sharing physical properties of isolated single filaments. While propagating in air, filaments transfer a portion of the laser energy to the medium, mainly through Raman rotational excitation of air molecules, ionization and inverse Bremsstrahlung in the plasma. This energy is redistributed in one nanosecond and almost entirely converted into air molecule translational energy, that is heat. The medium reacts to this rapid heating by launching a cylindrical pressure wave that brings the system back to pressure equilibrium by ejecting matter from the center. This results in the formation of a hot underdense air channel, which slowly resorbs by diffusion at timescales $>$ 1 ms. My work as a Ph. D. student first focused on the study and the optimization of laser energy deposition in air by filamentation. Thus, I investigated the influence of laser parameters such as pulse energy, focusing strength or pulse duration on deposited energy. To this purpose, I used several complementary diagnostics: study of pressure waves using microphones, characterization of the filamentation plasma by means of spectroscopy and time resolved study of underdense air channels using interferometry. I demonstrated in the single filamentation regime that above a given pulse energy, energy deposition becomes so important that the medium generates a shock wave instead of a sound wave, and that underdense channels can last for more than 100 ms. I also studied and characterized the high energy multifilamentation regime, showing that moderately focusing the pulse leads to a reorganization of filaments in the focal zone, generating large structures with a resulting plasma ten times denser than filaments. Filamentation-induced hydrodynamic effects lead to a transient reduction of the air breakdown voltage along the path of the laser pulse, enabling one to trigger and guide electric discharges. The second part of my thesis focused on the study and the optimization of such guided discharges for the design of a radio-frequency plasma antenna, contactless high-voltage switches or a laser lightning rod. To this purpose I developed and built an interferometric plasma diagnostic, allowing to measure the lifetime of generated plasmas. I also contributed to the proof of principle for a filament induced plasma antenna emitting RF signal. Finally, I took part to prospective experimental studies for the development of a laser lightning rod.

Keywords: nonlinear optics, ultrashort lasers, cold plasmas, hydrodynamics, spark discharges, guided optics

Résumé

La filamentation laser est un régime de propagation optique spectaculaire atteint pour des impulsions dont la puissance crête excède quelques gigawatts dans l'air. Le filament se forme sous l'action de l'effet Kerr optique du milieu traversé qui tend à auto-focaliser le faisceau jusqu'à ce que l'intensité résultante atteigne le seuil d'ionisation du milieu par absorption multiphotonique. Une compétition dynamique complexe s'établit alors entre l'effet Kerr, d'une part, et la diffraction, l'absorption non-linéaire de l'énergie laser et l'effet défocalisant du plasma d'autre part. Il en résulte une réorganisation du profil du faisceau, caractérisée par un coeur mince (100 µm) et intense (10^{18} W $\cdot$ m^{-2}) pouvant se maintenir sur une distance égale à plusieurs longueurs de Rayleigh. Lorsque la puissance initiale de l'impulsion dépasse largement le seuil de filamentation, on assiste à la formation de plusieurs filaments co-propagatifs au sein du même faisceau, chacun de ces multifilaments possédant des caractéristiques physiques proches de monofilaments isolés. Au cours de sa propagation dans l'air, le filament transfère une partie de l'énergie laser au milieu, principalement via l'excitation rotationnelle Raman des molécules d'air, l'ionisation de l'air et l'effet de Bremsstrahlung inverse au sein du plasma. Cette énergie est redistribuée au cours de la nanoseconde suivant le passage du laser, principalement sous forme d'énergie translationnelle des molécules d'air, c'est-à-dire de chaleur. Le milieu réagit à ce chauffage rapide par la formation d'une onde de pression cylindrique, qui ramène le système à l'équilibre de pression en éjectant de la matière du centre. Il en résulte la formation d'un canal d'air sous-dense et chaud, qui se résorbe par diffusion à des échelles de temps supérieures à la milliseconde. Ma thèse s'est en premier lieu focalisée sur l'étude et l'optimisation du dépôt d'énergie dans l'air par filamentation. J'ai ainsi étudié l'influence des différents paramètres laser, comme l'énergie de l'impulsion, la focalisation employée et la durée d'impulsion sur la densité d'énergie déposée. Pour ce faire, j'ai employé plusieurs diagnostics complémentaires : mesure des ondes de pression à l'aide de microphones, analyse du plasma de filament par spectroscopie et mesure résolue en temps des canaux sous-dense par interférométrie. J'ai ainsi montré en régime de monofilamentation qu'au-delà d'une certaine énergie laser initiale, le dépôt d'énergie devient si important qu'une onde de choc est générée en lieu et place d'une onde sonore, et que les canaux sous-denses résultant ont des durées de vie de l'ordre de 100 ms. J'ai également étudié et caractérisé le régime de multifilamentation à haute énergie, montrant qu'en focalisant modérément l'impulsion, les filaments se réorganisent dans la zone focale pour former des structures plus larges générant un plasma dix fois plus dense que les filaments. Les effets hydrodynamiques engendrés par filamentation entraînent un abaissement transitoire du seuil de claquage électrique de l'air le long du trajet de l'impulsion laser, permettant ainsi de déclencher et de guider des décharges électriques. La seconde partie de ma thèse avait pour objet l'étude et l'optimisation de telles décharges guidées pour la mise au point d'une antenne plasma radio-fréquence, de commutateurs haute tension sans contact ou encore d'un paratonnerre laser. Pour ce faire, j'ai développé et construit un diagnostic plasma interférométrique à deux couleurs permettant de caractériser la durée de vie des plasmas générés. J'ai également participé à une expérience de principe démontrant la possibilité de réaliser une antenne plasma RF à partir d'un filament laser. Enfin, j'ai participé à diverses études expérimentales prospectives dans l'optique du développement d'un paratonnerre laser.

Mots-clés : optique non-linéaire, lasers ultracourts, plasmas froids, hydrodynamique, décharges spark, optique guidée